

# **Atom-chip Bose-Einstein condensation in a portable vacuum cell**

by

**Shengwang Du**

B.S., Electrical Engineering, Nanjing University, China, 1996

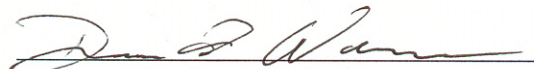
M.S., Physics, Peking University, China, 1999

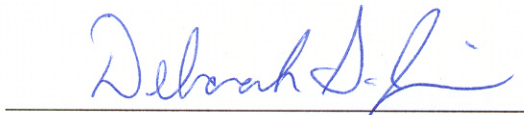
M.S., Electrical Engineering, University of Colorado at Boulder, 2002

A thesis submitted to the  
Faculty of the Graduate School of the  
University of Colorado in partial fulfillment  
of the requirements for the degree of  
Doctor of Philosophy  
Department of Physics

2005

This thesis entitled:  
Atom-chip Bose-Einstein condensation in a portable vacuum cell  
written by Shengwang Du  
has been approved for the Department of Physics

  
Dr. Dana Z. Anderson

  
Dr. Deborah S. Jin

Date April 5<sup>th</sup>, 2005

The final copy of this thesis has been examined by the signatories, and we find that both the content and the form meet acceptable presentation standards of scholarly work in the above mentioned discipline.

Du, Shengwang (Ph.D., Physics)

Atom-chip Bose-Einstein condensation in a portable vacuum cell

Thesis directed by Prof. Dana Z. Anderson

Cold atom guiding and manipulation using lithographically patterned wires on substrates have demonstrated the possibility of making small-scale atom-chip devices for practical applications. Nevertheless, like all Bose-Einstein condensate (BEC) systems developed to date, chip-scale atomic systems require an unwieldy assembly of electronic, optical, and vacuum instrumentation. This thesis reports on the significant simplification and size reduction of the vacuum system for atom-chip-based BEC production. The atom chip itself forms one wall of the vacuum system and enables direct electrical connections outside of vacuum to the chip instead of relying on vacuum feed-throughs. We have produced a portable system that can be assembled, processed, and then inserted into an ultracold atom apparatus in much the same way that an electronic vacuum tube can be plugged into an existing receiver. Our portable atom-chip cell has a total size of less than  $30 \times 30 \times 15$  cm. The ultrahigh vacuum of  $10^{-10}$  torr is maintained by a small, 8 L/s ion pump and nonevaporable getter. We have successfully achieved a  $^{87}\text{Rb}$  BEC in a micro Z-wire trap. The condensate has about 2,000  $^{87}\text{Rb}$  atoms in the  $F=2$ ,  $M_F=2$  state. All cooling and trapping processes occur from 2 mm to 80  $\mu\text{m}$  below the chip. This work suggests that a chip-based BEC-compatible vacuum system can occupy a volume of less than 0.5 liter.

## **Dedication**

To my dear wife, Lijing Ye (叶丽静),  
and new born son, Preston Y. Du (杜泽豪)



## Acknowledgment

In 1999, when I entered the United States and Boulder city for the first time, I knew little about this country and this university. Like most other foreigners, I have been pursuing my own American dream. Six years' PhD Physics study and research at the University of Colorado at Boulder has been filled with joy and hope. Although it is my passion and enthusiasm for physics that led me through all the years, it was impossible to finish my PhD study and this thesis without many people's support.

First, I thank my advisor, Dr. Dana Z. Anderson, for all his support. Without him, I would not have gained so much during my research work. Five years ago, I didn't have any optical experimental experience: I did not know a wave plate, a beam splitter, or even a dielectric mirror. But he trusted me and said, "I will train you to be an experimental physicist." At many times, when many people, including myself, doubted if it was possible to create a Bose-Einstein condensation (BEC) in such a small cell, he always put his faith on it. Sometimes when I was sad and upset about zero progress, he encouraged me and directed me. As an advisor, Dana discovered and explored my capability and built my confidence for the future.

Second, I would like to acknowledge Leslie Czaia. She is the one who assembles the atom chip and quartz cell together. Without her magical hands, it would be impossible to build up the portable atom-chip cell, and impossible for me to carry out all the experiments. What is the most important is that she treats me like her younger brother and makes me feel at home in the lab. I have learned a lot from her.

Dr. Patrick Berthoud, a previous postdoctoral associate during my first year in the group, taught me how to build and make an optical-magnetic trap (MOT). From him, I learned the fundamentals of laser cooling experimental skills. The most important inheritance he left me is the design of the JILA-mount external cavity laser diode system (section 4.2) with which I have built all the lasers.

I miss Yutaka Imai, who returned to the Sony Corporation after the summer of 2003. The

year I had spent with him was the most fruitful one in completing the entire optical-electronic system. For many nights, we worked together in debugging the system and taking measurements. He was my best company during that period of time. Without his contribution, the optical system could not have been completed.

Now, I want to express my appreciation to my coworker, Matthew B. Squires. We have been working together for the past four years on this project and experienced through all the sad and exciting moments.

I highly appreciate the cooperation with Dr. Victor M. Bright's group at Department of Mechanical Engineering for fabricating chips for us.

Meanwhile, I want to remember all the following people: Benjamin Luey, Brain McCarthy, R. A. Saravanan, Evan Salim, Seth Frader-Thompson, Ying-ju Wang, Dirk Muller, Tetsuo Kishimoto, Peter Schwindt, Quentin Diot, Stephen Segal, Paul Smith, Marty Baylor, Steven Hughes, Edeline Fortheringham, and Hongke Ye. I thank Zhigang Chen for his magnetic wire coils and some startup work for the project. I thank S. Inoyoe and J. Goldwin from D. Jin's group for helpful discussions about RF evaporative cooling. I thank Eun Oh from US Naval Research Lab (NRL) for his help in the English writing of this thesis and discussion of Physics. I thank Julie Phillips at Scientific Reports Office (SRO) for teaching me in scientific writing and helping me throughout editing the thesis. I also want to thank the electronic and machine shops for their wonderful technical services.

During the years of my study and research, I have received advice and suggestion from Professor Eric Cornell and Carl Wieman about vacuum and cold atoms. Especially when Dana was out of town, they used their expensive time to give us their knowledge and experience. I also thank them for joining my compressive examination III committee. Most importantly because of their original work on the first BEC in 1995, I now see the future of BEC atom chips.

Here, I appreciate the support from my final defense committee. They are Dr. Dana Z. Anderson, Dr. Deborah S. Jin, Dr. Jun Ye, Dr. Senarath De Alwis, and Dr. Victor M. Bright.

I want to thank my American host family, Mr. and Mrs. Caldwell. They never hesitate to

give me and my wife any help we need, and make us feel at home in the state.

At last, I want to thank my family in China: my mother and father. It is they who have been encouraging me to pursue my dream for the past thirty years even though they never received any high education at their age. Now it is time to do something for them after my graduation.

The most important support and driving force I received is from my own family: my dear wife Lijing Ye (叶丽静), and our new born son Preston Y. Du (杜泽豪). To support my work, my wife married me as early as she could and moved with me to Boulder from China. Without her support, I was not able to work later than midnight and overnight. For our own family, she put her dream into mine.

My PhD study is over, but my life will move on. Thanks, JILA! Thanks, the department of physics at CU-Boulder! Thanks for all the people I have worked and lived with.

# Contents

1.	Introduction	1
2.	Theory of cooling and trapping on an atom chip	3
2.1	Two-state laser-coupled system-----	3
2.1.1	Hamiltonian-----	3
2.1.2	Steady-state population-----	5
2.1.3	Photon-atom scattering cross section-----	6
2.1.4	Optical force-----	10
2.2	Magneto-optical trap -----	11
2.2.1	Optical molasses-----	11
2.2.2	MOT configurations-----	13
2.2.3	Capture velocity-----	16
2.2.4	Capture volume-----	17
2.2.5	Loading equation-----	18
2.2.6	Polarization gradient cooling -----	19
2.3	Atom-chip magnetic trap-----	21
2.3.1	Chip wire micro trap-----	22
2.4	Adiabatic compression-----	30
2.4.1	Linear trap-----	31
2.4.2	Harmonic trap-----	32
2.4.3	Atom-chip Z-wire trap-----	32
2.4.4	Adiabatic requirement-----	33
2.5	Trap-depth dependent lifetime-----	34
2.6	Forced evaporative cooling-----	36
2.6.1	RF-forced evaporation-----	37
2.6.2	Surface-induced evaporation on an atom chip-----	38

2.6.3	Direct evaporation on an atom chip-----	39
2.7	Bose-Einstein Condensation -----	41
2.7.1	Noninteracting BEC-----	41
2.7.2	Interaction between atoms-----	42
2.8	Measurement-----	42
2.8.1	Absorption and fluorescence imaging-----	42
2.8.2	Time of flight -----	44
3.	A portable atom-chip vacuum cell	48
3.1	Introduction-----	48
3.2	First generation atom-chip vacuum system-----	50
3.3	A portable atom-chip vacuum cell-----	52
3.3.1	Fabrication of the atom-chip glass cell-----	53
3.3.2	Rubidium dispenser-----	56
3.3.3	Pyrex helix-----	58
3.3.4	Nonevaporable getter -----	59
3.3.5	Small ion pump -----	60
3.3.6	Pinch-off tube-----	60
3.4	Pumping station-----	60
3.5	Baking out and pumping down procedure -----	62
3.6	Conclusion -----	63
4.	Optical system	64
4.1	Overview -----	64
4.2	JILA-mount external cavity laser diode -----	66
4.3	Cooling laser-----	71
4.4	Repumping laser-----	76
4.5	Pumping/probe laser-----	78

4.6	Fiber coupling -----	81
4.7	Atom-chip cell optical table-----	82
4.8	Imaging setup-----	83
4.8.1	Camera configuration-----	83
4.8.2	Atom-chip surface reflection imaging-----	84
5.	Electronic system	86
5.1	Computer-control system-----	87
5.2	Imaging control and DAQ-----	94
5.3	Magnetic coil hat-----	97
5.3.1	Circular coil hat-----	98
5.3.2	Rectangular coil hat-----	100
5.4	Current power supplies-----	102
5.5	RF drive-----	105
5.5.1	AOM driver-----	105
5.5.2	RF coil driver-----	106
6.	Preparation and optimization	107
6.1	Atom-chip cell-----	107
6.2	Laser powers and frequencies-----	108
6.3	External coil mirror MOT-----	108
6.4	Dispenser operating current-----	110
6.5	UV mirror MOT-----	111
6.6	Bias coils field calibration-----	113
6.7	Transferring to the chip U-wire MOT-----	115
6.8	Imaging camera calibration -----	116
6.9	Mirror CMOT -----	118
6.10	Chip CMOT optimization-----	118

6.11 Polarization gradient cooling -----	118
6.12 Optical pumping-----	119
6.13 ZMT loading optimization-----	119
6.14 Final loading optimization-----	120
6.15 Summary and conclusion-----	121
7. Bose-Einstein condensation on the chip	122
7.1 Charging the cell-----	123
7.2 UV mirror MOT-----	123
7.3 External coil mirror CMOT-----	126
7.4 Chip U-wire CMOT-----	128
7.5 Polarization gradient cooling-----	130
7.6 Optical pumping-----	132
7.7 Z-wire magnetic trap -----	134
7.8 ZMT initial compression-----	134
7.9 ZMT compression and forced evaporative cooling-----	134
7.10 BEC on the chip-----	137
7.11 Summary and conclusion-----	139
8. Other atom-chip experiments	140
8.1 Atom splitting during polarization gradient cooling-----	140
8.2 Rethermalization in the Z-wire magnetic trap-----	142
8.3 Surface-induced evaporative cooling-----	144
8.4 Sloshing in the Z-wire magnetic trap-----	146
8.5 Parametric heating in a tightly confined magnetic trap-----	148
8.6 Atom-chip BEC lifetime-----	150
Bibliography	153
Appendix 1 Atom-chip cell vacuum lifetime -----	160

Appendix 2 A miniature atom-chip vacuum cell ----- 164



## Figures

2.1	A two-state system coupled with a laser field -----	4
2.2	A finite-lifetime two-state system coupled with a laser field -----	5
2.3	A standard six-beam MOT setup -----	14
2.4	A Mirror MOT configuration -----	15
2.5	A chip U-wire surface MOT configuration -----	16
2.6	Zeeman splitting and level crossing of $^{87}\text{Rb}$ $5P_{3/2}$ states $F=3$ and $F=2$ -----	17
2.7	One-dimensional schematic diagram of polarization gradient cooling -----	20
2.8	A two-dimensional quadrupole magnetic field generated by a single current wire augmented with a uniform transverse bias magnetic field -----	23
2.9	U-wire, Z-wire magnetic-trap configurations and potential plots -----	24
2.10	A Z-wire magnetic trap -----	25
2.11	The transverse quadrupole two-dimensional trap center offset due to the z-directional bias field induced by the two y-directional wires -----	26
2.12	Z-wire magnetic traps -----	29
2.13	The Z-wire trap loss rate vs the mirror MOT loss rate-----	35
2.14	Zeeman level splitting and RF evaporative cooling -----	37
2.15	Z-wire magnetic trap for surfaced-induced evaporative cooling-----	39
2.16	An H-wire trap pattern design -----	39
2.17	Trap potentials of the H-wire trap as in figure 2.16 -----	40
3.1	Traditional BEC systems with large and complicated vacuum components -----	48
3.2	Apparatuses for the two first BECs on a chip reported in 2001 -----	49
3.3	Diagram of the first-generation- atom-chip cell -----	51
3.4	Portable miniature vacuum cell for the production of a chip BEC -----	52
3.5	The atom chip and its wire pattern -----	54
3.6	Cell construction procedure diagram -----	56

3.7	Results of a pulsed dispenser mode at 6 A -----	57
3.8	Cell pressure P vs Rubidium dispenser current $I_d$ -----	58
3.9	SAES NEG ST172 configuration and activation conditions -----	59
3.10	A portable atom-chip cell is connected to the pumping station via a pinch-off tube. 61	
4.1	Laser optical setup on the optical table -----	64
4.2	Top view of laser optical setup on the small aluminum optical board -----	65
4.3	Pictures of the JILA mount ECLD laser head system -----	67
4.4	Drawing of JILA mount ECLD mechanical components -----	68
4.5	Result of one of the JILA mount ECLD lasers -----	70
4.6	$^{87}\text{Rb}$ D2 line hyperfine energy levels and the MOT cooling transition -----	71
4.7	Cooling laser optical setup before coupled to the fiber -----	72
4.8	Master-slave injection locking signals -----	73
4.9	Slaver laser locked output fraction vs injected master laser power -----	75
4.10	Injection locking range vs injected laser power-----	76
4.11	$^{87}\text{Rb}$ D2 line hyperfine energy levels and the MOT repumping transition -----	77
4.12	Repumping laser optical setup before coupled to the fiber -----	77
4.13	$^{87}\text{Rb}$ D2 line hyperfine energy levels and the pumping and probe transitions -----	79
4.14	Pumping/probe laser optical setup before coupled to the fiber -----	79
4.15	Schematic of the optical pumping effect -----	80
4.16	Schematic of the probe absorption under a bias magnetic field -----	81
4.17	Optical fiber coupling system diagram -----	82
4.18	Atom-chip cell table -----	83
4.19	Camera setup for atom-chip experiments-----	84
4.20	Atom-chip surface reflection imaging -----	85
5.1	Schematic diagram of the atom-chip computer-based control and DAQ system ----	86
5.2	Front panel of MirrorMOT2004V3.1.VI with single-update configuration -----	88

5.3	An example of a single channel wave form with only linear ramps -----	89
5.4	An example of a 2-channel wave forms with only linear ramps -----	89
5.5	Timing table editor front panel sheet -----	91
5.6	Channel timing array editor front panel -----	91
5.7	Imaging controller front panel -----	92
5.8	Waveform browser front panel -----	92
5.9	PDXI-AO-32/16 board configuration front panel sheet -----	93
5.10	RF sweep controller front panel (for forced evaporative cooling) -----	93
5.11	Absorption and background imaging timing with a probe pulse -----	95
5.12	Imaging timing for the dark frame -----	95
5.13	Part of the Labview front panel of the absorption imaging process program -----	96
5.14	Part of the Labview front panel of the absorption imaging process program shows our first BEC on the atom chip with x and y cross section plots and 2-D fitting -----	96
5.15	Atom-chip mirror MOT configuration -----	97
5.16	Dimensions of a circular coil pair -----	98
5.17	Pictures of the circular coil hat -----	99
5.18	Dimensions of a rectangular coil pair -----	100
5.19	Pictures of the rectangular coil hat -----	101
5.20	Switching on and off time of X, Y, and Z bias coils vs current -----	103
5.21	The effect of the 1.9 $\mu$ F capacitor to the MOT coil current stability and its switching time measurement -----	104
5.22	System diagram of AOM RF driver -----	105
5.23	System diagram of the RF coil driver -----	106
6.1	The atom-chip wire pattern -----	107
6.2	External coil mirror MOT fluorescence images -----	109
6.3	The external coil mirror MOT loading vs dispenser current -----	110

6.4	UV mirror MOT loading and lifetime measurement-----	112
6.5	UV LIAD cell pressure recovery time measurement -----	113
6.6	Bias coils calibration -----	114
6.7	Chip U-wire surface mirror MOT fluorescence images -----	115
6.8	Imaging probe beam configuration for both direct through and reflection imaging--	117
6.9	An Apogee CCD camera image of the atom-chip wire pattern -----	117
6.10	The Z-wire current and y bias field ramps during ZMT loading and compression --	120
6.11	Reflection absorption imaging of atoms in a Z-wire trap -----	121
7.1	Time-of-flight (TOF) measurement of the external coil mirror MOTs -----	124
7.2	Absorption image of the external coil mirror MOT -----	125
7.3	TOF measurement of the external coil mirror CMOT -----	126
7.4	Absorption imaging of the external coil mirror CMOT -----	127
7.5	TOF measurement of the chip U-wire CMOT -----	128
7.6	Absorption imaging of the Chip U-wire CMOT -----	129
7.7	TOF measurement after PGC -----	130
7.8	Absorption imaging after PGC -----	131
7.9	TOF measurement after optical pumping-----	132
7.10	Absorption imaging after optical pumping -----	133
7.11	The atom number $N$ , temperature $T$ , peak OD and average PSD as functions of the stop frequency $\nu_3$ at the third RF sweep -----	136
7.12	RF logarithmic sweeps for forced evaporative cooling -----	137
7.13	Images of a Bose-Einstein Condensation -----	138
7.14	Longitudinal BEC atom cloud's optical depth profile, taken at TOF 9ms, fitted to a double gaussian distribution-----	138
8.1	The atom cloud split into three after 4 ms polarization gradient cooling -----	141
8.2	The long rethermalization of atoms in the Z-wire trap -----	143

8.3	The fast rethermalization of atoms in the Z-wire trap -----	144
8.4	Surface-induced evaporative cooling -----	145
8.5	Axial sloshing fitted to an exponential decay oscillation -----	147
8.6	Z-wire current modulation block diagram for parametric heating experiment -----	149
8.7	Parametric heating effect of the Z-wire magnetic trap -----	149
8.8	BEC heating measurement in the compressed and decompressed traps -----	152
8.9	Atom-chip BEC lifetime -----	152
A1.1	UV MOT lifetime history after pinching off -----	160
A1.2	Helium leak and diffusion test -----	161
A1.3	UV MOT lifetime of the cell without flashing -----	162
A2.1	Miniature atom-chip vacuum cell with a 2 L/s ion pump -----	164

## Tables

3.1	Atom-chip cell parts list -----	52
3.2	Pumping station parts list -----	61
3.3	Atom chip cell bakeable and baking temperature -----	62
3.4	Pumping station bakeable and baking temperature -----	62
4.1	Cooling laser frequencies at different cooling stages -----	74
4.2	Commercial part list of fiber coupling-----	82
5.1	2-D array representation of the waveform -----	89
5.2	3-D timing array for 2-channel waveforms -----	90
5.3	Timing table for 2-channel waveforms -----	90
5.4	Specification of the circular coil hat -----	98
5.5	Specification of the rectangular coil hat -----	100
5.6	Commercial part list of AOM drivers purchased from Mini-Circuits -----	105
5.7	Commercial part list of the RF coil driver -----	106
7.1	Atom number $N$ , temperature $T$ , peak OD, collision rate, and PSD after each RF sweep -----	137

## Chapter 1. Introduction

The wave nature of matter in the microscopic world has been an important topic of physics research and a driving force in developing modern scientific technologies for the past one hundred years. Albert Einstein proposed two well-known wave coherence theories for massless photons and massive bosonic atoms, i.e., stimulated emission theory in 1916 [1] and the Bose-Einstein condensation (BEC) predicted in 1924 [2]. Stimulated emission underlied the fundamental of photon-based lasers 40 years later. BECs are now often referred to as “atom lasers.” However, the scientific path lengths of photon and atom lasers are quite different because of their different “inertial masses.” The first maser, or called microwave laser, was realized in 1954. Now laser optical technologies have entered into our daily life. The first BEC with dilute neutral atoms was not accomplished until 1995 by Eric Cornell and Carl Weimann at JILA [3], and Wolfgang Ketterle at MIT [4], and further research can only be done within atomic research labs with complicated and huge system setups. As we look back to the 50 years’ development of laser optical applications, we see a clear and bright future for the atom lasers and atom optics, which may take an even longer time to develop than photon optics. The invention and development of portable, miniature atom-laser sources and devices are the key to transferring the scientific knowledge from atomic physicists to nonexpert engineers’ hands.

The “atom chip” is one of the key elements in minimizing atom-optics systems. In contrast to the electronic micro chips that drive electrons, an atom chip drives and manipulates cold atoms with magnetic field circuits on the chip surface generated by micro-patterned wires and magnets [5–12]. The use of free-standing wires for magnetic atom guiding started as early as 1992 [13]. However, the first realization of BEC on a chip did not occur until 2001 [14, 15]. This breakthrough opened the door towards micro-chip-scale coherent matter-wave devices.

Unfortunately, atom-chip systems still look complicated and huge. First, atom chips are inserted into a relatively large vacuum chamber. Second, the vacuums still require a large pumping station that dominates the system size. In this thesis, I report our achievement of a

portable BEC atom-chip cell system. For the first time, we use the atom chip itself to seal the vacuum cell thus dramatically simplifying the vacuum and feed-through construction. The ultrahigh vacuum is maintained by only a nonevaporable getter (NEG) and a small, 8 L/s, ion pump. The entire vacuum cell has a size of  $30 \times 30 \times 15$  cm [16].

The thesis is organized in the following way. Chapter 2 provides some basic theoretical tools to understand laser cooling and trapping on a chip. Then, we describe the atom-chip cell vacuum construction in detail in chapter 3. Chapters 4 and 5 describe the optical and electronic systems. In chapter 6, I give the procedures for preparing and optimizing the atom-chip experiments. The recipe for making a BEC on the atom-chip is described in chapter 7. Chapter 8 includes other atom-chip related experiments.

My thesis research work focuses on developing the portable BEC atom-chip cell system. Our original work is described in detail from chapter 3 to chapter 8, from the vacuum cell, optical system, and electronic system to the recipe of making BEC on the chip. One thing I must mention is that the atom chip is fabricated by Dr. Victor M. Bright's group in the Mechanical Engineering Department at the University of Colorado. To make this thesis more complete, I summarize their chip fabrication recipe in section 3.3.1. To help readers – most of them will be graduate students – pick up the theoretical tools quickly and understand rest of the thesis, I spend forty pages to review and summarize some important theories of laser cooling and trapping in chapter 2, which I also use to propose some new issues about atom chips, e.g., *Z*-wire trap symmetry axes (section 2.3.1), a new method in realizing atom-chip surface-induced evaporative cooling (section 2.6.2), and direct forced evaporation without any external components (section 2.6.3). Most parts in chapter 2 are not my original work but, as part of this dissertation, are extremely important to understand our atom-chip system and experiments.



## Chapter 2. Theory of cooling and trapping on an atom chip

The physics principles involved in laser cooling and trapping, which have been well developed since the 1980s, are essential for understanding atom-chip experiments. The theoretical analysis can be found in numerous textbooks and publications [17–20]. However, most of those books and review articles are written from the experimentalist’s perspective, and hence no formal derivations are given. From my experience as a graduate student, I often find myself in darkness, not precisely understanding the physics even though I am able to run the experiments. I attempt to clarify here some of the most important derivations step by step, while still siding on the experimentalist’s side. This chapter reviews laser cooling and trapping mechanisms from a two-state laser-coupled system and then explains the fundamentals of magnetic traps, evaporative cooling, and Bose-Einstein condensation (BEC). In the last part, we discuss some concerns about cold-atom imaging.

### 2.1 Two-state laser-coupled system

Laser cooling and trapping are based on the quantum theory of a two-state system, even though all experimental systems actually involve many levels. The simple picture of a two-state system not only allows physicists to interpret the fundamentals, but also opens the door to discovering the secrets of the atomic world.

#### 2.1.1 Hamiltonian

The Hamiltonian of a system takes different forms in specific reference frames, hence finding the simplest Hamiltonian becomes extremely important to physicists. In a two-state quantum system driven by a laser field, the Hamiltonian in the lab reference frame is time dependent. However, as shown later in this section, such a Hamiltonian can be expressed time independently by applying a unitary transformation. After transform, the new frame is referred to as the dressed-state picture [21] or the rotational reference frame.

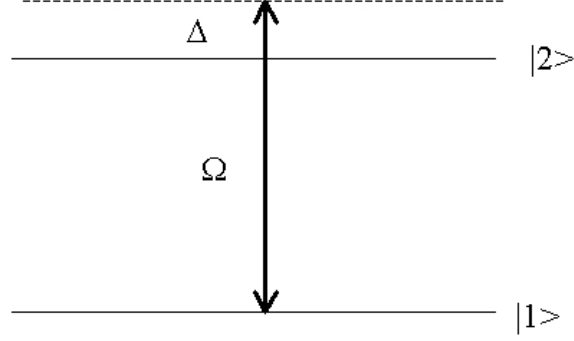


Figure 2.1: A two-state system coupled with a laser field that has a frequency detuning  $\Delta$ .

The diagram of a two-state system coupled with a laser field is shown in figure 2.1. The laser field with a single frequency  $\omega$  is dealt with as a classical electric field

$$\vec{E}(\vec{r}, t) = \frac{1}{2} [\vec{E}(\vec{r}) e^{i\omega t} + \vec{E}(\vec{r})^* e^{-i\omega t}] = \frac{1}{2} [\vec{E}(\vec{r}) e^{i\omega t} + c.c.]. \quad (2.1)$$

When the electric field couples the two-state quantum system, the Hamiltonian can be written from the lab reference frame as

$$\hat{H}(t) = \begin{bmatrix} \varepsilon_1 & \frac{1}{2} \hbar \Omega e^{i\omega t} \\ \frac{1}{2} \hbar \Omega^* e^{-i\omega t} & \varepsilon_2 \end{bmatrix}, \quad (2.2)$$

where we use “ $\wedge$ ” to represent an operator, and  $\varepsilon_1$ ,  $\varepsilon_2$  are energy eigenvalues of the states  $|1\rangle$  and  $|2\rangle$  without any external fields. The Rabi frequency  $\Omega$  is defined by

$$\hbar \Omega = e \langle 1 | \hat{E}(\vec{r}) \cdot \hat{\vec{r}} | 2 \rangle, \quad (2.3)$$

where  $e$  is the absolute value of an electron charge. Thus the time-dependant Schrödinger equation is

$$i\hbar \frac{\partial}{\partial t} |\Psi; t\rangle_s = \hat{H}(t) |\Psi; t\rangle_s. \quad (2.4)$$

The Hamiltonian (2.2) can be transformed into a time independent operator by applying the following unitary transform of

$$\hat{U}_d = e^{i\hat{H}_d t / \hbar} \quad (2.5)$$

with

$$\hat{H}_d = \begin{bmatrix} \varepsilon_1 & 0 \\ 0 & \varepsilon_1 + \hbar\omega \end{bmatrix}. \quad (2.6)$$

Under this transformation, in the new reference frame, the Hamiltonian and wave function go to

$$\hat{H}_1 = \hat{U}_d \hat{H} \hat{U}_d^\dagger = \begin{bmatrix} \varepsilon_1 & \frac{1}{2} \hbar \Omega \\ \frac{1}{2} \hbar \Omega^* & \varepsilon_2 \end{bmatrix} \quad (2.7)$$

and

$$|\Psi; t\rangle_d = \hat{U}_d |\Psi; t\rangle_s = e^{i\hat{H}_d t/\hbar} |\Psi; t\rangle_s. \quad (2.8)$$

The new Schrödinger equation becomes

$$i\hbar \frac{\partial}{\partial t} |\Psi; t\rangle_d = i\hbar \frac{\partial}{\partial t} U_d |\Psi; t\rangle_s = \hat{H}_d |\Psi; t\rangle_d, \quad (2.9)$$

where the new Hamiltonian is

$$\hat{H}_d = \hat{H}_1 - \hat{H}_d = \begin{bmatrix} 0 & \frac{1}{2} \hbar \Omega \\ \frac{1}{2} \hbar \Omega^* & -\hbar \Delta \end{bmatrix}, \quad (2.10)$$

where  $\Delta = \omega - \omega_{21} = \omega - (E_2 - E_1)/\hbar$  is the frequency detuning.

The new Hamiltonian equation (2.10) is the key to studying the two-state system. In the following sections, by solving the population steady-state equation of the quantum ensemble, we understand how the laser field changes the atom population in the states  $|1\rangle$  and  $|2\rangle$ , how the atoms scatter the photons, and what the origin of optical trapping forces is.

### 2.1.2 Steady-state population

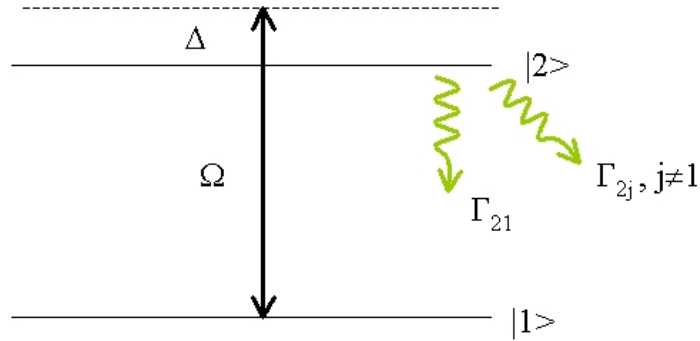


Figure 2.2: A finite-lifetime two-state system coupled with a laser field that has a frequency detuning  $\Delta$ . The atoms in the excited state  $|2\rangle$  decay to the ground state  $|1\rangle$  and the other states with decay rates  $\Gamma_{21}$  and  $\Gamma_{2j}$  ( $j \neq 1$ ), respectively.

To derive the evolution of the population density matrix, we must take into account the finite atom lifetime at the excited state  $|2\rangle$  due to spontaneous emission and other processes. The decay rate from the excited state  $|2\rangle$  to the ground state  $|1\rangle$  is denoted as  $\Gamma_{21}$ , and the decay rates from  $|2\rangle$  to other non- $|1\rangle$  states are represented by  $\Gamma_{2j}$  ( $j \neq 1$ ), as shown figure 2.2. Then the total decay rate is

$$\Gamma_2 = \sum_j \Gamma_{2j} = \Gamma_{21} + \sum_{j \neq 1} \Gamma_{2j}. \quad (2.11)$$

We define the decay operator as

$$\hat{\Gamma} = \begin{bmatrix} 0 & 0 \\ 0 & \Gamma_2 \end{bmatrix}. \quad (2.12)$$

The population evolution equation can be written down as

$$\frac{d}{dt} \rho_{ij} = \left( -\frac{1}{2} \{\hat{\Gamma}, \hat{\rho}\} + \frac{1}{i\hbar} [\hat{H}_d, \hat{\rho}] \right)_{ij}, \quad (i, j) \neq (1,1), \quad (2.13)$$

$$\frac{d}{dt} \rho_{11} = \left( -\frac{1}{2} \{\hat{\Gamma}, \hat{\rho}\} + \frac{1}{i\hbar} [\hat{H}_d, \hat{\rho}] \right)_{11} + \Gamma \rho_{22}, \quad (2.14)$$

under the conservation conditions of

$$\text{Tr} \rho = \rho_{11} + \rho_{22} = 1. \quad (2.15)$$

At the steady state, the atom populations reach equilibrium, i.e.,

$$\dot{\rho}_{ij} = 0, \quad (i, j=1,2). \quad (2.16)$$

Solving the above equations (2.13)–(2.16), we get the following steady-state solutions:

$$\rho_{11} = \frac{\Gamma_2^2 + 4\Delta^2 + |\Omega|^2}{\Gamma_2^2 + 4\Delta^2 + 2|\Omega|^2} = \frac{2+S}{2(1+S)}, \quad (2.17)$$

$$\rho_{22} = \frac{|\Omega|^2}{\Gamma_2^2 + 4\Delta^2 + 2|\Omega|^2} = \frac{S}{2(1+S)}, \quad (2.18)$$

$$\rho_{12} = \frac{(i\Gamma_2 + 2\Delta)\Omega}{\Gamma_2^2 + 4\Delta^2 + 2|\Omega|^2} = \frac{i\Omega}{\Gamma_2 - i2\Delta} \cdot \frac{1}{1+S}, \quad \text{and} \quad (2.19)$$

$$\rho_{21} = \frac{(-i\Gamma_2 + 2\Delta)\Omega^*}{\Gamma_2^2 + 4\Delta^2 + 2|\Omega|^2} = \frac{-i\Omega^*}{\Gamma_2 + i2\Delta} \cdot \frac{1}{1+S} = \rho_{12}^*. \quad (2.20)$$

Here the saturation factor  $S$  is given by

$$S \equiv \frac{|\Omega|^2}{2|\Gamma_2/2 - i\Delta|^2} = \frac{|\Omega|^2/2}{\Delta^2 + \Gamma_2^2/4} \equiv \frac{S_0}{1 + (2\Delta/\Gamma_2)^2}, \quad (2.21)$$

where the last step defines the on-resonance saturation parameter

$$S_0 \equiv \frac{2|\Omega|^2}{\Gamma_2^2}. \quad (2.22)$$

The meanings of the saturation factor and parameter will be further explained in the next section.

### 2.1.3 Photon-atom scattering cross section

The photon-atom scattering cross section is a frequently used parameter to characterize the

interaction strength between photons and atoms. In general laser physics, the light scattering cross-section  $\sigma_s$  is defined through the following population evolution equation [22]:

$$\frac{d}{dt}\rho_{22} = -\Gamma_2\rho_{22} - \frac{\sigma_s I}{\hbar\omega}(\rho_{22} - \rho_{11}), \quad (2.23)$$

where  $I$  is the laser intensity and  $\sigma_s I / \hbar\omega$  is the number of photons per unit time absorbed by a single ground-state atom or emitted from a single excited-state atom because of the laser field. Therefore, the first term on the right side of equation (2-23) represents the spontaneous emission, and the second term represents the stimulated emission and absorption. At the steady-state condition, equation (2.23) goes to

$$\frac{d}{dt}\rho_{22} = -\Gamma_2\rho_{22} - \frac{\sigma_s I}{\hbar\omega}(\rho_{22} - \rho_{11}) = 0. \quad (2.24)$$

Using the conservation condition equation (2.15), the steady-state solution is given by

$$\rho_{22} = \frac{\frac{\sigma_s I}{h\nu}}{\Gamma_2 + \frac{2\sigma_s I}{h\nu}} = \frac{\frac{\sigma_s I}{h\nu}\Gamma_2}{\Gamma_2^2 + \frac{2\sigma_s I}{h\nu}\Gamma_2}. \quad (2.25)$$

Solving equations (2.18) and (2.25), we find the expression for  $\sigma_s$

$$\sigma_s = \frac{\Gamma_2 h\nu |\Omega|^2}{I(\Gamma_2^2 + 4\Delta^2)}. \quad (2.26)$$

When only spontaneous emission is considered, we have the relationship between the decay rate

$\Gamma_{21}$  and electric dipole element  $\vec{d}_{12} = \langle 1 | \hat{r} | 2 \rangle$  [23]:

$$\Gamma_{21} = \frac{8\pi^2 d_{12}^2}{3\varepsilon_0 \hbar \lambda^3}, \quad (2.27)$$

where  $\varepsilon_0$  is the vacuum electric constant and  $\lambda$  is the transition wavelength. The Rabi frequency defined in equation (2.3) can be rewritten as

$$\Omega = \vec{E} \cdot \vec{d}_{12} / \hbar. \quad (2.28)$$

From the intensity expression  $I = \frac{1}{2} c \varepsilon_0 E^2$ , we get

$$|\Omega|^2 = I \frac{3\lambda^3 \Gamma_{21}}{4\pi^2 \hbar c} = I \frac{3\lambda^3 \Gamma_{21}}{2\pi \hbar c}, \quad (2.29)$$

where we have used  $\hbar = 2\pi\hbar$  and  $c$  is the speed of light in vacuum. Then we rewrite the cross section equation (2.26) as

$$\sigma_s = \frac{3\lambda^2}{2\pi} \frac{\Gamma_{21}}{\Gamma_2} \frac{(\Gamma_2/2)^2}{\Delta^2 + (\Gamma_2/2)^2} = \sigma_0 \frac{1}{1 + \delta^2} = \sigma_0 \frac{\Gamma}{4} g_N(\nu), \quad (2.30)$$

where we use  $\omega = 2\pi\nu$ ,  $\Delta = 2\pi\Delta\nu = 2\pi(\nu - \nu_0)$ . The on-resonance cross section is

$$\sigma_0 = \frac{3\lambda^2}{2\pi} \frac{\Gamma_{21}}{\Gamma_2}, \quad (2.31)$$

the dimensionless frequency detuning is defined by

$$\delta \equiv \frac{\Delta}{\Gamma_2/2} = \frac{\Delta\nu}{\gamma_2/2}, \quad (2.32)$$

and the Lorentz line-shape function is

$$g_N(\nu) = \frac{\Gamma_2}{\Delta^2 + (\Gamma_2/2)^2} = \frac{1}{2\pi} \frac{\gamma_2}{(\nu - \nu_0)^2 + (\gamma_2/2)^2}, \quad (2.33)$$

with a natural line width  $\gamma_2 = \Gamma_2/2\pi$ .

To calculate the net absorption, we must take into account both the absorption and stimulated emission. From the steady-state equation (2.24), we have

$$\hbar\omega\Gamma_2\rho_{22} = I\sigma_s(\rho_{11} - \rho_{22}) \equiv I\sigma_{abs}, \quad (2.34)$$

where  $\sigma_{abs}$  is the net absorption cross section. Equation (2.34) shows the energy conservation law that the net absorbed light power (right side of equation) equals the spontaneous emission power (left side of equation). Using the solutions (2.17) and (2.18), we express the net absorption cross section as

$$\sigma_{abs} = \sigma_0 \frac{1}{1 + \delta^2 + I/I_{s0}}, \quad (2.35)$$

where the on-resonance saturation intensity is

$$I_{s0} \equiv \frac{1}{3} \frac{\Gamma_2}{\Gamma_{21}} \frac{\pi\hbar c\Gamma_2}{\lambda^3} = \frac{h\nu\Gamma_2}{2\sigma_0}. \quad (2.36)$$

As shown in equation (2.35), the laser intensity plays the same role as the frequency detuning and broadens the effective line width. The line width broadening caused by the laser power is called the power broadening effect [24, 25]. To separate the natural line-shape function and the power broadening effect, equation (2.35) can be rewritten as

$$\begin{aligned}\sigma_{abs} &= \sigma_0 \frac{1}{1 + \delta^2 + I/I_{s0}} = \sigma_0 \frac{1}{1 + \delta^2} \frac{1}{1 + I/I_s(\nu)} \\ &= \sigma_0 \frac{\Gamma}{4} g_N(\nu) \frac{1}{1 + I/I_s(\nu)},\end{aligned}\quad (2.37)$$

where the frequency-dependent saturation intensity is

$$I_s(\nu) = I_{s0}(1 + \delta^2). \quad (2.38)$$

The on-resonance saturation parameter defined in equation (2.22) can be expressed by laser intensity

$$S_0 \equiv \frac{2|\Omega|^2}{\Gamma^2} = \frac{I}{I_{s0}}, \quad (2.39)$$

and the saturation factor  $S$  defined in equation (2.21) is given by

$$S \equiv \frac{S_0}{1 + \delta^2} = \frac{I}{I_{s0}(1 + \delta^2)} = \frac{I}{I_s(\nu)}. \quad (2.40)$$

As shown in equation (2.37), a large intensity  $I > I_{s0}$  reduces the net absorption cross-section and broadens the line width, i.e., the absorption is saturated. This saturation comes from the saturation of the atom population in the excited state and ground state as shown in equations (2.17) and (2.18). The higher the laser intensity, the more atoms that are pumped from the ground state  $|1\rangle$  to the excited state  $|2\rangle$ , and thus the fewer atoms are left for net absorption.

Now, let's look at some examples of  $^{87}\text{Rb}$  transitions. When the atoms are polarized by an external bias magnetic field, the transition from  $|1\rangle = |5S1/2, F=2, M_F=2\rangle$  to  $|2\rangle = |5P3/2, F=3, M_F=3\rangle$  ( $\lambda=780$  nm) is a pure closed two-state system, where  $\Gamma_{21} = \Gamma_2 = 2\pi \times 6$  MHz. Its on-resonance saturation intensity is  $I_{s0} = 1.65$  mW/cm<sup>2</sup>, and its on-resonance cross section is

$$\sigma_0 = 3\lambda^2 / 2\pi = 0.29 \mu\text{m}^2. \quad (2.41)$$

This transition is often used to image cold atom clouds in a magnetic trap because of its closed cycle transition and large cross section.

However, if there is no external magnetic field, the atoms are nonpolarized and all Zeeman sublevels are degenerate. One example is atoms in a magneto-optical trap (MOT). The  $^{87}\text{Rb}$  MOT

cooling transition is from  $|1\rangle=|5S_{1/2}, F=2\rangle$  to  $|2\rangle=|5P_{3/2}, F=3\rangle$ . In this case, we average the decay rate  $\Gamma_{21}$  to the degeneracy of ground states  $g_1 = 5$ . The total decay rate  $\Gamma_2$  is averaged over the degeneracy of the excited states  $g_2 = 7$ , with a sum of three photon-spin polarizations of the spontaneous emission:

$$\langle \Gamma_{21} \rangle_1 = \frac{1}{g_1} \sum_{i,j} \Gamma_{2i,1j}, \quad (2.42)$$

$$\text{and } \langle \Gamma_2 \rangle_2 = \frac{1}{g_2} \sum_{i,j,x} \Gamma_{2i,j}^x = \frac{3}{g_2} \sum_{i,j} \Gamma_{2i,1j} = 3 \frac{g_1}{g_2} \langle \Gamma_{21} \rangle_1, \quad (2.43)$$

where x corresponds to 3 polarization freedoms and  $g_i$  ( $i=1, 2$ ) is the degeneracy. Then we obtain

$$\langle \sigma_0 \rangle = \frac{g_2}{g_1} \frac{\lambda^2}{2\pi}. \quad (2.44)$$

With  $g_1 = 5$  and  $g_2 = 7$ , we get the on-resonance cross section  $\sigma_0 = 7\lambda^2/10\pi = 0.136 \mu\text{m}^2$  and the on-resonance saturation intensity  $I_{s0} = 3.54 \text{ mW/cm}^2$ . The saturation intensity is  $35.4 \text{ mW/cm}^2$  with a red detuning  $\Delta = 2\pi \times 9 \text{ MHz}$  in our MOT configuration. Our cooling laser has a diameter of 8 mm, and we find that the additional laser power does not help to increase the atom number in the trap if the total power is more than 30 mW. This experimental result is consistent with a theoretical saturation intensity of  $35.4 \text{ mW/cm}^2$ .

Comparing the cross section equations (2.41) and (2.44), we find there is a factor of 3 difference in the on-resonance cross sections as  $g_1 = g_2$ . This difference is simply caused by the polarization freedoms of spontaneous emission. For a pure two-state closed system, the spontaneous emission can take only one polarization, the same as the absorbed photons. However, in a degenerate two-state system like the MOT cooling transition, the spontaneous emission occurs in all three polarization degrees of freedom.

## 2.1.4 Optical force

In laser cooling and trapping, understanding where the damping cooling and trapping forces come from is essential. These optical forces may vary completely in different configurations. However, there is only one fundamental physics equation.



From the expression (2.10), we get the force operator

$$\hat{F} = -\nabla \hat{H}_d = \frac{\hbar}{2} \begin{bmatrix} 0 & \nabla \Omega \\ \nabla \Omega^* & 0 \end{bmatrix}. \quad (2.45)$$

The average force on an atom by the laser field can be calculated by

$$\langle \vec{F} \rangle = \text{Tr} \left( \hat{\rho} \hat{F} \right). \quad (2.46)$$

In general, the Rabi frequency  $\Omega$  is a complex function as

$$\Omega(\vec{r}) = \frac{e}{\hbar} \langle 1 | \hat{E}(\vec{r} - \vec{r}_a) \cdot \hat{r}_a | 2 \rangle, \quad (2.47)$$

where  $\vec{r}_a$  is the relative displacement from the atom. The amplitude gradient of the Rabi frequency gives the dipole force necessary for optical traps [26–28]. The phase gradient raises the radiation pressure force in a MOT as shown in section 2.2.

## 2.2 Magneto-optical trap

Since the first magneto-optical trap (MOT) was demonstrated in 1987 [29], the MOT has become the most widely used trap for neutral atoms. In most BEC experiments, the MOT is used for initial cooling and trapping to capture a large number of atoms with a temperature range of 10–1000  $\mu\text{K}$ . Then the precooled atoms are transferred into a magnetic or optical trap for evaporative cooling. The MOT is a very robust trap that does not require very precise optical alignment. In the MOT, the radiation interaction between atoms and photons provides both cooling and trapping. The Doppler frequency shift results in an optical molasses to cool atoms [30, 31], and the frequency modulation from inhomogeneous magnetic fields produces a restoration force to trap atoms [29]. In our atom-chip system, the magnetic field gradients are modest and can readily be achieved with simple coils and atom-chip wires.

### 2.2.1 Optical molasses

First, we look at the atoms in a plane wave optical field that propagates along the  $z$  direction. The complex electric field and Rabi frequency are represented by

$$\vec{E}(\vec{r}) = \vec{E}_0 e^{-ikz}, \quad (2.48)$$

$$\Omega(z) = \Omega_0 e^{-ikz}, \quad (2.49)$$

where

$$\Omega_0 = \frac{e}{\hbar} \langle 1 | \vec{E}_0 \cdot \vec{r} | 2 \rangle. \quad (2.50)$$

Then the Hamiltonian in equation (2.10) can be expressed as

$$\hat{H}_d = \hbar \begin{bmatrix} 0 & \frac{1}{2} \Omega \\ \frac{1}{2} \Omega^* & -\Delta \end{bmatrix} = \hbar \begin{bmatrix} 0 & \frac{1}{2} \Omega_0 e^{-ikz} \\ \frac{1}{2} \Omega_0^* e^{ikz} & -\Delta \end{bmatrix}. \quad (2.51)$$

From equation (2.45), we derive the force operator

$$\hat{F} = -\frac{\partial}{\partial z} \hat{H}_d = \frac{\hbar}{2} \begin{bmatrix} 0 & ik\Omega \\ -ik\Omega^* & 0 \end{bmatrix} \quad (2.52)$$

and its average expected value

$$F = \langle \hat{F} \rangle = \text{Tr}(\hat{\rho} \hat{F}) = \hbar k \text{Im} \{ \rho_{12} \Omega^* \}. \quad (2.53)$$

From equations (2.18) and (2.19), we get

$$\text{Im} \{ \rho_{12} \Omega^* \} = \frac{\Gamma_2 |\Omega|^2}{\Gamma_2^2 + 4\Delta^2 + 2|\Omega|^2} = \Gamma_2 \rho_{22} \equiv \gamma_p, \quad (2.54)$$

where  $\gamma_p$  is defined as the pumping rate. Then the force is expressed by

$$F = \hbar k \gamma_p = \hbar k \rho_{22} \Gamma_2 = \frac{\hbar k \Gamma_2 |\Omega|^2}{\Gamma_2^2 + 4\Delta^2 + 2|\Omega|^2} = \frac{\hbar k \Gamma_2}{2} \frac{S_0}{1 + S_0 + \left( \frac{\Delta}{\Gamma_2/2} \right)^2}. \quad (2.55)$$

From equation (2.34) under the steady-state condition, equation (2.55) can be rewritten as

$$F = \hbar k \frac{I \sigma_s (\rho_{11} - \rho_{22})}{\hbar \omega} = \hbar k \times \text{net absorbed photon \# per unit time} \quad (2.56)$$

The physics of equation (2.56) is very clear: the force comes from momentum transferred from the net absorbed photons.

A one-dimensional (1D) optical molasses (OM) can be produced by two counter-propagating laser beams with red frequency detuning, i.e.,  $\Delta = -|\Delta| < 0$ . For atoms moving along the  $z$  direction with a velocity  $v$ , there is a Doppler shift in the frequency in the atom's moving reference frame:

$$\Delta \rightarrow \Delta \mp kv \quad (\text{to the } \pm z \text{ propagating beam}). \quad (2.57)$$

The expression (2.57) gives the forces from the two individual laser beams

$$F_{\pm} = \pm \frac{\hbar k \Gamma}{2} \frac{S_0}{1 + S_0 + \left( \frac{\Delta \mp kv}{\Gamma/2} \right)^2}, \quad (2.58)$$

where  $\pm$  represents beam propagating directions. The net damping force from the optical molasses can be written by:

$$F_{OM} = F_+ + F_- \cong -\beta v, \quad (2.59)$$

where the damping coefficient is

$$\beta \equiv - \left. \frac{dF_{OM}}{dv} \right|_{v=0} = \frac{4\hbar k^2 S_0 (2|\Delta|/\Gamma)}{\left(1 + S_0 + (2\Delta/\Gamma)^2\right)^2}. \quad (2.60)$$

The 1D model can be easily extended to a 3D case with three pairs of laser beams.

## 2.2.2 MOT configurations

The damping force of the optical molasses provides a Doppler cooling mechanism. However, to trap atoms, there must be a position-dependant restoration force. This restoration force can be obtained by adding a position-dependant frequency modulation into the Doppler shift in equations (2.57) in the following way:

$$\Delta \rightarrow \Delta \mp kv \mp \xi z \quad (\pm z \text{ propagation beam}). \quad (2.61)$$

Then the force equation (2.58) can be corrected to become:

$$F_{\pm} = \pm \frac{\hbar k \Gamma}{2} \frac{S_0}{1 + S_0 + \left( \frac{\Delta \mp kv \mp \xi z}{\Gamma/2} \right)^2}. \quad (2.62)$$

The net force from the two counter-propagating beams becomes

$$F_{MOT} = F_+ + F_- \cong -\beta v - Kz, \quad (2.63)$$

where

$$K \equiv - \left. \frac{\partial F_{MOT}}{\partial z} \right|_{v=0, z=0} = \frac{\xi}{k} \beta. \quad (2.64)$$

In a MOT, as described later, the position-dependant frequency modulations shown in equations (2.61) are accomplished with different circular polarizations in a quadruple magnetic

field.

### 2.2.2.1 Standard six-beam MOT

A standard six-beam MOT configuration is shown in figure 2.3. It consists of an anti-Helmholtz coil pair and six red-detuned laser beams [29]. As discussed previously, the six red-detuned laser beams and the quadrupole magnetic field provide three-dimensional optical molasses cooling and trapping. As shown in figure 2.3(b), the Zeeman energy level splitting and crossing in the quadrupole magnetic field meet the requirements of equation (2.61) for two counter-propagating laser beams with  $\sigma_+$  and  $\sigma_-$  polarizations. The position-dependant radiation optical force provides a restoration-trapping force toward the coil center, i.e., the atoms at a displacement  $x > 0$  (or  $x < 0$ ) absorb more light from the  $\sigma_+$  (or  $\sigma_-$ ) beam such that they get a net force toward the origin.

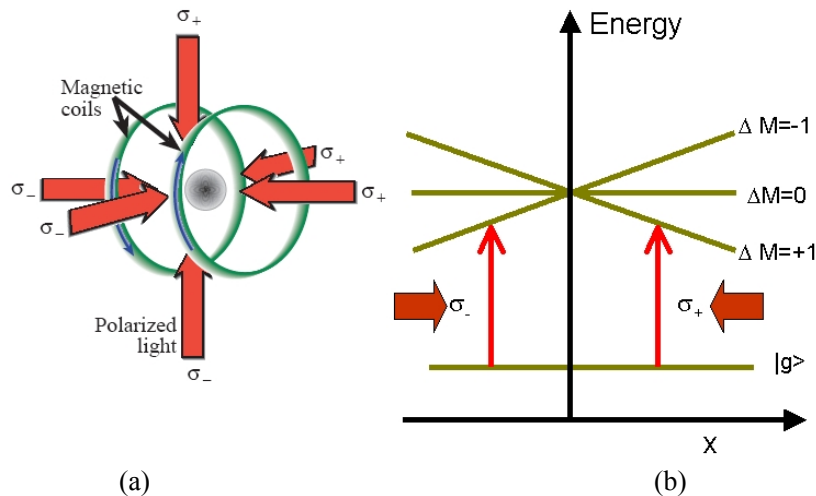


Figure 2.3: A standard six-beam MOT setup. (a) Field configuration. (b) Energy level splitting and crossing due to the Zeeman effect at a linear magnetic field.  $|g\rangle$  is the ground states.  $M$  is the magnetic momentum quantum number.

### 2.2.2.2 Mirror MOT

There is a reflection symmetry in the standard six-beam MOT geometry. As shown in figure 2.4 where we rotate the system by  $45^\circ$  for convenience, the atoms do not experience any difference in the magneto-optical field if the two upper laser beams [figure 2.4(a)] are replaced

with a mirror [figure 2.4(b)]. The MOT configuration with a mirror is called a mirror MOT [6] and requires only four laser beams. The mirror MOT does not only reduce the number of laser beams, but also prepares the cold atoms on the mirror surface for atom-chip loading.

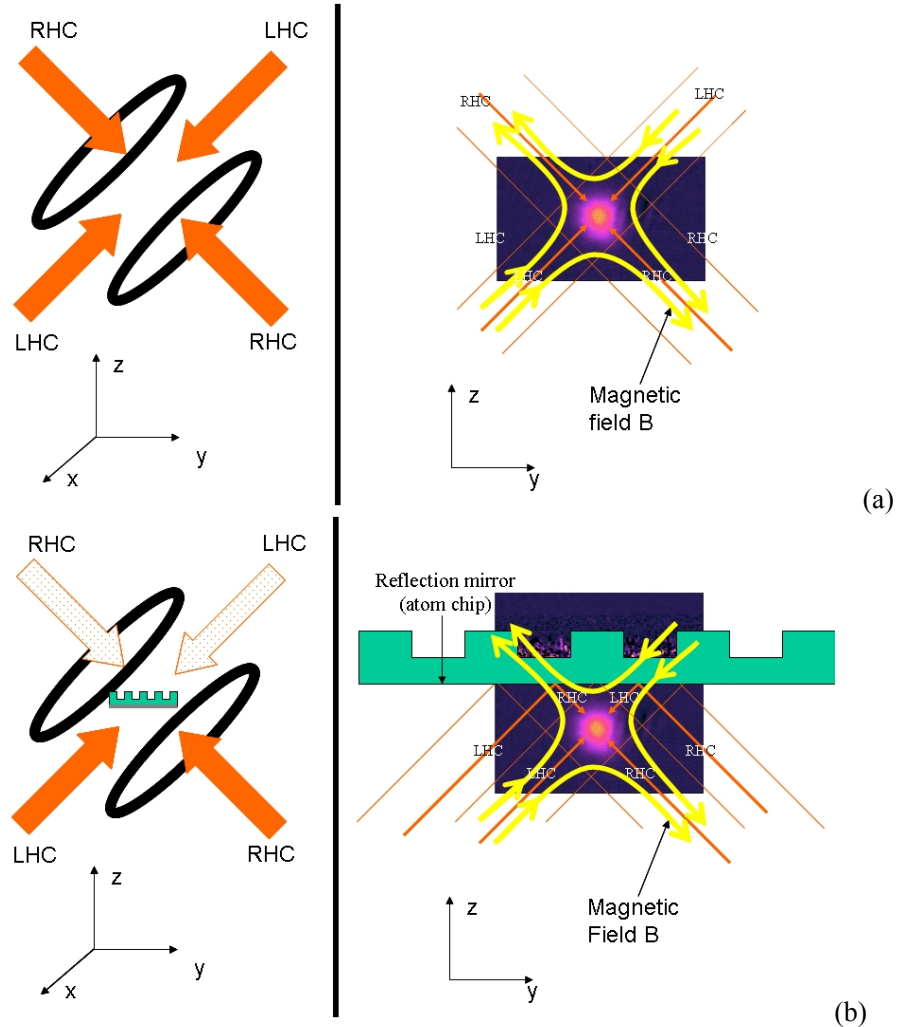


Figure 2.4: A Mirror MOT configuration (b) vs a standard six-beam MOT (a)

### 2.2.2.3 Chip U-wire surface MOT

The anti-Helmholtz coil is not the only way to produce the quadrupole magnetic field for a MOT. In the mirror-MOT configuration, the  $45^\circ$  MOT coils can be replaced by a U-shaped wire on the back of the mirror, as shown in figure 2.5. The U-wire current and a  $y$ -bias magnetic field create a three-dimensional quadrupole magnetic field below the wire [32]. The beauty of this U-wire is that we can integrate it into an atom-chip.

The U-wire dimension in our BEC atom chip has  $L = 0.8$  mm and  $d = 200$   $\mu\text{m}$ . With the

current  $I_U = 2$  A and y-bias field  $B_y = 1$  G, we create a chip MOT at 1 mm below the chip surface. With the integrated U-wire chip MOT, it is possible to precisely move atoms to the location of an atom-chip micro trap (section 2.3).

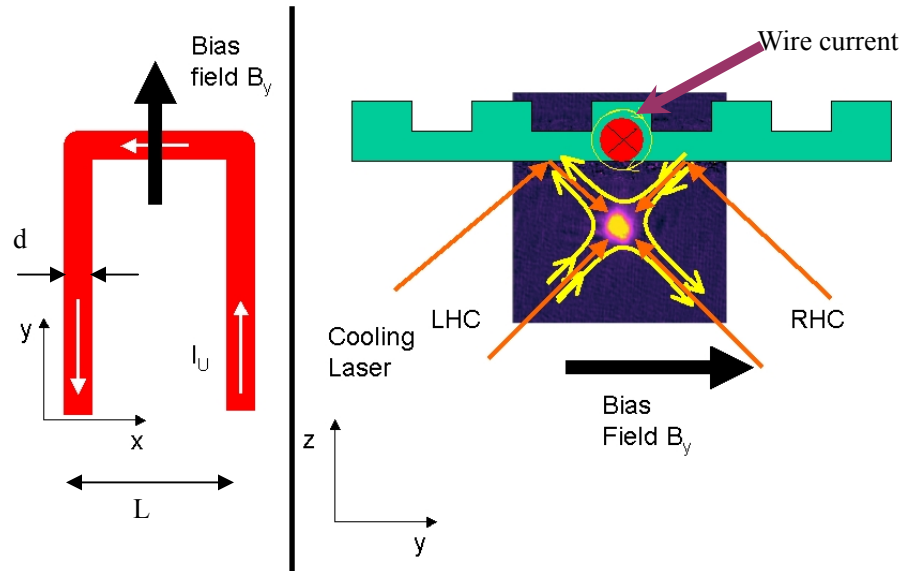


Figure 2.5: A chip U-wire surface MOT configuration.

### 2.2.3 Capture velocity

The capture velocity is defined as the maximum velocity that can be cooled and trapped by the MOT. It is not obvious how to determine the capture velocity because it is influenced by many factors such as beam alignment and laser power. Here a very simple one-dimensional model is provided to estimate the order of the capture velocity.

The maximum force can be calculated from equation (2.55) in a saturation case:

$$F_{\max} = \hbar k \gamma_{\rho_{\max}} = \hbar k \Gamma \rho_{ee \max} = \hbar k \Gamma / 2. \quad (2.65)$$

Then the average force can be estimated as

$$F_{av} \approx F_{\max} / 2 = \hbar k \Gamma / 4. \quad (2.66)$$

We then consider the energy conservation:

$$\frac{1}{2} m v_c^2 = F_{av} L = \frac{1}{4} \hbar k \Gamma L, \quad (2.67)$$

where  $L$  is the optical molasses dimension size. The capture velocity  $v_c$  is determined by

$$v_c \cong \sqrt{\frac{\hbar k \Gamma L}{2m}}. \quad (2.68)$$

Equation (2.68) gives the maximum possible capture velocity in a MOT saturated by laser power. A more precise capture range can be obtained by Monte-Carlo simulations.

## 2.2.4 Capture volume

One of the big issues in designing a MOT system is the capture volume. The atom number  $N$  in a MOT depends on the capture dimension size  $L$  [33]:

$$N \propto L^4. \quad (2.69)$$

The ultimate limit of the capture volume comes from level crossing of cooling excited states and their neighbor hyperfine structures. For  $^{87}\text{Rb}$ , the cooling transition is from  $|5S_{1/2}, F=2\rangle$  to  $|5P_{1/2}, F=3\rangle$ . As shown in figure 2.6, the level  $|F=3, M_F=-3\rangle$  crosses with  $|F=2, M_F=2\rangle$  at  $x=L$  if we still take the picture of figure 2.3(b). To keep the Zeeman splitting in figure 2.3(b) valid, the  $L$ , i.e., the maximum MOT capture dimension, is decided by:

$$L = \frac{\Delta E}{(Fg_F + F'g'_F)\mu_B B'}, \quad (2.70)$$

where  $\Delta E$  is the hyperfine energy splitting between  $F=3$  and  $F'=2$ ,  $g_F$  is the landau factor,  $\mu_B$  is

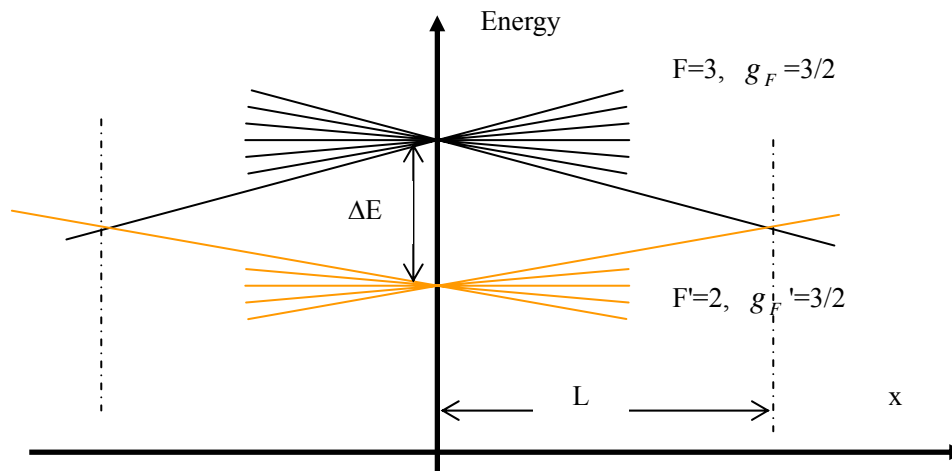


Figure 2.6: Zeeman splitting and level crossing of  $^{87}\text{Rb}$   $5P_{3/2}$  states  $F=3$  and  $F=2$  due to a linear magnetic field  $B(x)=B'x$ .

the Bohr magneton, and  $B'$  is the magnetic field gradient. For  $^{87}\text{Rb}$   $F=3$  and  $F'=2$  states,  $\Delta E = 267$  MHz,  $g_F \mu_B = g'_F \mu_B = 0.93$  MHz/G. For a typical field with  $B' = 10$  G/cm,  $L = 5.74$  cm. For a big chamber MOT system, whose capture volume is mostly limited by laser beam size, equation (2.70) can be used to optimize the magnetic field gradient.

A standard six-beam MOT and mirror MOT with external coils typically have large capture volume, limited only by the laser beam sizes. “For a beam diameter of  $<2$  cm, 10-G/cm gradient and detuning of 10–15 MHz yield the most trapped atoms. For larger beams, however, larger detunings and smaller gradients trap the largest number of atoms. [33]” The capture volume of a U-wire MOT is limited by the U-wire dimensions.

### 2.2.5 Loading equation

The MOT loading can be described by the following equation

$$\frac{dN}{dt} = R - \frac{N}{\tau} - \beta \int n^2(\vec{r}) d^3r. \quad (2.71)$$

The first term  $R$  on the right side is the loading rate, defined as the number of atoms per second entering the trap volume  $V$  with low enough velocities ( $v < v_c$ ) to be captured. It is a function of trap volume  $V$ , capture velocity  $v_c$ , trappable atom partial pressure  $P_{\text{atom}}$ , and temperature  $T$  [34]:

$$R \cong \frac{P_{\text{atom}}}{2K_B T} V^{2/3} v_c^4 \left( \frac{m}{2K_B T} \right)^{3/2}. \quad (2.72)$$

The second and third terms of the left side of equation (2.71) are the losses caused by elastic collisions between trapped atoms and background atoms and light-assisted inelastic collisions between trapped atoms [35]. For typical MOT systems, the loss rate from the trap, i.e.,  $1/\tau$ , is primarily limited by the elastic collisions between trapped atoms and background gases:

$$1/\tau = \sqrt{\frac{3K_B T}{m}} n \sigma = \frac{\sqrt{3P\sigma}}{\sqrt{mK_B T}}. \quad (2.73)$$

Therefore, we ignore the third term in equation (2.71) and get



$$\frac{dN}{dt} = R - \frac{N}{\tau}. \quad (2.74)$$

For Rb atoms with average atomic mass 85.4678 and atomic radius 2.98 Å, the collision cross section can be estimated by

$$\sigma = \pi(2r_{Rb})^2 = 4\pi r_{Rb}^2 = 1.12 \times 10^{-18} \text{ m}^2. \quad (2.75)$$

This leads to

$$P = \frac{\sqrt{mK_B T}}{\sqrt{3\tau\sigma}} = \frac{9.44 \times 10^{-8}}{\tau / \text{second}} \text{ torr}, \quad (2.76)$$

which has the same order as the experimental formula [36]:

$$P_{\text{exp}} \approx \frac{3 \times 10^{-8}}{\tau / \text{second}} \text{ torr}. \quad (2.77)$$

The steady-state atom number  $N_s$  is then given by

$$N_s = R\tau = \frac{P_{\text{atom}}}{P} \frac{V^{2/3} v_c^4}{\sqrt{6}\sigma} \left( \frac{m}{2K_B T} \right)^2. \quad (2.78)$$

The atom number in an  $^{87}\text{Rb}$  MOT is determined by the ratio of the  $^{87}\text{Rb}$  partial pressure to the total pressure. At very low pressure, non- $^{87}\text{Rb}$  atoms in vacuum are not negligible; thus the total number in the MOT increases with increasing  $^{87}\text{Rb}$  pressure. The MOT atom number gets saturated as  $P_{\text{atom}} \rightarrow P$ .

## 2.2.6 Polarization gradient cooling

Unfortunately, Doppler cooling can not cool atoms below the limit

$$T_D \equiv \hbar\Gamma / 2K_B \quad (2.79)$$

resulting from heating of the discrete size of the momentum steps the atoms undergo with each emission or absorption in a two-state system [19]. To overcome the Doppler cooling limit, we must use non-Doppler mechanisms. Polarization gradient cooling (PGC) with  $\sigma_+$  and  $\sigma_-$  configuration is one such sub-Doppler cooling technique [37].

Using  $^{87}\text{Rb}$  cooling transition from  $|F=2\rangle$  to  $|F=3\rangle$  as an example, the PGC cooling schematic diagram is shown in figure 2.7. The two laser beams are red-detuned for the atoms at

rest ( $v=0$ ) [figure 2.7(b)]. The atoms moving toward the  $\sigma_+$  beam, i.e.,  $v>0$ , see different frequency shifts to the  $\sigma_+$  and  $\sigma_-$  beams. Thus there are more atoms in the  $M_F=+2$  state than  $M_F=-2$  state because of the optical pumping effect [figure 2.7(c)]. This population difference makes atoms absorbing more photons from the  $\sigma_+$  beam than the  $\sigma_-$  beam, resulting in a net damping force along the  $\sigma_+$  propagation, i.e.,  $F<0$ . In a similar way, the atoms moving with  $v<0$  get a net force  $F>0$  [figure 2.7(d)]. Therefore, the atoms feel a damping force opposite to their motion depending on the differential scattering of light from the two laser beams. This damping force is able to cool atoms below the Doppler limit because it is caused by the population imbalance of ground-state Zeeman sub levels rather than a Doppler shift.

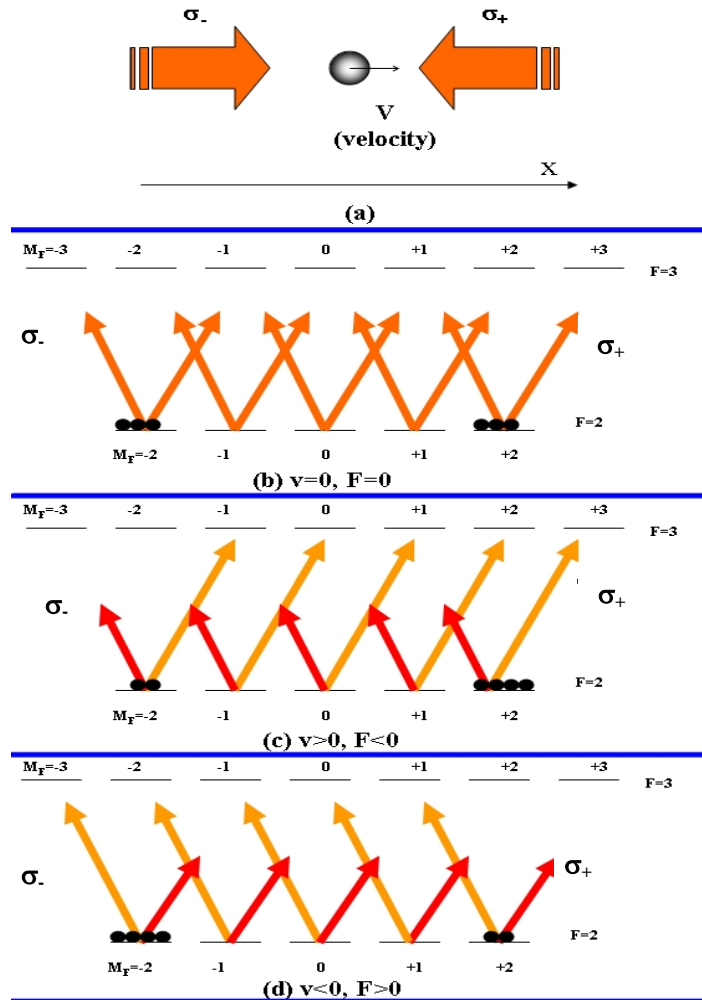


Figure 2.7: One-dimensional schematic diagram of polarization gradient cooling. (a) Two counter-propagating laser beams with  $\sigma_+$  and  $\sigma_-$  polarizations and an atom moving with velocity  $v$ . (b)  $v=0$ ,  $F=0$  for rest atoms. (c)  $v>0$ ,  $F<0$  for atoms moving toward the  $\sigma_+$  beam. (d)  $v<0$ ,  $F>0$  for atoms moving toward the  $\sigma_-$  beam.

## 2.3 Atom-chip magnetic trap

Magnetic trapping of neutral atoms [38] has been proven to be an efficient way to trap and compress precooled atoms for BEC production and manipulation. Moreover, integration of magnetic traps and wave guides with a microfabricated wire substrate surface, i.e., atom chip, provides a new way to make and manipulate cold atom optics [5–9, 14, 15, 32].

A magnetic trap makes use of the interaction between the magnetic moment  $\vec{\mu}$  of a neutral atom and external magnetic field  $\vec{B}(\vec{r})$  as

$$U(\vec{r}) = -\vec{\mu} \cdot \vec{B}(\vec{r}). \quad (2.80)$$

For an atom trapped in a pure Zeeman sublevel  $|F, M_F\rangle$ , the potential can be rewritten as

$$U(\vec{r}) = -\vec{\mu} \cdot \vec{B}(\vec{r}) = M_F g_F \mu_B B(\vec{r}), \quad (2.81)$$

where  $g_F$  and  $\mu_B$  are the Lande g-factor and Bohr magneton, respectively. Depending on the sign of  $g_F M_F$ , atoms are trapped to either the maximum ( $g_F M_F < 0$ , strong-field-seeking state) or the minimum ( $g_F M_F > 0$ , weak-field-seeking state) of the field magnitude. Since there is no maximum point of magnetic-field magnitude allowed in free space [39, 99], a stable magnetic trap must work with weak-field-seeking state atoms. The two lowest-order magnetic traps are quadrupole [38] and Ioffe-Pritchard (IP) traps [40, 41]. The quadrupole trap is a linear (first-order) potential trap that has a zero crossing of the magnetic field; The IP (second-order, i.e., harmonic) trap has a non-zero minimum.

Quadrupole linear traps offer very tight three dimensional confinements. Unfortunately, atoms entering the zero magnetic-field crossing get “confused” about the direction of the field that they follow. The zero magnetic-field crossing results in a trap loss due to spin flips, i.e., Majorana flops.

The most commonly used magnetic traps for BEC experiments have become IP traps that avoid spin flip loss at the trap center. As we know in both classical and quantum mechanics, the atoms’ magnetic moment adiabatically follows the direction of the magnetic field if the direction of the field changes slowly enough, i.e.,

$$\omega = \frac{d\theta}{dt} \ll \omega_L = g_F \mu_B |\vec{B}| / \hbar, \quad (2.82)$$

where  $\omega$  is the trap frequency and  $\omega_L$  is the Larmor precession frequency.

Applying Maxwell's equations ( $\nabla \cdot \vec{B} = 0, \nabla \times \vec{B} = 0$ ), an IP type trap magnetic field with axial symmetry can be expressed by [42]

$$\begin{aligned} \vec{B} &= \begin{bmatrix} (B_{\perp}' - \frac{1}{2} B_z'' z)x \\ -(B_{\perp}' + \frac{1}{2} B_z'' z)y \\ B_{z0} + \frac{1}{2} B_z'' z^2 - \frac{1}{4} B_z'' (x^2 + y^2) \end{bmatrix} \\ &= B_{z0} \begin{bmatrix} 0 \\ 0 \\ 1 \end{bmatrix} + B_{\perp}' \begin{bmatrix} x \\ -y \\ 0 \end{bmatrix} + \frac{B_z''}{2} \begin{bmatrix} -xz \\ -yz \\ z^2 - \frac{1}{2}(x^2 + y^2) \end{bmatrix}, \end{aligned} \quad (2.83)$$

where the z-axis is the longitudinal symmetry axis and the x-y plane is the transverse plane. Around the trap center,

$$B \cong B_{z0} + \frac{1}{2} (B_{\rho}'' \rho^2 + B_z'' z^2), \quad (2.84)$$

where

$$B_{\rho}'' \equiv \frac{B_{\perp}'^2}{B_{z0}} - \frac{B_z''}{2}. \quad (2.85)$$

### 2.3.1 Chip wire micro trap

An atom chip uses its lithographically fabricated circuit patterns to generate magnetic traps on its substrate surface. An atom chip has two major advantages over the traditional coil setup: (1) Very tight confinements on the chip surface, where atoms are very close to the micro wires, can be achieved with low current of several A; (2) Many different types of traps, e.g., waveguides, beam splitters, and interferometers, can be integrated into a small scale chip. The first advantage results directly from the fact that the magnetic field gradient scales as  $1/r^2$  where r is the distance from a wire. In a coil system, typically r is  $>1$  cm and it requires many turns and a large current ( $>100$  A). However, on an atom chip, the distance from a trap to the chip surface can be easily

reduced down to  $<100 \mu\text{m}$  and only a very low current ( $\sim 1 \text{ A}$ ) is required to create a much tighter trap that dramatically reduces the evaporation time (Section 2.6) to BEC. The second advantage holds the key to developing practical cold atom small-scale sensors in the future. The disadvantage of an atom chip is the small capture volume that requires care in loading atoms onto the chip. Atoms in an atom-chip micro trap are also more sensitive to current noise than those in free space [43, 44].

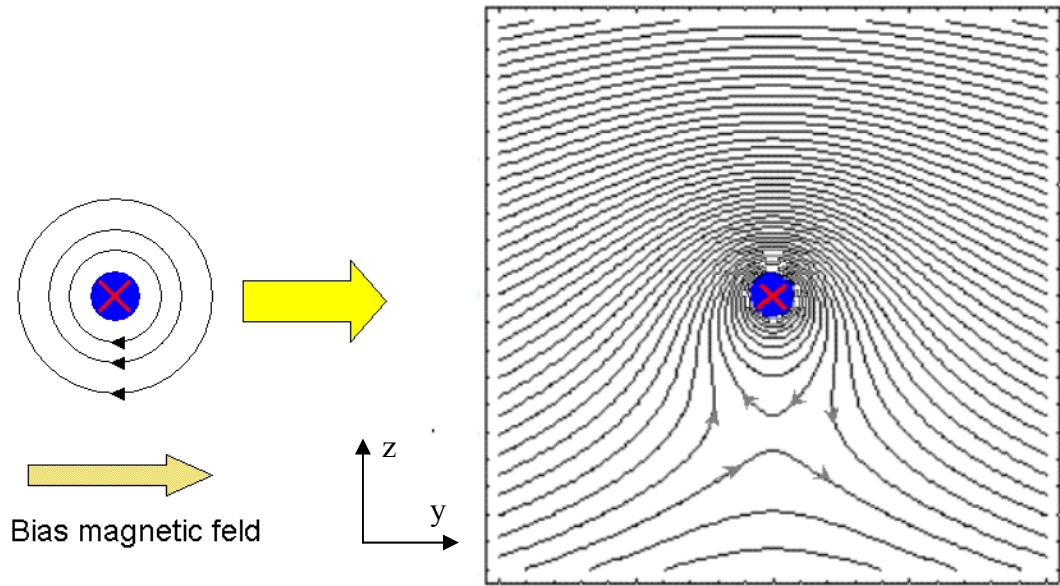


Figure 2.8: A two-dimensional quadrupole magnetic field generated by a single current wire augmented with a uniform transverse bias magnetic field.

This section reviews the principle of atom-chip wire traps, and two basic atom-chip-trap wire structures, i.e., the U-wire magnetic trap (UMT) and Z-wire magnetic trap (ZMT) [32].

As shown in figure 2.8, a two-dimensional quadrupole magnetic field is produced below a single wire of current  $I$  with a bias magnetic field  $B_{\text{bias}}$  perpendicular to the current. The total magnetic field can be expressed by

$$\vec{B} = \vec{B}_{\text{wire}} + \vec{B}_{\text{bias}} = \frac{\mu_0 I}{2\pi\rho} (\hat{\rho} \times \hat{x}) + \vec{B}_{\text{bias}}, \quad (2.86)$$

where  $\rho^2 = y^2 + z^2$ . The fields are canceled at

$$z_0 = -\frac{\mu_0 I}{2\pi B_{\text{bias}}}, \quad (2.87)$$

where the field gradient is

$$B_{\perp}' = \left| \frac{d|\vec{B}|}{d\rho} \right|_{z_0} = \left| \frac{d|\vec{B}_{wire} + \vec{B}_{bias}|}{d\rho} \right|_{z_0} = \left| \frac{d|\vec{B}_{wire}|}{d\rho} \right|_{z_0} = \frac{\mu_0 I}{2\pi z_0^2} \quad (2.88)$$

$$= \frac{B_{bias}}{|z_0|} \quad (2.89)$$

$$= \frac{2\pi B_{bias}^2}{\mu_0 I}. \quad (2.90)$$

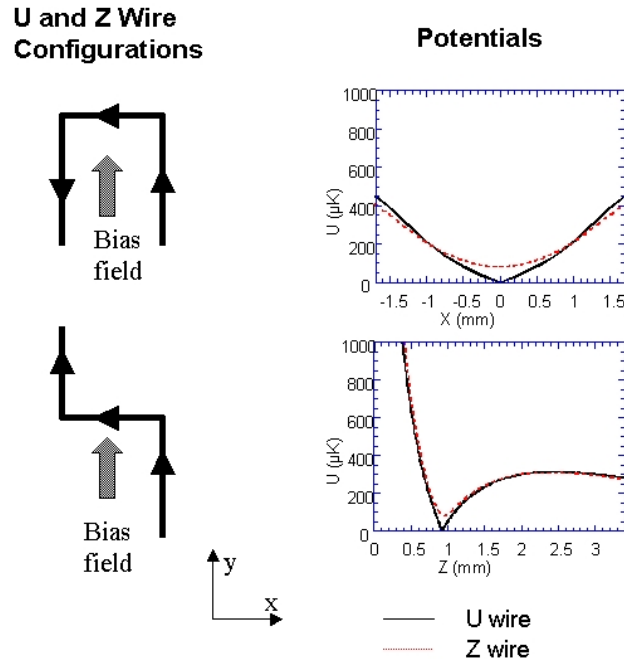


Figure 2.9: U-wire, Z-wire magnetic-trap configurations and potential plots.

Depending how the wire is bent, a single wire in a U shape can create a three-dimensional quadrupole trap, and a Z-shaped wire can create an IP type trap, as shown in figure 2.9. The two-dimensional quadrupole field is produced by the x-directional current and the y-directional bias field. In the U-wire, the two opposite currents along the y direction cancel each other at the trap center. This results in a three-dimensional quadrupole trap that has a zero-field crossing point. In the Z-wire configuration, the two y-directional currents are in the same sign and provide an x-directional field minimum at the trap center. We discuss only the Z-wire trap in detail here because the IP type trap without spin-flip loss is a better candidate for making a BEC on chip.

A typical Z-wire Magnetic Trap (ZMT) is shown in figure 2.10, where  $I$  is the wire current and  $\vec{B}_{yBias}$  is the y-directional external bias field. We find that the symmetry axis of the trap is not exactly along the x direction. As shown in figure 2.10 (c), at the trap center  $(0, 0, z_0)$  the magnetic field is really along the x direction because of canceling of the z-directional fields. However, considering some offset from the trap center  $(x, 0, z_0)$ , the z-directional fields do not cancel completely and the magnetic field does not point along the x direction any more. As shown later, this position-dependent z-directional field rotates the IP trap slow axis through an angle  $\theta$  with to the x direction as shown in figure 2.10(a). Knowing what the symmetry axis is and in which direction it points are important to calculate the trap frequencies.

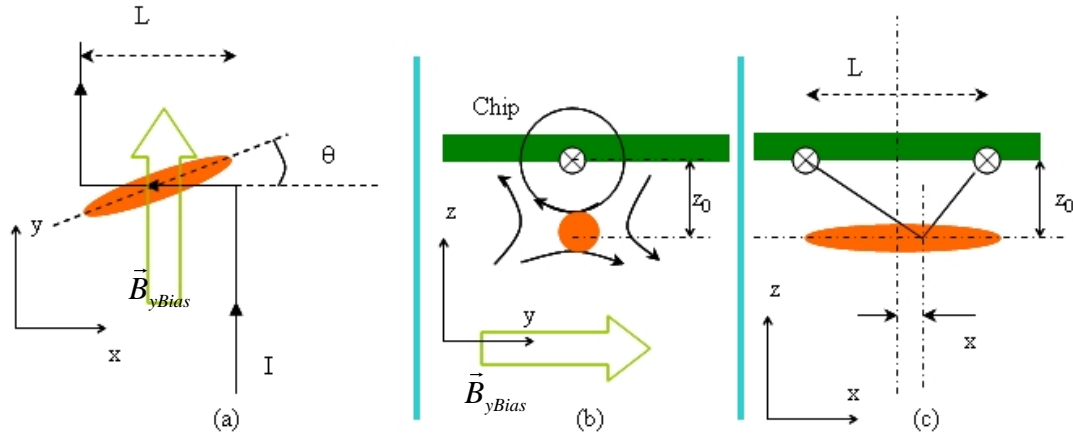


Figure 2.10: A Z-wire magnetic trap. The trap center lies at  $(0, 0, z_0)$ .

First, we look at the magnetic field produced by two half-infinite y-directional wires [figure 2.10(c)]:

$$\vec{B}_a = -\frac{1}{2} \frac{\mu_0 I}{2\pi} \left[ \frac{|z_0|}{(L/2+x)^2 + z_0^2} + \frac{|z_0|}{(L/2-x)^2 + z_0^2} \right] \hat{x} - \frac{1}{2} \frac{\mu_0 I}{2\pi} \left[ \frac{L/2+x}{(L/2+x)^2 + z_0^2} - \frac{L/2-x}{(L/2-x)^2 + z_0^2} \right] \hat{z}. \quad (2.91)$$

The tilted angle  $\theta$  can be obtained from expression (2.91) combined with the y bias field. The z-directional field of equation (2.91) can be expressed by

$$\begin{aligned}
B_{az} &= -\frac{\mu_0 I}{4\pi} \left[ \frac{L/2+x}{(L/2+x)^2+z_0^2} - \frac{L/2-x}{(L/2-x)^2+z_0^2} \right] \\
&\cong \frac{\mu_0 I}{2\pi} \frac{(L/2)^2-z_0^2}{[(L/2)^2+z_0^2]^2} x.
\end{aligned} \tag{2.92}$$

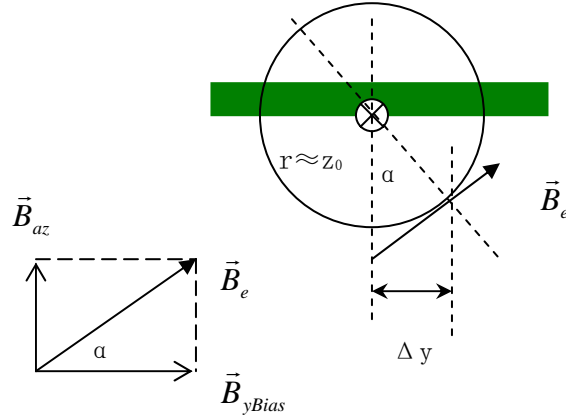


Figure 2.11: The transverse quadrupole two-dimensional trap center offset due to the z-directional bias field induced by the two y-directional wires.

As shown in figure 2.11, the transverse two-dimensional quadrupole trap center offset  $\Delta y$  due to this z-directional field can be obtained by ( $B_{az} \ll B_{yBias}$ )

$$\Delta y \cong |z_0| \sin \alpha \cong |z_0| \alpha \cong |z_0| \frac{B_{az}}{B_{yBias}} = \frac{\mu_0 I}{2\pi} \frac{(L/2)^2 - z_0^2}{[(L/2)^2 + z_0^2]^2} \frac{|z_0| x}{B_{yBias}}. \tag{2.93}$$

The tilted angle  $\theta$  of the slow axis [figure 2.10 (a)] then can be calculated by:

$$\theta \cong \frac{\Delta y}{x} = \frac{\mu_0 I}{2\pi} \frac{(L/2)^2 - z_0^2}{[(L/2)^2 + z_0^2]^2} \frac{|z_0|}{B_{yBias}}. \tag{2.94}$$

For  $z_0 \ll L/2$ , i.e., the trap is very close to the chip surface, equation (2.94) then goes to

$$\begin{aligned}
\theta &\xrightarrow{z_0 \ll L/2} \frac{\mu_0 I}{2\pi} \frac{1}{(L/2)^2} \frac{z_0}{B_{yBias}} = \frac{\mu_0 I}{2\pi z_0} \frac{1}{(L/2)^2} \frac{z_0^2}{B_{yBias}} = B_{yBias} \frac{1}{(L/2)^2} \frac{z_0^2}{B_{yBias}} \\
&= \left( \frac{z_0}{L/2} \right)^2.
\end{aligned} \tag{2.95}$$

When  $\theta$  is a very small angle, we can use the x-directional component of expression (2.91) to estimate the longitudinal trap frequency. From



$$B_{ax} = -\frac{\mu_0 I}{4\pi} \left[ \frac{|z_0|}{(L/2+x)^2 + z_0^2} + \frac{|z_0|}{(L/2-x)^2 + z_0^2} \right] \quad (2.96)$$

$$\cong -B_{yBias} \frac{z_0^2}{(L/2)^2 + z_0^2} - \frac{1}{2} B_{yBias} \frac{8z_0^2 [3(L/2)^2 - z_0^2]}{[(L/2)^2 + z_0^2]^3} x^2, \quad (2.97)$$

we get

$$B_0 = B_{yBias} \frac{z_0^2}{(L/2)^2 + z_0^2}, \text{ and} \quad (2.98)$$

$$B''_{Longitudinal} = B_{yBias} \frac{8z_0^2 [3(L/2)^2 - z_0^2]}{[(L/2)^2 + z_0^2]^3}. \quad (2.99)$$

In the transverse x-y plane, we have

$$B'_\perp = \frac{\mu_0 I}{2\pi z_0^2} = \frac{B_{yBias}}{|z_0|} \text{ and} \quad (2.100)$$

$$B''_\rho = \frac{(B'_\perp)^2}{B_0} - \frac{B''_{Longitudinal}}{2} = B_{yBias} \left( \frac{(L/2)^2 + z_0^2}{z_0^4} - \frac{4z_0^2 [3(L/2)^2 - z_0^2]}{[(L/2)^2 + z_0^2]^3} \right). \quad (2.101)$$

For a trap very close to the surface, i.e.,  $z_0 \ll L/2$ , the above expressions can be simplified to

$$B_0 \xrightarrow{z_0 \ll L/2} B_{yBias} \frac{z_0^2}{(L/2)^2}, \quad (2.102)$$

$$B''_{longitudinal} \xrightarrow{z_0 \ll L/2} B_{yBias} \frac{24z_0^2}{(L/2)^4}, \text{ and} \quad (2.103)$$

$$B''_\rho \xrightarrow{z_0 \ll L/2} B_{yBias} \left( \frac{(L/2)^2}{z_0^4} - \frac{12z_0^2}{(L/2)^4} \right). \quad (2.104)$$

The trap frequencies are

$$\omega_{longitudinal} = \sqrt{\frac{g_F M_F \mu_B B''_{Longitudinal}}{m}} \text{ and} \quad (2.105)$$

$$\omega_\rho = \sqrt{\frac{g_F M_F \mu_B B''_\rho}{m}}. \quad (2.106)$$

Now let's design a Z-wire trap that can load atoms directly from a surface MOT with a temperature  $T$  and position  $z_0$  below the chip. To reduce the trap loss caused by the finite trap depth, we require that the ZMT trap depth is  $\alpha$  times higher than the cloud temperature, i.e.,

$$\Delta U \cong M_F g_F \mu_B B_{ybias} \geq \alpha K_B T, \quad (2.107)$$

$$\text{or } B_{y\text{bias}} \geq \frac{\alpha K_B T}{M_F g_F \mu_B}. \quad (2.108)$$

On the other hand, the magnetic field gradient force toward the chip must be larger than the gravity force that pulls atoms down:

$$M_F g_F \mu_B B' \geq mg. \quad (2.109)$$

Inserting formula (2.89) into the above equation, we get

$$M_F g_F \mu_B \frac{B_{y\text{bias}}}{|z_0|} \geq mg \quad (2.110)$$

$$\text{or } B_{y\text{bias}} \geq \frac{mg |z_0|}{M_F g_F \mu_B}. \quad (2.111)$$

Combining equations (2.108) and (2.111), we get the requirement for the y-bias field

$$B_{y\text{bias}} \geq B_{y\text{bias min}} = \frac{\text{Max}\{\alpha K_B T, mg |z_0|\}}{M_F g_F \mu_B}. \quad (2.112)$$

Then using equation (2.90), we get the current requirement

$$I = \frac{2\pi}{\mu_0} B_{y\text{Bias}} |z_0| \geq \frac{2\pi}{\mu_0} B_{y\text{Bias min}} |z_0| = I_{\text{min}}. \quad (2.113)$$

To obtain a minimum field magnitude point at the trap center, equations (2.97) and (2.99) require that:

$$B_{\text{Longitudinal}}'' = B_{y\text{Bias}} \frac{8z_0^2 [3(L/2)^2 - z_0^2]}{[(L/2)^2 + z_0^2]^3} \geq 0 \quad (2.114)$$

$$\text{or } L \geq L_{\text{min}} = 2 |z_0|. \quad (2.115)$$

However, from equation (2.103), a longer L results in a looser confinement in the slow axis when atoms are compressed toward the chip surface. On one hand, we like to have a larger Z size, i.e., longer L, to simplify the loading procedure because it is not easy to bring an external MOT close to the surface. On the other hand, we prefer the smaller Z size to get very tight confinement for forced evaporative cooling. There are several solutions to this problem. The first solution is to have two ZMTs of different sizes and adiabatically transfer atoms from the bigger ZMT to the smaller ZMT after initial loading. In our atom chip, we have demonstrated that we are able to make BEC on a chip with a single Z wire of L = 2 mm by using a U-wire MOT to move atoms

very close the surface ( $|z_0| = 500\text{--}800\ \mu\text{m}$ ) before loading into the ZMT.

For typical parameters, such as  $T = 30\ \mu\text{K}$ ,  $z_0 = -1\ \text{mm}$  and  $\alpha = 20$  for  $^{87}\text{Rb}$  in the state  $|5S_{1/2}, F=2, M_F=2\rangle$  ( $g_F = 1/2$  and  $M_F g_F \mu_B / K_B = 67.2\ \mu\text{K/G}$ ), we can solve equations (2.112),

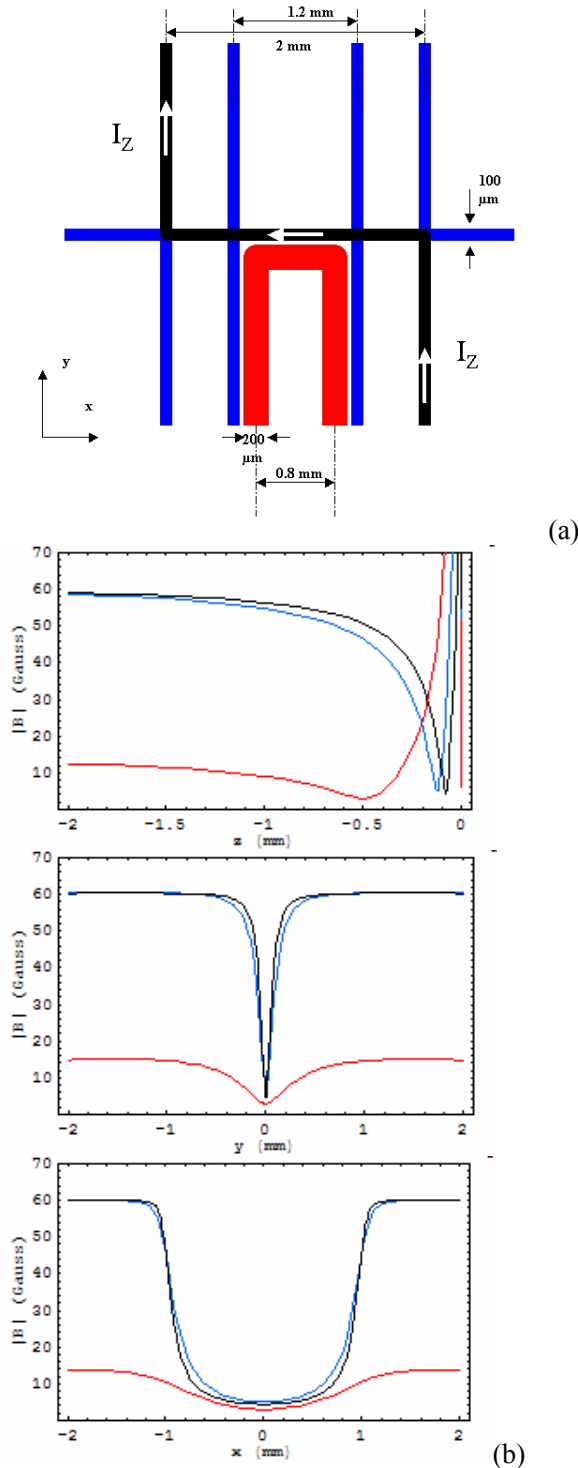


Figure 2.12: Z-wire magnetic traps. (a) The central part of the atom-chip design. The black wire labeled with current  $I_Z$  is the Z-wire. The thickness of the wire on an AlN substrate is about  $10\ \mu\text{m}$ . (b) B-field cross section plots. The red curve is the initial trap:  $I_Z = 4\ \text{A}$ , bias field  $\vec{B}_{bias} = (0, 14, 0)\ \text{G}$ , trap frequency  $2\pi\omega = (36, 215, 215)\ \text{Hz}$ , and trap position from the surface  $z_0 = -500\ \mu\text{m}$ . The green curve is the intermediate trap during the compression:  $I_Z = 4\ \text{A}$ , bias field  $\vec{B}_{bias} = (-4, 60, 0)\ \text{G}$ , trap frequency  $2\pi\omega = (30, 2500, 2500)\ \text{Hz}$ , and trap position from the surface  $z_0 = -120\ \mu\text{m}$ . The black curve is the final trap:  $I_Z = 2.75\ \text{A}$ , bias field  $\vec{B}_{bias} = (-4, 60, 0)\ \text{G}$ , trap frequency  $2\pi\omega = (23, 3600, 3600)\ \text{Hz}$ , and trap position from the surface  $z_0 = -82\ \mu\text{m}$ . The calculation takes into account the wire width.

(2.113) and (2.114) to get  $B_{y\text{biasmin}}=9$  G,  $I_{\text{min}}=4.5$  A, and  $L_{\text{min}}=2|z_0|=2$  mm. In the real chip, we make copper wire patterns on an AlN substrate with  $L=2$  mm, wire width  $w=100$   $\mu\text{m}$ , and thickness  $d=10$   $\mu\text{m}$ . This Z wire can take 4 A for at least 4 minutes before it breaks.

Figure 2.12 shows the dimensions of the Z wire in our atom chip and its potential plots. High trap frequencies (23, 3600, 3600) Hz are obtained with only  $I_z=2.75$  A and  $B_{\text{bias}}=(-4, 60, 0)$  G. A traditional coil BEC system can only achieve  $<1000$  Hz with a current  $>100$  A. As shown in chapter 7, we have achieved BEC in this compressed ZMT with only about a 4 s RF evaporation.

## 2.4 Adiabatic compression

In a lifetime-limited atom trap, a fast and efficient forced evaporative cooling toward BEC requires a high collision rate for rethermalization. Adiabatic compression of a magnetic trap allows an increase in the atom elastic collision rate by several orders of magnitude while maintaining the phase-space density (PSD). This section derives the conditions for adiabatic compression in a magnetic trap, and describes how the compression affects physics quantities, e.g., temperature, collision rate, and PSD.

For an ideal gas, we have the state equation

$$PV = NK_B T \quad (2.116)$$

and work-energy conservation for an adiabatic compression

$$-PdV = CdT, \quad (2.117)$$

where P is the pressure, V is the volume, N is the total atom number,  $K_B$  is the Boltzman constant, T is the temperature, and  $C = 3NK_B/2$  is the heat capacity. From equations (2.116) and (2.117), we get

$$NK_B \frac{dP}{P} = (C + NK_B) \frac{dT}{T}, \quad (2.118)$$

with the solution given by

$$T = AP^{\frac{NK_B}{C+NK_B}} = AP^{\frac{2}{5}} \quad (2.119)$$

or

$$\frac{T_f}{T_i} = \left( \frac{P_f}{P_i} \right)^{\frac{2}{5}}. \quad (2.120)$$

Using the state equation (2.116) and equation (2.119), we obtain

$$V = \frac{NK_B T}{P} = ANK_B P^{\frac{2}{5}-1} = ANK_B P^{-\frac{3}{5}}. \quad (2.121)$$

Solving equations (2.119) and (2.121), we express the volume V with the temperature as follows:

$$V = A^{\frac{5}{2}} NK_B T^{-\frac{3}{2}} \propto T^{-\frac{3}{2}}. \quad (2.122)$$

The collision rate is

$$\gamma = n\sigma\bar{v} = \frac{N}{V}\sigma\bar{v} \propto V^{-1}\bar{v} \propto T^{3/2}T^{1/2} = T^2, \quad (2.123)$$

where  $n=N/V$  is the atom number density,  $\sigma$  is the elastic collision rate, and  $\bar{v}$  is the root-mean-square (RMS) thermal speed. The PSD stays constant

$$PSD = n\lambda_T^3 \propto T^{3/2}T^{-3/2} = 1 = \text{constant}, \quad (2.124)$$

where the thermal wavelength is defined by

$$\lambda_T \equiv \frac{h}{\sqrt{2\pi m K_B T}}. \quad (2.125)$$

During the adiabatic compression, the collision rate increases because of increasing density and temperature due to the external work, but the PSD stays constant. The general equations (2.119)–(2.124) work for all types of trapped noninteracting atom-gas systems.

### 2.4.1 Linear trap

A three-dimensional linear trap potential can be described as

$$U(\vec{r}) = \beta_1 x_1 + \beta_2 x_2 + \beta_3 x_3, \quad (2.126)$$

where  $x_i$  ( $i=1, 2, 3$ ) are coordinates, and  $\beta_i$  ( $i=1, 2, 3$ ) are potential gradients. At the thermal equilibrium, each dimension has equal potential energy, i.e.,

$$\frac{1}{2} K_B T = \beta_i L_i = (\beta_1 \beta_2 \beta_3 L_1 L_2 L_3)^{1/3} = (\beta_1 \beta_2 \beta_3 V)^{1/3} \quad (2.127)$$

or

$$T \propto (\beta_1 \beta_2 \beta_3 V)^{1/3}, \quad (2.128)$$

where  $L_i$  ( $i=1, 2, 3$ ) are effective trap dimension sizes and  $V$  is the effective volume. Solving equations (2.128) and (2.122), we get

$$T \propto (\beta_x \beta_y \beta_z)^{2/9}, \quad (2.129)$$

$$L_i \propto \frac{T}{\beta_i} = \beta_i^{-7/9} \beta_j^{2/9} \beta_k^{2/9}, \text{ and the collision rate} \quad (2.130)$$

$$\gamma \propto T^2 \propto (\beta_x \beta_y \beta_z)^{4/9}. \quad (2.131)$$

### 2.4.2 Harmonic trap

A three-dimensional harmonic trap potential can be described as

$$U(\vec{r}) = \frac{1}{2} m \omega_1^2 x_1^2 + \frac{1}{2} m \omega_2^2 x_2^2 + \frac{1}{2} m \omega_3^2 x_3^2, \quad (2.132)$$

where  $\omega_i$  ( $i=1, 2, 3$ ) are trap frequencies. Following the same procedure as in section 2.4.1, we get the following results:

$$T \propto (\omega_{1f} \omega_{2f} \omega_{3f})^{\frac{1}{3}} \quad \text{and} \quad (2.133)$$

$$\gamma \propto (\omega_{1f} \omega_{2f} \omega_{3f})^{\frac{2}{3}}. \quad (2.134)$$

### 2.4.3 Atom-chip Z-wire trap

As discussed in section 2.3, the atom-chip Z-wire trap is an IP type trap. When atoms are very cold and most of them sit on the bottom of the trap, they see a three-dimensional harmonic trap. However, when atoms are thermally hot, i.e.,  $>100 \mu\text{K}$ , most atoms experience a two-dimensional linear trap potential in the transverse plane and one-dimensional harmonic potential along the slow axis. In this region, the potential can be described by

$$U(\vec{r}) = \frac{1}{2} m \omega_1^2 x_1^2 + \beta_2 x_2 + \beta_3 x_3. \quad (2.135)$$

The trap dimensions are

$$L_1 \propto \frac{T^{1/2}}{\omega_1}, \quad L_2 \propto \frac{T}{\beta_2}, \quad L_3 \propto \frac{T}{\beta_3} \quad \text{and} \quad (2.136)$$

$$V = L_1 L_2 L_3 \propto \frac{T^{5/2}}{\omega_1 \beta_2 \beta_3}. \quad (2.137)$$

Solving (2.137) and (2.122) we get

$$T \propto (\omega_1 \beta_2 \beta_3)^{1/4} \quad (2.138)$$

and the following:

$$L_1 \propto \omega_1^{-7/8} \beta_2^{1/8} \beta_3^{1/8}, \quad (2.139)$$

$$L_2 \propto \omega_1^{1/4} \beta_2^{-3/4} \beta_3^{1/4}, L_3 \propto \omega_1^{1/4} \beta_2^{1/4} \beta_3^{-3/4} \quad \text{and} \quad (2.140)$$

$$\gamma \propto T^2 \propto (\omega_1 \beta_2 \beta_3)^{1/2}. \quad (2.141)$$

#### 2.4.4 Adiabatic requirement

We have derived many results from the adiabatic compression, but not touched one question: what compression can be called an adiabatic compression? What's the requirement to make an adiabatic compression in a magnetic trap? This section uses a spherical harmonic trap as an example to derive the adiabatic condition requirement. The result can be easily extended to non-spherical cases and other type traps.

In a spherical harmonic trap with an initial trap frequency  $\omega_0$ , its trap frequency  $\omega$  increases during the compression. The adiabatic condition means that the atoms do not feel the small change of potential because they move much faster than the compression speed, i.e., the velocity change caused by the compression is far less than the velocity itself so that the modification of the compression is very small. In this case, the atoms can follow the slow change of compression and fit themselves to a compressed trap. We require that the change of the trap size be less than the average atom velocity

$$\frac{dL}{dt} \ll v. \quad (2.142)$$

From equations (2.122) and (2.133), we get

$$L = V^{1/3} = L_0 \left( \frac{T}{T_0} \right)^{-1/2} = L_0 \left( \frac{\omega}{\omega_0} \right)^{-1/2} \quad (2.143)$$

and the mean velocity

$$v = v_0 \left( \frac{\omega}{\omega_0} \right)^{1/2}. \quad (2.144)$$

Then inserting equations (2.143) and (2.144) into equation (2.142), we get

$$\frac{1}{2} L_0 \omega_0^{1/2} \omega^{-3/2} \frac{d\omega}{dt} \ll v_0 \omega_0^{-1/2} \omega^{1/2} \quad (2.145)$$

and

$$\frac{d\omega}{dt} \ll 2 \frac{v_0}{L_0 \omega_0} \omega^2. \quad (2.146)$$

Using the fact that

$$v_0 = a_0 \omega_0 = \frac{1}{2} L_0 \omega_0, \quad (2.147)$$

equation (2.146) becomes [45]:

$$\frac{d\omega}{dt} \ll \omega^2. \quad (2.148)$$

Equation (2.148) can be used to design an adiabatic compression by solving the following equation:

$$\frac{d\omega}{dt} = \eta\omega^2 \quad (\eta \ll 1). \quad (2.149)$$

The solution is

$$\omega(t) = \frac{\omega_0}{1 - \eta\omega_0 t}. \quad (2.150)$$

An interesting aspect of equation (2.150) is that it takes a finite time  $t_m$  to compress the trap to an infinitely tight trap ( $\omega \rightarrow \infty$ ):

$$t_m = \frac{1}{\eta\omega_0}. \quad (2.151)$$

For example, if we start a trap from  $\omega_0=100$  Hz and require  $\eta=0.1$ , it takes less than  $t_m=100$  ms to finish the adiabatic compression.

## 2.5 Trap-depth-dependent lifetime

Atom-trap lifetime is always limited by background room temperature gas collisions due to the shallow trap depth. In Section 2.2.5, we briefly discussed background collision-caused trap loss by assuming that the collision cross section was constant and the collision loss rate could be simply expressed by

$$\gamma = n\bar{v}\sigma_{eff}, \quad (2.152)$$

Where  $n$  is the background vapor gas density,  $\bar{v}$  is the average speed of background thermal atoms, and  $\sigma_{eff}$  is the effective collision cross section for an atom in the vapor to eject a trapped atom. However, this situation does not always hold true in real systems. When a vapor gas atom collides with a trapped atom, some kinetic energy is transferred to the trapped atom; it escapes if this transferred energy is larger than the trap depth. Since atoms are not hard spheres but diffuse objects with long interactions, the effective collision cross section to transfer a small amount of



energy is bigger than the cross section to transfer a large amount of energy. This means that the effective collision cross section and the collision loss rate weakly depend on the trap depth. This explains why we observe differences in the Mirror MOT, Chip MOT and Z-wire magnetic trap lifetimes, as well as other early experiments [34, 46].

It can be proven that with an atom-atom interaction potential of

$$U(r) = C_n / r^n, \quad (2.153)$$

the collision loss rate  $\gamma$  depends on the trap depth  $U_0$  [47]

$$\gamma \propto U_0^{-1/n}. \quad (2.154)$$

With a typical potential of  $n=5$  [47], we have

$$\tau = 1/\gamma \propto U_0^{1/5}. \quad (2.155)$$

In our atom chip system, we measure the difference between the Z-wire magnetic trap and external coil mirror MOT lifetimes by varying the background pressure. From theoretical calculation, the Z-wire trap and mirror MOT have trap depths of 3 mK and 1 K, respectively. The experimental data in figure 2.13 show a factor of 2.77 difference between the mirror MOT and the Z-wire magnetic trap loss rates. This result is consistent with the theoretical expectation of  $3.2 = (1 \text{ K} / 3 \text{ mK})^{1/5}$ .

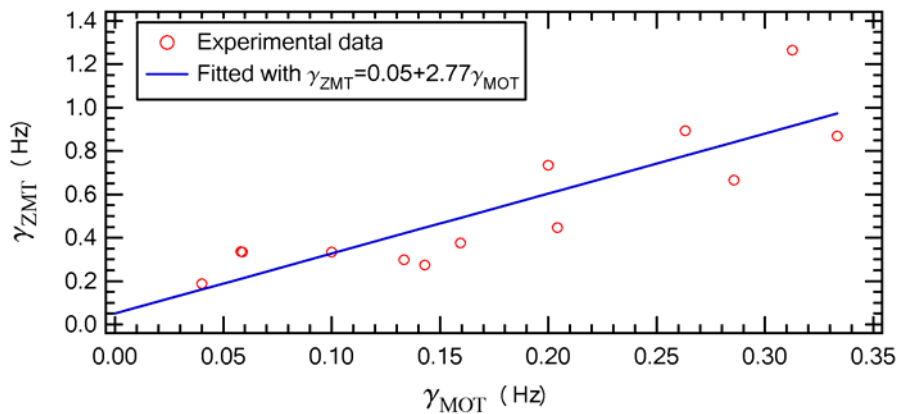


Figure 2.13: The Z-wire trap loss rate vs the mirror MOT loss rate at different vacuum level.

## 2.6 Forced evaporative cooling

Evaporative cooling is neither a new idea nor a physics patent, but always part of our daily life. For thousands of years, people have used this technology to cool boiled water. Just as high-temperature molecules escape from hot water so that the remaining water is cooled down, evaporation continuously removes atoms in the high-energy tail of the thermal distribution from the trap. Collisions rethermalize the remaining atoms to a new thermal equilibrium and repopulate atoms into the high-energy tail, furthering the cooling process. To maintain a high cooling rate within the lifetime of a trap, the trap depth, or truncation energy, must be ramped down over time. This process is called forced evaporative cooling. The ramping must be slow enough to allow rethermalization. Evaporative cooling also helps to increase phase space density, which is the key to achieve a Bose-Einstein Condensation [section 2.7]. By now, gaseous Bose-Einstein condensates have so far only been obtained by using evaporative cooling.

Thus, the lifetime and rethermalization rate of a trap play important roles in forced evaporative cooling. Monte Carlo simulation study shows that a complete rethermalization takes about 2.7 collisions per atom [48, 100]. Thus the rethermalization rate is simply the collision rate divided by a factor of 2.7:

$$\gamma_{th} = \gamma_{col} / 2.7. \quad (2.156)$$

Runaway evaporation is defined as a situation in which the collision rate increases as the cloud cools [49]. What makes such runaway evaporation is having the product of trap lifetime and rethermalization rate of at least 100-200 [35], or

$$\tau\gamma_{th} > 100. \quad (2.157)$$

A straightforward way to realize forced evaporative cooling for trapped neutral atoms is only to reduce the trap depth and keep its tightness untouched. This method keeps a high enough collision rate to maintain a continuous cooling process. However, in early magnetic trap configurations using current coils, the trap frequencies became smaller when the trap depth went

down because of reducing the current in the coils.

Pritchard [50] and Walraven [51] suggested using RF-induced spin flip to effectively reduce the trap depth and get forced evaporation. The first RF-forced evaporative cooling was demonstrated by an MIT group [52]. Another more direct way, surface evaporation, is to use a flat solid surface as a knife to cut the trap depth from top to bottom [54, 55]. In this section, we will also propose a direct evaporation without any external components.

## 2.6.1 RF-forced evaporation

To understand physics of RF-forced evaporation, we assume the atoms are trapped in  $M_F=2$  state, as shown in figure 2.14. If we apply a rotating magnetic field that can drive transitions with  $\Delta M_F=\pm 1$ , the on-resonance trapped atoms will be transferred to untrapped states. Forced evaporative cooling can be achieved by changing the RF frequency to lower the effective trap depth. In practice, a rotating magnetic field may be difficult to produce experimentally. Fortunately, a vertically (respect to the quantum axis) oscillating magnetic field, for instance, in the x-direction, can be decomposed into positive and negative circular polarizations.

$$\begin{aligned}\bar{B}_{RF} &= \text{Re}\{B_{RF} \hat{x} e^{i\omega t}\} = \text{Re}\left\{\frac{1}{2} B_{RF} [(\hat{x} + i\hat{y}) + (\hat{x} - i\hat{y})] e^{i\omega t}\right\} \\ &= \text{Re}\left\{\frac{1}{2} B_{RF} [\hat{\sigma}_+ + \hat{\sigma}_-] e^{i\omega t}\right\} = \frac{1}{2} B_{RF} [\hat{\sigma}_+ + \hat{\sigma}_-] e^{i\omega t} + c.c.\end{aligned}\quad (2.158)$$

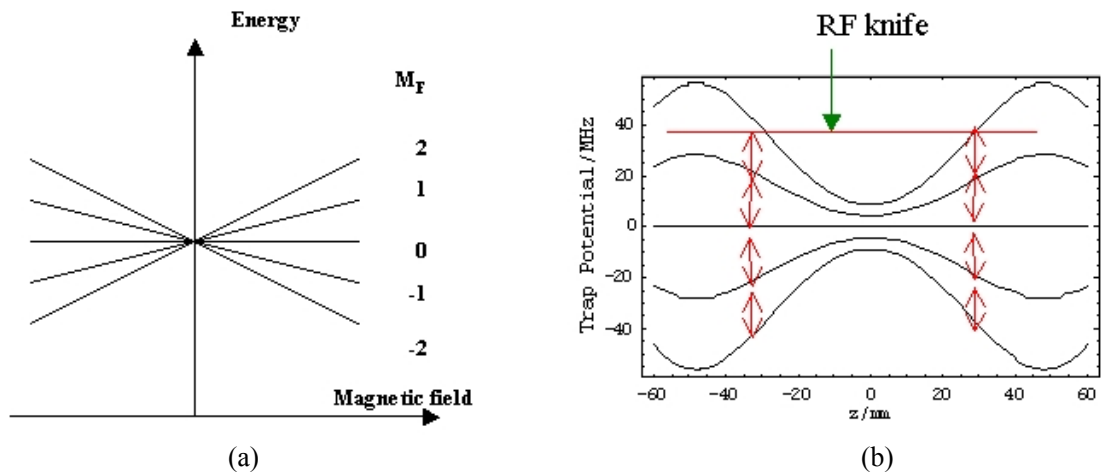


Figure 2.14: Zeeman level splitting and RF evaporative cooling. (a) Zeeman level splitting under an external magnetic field for  $F=2$  states. (b) Potentials of a magnetic trap for all trapped and untrapped states.

As shown in figure 2.14(b), the RF-induced spin flips ( $\Delta M_F = \pm 1$ ) transfer atoms from trapped states to untrapped states after several cycles. For more about this induced spin transition, please check J.J. Sakurai's *Modern Quantum Mechanics* [53].

## 2.6.2 Surface-induced evaporation on an atom chip

Surface-induced evaporation has a more direct picture than RF evaporation: a flat surface removes hot atoms when the trap moves close to the surface. Hansch's group did the first surface evaporation with a chip U-wire trap by increasing the bias field and keep U-wire current fixed [6], and a cooling effect was observed. However, no BEC has been reported using this method because the field gradients and curvatures are increased so much that they induce three-body inelastic collisions (due to increasing density) and spin-flip losses.

An efficient forced evaporative cooling to the BEC range requires keeping trap gradients and frequencies constant during reduction of the trap depth. This can be obtained if a conventional IP trap configuration is combined with a flat surface. The position of the trap can be adjusted by applying additional bias fields without affecting the trap frequencies. This work was recently done by one of Eric Cornell's labs at JILA and BEC was achieved by purely using surface-induced evaporation [54]. An alternative way to achieve surface evaporative cooling toward BEC is to move the atom cloud very close to an atom-chip substrate surface while keeping the trap frequencies constant by applying time-varying wire currents and bias fields [55].

Here I propose a simple way to carry out surface evaporative cooling by only adjusting external bias fields. As shown in figure 2.15, a wire with current  $I$  along the negative  $x$ -direction and a magnetic bias field in the  $y$ - $z$  plane produce a two-dimensional quadropole magnetic trap in the  $y$ - $z$  plane. If the bias field rotates with an angular frequency of  $\Omega$  in the  $y$ - $z$  plane:

$$\vec{B}_{bias}(t) = B_{b0}(\hat{y} \cos \Omega t + \hat{z} \sin \Omega t), \quad (2.159)$$

the position of the trap center moves along a circular orbit

$$\vec{r}(t) = r_0(\hat{y} \sin \Omega t - \hat{z} \cos \Omega t). \quad (2.160)$$

The field gradient stays constant

$$B' = \frac{\mu_0 I}{2\pi r_0^2} = \frac{B_{b0}}{r_0} = \frac{2\pi B_{b0}^2}{\mu_0 I} = \text{constant.} \quad (2.161)$$

The trap frequency in the axial x direction does not change so much because it is mainly determined by the current itself and the separation of the two y directional currents.

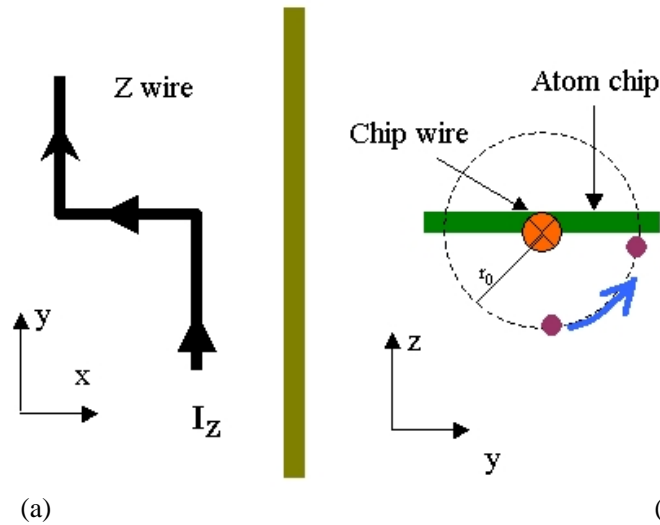


Figure 2.15: Z-wire magnetic trap for surfaced-induced evaporative cooling. (a) Z-wire with current  $I$ . (b) Trap position orbit when bias fields change properly.

### 2.6.3 Direct evaporation on an atom chip

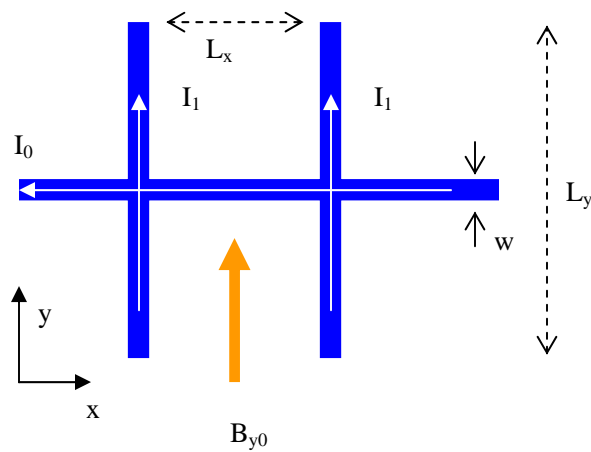


Figure 2.16: An H-wire trap pattern design.

Direct evaporative cooling without RF and surface collisions will be very attractive if it can be done simply by lowering the trap depth. The advancement of microchip wire-trap technology provides the possibility of realizing this. Here, I propose direct evaporation by adjusting the wire

current and bias fields based on an H-trap, as shown in figure 2.16. The negative x-directional current  $I_0$  and an external bias field  $B_{y0}$  produce a y-z plane two-dimensional quadrupole magnetic trap. Two y-directional currents,  $I_1$ , give an axial confinement. As shown in equation (2.161), the quadrupole field gradient is only determined by the bias field  $B_{y0}$  and the current  $I_0$

$$B' = \frac{2\pi B_{y0}^2}{\mu_0 I_0}. \quad (2.162)$$

The trap depth is controlled by the bias field strength. Therefore, we can keep the trap tightness by just holding the ratio of  $B_{y0}^2$  and  $I_0$  constant while the trap depth is lowered.

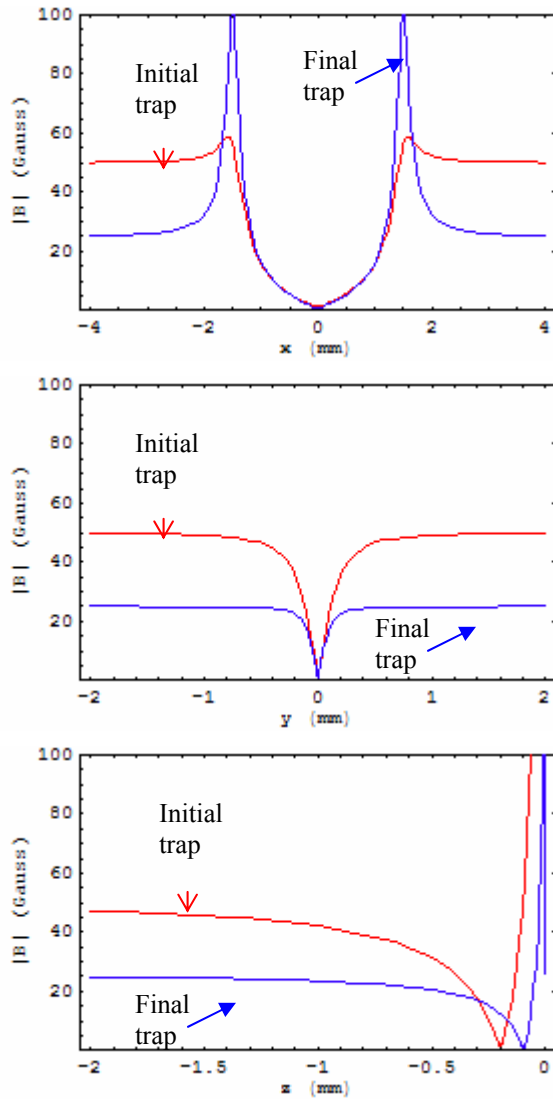


Figure 2.17: Trap potentials of the H-wire trap as in figure 2.16, with  $w=50 \mu\text{m}$ ,  $L_x=3\text{mm}$ ,  $L_y=6\text{mm}$ , and  $I_1=5\text{A}$ .  $I_0$  ramps from 5 to 1.25A while the bias field  $B_{y0}$  ramps from 50 to 25 G. The initial trap has trap frequencies are  $\{97, 2555, 2573\}$  Hz, with a distance of 198  $\mu\text{m}$  from the surface. The final trap frequencies are  $\{137, 3550, 3578\}$  Hz, with a distance of 97  $\mu\text{m}$  from the surface. The trapped state is  $^{87}\text{Rb } 5S_{1/2}, F=2, M_F=2$ .

Figure 2.17 shows the trap potentials with  $w=50 \mu\text{m}$ ,  $L_x=3 \text{ mm}$ ,  $L_y=6 \text{ mm}$ ,  $I_1=5 \text{ A}$ .  $I_0$  ramps

from 5 to 1.25A while the bias field  $B_{y0}$  ramps from 50 to 25 G. The y-z plane trap depth and frequencies change as expected, though in the x direction the trap depth increases. The trap depth is determined by the y and z directions.

## 2.7 Bose-Einstein Condensation

In 1925, Einstein predicted ideal gas Bose-Einstein Condensation (BEC) with Bose statistics [2]. The quantum physics picture of BEC is very simple to understand. From quantum mechanics, we know that every particle with momentum  $p$  is associated with a matter wavelength  $\lambda=h/p$ , where  $h$  is Planck constant. In a many-body system, the atoms interfere with each other and become identical when their matter wavelengths are comparable to their separations, i.e., the phase-space density (PSD)

$$PSD = \lambda_T^3 n \geq 1, \quad (2.163)$$

where

$$\lambda_T = \frac{h}{\sqrt{2\pi m K_B T}} \quad (2.164)$$

is the thermal wavelength and  $n$  is the number density. Similar to photons that are attracted into the bright “condensate” spots of interference, atoms tend to occupy a single quantum state and form a condensate. From equations (2.163) and (2.164), BEC requires a high atom density and a very low temperature. The first BEC in a dilute neutral atom gas was demonstrated at JILA [3] and MIT [4] groups in 1995 after laser cooling and evaporative cooling made it possible to approach the nano-Kelvin temperature region.

### 2.7.1 Noninteracting BEC

Noninteracting BEC atoms in a trap occupy a single particle state  $\psi(\vec{r})$  and follow the general linear time-independent Schrödinger equation

$$\left[ \frac{\hat{P}^2}{2m} + U(\vec{r}) \right] \psi(\vec{r}) = E \psi(\vec{r}). \quad (2.165)$$

For a harmonic trap described by

$$U(\vec{r}) = \frac{1}{2} m \sum_{i=1}^3 \omega_i^2 x_i^2, \quad (2.166)$$

its ground-state solution is

$$\psi(\vec{r}) = \prod_{i=1}^3 \frac{1}{(2\pi)^{1/4} \sigma_i^{1/2}} \text{Exp}\left(-\frac{x_i^2}{4\sigma_i}\right), \quad (2.167)$$

where

$$\sigma_i = \sqrt{\hbar / 2m\omega_i} \quad (i=1, 2, 3). \quad (2.168)$$

The time-dependent Schrödinger equation is

$$i\hbar \frac{\partial}{\partial t} \psi(\vec{r}, t) = \left[ \frac{\hat{p}^2}{2m} + U(\vec{r}) \right] \psi(\vec{r}, t). \quad (2.169)$$

## 2.7.2 Interaction between atoms

All real atom-trap systems have atom-atom interaction that may not be ignored in some cases. A single Bose atom satisfies the nonlinear Gross-Pitaevskii equations [56–58]

$$i\hbar \frac{\partial}{\partial t} \psi(\vec{r}, t) = \hat{H}_0 \psi(\vec{r}, t) + (N-1) \frac{4\pi\hbar^2}{m} a |\psi(\vec{r}, t)|^2 \psi(\vec{r}, t), \quad \text{and} \quad (2.170)$$

$$\mu \psi(\vec{r}) = \hat{H}_0 \psi(\vec{r}) + (N-1) \frac{4\pi\hbar^2}{m} a |\psi(\vec{r})|^2 \psi(\vec{r}). \quad (2.171)$$

where  $a$  is the S-wave scattering length and  $\mu$  is the chemical potential..

## 2.8 Measurement

Interpreting the experimental data and results relies on how measurements are taken. In cold atom research, imaging, including fluorescence and absorption, is the most important technical tool for studying the temperature, number and density distribution of an atom cloud. In this section, we describe the physics involved in both fluorescence and absorption imaging, and derive time-of-flight (TOF) pictures of thermal and BEC clouds.

### 2.8.1 Absorption and fluorescence imaging

To measure cold-atom density distribution, we record an image with a CCD camera. As we discussed earlier, light scattering, including absorption and reemission, happens when a laser beam passes through the atoms. The fluorescence imaging measures the scattered light, and the



absorption detection measures the missing light from the laser beam. They are the two sides of the energy conservation equation:

$$\begin{aligned} & \text{Energy of Scattered light} = \text{Energy of Spontaneous Emission} \\ & = \text{Absorbed Energy} - \text{Stimulated Emission Energy} = \text{Net Absorbed Energy}. \end{aligned} \quad (2.172)$$

For a two-state system described in section 2.1, the fluorescence power, scattered (or missing) from the incident laser beam, is determined by the spontaneous emission:

$$P = n\Gamma_2\rho_{22}\hbar\omega = nI\sigma_{abs}. \quad (2.173)$$

The density distribution can be calculated from the imaging of fluorescence:

$$n(\vec{r}) = \frac{P(\vec{r})}{I\sigma_{abs}}, \quad (2.174)$$

and the total number is given by

$$N = \int n(\vec{r})dV = \frac{\int P(\vec{r})dV}{I\sigma_{abs}} = \frac{\Phi}{I\sigma_{abs}}, \quad (2.175)$$

where  $\Phi$  is the total fluorescence power.

For absorption imaging, on the other hand, the laser intensity after passing through an atom cloud can be described as

$$I_{out} = I_{in}e^{-\sigma_{abs}\int ndz} = I_{in}e^{-\sigma_{abs}\tilde{n}} = I_{in}e^{-OD}, \quad (2.176)$$

where  $I_{in}$  and  $I_{out}$  are the incident and output laser intensities,  $z$  is the laser beam propagation direction,  $\tilde{n} = \int ndz$  is the two-dimensional density, and  $OD = \sigma_{abs}\tilde{n}$  is the optical depth.

Therefore the two-dimensional density distribution is given by measuring the output, i.e., the shadow of the atom cloud after absorption:

$$\tilde{n}(x, y) = \int n(x, y, z)dz = \frac{OD(x, y)}{\sigma_{abs}} = \frac{1}{\sigma_{abs}} \ln \frac{I_{in}(x, y)}{I_{out}(x, y)}, \quad (2.177)$$

and the total number is given by

$$N = \iint \tilde{n}(x, y)dx dy. \quad (2.178)$$

## 2.8.2 Time of flight

A common way to measure a cold atom cloud is to watch its free-space expansion after releasing the trap potential. The time-of-flight (TOF) measurement provides information about the cloud, including its momentum distribution, temperature, PSD and entropy. The nonisotropic shape evolution during TOF from a nonisotropic trap is a clear signature of BEC.

The following sections show the derivation of the TOF evolution of both the thermal and BEC clouds after the atoms are released from a harmonic trap. A thermal atom cloud in free space satisfies the Boltzman-Maxwell distribution, and there is equal thermal energy in every dimension, i.e, it expands equally fast in all directions. After sufficiently long expansion time, the thermal atom cloud looks isotropic. However, in a BEC state, atoms must be described by quantum mechanics; thus energy in different dimensions depends on the cloud's shape, i.e., the wave function. It will be shown later that the time evolution of a BEC in the free space is exactly the same as a Gaussian laser beam propagating in free space [22]. Only one-dimension case is discussed here because a three-dimensional harmonic trap can be separated as three one-dimensional traps.

### 2.8.2.1 Thermal atom cloud

A thermal atom cloud (ideal gas) satisfies the Maxwell velocity distribution

$$f(v) = \sqrt{\frac{m}{2\pi K_B T}} \exp\left(-\frac{mv^2}{2K_B T}\right). \quad (2.179)$$

With the transformation

$$x = vt \quad \text{and} \quad \frac{\partial v}{\partial x} = \frac{1}{t}, \quad (2.180)$$

we rewrite equation (2.179) and get the expression in position space:

$$\begin{aligned} h(x;t) &= f(v) \frac{\partial v}{\partial x} \\ &= \sqrt{\frac{m}{2\pi K_B T}} \frac{1}{t} \exp\left(-\frac{mx^2}{2K_B T t^2}\right) = \frac{1}{\sqrt{2\pi\sigma_{ht}^2}} \exp\left(-\frac{x^2}{2\sigma_{ht}^2}\right), \end{aligned} \quad (2.181)$$

$$\text{with } \sigma_{ht} = \sqrt{\frac{K_B T}{m}} t. \quad (2.182)$$

Equation (2.181) is the expansion or propagation function of a point cold-atom source. For an atom cloud with a finite initial size and distribution, we apply the convolution as the following:

$$u(x;t) = \int u_0(\xi)h(x-\xi)d\xi = u_0 * h, \quad (2.183)$$

where  $u_0(x;t) = u(x;t=0)$  is the initial density distribution.

Considering an initial Gaussian atom cloud:

$$u_0(x) = \frac{1}{\sqrt{2\pi}\sigma_0} \exp\left(-\frac{x^2}{2\sigma_0^2}\right), \quad (2.184)$$

and using the Fourier transform F, we get

$$u(x;t) = u_0 * h = F^{-1}\{F\{u_0 * h\}\} = F^{-1}\{F\{u_0\}F\{h\}\} = F^{-1}\{U_0H\}, \quad (2.185)$$

where

$$U_0(f) = F\{u_0\} = \exp\left(-\frac{\sigma_0^2(2\pi f)^2}{2}\right) \text{ and} \quad (2.186)$$

$$H(f;t) = F\{h\} = \exp\left(-\frac{\sigma_{ht}^2(2\pi f)^2}{2}\right). \quad (2.187)$$

We have then

$$\begin{aligned} U(f;t) &= F\{u(x;t)\} = H(f;t)U_0(f) = \exp\left(-\frac{(\sigma_0^2 + \sigma_{ht}^2)(2\pi f)^2}{2}\right) \\ &= \exp\left(-\frac{\sigma_t^2(2\pi f)^2}{2}\right), \end{aligned} \quad (2.188)$$

where

$$\sigma_t^2 = \sigma_0^2 + \sigma_{ht}^2. \quad (2.189)$$

Therefore the final distribution at time t is also a Gaussian distribution

$$u(x,t) = F^{-1}\{U\} = \frac{1}{\sqrt{2\pi}\sigma_t} \exp\left(-\frac{x^2}{2\sigma_t^2}\right). \quad (2.190)$$

### 2.8.2.2 BEC atom cloud

For a BEC atom cloud without atom-atom interaction, we need to solve the time-dependent Schrödinger equation

$$i\hbar \frac{\partial}{\partial t} \psi(x,t) = -\frac{\hbar^2}{2m} \frac{\partial^2}{\partial x^2} \psi(x,t) \quad (2.191)$$

It can be proven that, if the initial wave packet is a Gaussian function as

$$\psi(x, t = 0) = C \exp\left[-\frac{x^2}{w_0^2}\right], \quad (2.192)$$

where C is the normalization factor and

$$w_0^2 = 4\sigma_0^2 \quad (2.193)$$

is the initial waist size, the solution to equation (2.8-49) is given by [22]

$$\psi(x,t) = C \sqrt{\frac{w_0}{w(t)}} \exp\left[-\frac{x^2}{w^2(t)}\right] \exp\left[-i\frac{kx^2}{2R(t)}\right] \exp\left[i\frac{1}{2} \tan^{-1}(t/t_0)\right], \quad (2.194)$$

where

$$t_0 = kw_0^2/2 = \frac{1}{2} \frac{m}{\hbar} 4\sigma_0^2 = 2m\sigma_0^2/\hbar, \quad (2.195)$$

$$w^2(t) = 4\sigma^2(t), \text{ and} \quad (2.196)$$

$$\sigma^2(t) = \sigma_0^2 \left[1 + (t/t_0)^2\right] = \sigma_0^2 \left[1 + \left(\frac{\hbar t}{2m\sigma_0^2}\right)^2\right]. \quad (2.197)$$

If the atoms are released from a harmonic trap with frequency  $\omega$ , we have

$$\sigma_0^2 = \hbar / 2m\omega, \quad (2.198)$$

$$t_0 = 1/\omega, \quad (2.199)$$

$$\sigma^2(t) = \sigma_0^2 \left[1 + (t/t_0)^2\right] = \sigma_0^2 \left[1 + \omega^2 t^2\right], \text{ and} \quad (2.200)$$

$$\begin{aligned} R(t) &= -t \left[1 + (t_0/t)^2\right] = -t(t_0/t)^2 \left[1 + (t/t_0)^2\right] \\ &= -t \frac{t_0^2}{t^2} \frac{\sigma_0^2}{\sigma_0^2} \left[1 + (t/t_0)^2\right] = -\frac{t_0^2}{t\sigma_0^2} \sigma^2(t) = -\frac{\sigma^2(t) t_0^2}{t \sigma_0^2} \\ &= -\frac{\sigma^2(t)}{t} \frac{1}{\sigma_0^2} \frac{4m^2 \sigma_0^4}{\hbar^2} \\ &= -\frac{\sigma^2(t)}{t} \frac{4m^2 \sigma_0^2}{\hbar^2}. \end{aligned} \quad (2.201)$$

Finally, solution (2.194) can be rewritten as

$$\psi(x,t) = C \sqrt{\frac{\sigma_0}{\sigma(t)}} \exp\left[-\frac{x^2}{4\sigma^2(t)}\right] \exp\left[i\frac{x^2 \hbar t / 2m\sigma_0^2}{4\sigma^2(t)}\right] \exp\left[-i\frac{1}{2} \tan^{-1}\left(\frac{t}{2m\sigma_0^2/\hbar}\right)\right]$$

$$= C \sqrt{\frac{\sigma_0}{\sigma(t)}} \exp\left[-\frac{x^2}{4\sigma^2(t)}\right] \exp\left[-i\left\{\frac{1}{2} \tan^{-1}(\omega t) - \frac{x^2 \omega t}{4\sigma^2(t)}\right\}\right]. \quad (2.202)$$

Thus, the TOF after releasing a BEC cloud from a harmonic trap satisfies Gaussian evolution similar to optical Gaussian beam propagation.

As a summary, we have reviewed the mechanisms of laser cooling and trapping on the atom-chip. Although most cooling and trapping technologies have been well developed in the past twenty years, understanding them precisely are important and crucial to our BEC production in the portable atom-chip vacuum cell, described in next chapter, because of its ultimate small capture volume of the MOT.

## Chapter 3. A portable atom-chip vacuum cell

### 3.1 Introduction

The term “atom chip” connotes a picture of microscale atom-optics devices, perhaps integrated with optics and electronics on a single substrate. Our effort in developing a portable and compact vacuum cell system for Bose-Einstein condensation (BEC) atom-chip production is a significant step toward realizing this picture. We have produced a portable system that can be assembled, processed, and inserted into an ultracold atom apparatus in much the same way that an electronic vacuum tube can be plugged into an existing receiver. By separating the vacuum processing from the remaining BEC instrumentation, we seek to speed-up ultracold atom-chip development and, eventually, to make ultracold atom science more accessible to those without expertise in ultrahigh-vacuum (UHV) systems.

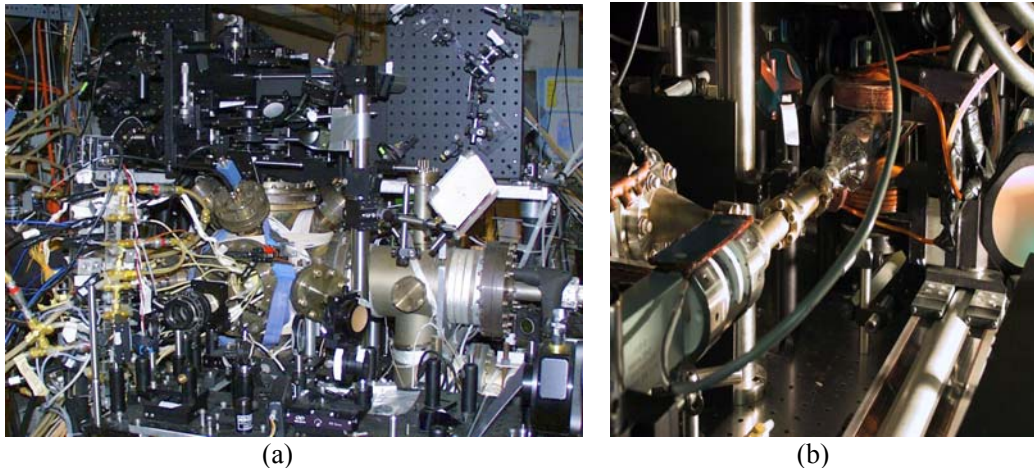


Figure 3.1: Traditional BEC systems with large and complicated vacuum components. (a) an MIT BEC system [69]. (b) A JILA standard BEC system [70].

As we know, different stages in a BEC experiment require different vapor pressures. For instance, the magneto-optical trap (MOT) requires high rubidium vapor pressure ( $\sim 10^{-8}$  torr) to capture a large number of atoms, while evaporative cooling toward final BEC creation requires UHV ( $< 10^{-11}$  torr) to maintain a long magnetic-trap lifetime. The conflict between the two different pressure ranges can be solved with a double-chamber design consisting of a vapor cell

chamber and a science chamber [59, 60]. After the atoms are loaded into the MOT in the high-pressure vapor cell chamber, they are mechanically moved into the UHV science chamber where the atoms are further cooled toward BEC. The two chambers are connected via a small tube of low conductance that maintains the pressure difference. Another example of double chamber BEC systems, using Zeeman slower, consists of a hot oven high pressure chamber and a UHV chamber [101]. As shown in figure 3.1, such traditional BEC vacuum systems are large and complicated, normally occupying more than half of an optical table ( $1.22 \times 3.66$  m).

Some atom-chip research groups still take advantage of this double-chamber structure [61, 62]. To reduce the complexity of the vacuum system, an alternative solution is to control the pressure temporally, i.e., to separate the MOT and BEC at different times instead of different spaces. Several technologies have been developed to make controllable atom sources such as dispensers [63], and light-induced atomic-desorption (LIAD) [64–66]. These atom sources can be turned on to increase the vapor pressure at the MOT stage and off to recover the pressure for the magnetic trap in a single chamber. The realization of the first two chip-based BECs in 2001 [14, 15], using pulsed atom sources, was a scientific and technical milestone towards chip-scale coherent atom-chip devices. However, as shown in figure 3.2, these two BEC atom-chip vacuum systems are still not compact because they insert or embed their atom-chips into large vacuum

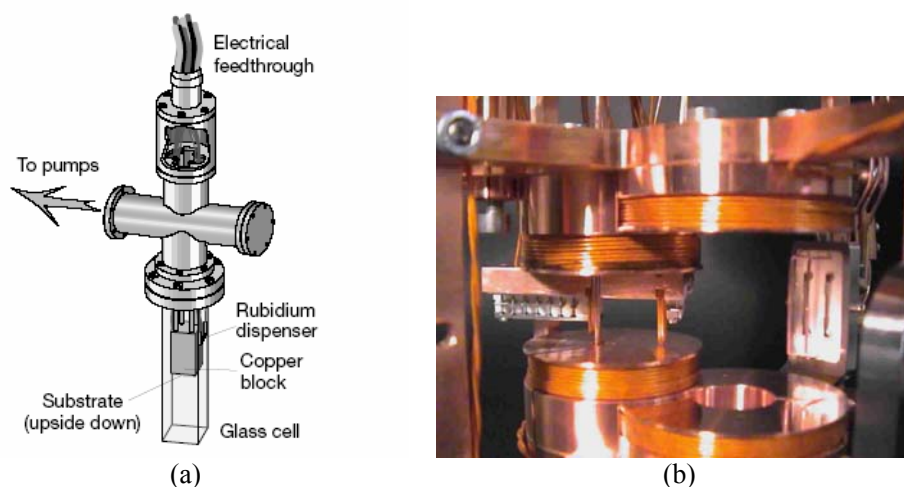


Figure 3.2: Apparatuses for the two first BECs on a chip reported in 2001. (a) System of W. Hänsel et al. [14]. The pumps are not drawn here. (b) System of C. Zimmermann et al. [67]. The vacuum chamber, not seen in the picture, is surrounded by huge water-cooled coils.

chambers that are backed by much larger pumping stations. Thus, atom-chip technology has successfully reduced BEC atom cloud sizes but until now has done little to simplify the entire vacuum system.

Our portable BEC atom-chip cell uses LIAD, one of the pulsed atom sources, but is constructed in a completely different way from all other atom-chip groups. In the following sections, we will present our first-generation vacuum setup where we learned how to assemble the chip to the cell. Then, we will provide the details of our unique portable atom-chip system.

## 3.2 First generation atom-chip vacuum system

A BEC atom-chip vacuum cell with a single chamber design must meet two general requirements:

- (1) It must be able to temporarily control cell vapor pressure to meet the pressure requirements at both the MOT and BEC stages. The pulsed atom source must be switched on and off within a few seconds. We use UV LIAD to realize this goal.
- (2) It must be able to maintain a UHV base pressure below  $10^{-10}$  torr. A traditional BEC system requires a pressure of  $<10^{-11}$  torr. However, an atom chip makes BEC production possible at  $10^{-10}$  torr because of its higher magnetic-trap compression and shorter forced evaporation time.

We designed our first generation atom-chip vacuum system to meet these two requirements but did not attempt to make it portable. The system diagram is shown in figure 3.3. The breakthrough at this stage was to simplify the way in which an atom chip is integrated into an entire system. For the first time, we successfully used the chip itself to seal a glass cell, thus making the chip part of the vacuum wall. The pin structure from the chip provided a direct connection to external current sources without requiring any vacuum feed-through. The details for integrating a chip with a glass cell are given in the next section.

As shown in figure 3.3, the system is comprised of most standard components for a UHV



system, including a turbo pump, an all-metal valve to separate the turbo pump after system baking-out and pumping-down, an ion pump (20 L/s), a Titanium sublimation pump (TSP), and an ion gauge. The whole system has a size of about  $70 \times 50$  cm on an optical table. The ion gauge reads  $< 3 \times 10^{-11}$  torr after the system is baked out.

The first generation system is still far from portable. On the other hand, the effective pumping speed at the chip port is very low because of the long distance from the chip to the Titanium sublimation pump (TSP) and ion pump. We have used this system to study atom-chip traps but not to achieve BEC. Our next step was to develop a functional portable atom-chip cell for BEC production.

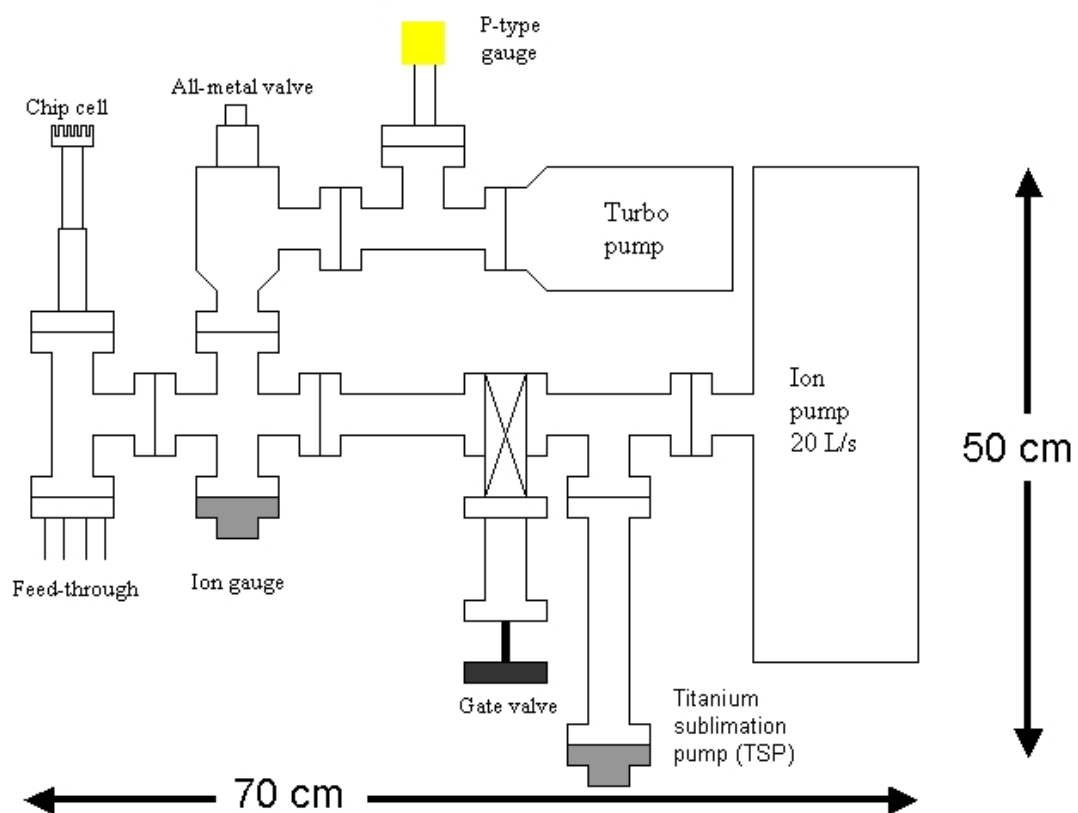


Figure 3.3: Diagram of the first-generation-atom-chip cell.

### 3.3 A portable atom-chip vacuum cell

Our portable vacuum cell system, shown in figure 3.4, consists of a single four-way cross that is attached to a small (8 L/s) ion pump, a four-pin feed-through providing connections to a rubidium dispenser and nonevaporable getter (NEG), a pinch-off tube, and a glass cell (the BEC chip cell). A 0.5 mm thick aluminum nitride (AlN) wafer (the atom-chip) closes the cell top, completing an ultrahigh-vacuum-compatible seal. A pyrex helix is used to increase the Rb atom adsorption surface for UV LIAD.

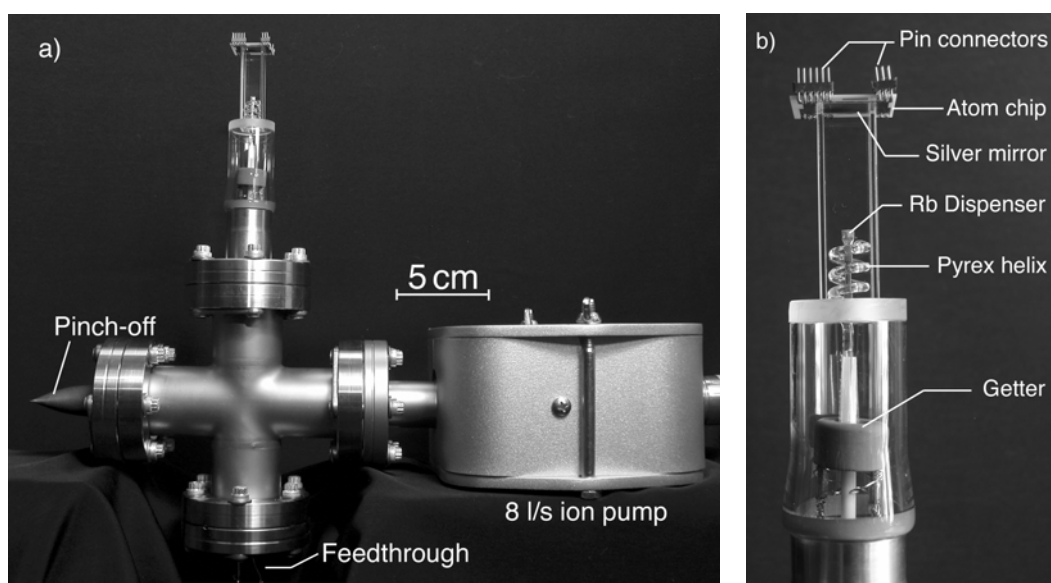


Figure 3.4: Portable vacuum cell for the production of a chip BEC. (a) Complete vacuum cell system. (b) Detail of cell assembly.

Table 3.1: Atom-chip cell parts list.

Part Name	Company	Description
Atom chip	Dept of Mechanical Engineering, Univ. of Colorado at Boulder.	Lithographically patterned copper on an 0.5 mm aluminum-nitride chip. The wire thickness is about 10–15 $\mu\text{m}$ .
Quartz cell	NSG Precision Cells, Inc.	Inner cross section 1 $\times$ 1 cm, type 3FL (UV or IR), 4 cm long
Rubidium dispenser	SAES	Model RB/NF/3.4/12FT10+10
Pyrex helix	JILA	Home built
NEG	SAES	ST172/HI/16-10/300C
Pinch-off tube	Huntington Mechanical Laboratories, Inc. <a href="http://vacuumfeedthru.com/">http://vacuumfeedthru.com/</a>	Model CPT-275-075, 1.91 cm (3/4 inch) tube diameter, copper. It can be modified by JILA mechanical shop if no compression port is used in other side.

The whole cell system measures  $30 \times 30 \times 15$  cm, and a person can hold it with two hands. As far as we know, it is the world's smallest BEC cell. The primary components are commercial products, as listed in table 3.1.

### 3.3.1 Fabrication of the atom-chip glass cell

The atom-chip glass cell consists of an atom chip and a quartz cell. The two components are prepared separately and then integrated in a final step of atom-chip–glass-cell assembly.

Atom-chip fabrication is done by Dr. Victor M. Bright's lab at the Micro-Electro-Mechanical Systems (MEMS) group at their facilities in the Mechanical Engineering Department at the University of Colorado at Boulder. The chips consist of electroplated copper wires on an aluminum nitride (AlN) substrate.

The AlN substrates are purchased from TFT (Thin Film Technology, Inc.). They come with a TiW adhesion layer (30–40 nm thickness) and a Cu seed layer (~250 nm thickness). The root-mean-square (rms) roughness of the Cu seed layer is measured to be 8–20 nm using a Zygo white-light interferometer. The properties of AlN, including its great thermal performance, low thermal expansion, and nontoxicity, make it a desirable electronic substrate material.

The wire pattern mask is ordered from Infinite Graphics (Infinite Graphics, 4611 E. Lake Street, Minneapolis, MN 55406). The mask consists of ink on a plastic sheet that is transferred to a glass mask using a standard lithographic technique on a blank sodalime glass mask. The transferred glass mask is then used as a primary mask for further patterning and etching. This technique has been used for feature sizes down to 10  $\mu\text{m}$ .

The first step in the chip fabrication process is to spin-coat the chip with photoresist. We use AZP 4620 photoresist (Clariant Corporation, Business Unit Electronic Materials, Somerville, NJ). After coating, the thickness is about 14  $\mu\text{m}$ . Once coated, photolithography is used in conjunction with the previously created mask to remove the photoresist where Cu wiring will be created. The patterned substrate is then electroplated using an electrolytic acid Cu bath process in

a tank purchased from Technical Inc. The final thickness of the Cu wires ranges from 8–14 $\mu\text{m}$ . After electroplating, the photoresist is stripped using acetone. The final step is to etch the remaining adhesion and seed layers that are not covered by electroplated Cu wiring. The Cu seed layer is removed using Cu etchant, and the TiW is removed using a hydrogen peroxide solution.

The above chip fabrication recipe is provided by Dr. Victor M. Bright's group. The atom chip and its wire pattern are shown in figure 3.5. The pins on the top and bottom sides provide a direct connection between the chip and current power supplies. The center area of the chip, 1  $\times$  1 cm, is used to seal the top of the glass cell.

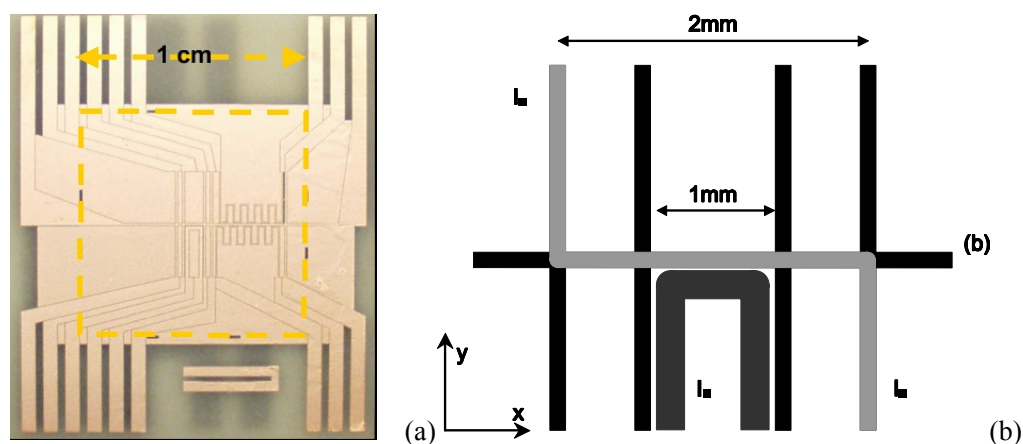


Figure 3.5: The atom chip and its copper wire pattern. (a) View of the whole copper chip pattern. (b) Center detail of wires where the BEC is produced. The widths of the U-wire ( $I_U$ ) and Z-wire are 200  $\mu\text{m}$  and 100  $\mu\text{m}$ , respectively. The height of the wires is about 10  $\mu\text{m}$

As soon as the chip is fabricated, we prepare the quartz cell at our lab for cell integration (by Leslie Czaia). A quartz cell is chosen to enhance the UV LIAD effect. Because LIAD is a non-thermal process (much like the photon-electron effect) and responds to short light wavelengths, the glass cell must be UV transparent. We use both UV and IR quartz cells from NSG Precision Cells, Inc. (inner cross section 1  $\times$  1 cm, length 4 cm, type 3FL). The only difference between UV and IR quartz cells is that the transmission on the IR quartz cell is higher at IR wavelengths. Experimentally we don't see any significant difference in loading the MOT with UV LIAD. The cell in which we have achieved BEC is a UV quartz cell.

Unfortunately, the thermal expansion coefficient ( $0.59 \times 10^{-6} \text{ }^\circ\text{C}^{-1}$ ) of quartz does not match

that of the AlN substrate ( $4.6 \times 10^{-6} \text{ }^\circ\text{C}^{-1}$ ) very well. The thermal mismatching gives an upper limit of the bakeable temperature of the cell about  $170 \text{ }^\circ\text{C}$  in our system.

We use the chip to form a UHV seal on one end of our BEC cell and to provide a reflective surface to create a mirror MOT [6]. Thus, there are a number of steps involved in integrating the chip with the cell (figure 3.7).

First, connector pins from Digikey (ED8850-ND) are soldered to the Cu wire leads at the chip edges using a soldering iron set to  $850 \text{ }^\circ\text{C}$ . Generic tin-lead solder is used. Care is taken to prevent solder from reaching the area where the chip will be attached to the BEC cell. Once the connectors are attached, the chip can no longer sit flat on the table. We mount it onto a heat sink for support. We can attach the chips to the heat sinks either with glue (Epotek H77) or with double-sided tape.

Once the chip is properly supported, a silver mirror is epoxied to the surface containing the Cu wiring. The mirrors are created by evaporating  $\sim 250 \text{ nm}$  of silver onto a glass block without any sort of adhesion layer underneath. Thus, the silver is only weakly bonded to the block and can be transferred to the atom chip. First, a drop of Epotek 353ND all-solids epoxy, free of air bubbles, is applied to the chip surface. Then an  $8 \text{ }\mu\text{m}$  thick piece of kapton film, the same size as the mirror, is placed on top of the epoxy and smoothed out to remove excess glue. Another drop of epoxy is applied before placing the brass block on the chip, mirror side down, as shown in figure 3.6 (a–b). Then excess epoxy is removed from the edges and the seal junction cures at  $100 \text{ }^\circ\text{C}$  for 15 min. The block can now be removed, leaving the mirror behind, as shown in figure 3.6 (c).

The chip is now ready to be attached to the square quartz cell, as shown in figure 3.6 (d). We place 353ND epoxy between glass slides and smear it to a thin layer. A small amount is then transferred to all edges of the cell, which is then seated on the chip on top of the mirror. The cell is weighted down with a brass block and baked at  $100 \text{ }^\circ\text{C}$  for 1.5 h using a minimum of 1.5 h for ramping up and down.

Finally, this assembly is epoxied to a UHV glass-to-metal transition using a glass disk with

a 1 cm bore to compensate for the size mismatch. Now the atom-chip glass cell looks exactly as shown in figure 3.4 (b) if we add a rubidium dispenser, Pyrex helix, and NEG.

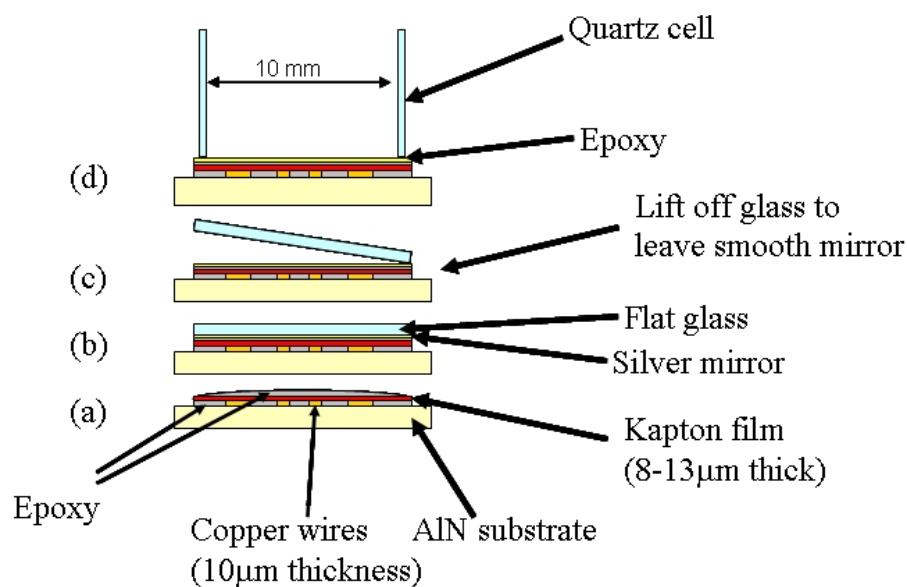


Figure 3.6: Cell construction procedure diagram.

### 3.3.2 Rubidium dispenser

Rubidium dispensers have been widely used to provide pure atom sources in atomic research systems [59] and pulsed atom sources in some atom-chip groups [15, 68]. In the dispenser, rubidium atoms are released from a metal surface when it reaches a critical temperature during heating by an electric current. After the current is switched off and the dispenser cools below the critical temperature, it stops dispensing. Heat loss dominated by radiation results in a very fast switch-off time constant of less than 10 s. Since the temperature of the dispenser directly depends on the electric current strength and the operating time length, a low dispenser current cannot provide enough Rb atoms to coat the cell wall for UV LIAD. On the other hand, a high dispenser current can lead to a high vapor pressure that quickly saturates the ion pump and NEG. Thus, it is very important to find out critical-temperature-related-operating-current parameters, which are not provided by the manufacturer, to run our portable vacuum chamber.

Our rubidium dispenser is a commercial product from SAES (RB/NF/3.4/12FT10+10). Figure 3.7 shows the experimental results of the dispenser at pulsed modes. We find there is a

threshold pulse length  $t_{th}=15$  s for observing rubidium from the dispenser at 6 A. This  $t_{th}$  is strong evidence for the existence of a critical temperature. It can also be clearly seen from the 20 and 30 s pulse curves in figure 3.7 (a) that there are no big pressure changes in the first 15 s. However, the pressure decreases after the current is switched off without any delay because of radiation heat loss. The exponential ( $1/e$ ) time constant of switching off is typically 5–10 seconds. These results show that the Rb dispenser can work as a fast atom-pulse source. However, we must wait for at least  $t_{th}=15$  s, the pulse length to reach the critical temperature for dispensing, to start a MOT. Therefore, the pulsed dispenser does not work for a fast MOT and BEC production. In our BEC experiment, we use the UV LIAD method to load our MOT within 3 seconds instead of controlling the dispenser current.

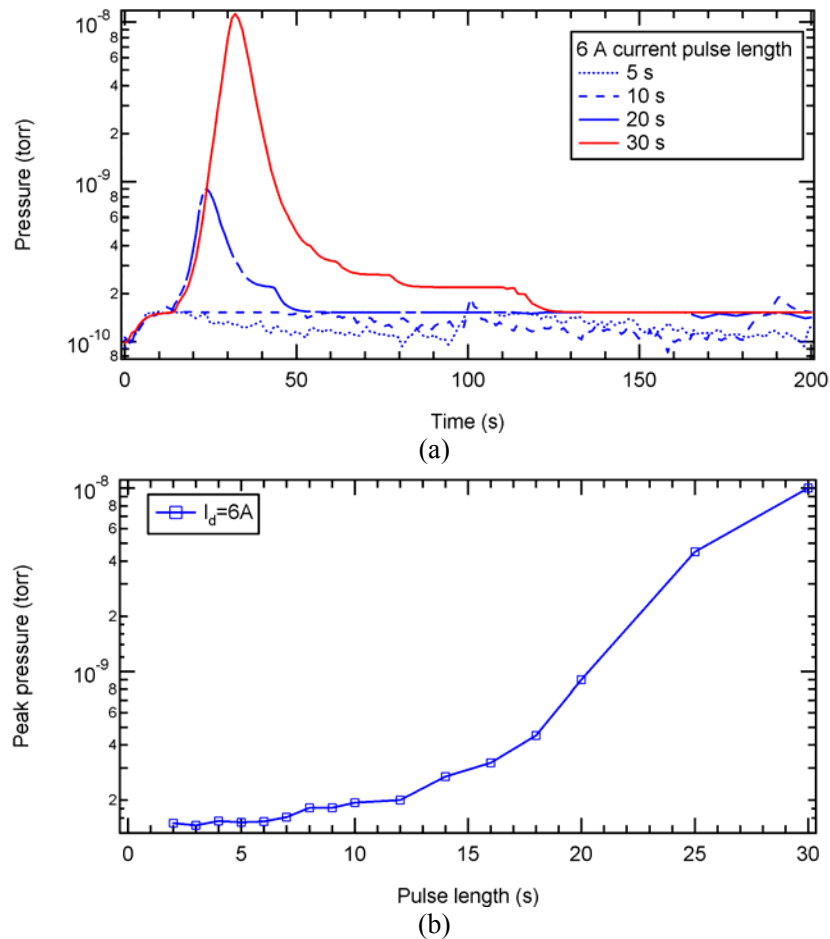


Figure 3.7: Results of a pulsed dispenser mode at 6 A. (a) Pressure response with different pulse lengths from 5 to 30 s. (b) The peak pressure vs pulse length. The pressure is measured by the small 8 L/s ion pump. A current pulse with length  $\Delta t$  starts at  $t=0$  and ends at  $t=\Delta t$ .

Other indirect evidence for the existence of a critical temperature comes from measuring steady-state pressure vs dispenser current, as shown in figure 3.8. The threshold current of about 3 A indicates that the rubidium atoms do not come out until the dispenser reaches a higher temperature. In our daily experiments, we use 3 A as the operating current to coat Rb atoms to the quartz cell wall for 15 to 30 minutes before starting a series of BEC experiments using the UV LIAD method. The operating current varies from 3 to 3.5 A for individual dispensers. In reality, we define an operating current  $I_{\text{dopt}}$  as one in which the MOT loading time is about 3 s ( $P = 1.0 \times 10^{-8}$  torr and magnetic trap life time about 0.8 s). Under the condition, typically  $6\text{--}8 \times 10^6$  atoms are loaded into the MOT at the dispenser operating current, and  $3 \times 10^6$  atoms are transferred into the Z-wire magnetic trap.

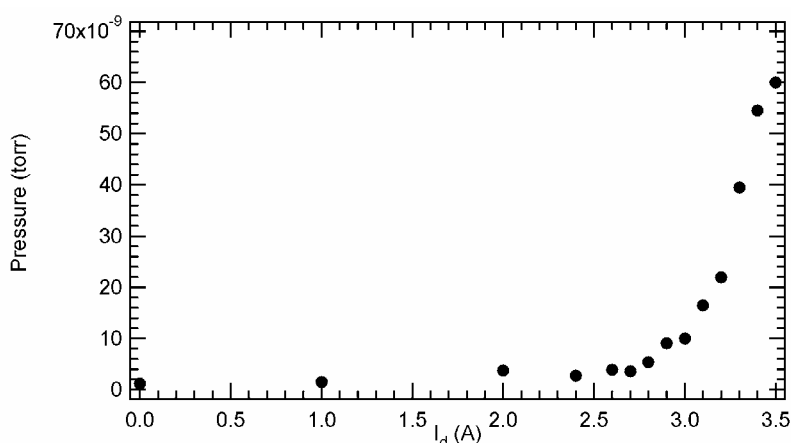


Figure 3.8: Cell pressure  $P$  vs Rubidium dispenser current  $I_d$ . The pressure is obtained from measuring the MOT loading time. A  $3 \times 10^{-8}$  Torr pressure results in a 1 s MOT loading time. The threshold current of the dispenser is about 3 A.

The above discussion assumes that the dispenser has been well prepared inside the vacuum. To use the dispenser in a UHV condition, it needs to be burned at high current, i.e., 6–7 A for several minutes to get rid of the protection layer.

### 3.3.3 Pyrex helix

The UV (or IR) quartz cell is transparent to UV light but has a low adsorption rate for Rb atoms to its inner wall. To use UV LIAD to control the Rb vapor pressure, we must use a material



like Pyrex with a high atomic adsorption rate. As shown in figure 3.4 (b), a Pyrex helix provides a good Rb desorption source with its large surface area. The atom number in a MOT loaded by UV is improved by a factor of two with the help of a Pyrex helix.

### 3.3.4 Nonevaporable getter

In NEG pumps, the getter material removes active gas from a vacuum via surface chemical adsorption and bulk diffusion. NEG pumps have some interesting advantages in UHV vacuum applications. They pump hydrogen better than other kinds of pumps. They usually operate without power. They are clean, lightweight, and compact. They can help provide lower ultimate vacuum than is achievable without them. They are vibration-free. They operate unaffected by magnetic fields and do not generate magnetic fields.

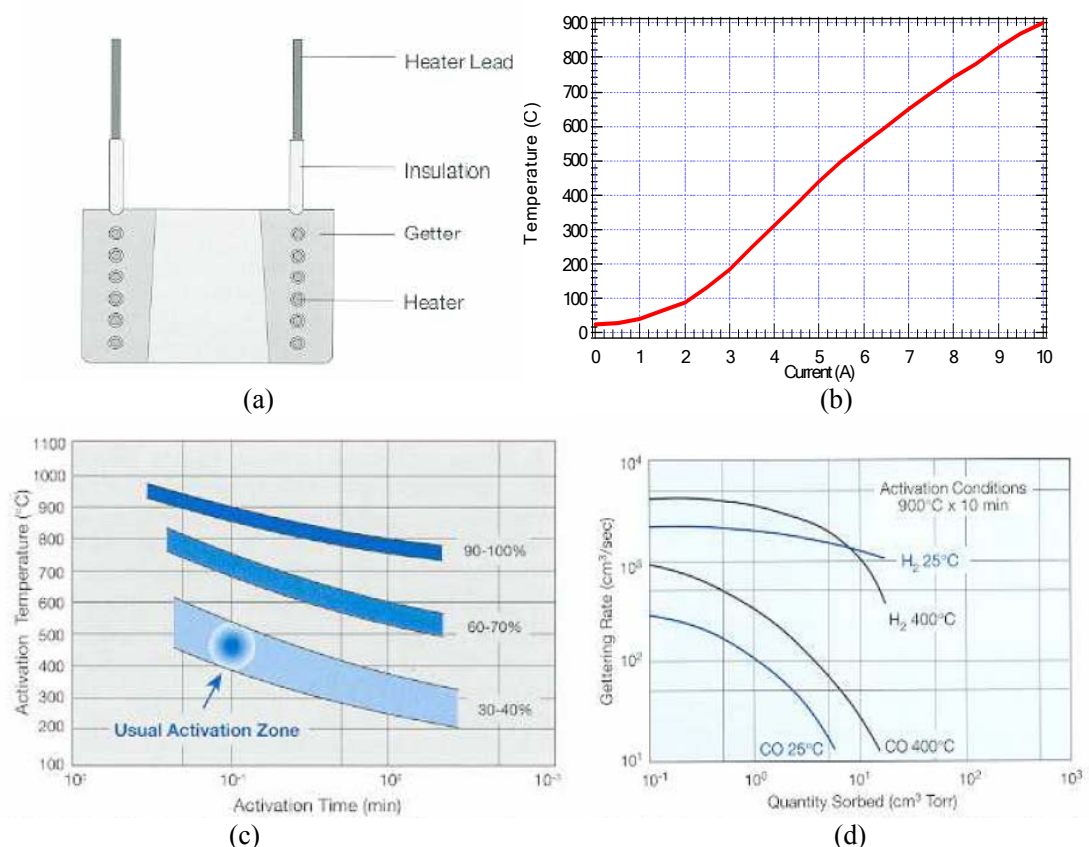


Figure 3.9: SAES NEG ST172 configuration and activation conditions. (a) A typical configuration of a zirconium-based, sintered porous getter. (b) A typical heating curve. (c) The getting efficiency (expressed as a percentage of the initial getting rate of a fully activated getter) after various activation conditions. (d) Sorption curves for CO and H<sub>2</sub> at room temperature and at 400 °C after an activation at 900 °C for 10 minutes. (The specification information about ST172 comes from SAES Getters.)

In our portable atom-chip cell system, we use a zirconium-based, sintered porous NEG from SAES (ST172/HI/16-10/300C). The ST172 is designed for low-temperature activation. At the recommended activation condition of 450 °C (5.2 A) for 10 minutes under a vacuum  $<10^{-3}$  torr, the getter reaches a degree of activation of about 35% with respect to a fully activated getter. Higher temperatures always yield better activation, e.g., a full activation can be reached with 900 °C (10 A) for 10 minutes [figure 3.9 (c)]. From our experience, the activation of ST172 NEG at  $10^{-9}$  torr always results in some extra gas load into the system that is extremely difficult to be pumped away. H<sub>2</sub> sorption capacity is reversible by activation but other gases are not because of their high-energy chemical bonding.

### **3.3.5 Small ion pump (8 L/s)**

The conductance of the square quartz cell for Rb atoms at room temperature is 2.2 L/s, and the conductance of the glass-to-metal transition tube (diameter 2.5 cm and length 9 cm) is 12.4 L/s. For air, they are 3.9 L/s and 21.2 L/s, respectively. Therefore, the small square quartz cell limits overall system conductance. A Varian 8 L/s small ion pump is enough to maintain the UHV pressure of the cell after pinch-off.

### **3.3.6 Pinch-off tube**

Pinch-off tubes are purchased from Huntington Mechanical Laboratories, Inc. (Model CPT-275-075, 0.75-inch tube diameter, copper). They provide a connection between the atom-chip cell and the pumping station. After the cell vacuum is prepared, the tube is pinched off and the atom-chip system becomes independent and portable.

## **3.4 Pumping station**

The portable atom-chip vacuum cell must be prepumped before the 8 L/s small ion pump and NEG can take charge of the UHV pressure. The portable cell is connected to a pumping station through the pinch-off tube (figure 3.10). The pumping station includes an ion gauge, an

all-metal valve, a turbo pump, a TSP, and a big ion pump (20 L/s). Backed by a mechanical rough pump (Varian SH-100), the pumping station is able to pump down the chip-cell chamber to  $10^{-10}$  torr after baking out. The system is assembled by using a torque wrench with a close torque of 90 ft-lbs. A Varian leak detector (model 979) is used to make sure there are no measurable leaks. The commercial parts list for the pumping station is shown in table 3.2.

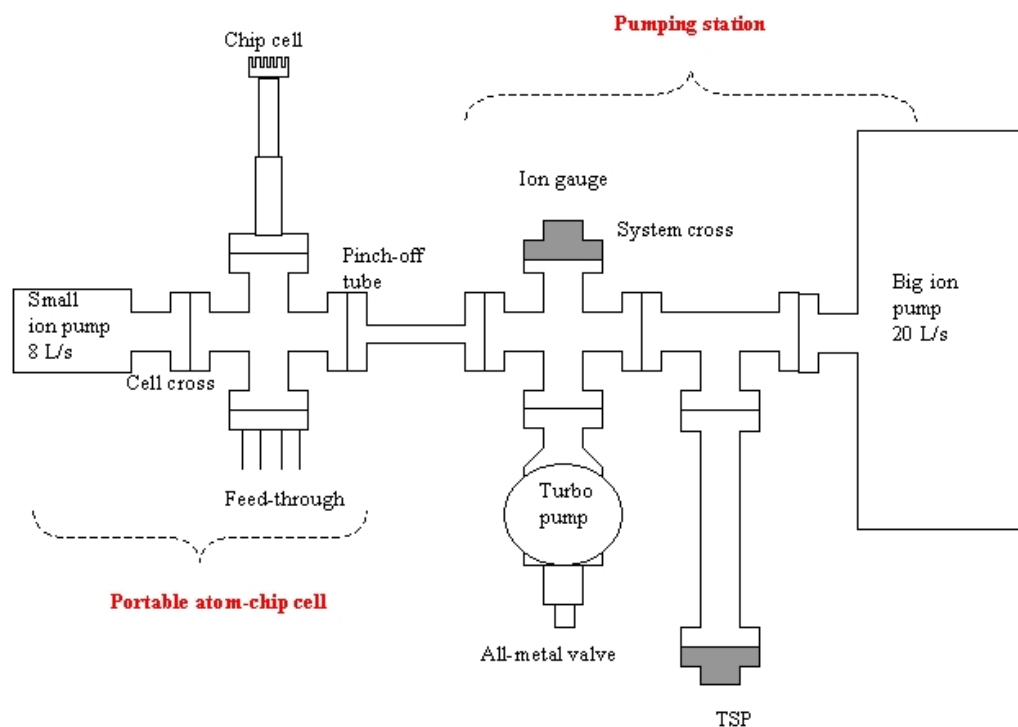


Figure 3.10: A portable atom-chip cell is connected to the pumping station via a pinch-off tube.

Table 3.2: Pumping station parts list.

Part Name	Company	Description
Big ion pump	Varian	Vaclon Plus 40, controlled by Varian MidiVac Controller.
Small ion pump	Varian	8 L/s pump, controlled by Varian MicroVac Controller
Turbo pump	Varian	Turbo-V 70LP
TSP	Varian	Filament-type TSP, Varian TSP Controller.
Ion gauge	Varian	UHV-24p extended-range nude Bayard-Alpert-type ionization gauge tube with a dual thoria-coated iridium filament. Controlled by SenTorr Vacuum Gauge Controller.
ConvecTorr gauge	Varian	ConvecTorr Simulator, controlled by SenTorr Vacuum Gauge Controller.
All-metal valve	Varian	UHV All-Metal Valve, right angle
Rough pump	Varian	SH-100, single scroll pump.
UHV compression port	Varian	3/4 inch port on 2.75 (NW35) ConFlat, part number FCP0075UHV. Used if the pinch-off tube is not modified.

### 3.5 Baking out and pumping down procedure

Baking out is an effective way to degas the vacuum chamber and remove most of the particles attached to the chamber wall, especially water. The turbo pump is used to pump the system during baking out, and the ion pumps and TSP are turned on when the system is cooled down to room temperature. The bakeable and baking temperatures of different components are shown in tables 3.3 and 3.4. In the baking schedule, first, the quartz cell is heated up with a slow temperature ramp, followed by heating the cell cross and the small ion pump. The pumping station is the last. The order is reversed when the system is cooled down. From our experience, the turbo pump itself can pump down to  $1-5 \times 10^{-8}$  torr when the system is still baking out and  $2-5 \times 10^{-10}$  torr after it cools down.

Table 3.3: Atom chip cell bakeable and baking temperature.

Part name	Bakeable temperature (°C)	Baking temperature (°C)
Quartz cell	130	120
Cell cross	>450	250
Small ion pump	400	300

Table 3.4: Pumping station bakeable and baking temperature.

Part name	Bakeable temperature (°C)	Baking temperature (°C)
Big ion pump	350	300
TSP	400	300
System cross	>450	300
Ion gauge	450	300
All-metal valve	450	300
Turbo pump	120	Water cooled

The dispenser and the getter must be well prepared before pinch-off so that they do not release excess contaminants. We prepare the dispenser and getter according to manufacture's instructions while the chip cell is hot and connected to the pumping station. The cell baking takes typically 2–5 weeks. After the cell cools down to room temperature, we clean the quartz cell's inner wall with a flash lamp (Perkin Elmer, Model # FYD-4400) and leave a fresh, uncoated surface for accepting Rb atoms. Then we do fluorescence test by turning on the dispenser to make sure the dispenser has been prepared properly. Finally the atom-chip cell is pinched off from the pumping station, and only the nonevaporable getter and the small ion pump will maintain the

vacuum in the cell of about  $10^{-10}$  Torr.

### **3.6 Conclusion**

We have built a portable atom-chip cell system ready for laser cooling and trapping. After 2–5 weeks of preparation, the self-vacuum-contained cell reaches  $10^{-10}$  torr, which is suitable for atom-chip BEC production. We present the details of making a BEC on the chip in chapter 7.



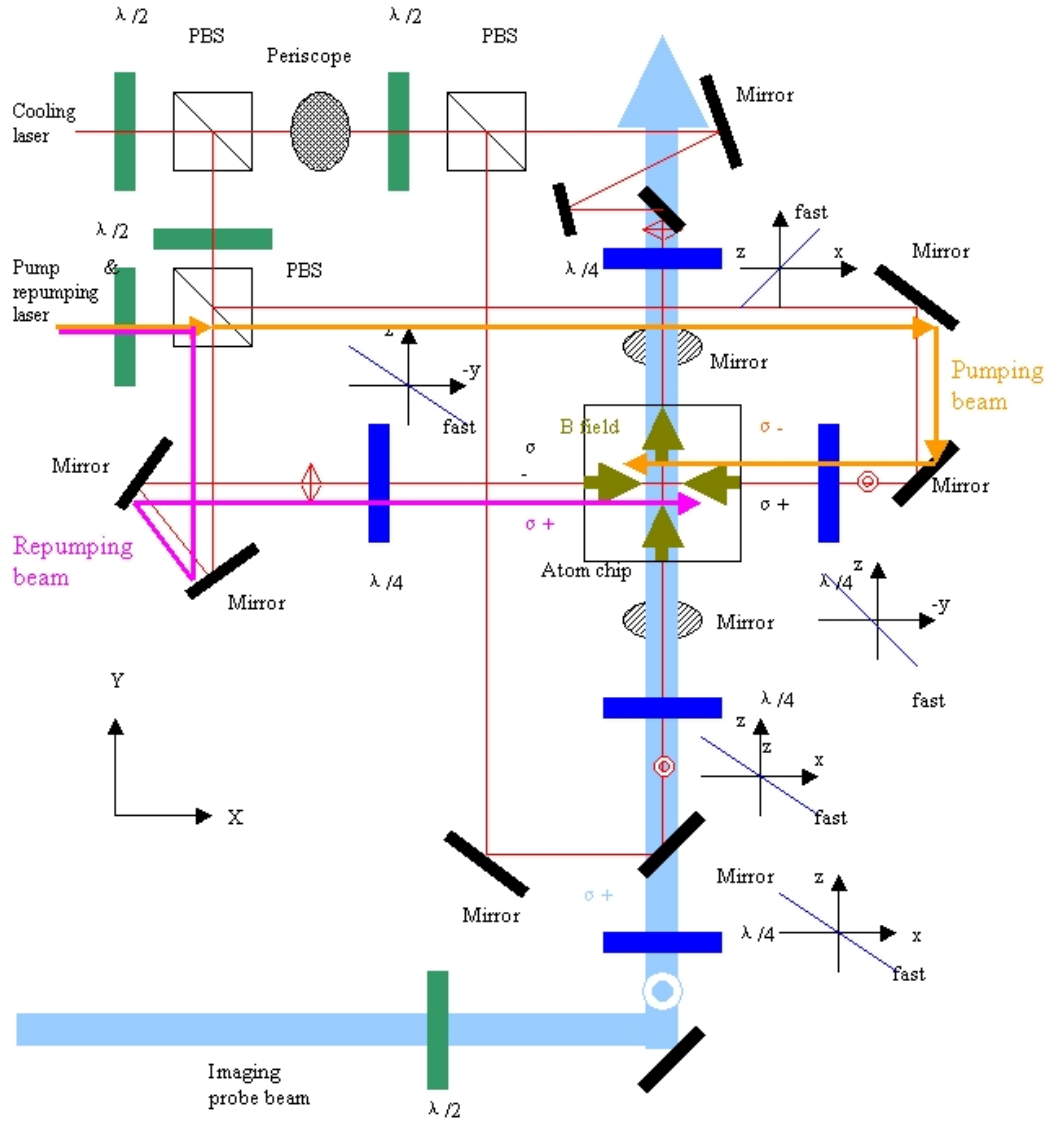


Figure 4.2: Top view of laser optical setup on the small aluminum optical board where we plug in the portable atom-chip cell.

In our atom-chip system, only about a 30 mW of magneto-optical trap (MOT) cooling laser power is required because of the small beam diameter of 8 mm. Such low power consumption allows for utilizing only inexpensive semiconductor laser diodes. We use injection locking with a double-path acousto-optical modulator (AOM) configuration for the cooling laser system, which allows us to change the laser frequency very rapidly (up to 80 MHz) without affecting the fiber-coupling efficiency. The master laser for the injection locking, repumping laser, and pumping/probe laser are home-built JILA-mount external cavity laser diodes (ECLD). The laser

system optical setup on the main optical table is shown in figure 4.1. After coupling to polarization-maintaining (PM) single-mode (SM) fibers, all the lasers are brought onto a small 61 × 61 cm aluminum board where we plug in the portable atom-chip cell, as shown in figure 4.2. When we switch to a new atom-chip cell, we only need to do a few adjustments on the small optical board to optimize the MOT setup. Reflection absorption imaging with an Apogee CCD camera is used to image and measure cold atoms on the chip.

## 4.2 JILA-mount external cavity laser diode

Our atom-chip experiment requires a total of three tunable single mode lasers: cooling laser, repumping laser, and pumping/probe laser. We have designed and built cheap diode laser systems based on a tunable Littrow configuration [71, 72] on a JILA mount. The output is single mode, with a reasonable tunable range (10 GHz), narrow linewidth (<100 kHz), and high power (50–60 mW). The JILA mount ECLD was originally designed by Dr. Patrick Berthoud, one of our previous postdoctoral associate.

In most ECLD systems, temperature stabilization is obtained by controlling the temperature of the entire cavity structure [73, 74] or even the enclosure [75]. The temperature servo system cannot respond adequately to very fast perturbations because of the large thermal mass. Although we follow the simplified mechanical idea of Arnold *et al.* [73], we only servo the temperature of the laser diode placed in its small mount instead of controlling the temperature of the whole external cavity to reduce heat dissipation. In our ECLD system, we modify a JILA mirror mount [component 1 in figure 4.3(a)] to integrate the laser diode (LD), grating and piezoelectric actuator (PZT) into one solid unit. The JILA mount, comparing to flexure structures in commercial ECLD products, works as a very stable mechanical cavity holder.

Our ECLD mechanical system is shown in figure 4.3. A cut in the back plate of the black anodized JILA mirror mount is made to accept the laser diode support [component 2 in figure 4.3 (a)], which includes a collimation tube. A thermoelectric heater/cooler (Peltier) is sandwiched



between the JILA mount and the laser mount to regulate only the temperature of the laser mount. The diffraction grating is glued on an adequate mount [component 3 in figure 4.3(a)] screwed on the front plate of the JILA mount. The three micro-control screws on the JILA mount provide very precise three-dimensional cavity feedback adjustment. The fine rotation of the grating is provided by a stacked piezoelectric actuator preloaded between the grating mount and one of the microcontrol screws by the restoring spring of the JILA mount.

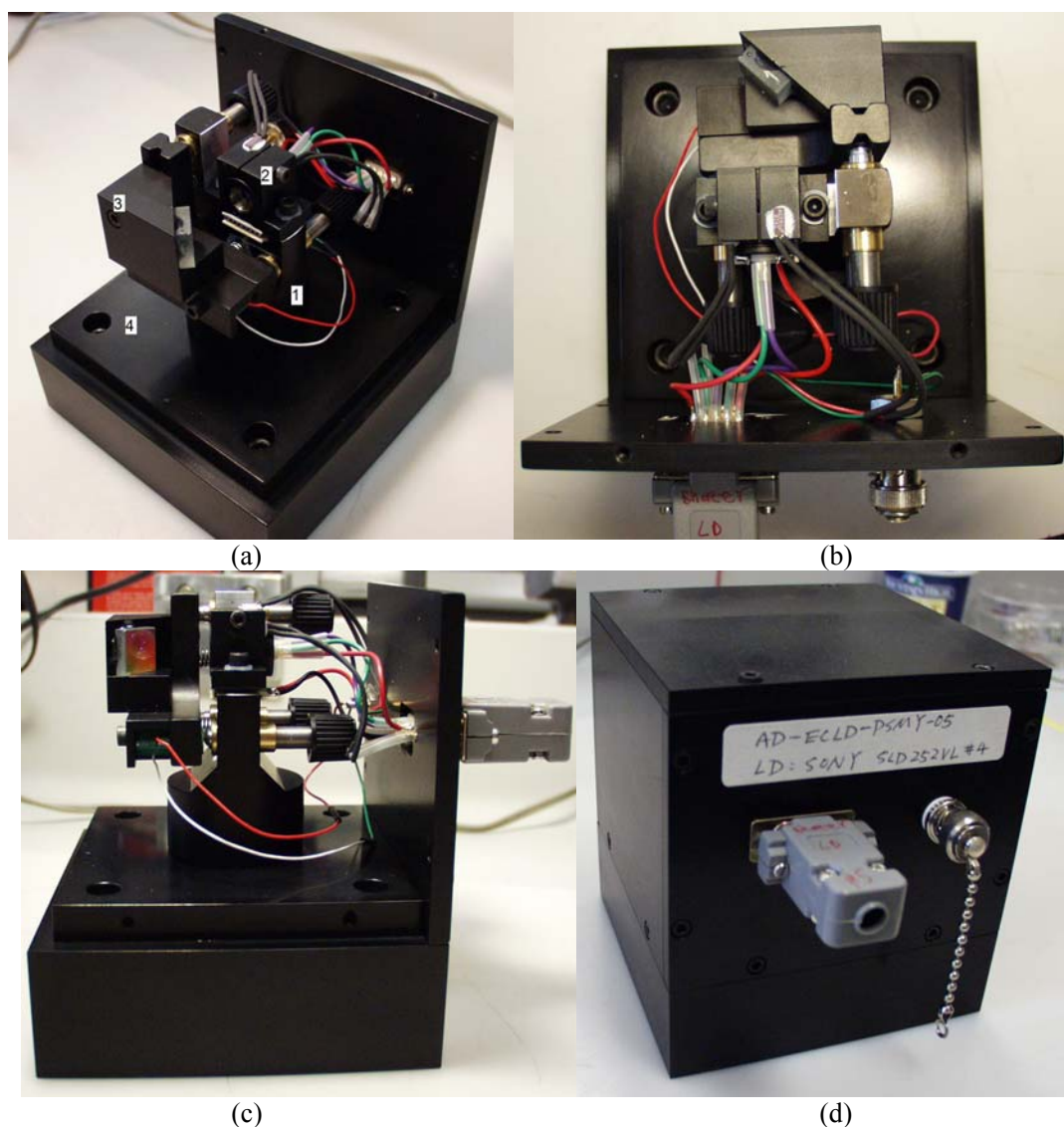
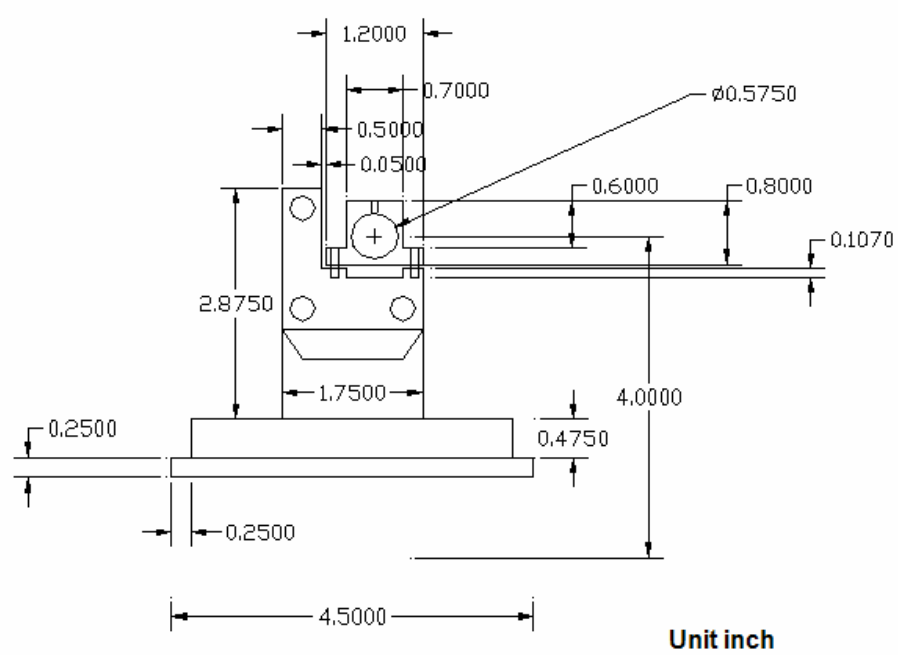


Figure 4.3: Pictures of the JILA mount ECLD laser head system. (a) (1) modified JILA mount, (2) laser diode collimation tube mount, (3) grating mount, (4) base. (b) top view. (c) side view. (d) An overview of the entire box.



Laser Header General View

JILA mount front part

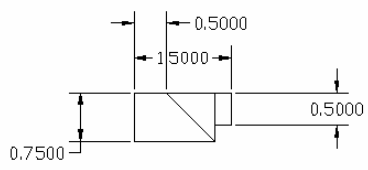
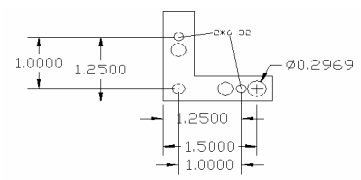
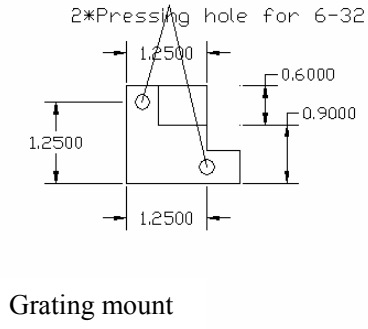
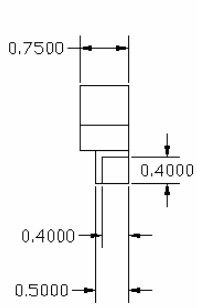


Figure 4.4: Drawing of the JILA mount ECLD mechanical components.

The mechanical drawings of the JILA mount, the laser diode collimation tube mount, and the grating mount are shown in figure 4.4. The following is a list of commercial elements of our ECLD system:

- (1) One JILA mount (solid back plate, L-shape front plate).

- (2) One Sony laser diode SLD252VL. The measured wavelength of this diode at room temperature is 782 nm. The maximum specified output power is 100 mW at its operating current of 120 mA.
- (3) One Schottky diode 1N5711 for laser diode protection (optional).
- (4) One Thorlabs collimation tube LT230P-B, which includes an aspheric lens C230TM-B with a focal length  $f=4.5$  mm and a numerical aperture  $NA=0.55$ .
- (5) One Marlow Industries Inc. TEC thermoelectric heater/cooler (Peltier) DT3-2.5 provided by Thorlabs (item # TEC3-2.5) with  $I_{\max}=2.5$ A,  $V_{\max}=3.6$ V, and a size of  $16 \times 16 \times 4$  mm.
- (6) One precision thermistor YSI44008 for the temperature servo loop.
- (7) One thermometer AD590 to monitor the temperature on the top of the laser diode mount.
- (8) One Edmund Scientific holographic diffraction grating L43-775, 1800 l/mm, VIS,  $12.5 \times 12.5$  mm.
- (9) One Thorlabs piezoelectric stack actuator AE0505D16 to tune the laser output wavelength.
- (10) One JILA laser diode current controller and temperature controller AD014-07.

After all the mechanical parts have been machined and the entire ECLD system has been assembled, we start to align the grating external cavity, adjust the lasing to the right wavelength, and optimize the mode-hop free range. The rough alignment of the cavity can be done by adjusting the three microcontrol screws of the JILA mount while watching the first-order feedback from the grating to the laser diode through a pinhole. Then the following two-step fine adjustment can be repeated to optimize the cavity feedback and obtain the right output wavelength:

- (1) We monitor the curve of the ECLD output power vs laser diode current by modulating the current around the threshold current  $I_{th}$  value. We minimize  $I_{th}$  by adjusting the cavity feedback with the upper microcontrol screw of the JILA mount.
- (2) We change the output wavelength and move it closer to 780.24 nm by adjusting the side microcontrol screw of JILA mount to change the grating angle and stop where the laser wavelength becomes unstable and multi mode. The wavelength is measured by a wavemeter (EXFO WA-1500).

Repeating the above two-step procedures, we successfully achieve a single mode output at 780.24 nm. In some of our ECLD systems, we have successfully pushed a 785 nm laser diode down to 780 nm (Rb D2 line) and 776 nm ( $^{87}\text{Rb}$  transition from  $5P_{3/2}$  to  $5D_{3/2}$ ), and up to 795 nm (Rb D1 line) without adjusting the LD temperature. A final optimization of the central frequency and mod-hop free range can be obtained by adjusting the LD temperature and current slightly. Figure 4.5 shows some results from one of our ECLD lasers. The mode-hop free range, in which the laser frequency can be freely tuned by the PZT, is about 10 GHz, as shown in figure 4.5(a). The threshold current  $I_{\text{th}}$  is lowered from the free-space-running value of 32 to 28 mA with the external cavity, as shown in figure 4.5(b). The output power at operating current 110 mA is 60 mW. For more about the ECLD design, please see references [76–78].

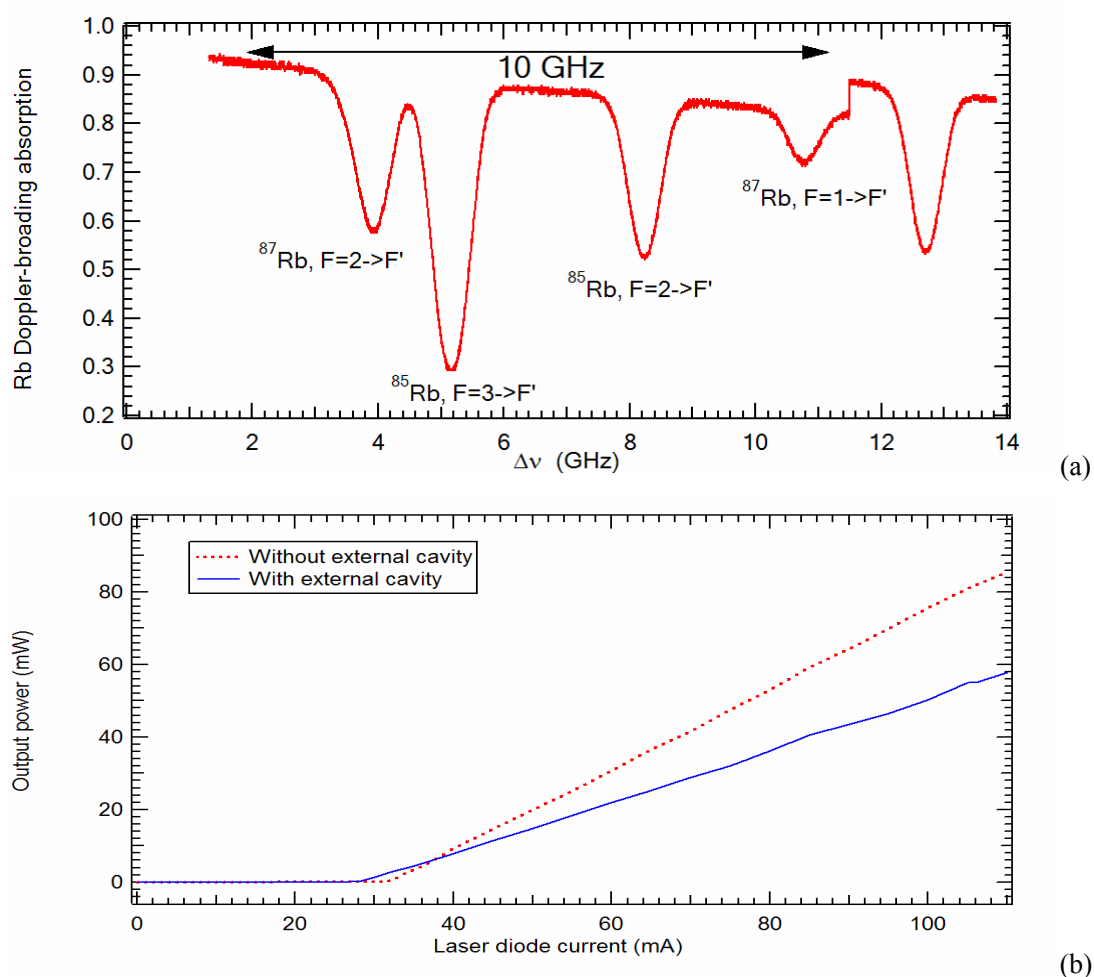


Figure 4.5: Result of one of the JILA mount ECLD lasers. (a) Rb Doppler-broadened D2 absorption spectrum. (b) Laser output power vs LD current.

### 4.3 Cooling laser

Our atom-chip mirror-MOT cooling laser is locked to the  $^{87}\text{Rb}$  D2 closed transition, from  $|5S_{1/2}, F=2\rangle$  to  $|5P_{1/2}, F'=3\rangle$ , with a certain amount of red detuning of  $\Delta\nu$ , as shown in figure 4.6. Limited by our atom-chip size of  $1 \times 1$  cm, the saturation power with a typical detuning of 9 MHz is about 35 mW. This low power requirement makes a diode laser suitable for obtaining cooling laser power without using any high power amplifiers. On the other hand, atom number and cooling efficiency are more important to us because of the small MOT capture volume. We must control the cooling frequency very rapidly with great precision, at different laser cooling stages, e.g., MOT, compressed MOT (CMOT), and polarization gradient cooling (PGC). Frequency control is readily achieved in our system with an injection locking method [79, 80] employing a two-diode-laser (master-slave) configuration.

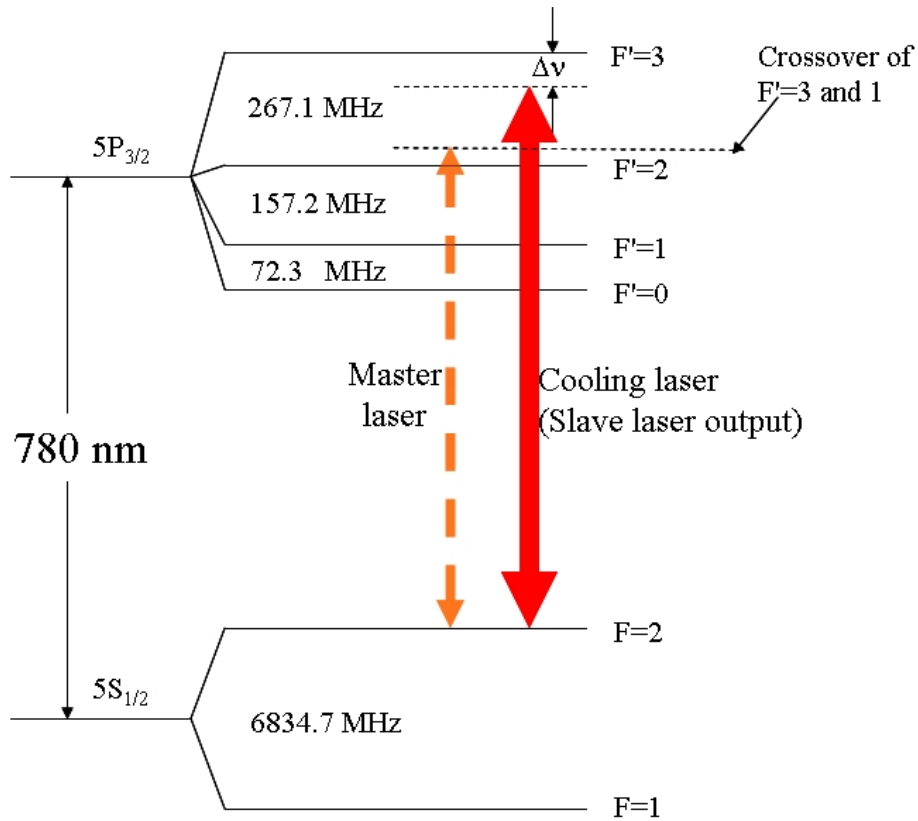


Figure 4.6:  $^{87}\text{Rb}$  D2 line hyperfine energy levels and the MOT cooling transition. The master laser is locked to the crossover of the transitions  $F=2$  to  $F'=3$  and  $F'=1$ . The slave laser is injection locked by the master laser beam after a double-path AOM that shifts the master laser frequency. The slave output, i.e., the MOT cooling laser, is red-detuned with  $\Delta\nu$  from the cycling transition from  $F=2$  to  $F'=3$ .

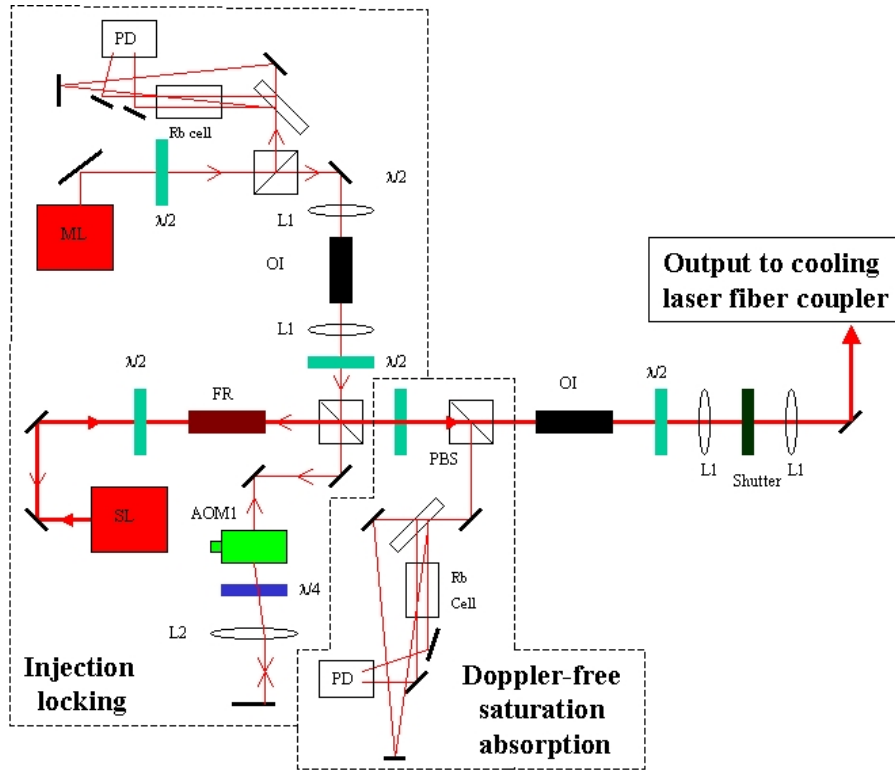


Figure 4.7: Cooling laser optical setup before coupled to the fiber. ML: master laser; SL: slave laser; PD: photodiode;  $\lambda/n$ :  $\lambda/n$  wave plate; L: lens; OI: optical insulator; FR: faraday rotator. AOM: acousto-optical modulator; PBS: polarization beam splitter.

The layout of the optical setup for the cooling laser is shown in figure 4.7. The master laser is a JILA-mount ECLD diode laser with a SONY 780 nm laser diode. It has an output power of 54 mW at its operating current of 106 mA. The slave laser is a bare SONY LD without an external grating cavity. As shown in figure 4.7, the master laser output is injected into the slave laser after passing through a double-path AOM setup, which shifts the master laser frequency with a double AOM RF frequency. The two lenses (L1,  $f=35$  mm, Thorlabs achromatic doublet LAC628-B) are used to shape the master laser beam. In a general system, not in our specific case, an anamorphic-prism pair may be used to shape the master laser beam for mode matching between the injected master laser beam and the slave laser field. The double-path AOM configuration with a mirror at one of the focal planes of the lens L2 ( $f=150$  mm, Thorlabs achromatic doublet LAC789-B) compensates for the change of beam direction that occurs after the beam passes through the AOM when changing the AOM RF frequency. The double passed  $\lambda/4$  wave plate

changes the polarization of the master laser from horizontal to vertical so that the master laser beam can be totally reflected by the polarization beam splitter (PBS) to overlap with the slave laser output. The  $\lambda/2$  wave plate and Faraday  $45^\circ$  rotator are used to match the linear polarizations between the injected master laser and slave laser fields. The slave laser frequency is monitored by a Doppler-free saturation absorption setup [81]. We use a mechanical shutter (Uniblitz LS2T2, 2 mm aperture) to switch the cooling laser on or off. To increase the switching speed of the shutter, We use two lenses to focus the beam at the shutter center. The optical switch rising (falling) time is about 200 (300)  $\mu\text{s}$ . The final output of cooling laser beam is coupled to a single-mode PM fiber that directs the laser beam to our atom-chip cell system.

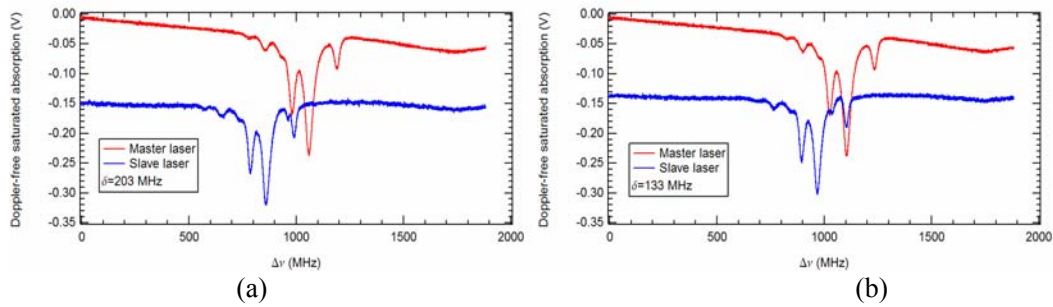


Figure 4.8: Master-slave injection locking signals. (a) Double-path AOM frequency shift is  $\delta=2f=203$  MHz. (b) Double-path AOM frequency shift is  $\delta=2f=133$  MHz. The red-detunings of the slave laser output to the cooling transition are 9 MHz and 79 MHz, respectively.

The master laser is locked to the crossover of the transitions  $F=2$  to  $F'=3$  and  $F'=1$ , i.e., 212 MHz red-detuned from the cooling transition  $F=2$  to  $F'=3$ , as shown in figure 4.6. The slave laser has an output power of 60 mW at the operating current of 92 mA. The operating RF frequency range of the AOM1 (Crystal Technology Inc, part number 3080-122, central RF frequency 80MHz, wavelength 780–850nm) is 60–110 MHz. The red-detuning of the cooling laser is calculated by

$$\Delta\nu = 212\text{MHz} - 2\delta, \quad (4.1)$$

where  $\delta$  is the AOM RF frequency. As shown in figure 4.8, we can freely tune the injection locked slave laser frequency red-detuning  $\Delta\nu$  from 9 MHz to 79 MHz. The operating cooling laser frequencies of different cooling stages are shown in table 4.1.

Table 4.1: Cooling laser frequency detuning at different cooling stages

	$\delta$ (MHz)	$\Delta\nu$ (MHz)
Mirror MOT	101.5	9
CMOT	94.5	23
PGC	70	72

To evaluate the performance of injection locking, we define two parameters: (1) the locking fraction (LF) and (2) the locking range (LR). The LF is defined as the ratio of the slave output power, locked to the injected master laser frequency, to the total slave-laser output power. The LR is defined as the frequency locking range, in which the slave laser stays locked while the frequency detuning  $\Delta\nu$  changes from 9 MHz to 9 MHz + LR by adjusting the AOM RF frequency. The LF tells us how well the slave laser is injection locked at some specific frequency, and the LR is crucial for obtaining a large frequency detuning ranges, as shown in table 4.1.

Figure 4.9 shows the LF vs the injected master laser power at  $\Delta\nu = 9$  MHz. The LF is measured with Doppler-free saturation absorption and compared to a reference ECLD output. At each point of injected master laser power, the injected laser beam alignment is optimized to maximize the LF. The required injected power to lock the slave laser with LF=1 is very low (<0.1 mW), as shown in figure 4.9.

In the experiment, we find that the injected master laser power only drops by a factor of 1/2 when changing  $\Delta\nu$  from 9 MHz to 72 MHz. Thus, from figure 4.9, we deduce that the LR is larger than 60 MHz if the injected laser power at  $\Delta\nu = 9$  MHz is more than 1 mW. However, this is not true because the double-path AOM setup is not ideal and the injected master laser beam changes its direction and wave front when we change the AOM frequency. As a result, the mode matching between the slave laser and master laser varies at different AOM frequencies. The LR vs the injected master laser power at  $\Delta\nu = 9$  MHz is shown in figure 4.10, which shows how the LR starts to drop linearly when the injected master laser power drops below 4 mW.



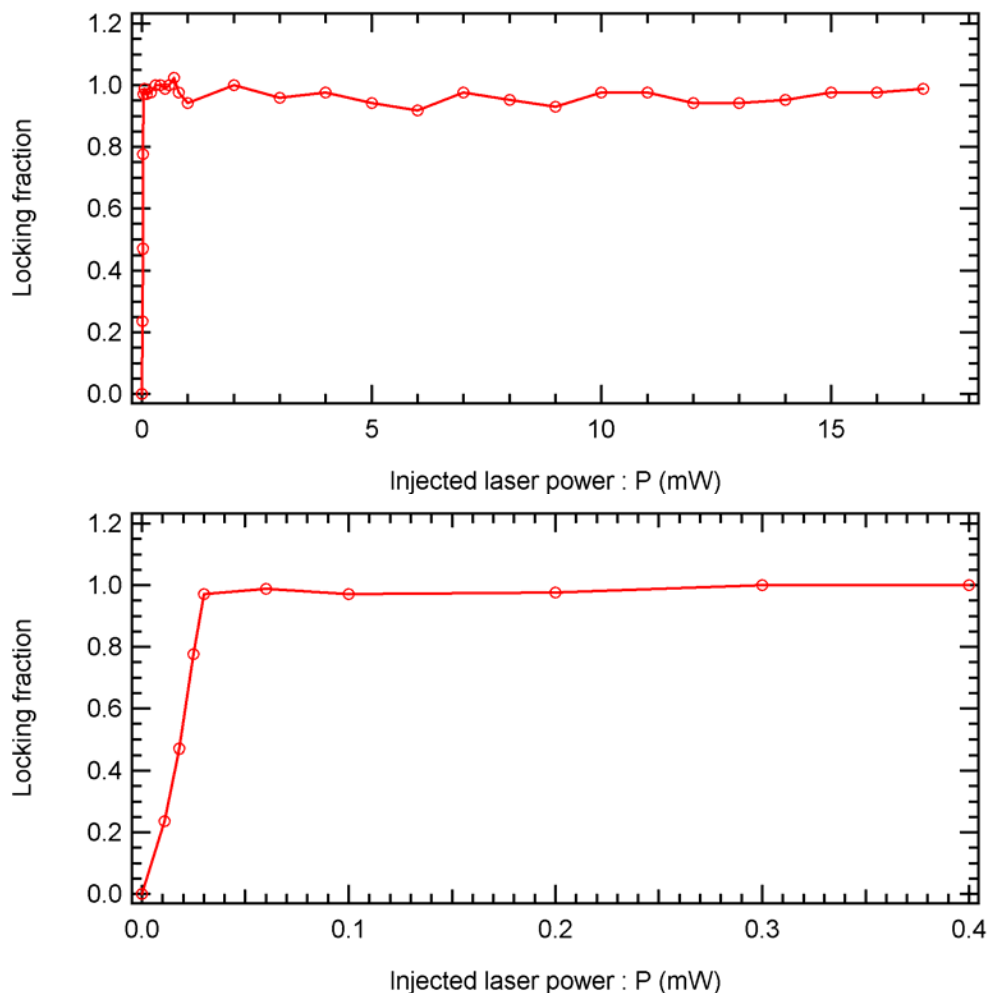


Figure 4.9: Slave laser locked output fraction vs injected master laser power.

Therefore, in the injection locking system, mode matching is more crucial than the injected master laser power. Mode mismatching dramatically reduces the locking range and requires much higher power to lock the slave laser. Mode mismatching in a real system is caused by many factors, including beam alignment, waveform distortion from the AOM, and the slave laser diode temperature. We find that, among these factors, the stability of the slave laser diode temperature is the most important. If the temperature controller cannot servo the LD temperature very well, changing laser power while switching the AOM frequency significantly affects the slave LD internal cavity modes. We have tested our system with more than 50 mW of injected master laser power, and we have not seen any improvement when compared to lower injected power (20 mW). However, a high injected master laser power makes it more difficult for the controller to stabilize

the LD temperature.

In our optimized injection locking system, the injected master laser power at  $\Delta\nu = 9$  MHz is about 24 mW. We run the slave laser diode at 92 mA, which is lower than the recommended operating current of 110 mA, to optimize temperature stability. The slave laser output is about 60 mW, and the final output after the fiber is about 30 mW. The system is capable of output up to 50 mW of power after fiber coupling if we operate the slave LD at 120 mA.

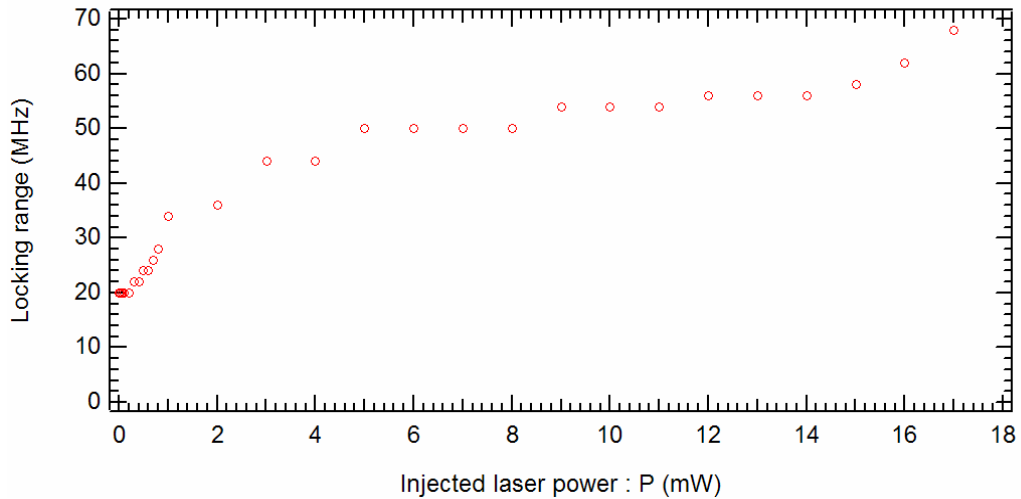


Figure 4.10: Injection locking range vs injected laser power.

## 4.4 Repumping laser

In an ideal two-state closed system, one cooling laser with six beams and a quadrupole magnetic field are enough to form a MOT. However, as shown in figure 4.6, there are many hyperfine levels in the real  $^{87}\text{Rb}$  D2 transitions where the cooling transition is not completely isolated. The cooling laser beam not only couples the ground state  $|5S_{1/2}, F=2\rangle$  with the excited state  $|5P_{3/2}, F'=3\rangle$  but also pumps the atoms from  $|5S_{1/2}, F=2\rangle$  to other excited hyperfine states  $|5P_{3/2}, F'=2\rangle$  and  $|5P_{3/2}, F'=1\rangle$  through nonresonance pumping effect. The atoms pumped to the  $F'=2$  and  $F'=1$  states have decay channels to the dark ground state  $|5S_{1/2}, F=1\rangle$ . Thus, all atoms finally fall away from the cooling transition. To have a continuous cooling process, we must repump the atoms back to the cooling transition. We do this by adding a repumping laser beam, which is locked to the on-resonance transition from  $F=1$  to  $F'=2$ , as shown in figure 4.11. The

on-resonance saturation intensity of the repumping transition is 5.94 mW/cm<sup>2</sup>.

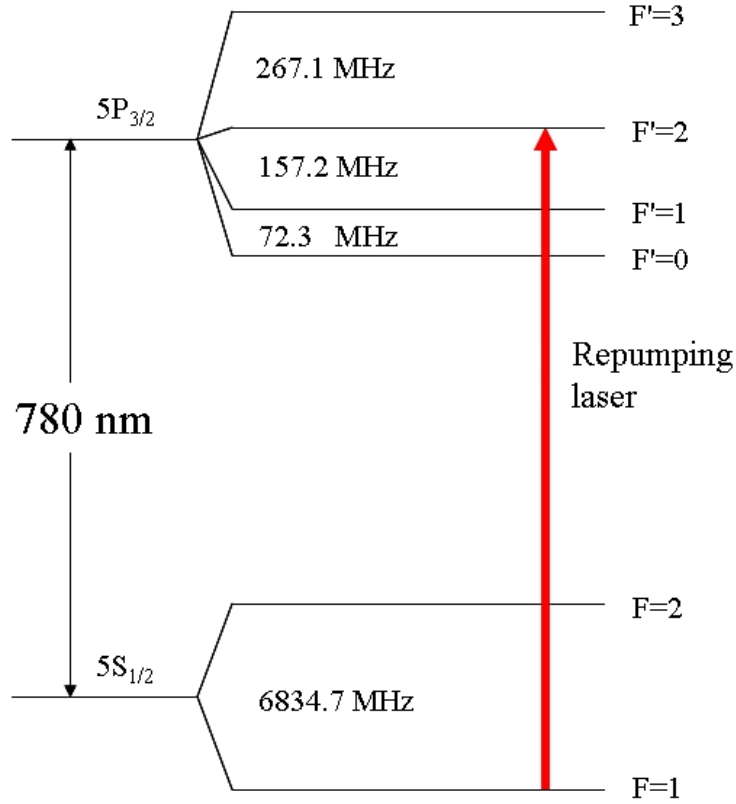


Figure 4.11: <sup>87</sup>Rb D2 line hyperfine energy levels and the MOT repumping transition. The repumping laser, locked to the on-resonance transition F=1 to F'=2, is used to repump atoms from the dark ground state |5S<sub>1/2</sub>, F=1> to the state |5S<sub>1/2</sub>, F=2>.

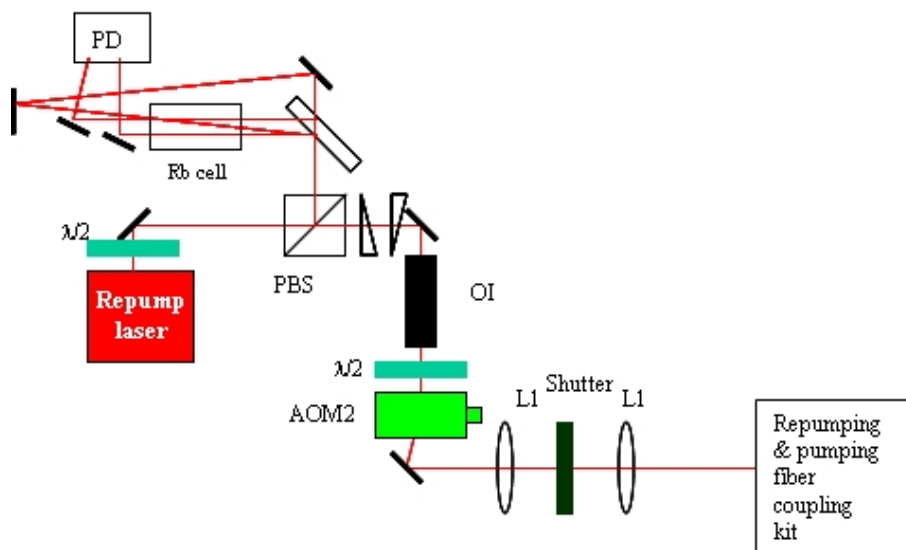


Figure 4.12: Repumping laser optical setup before coupled to the fiber.  $\lambda/2$ :  $\lambda/2$  wave plate; L: lens; OI: optical insulator; AOM: acusto-optical modulator; PBS: polarization beam splitter.

The repumping laser output optical setup is shown in figure 4.12. The repumping laser is one of our home built ECLD with a low power Sharp laser diode (LT024MD) and outputs about 12–15 mW. The laser frequency is locked to the crossover of the transitions from  $F=1$  to  $F'=2$  and  $F'=1$  and thus is 78.6 MHz red-detuned from the repumping transition  $F=1$  to  $F'=2$ . This frequency detuning is compensated by taking the first order diffraction beam from the AOM2 (Crystal Technology Inc, part number 3080-122, central RF frequency 80MHz, wavelength 780-850nm) operated at 78.6 MHz. The combination of the AOM2 and the optical mechanical shutter, shown in figure 4.12, provides rapid control of the repumping laser power.

After the shutter, the repumping laser is coupled, together with the pumping laser beam (section 4.5), into a single mode PM fiber that directs the laser to the atom-chip system. The power of the repumping laser from the fiber output is about 6 mW.

## 4.5 Pumping/probe laser

The optical pumping and imaging probe laser beams do not require high power and allow us to use a single home-built JILA mount ECLD to provide power for both of them. The pumping and probe transitions are shown in figure 4.13. The pumping/probe laser is locked to the crossover of the transitions from  $F=2$  to  $F'=3$  and  $F'=2$ . As shown in figure 4.14, the laser output from the ECLD is split in two with a PBS: a pumping laser beam and a probe laser beam, whose frequencies are controlled by the AOMs (Crystal Technology Inc, part number 3110-120, central RF frequency 110MHz). The pumping beam, together with the repumping laser beam, is coupled to a single-mode PM fiber. The probe beam is coupled to another single-mode PM fiber.

In the MOT, the atoms on average populate all Zeeman sublevels of state  $|5S_{1/2}, F=2\rangle$  because of the degeneracy caused by spherical symmetry. However, in the atom-chip magnetic trap, only atoms in weak-field-seeking states  $M_F=2$  and  $M_F=1$  can be trapped. To improve the magnetic trap loading efficiency, we optically pump all atoms to a single Zeeman sublevel  $|5S_{1/2}, F=2, M_F=2\rangle$  by applying a circularly polarized  $\sigma_+$  pumping laser beam and a magnetic bias field along the beam direction.

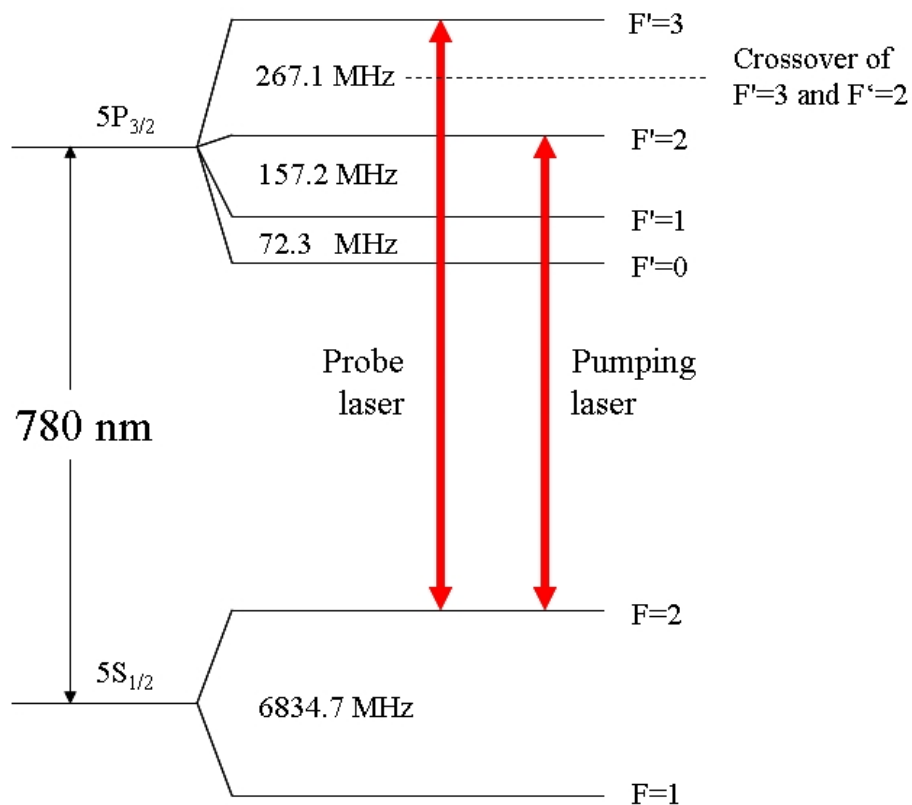


Figure 4.13:  $^{87}\text{Rb}$  D2 line hyperfine energy levels and the pumping and probe transitions.

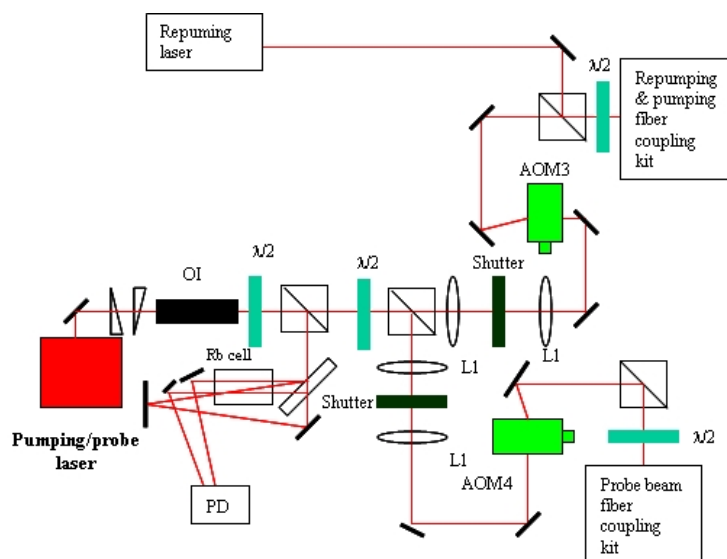


Figure 4.14: Pumping/probe laser optical setup before coupled to the fiber.  $\lambda/2$ :  $\lambda/2$  wave plate; L: lens; OI: optical insulator; AOM: acousto-optical modulator; PBS: polarization beam splitter.

Figure 4.15 shows the pumping effect schematically. Before optical pumping, the atoms on average populate all ground state Zeeman sublevels [figure 4.15(a)]. These Zeeman sublevels split under a uniform bias magnetic field  $B$ , and all the atoms are pumped into the dark state  $M_F=2$  after applying a  $\sigma_+$  circularly polarized beam [figure 4.15(b)]. The average frequency detuning  $\Delta\nu$  can be determined by

$$\Delta\nu = \frac{1}{4} B \mu_B \sum_{M_F=-2}^1 [g_{F'}(M_F + 1) - g_F M_F] = B \times 0.815 \text{ MHz/G}, \quad (4.2)$$

where  $g_F=1/2$  and  $g_{F'}=2/3$  are the Lande factors, and  $\mu_B$  is the Bohr magneton. In our experiment, we fix the frequency detuning of the pumping laser at 12.6 MHz and optimize the bias field at 13 G, which is fairly consistent with equation (4.2).

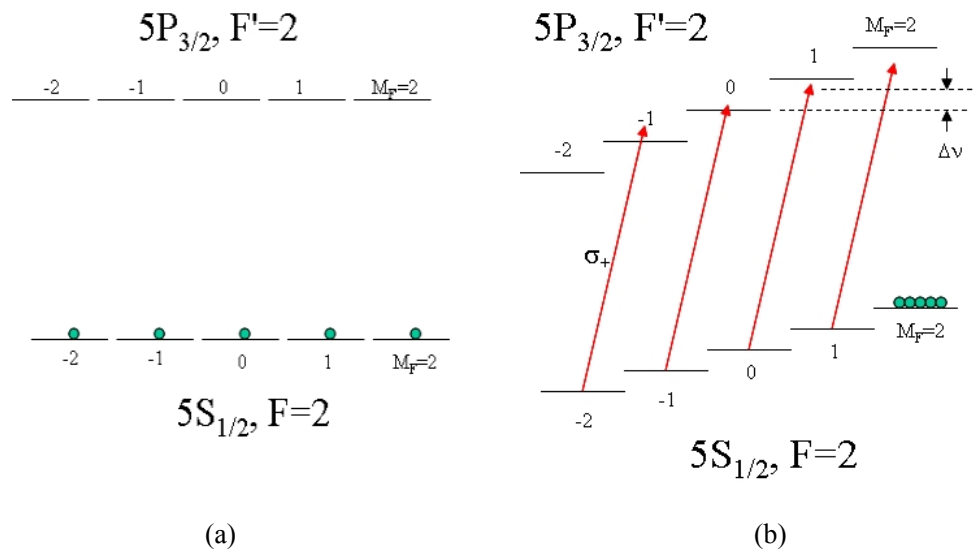


Figure 4.15: Schematic of the optical pumping effect. (a) Before optical pumping, the atoms on average populate the degenerated Zeeman sublevels. (b) With optical pumping, all the atoms are pumped to the  $M_F=2$  state.

The probe transition is from  $|F=2, M_F=2\rangle$  to  $|F'=3, M_F=3\rangle$ . Figure 4.16 shows the Zeeman sublevel splitting under a uniform bias magnetic field  $B$ . The frequency detuning  $\Delta\nu$  can be determined by

$$\Delta\nu = B \mu_B (3g_{F'} - 2g_F) = B \times 1.39 \text{ MHz/G}. \quad (4.3)$$

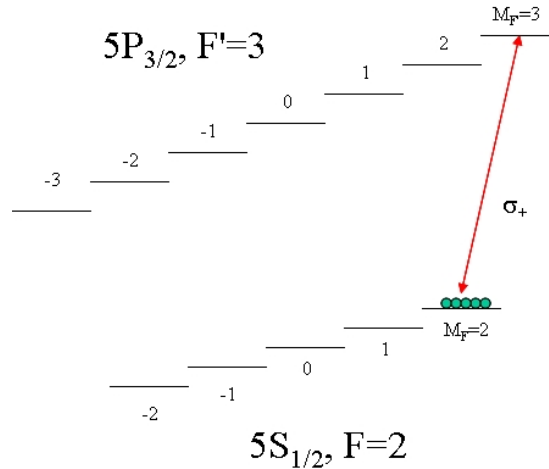


Figure 4.16: Schematic of the probe absorption under a bias magnetic field.

## 4.6 Fiber coupling

From the laser sources to the atom-chip system, the laser beam wave front is distorted by many optical components, including AOMs, isolators, and mirrors. We use single-mode PM fibers to get very clean Gaussian beam shapes. On the other hand, the fiber coupling is also part of our “plug-in” concept. We disconnect all the fibers before we assemble the atom-chip cell to the small table (figure 4.2). After the cell has been plugged in, we connect the fibers back to the atom-chip table directly.

Here we design an inexpensive PM fiber-coupling kit based on the commercially available components listed in table 4.2. The system setup diagram is shown in figure 4.17. The laser beam input comes from the forwarded AOM and mechanical shutter output. We use the two lenses to not only focus the laser beam onto the shutter plane to increase the shutter speed, but also to reshape the laser beam to optimize the mode matching for fiber coupling. The two mirrors are used to adjust the beam height and direction. The PBS works as a linear polarizer to remove the distortion of polarization before being coupled to the single-mode PM fiber. The  $\lambda/2$  wave plate in front of the coupling package is used to rotate the linear polarization to match the PM fiber axes. The coupling package, purchased separately from Thorlabs, includes a SM1 Z translator, a SM1

FC fiber adaptor, an aspheric lens, and other components as listed in table 4.2. The output, mounted on the atom-chip cell table, is collimated by an achromatic lens.

We have demonstrated that the above compact, simple, and inexpensive fiber-coupling system provides a coupling efficiency  $>70\%$  and an output extinction ratio of  $>30$  dB.

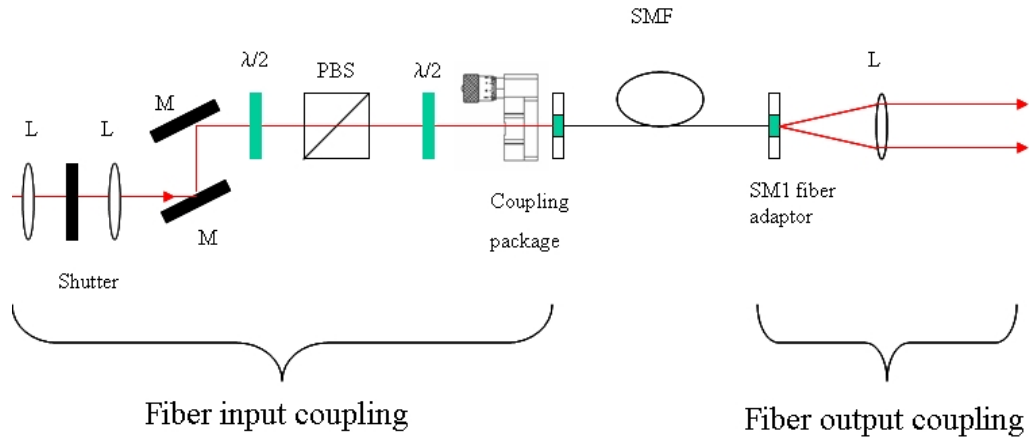


Figure 4.17: Optical fiber coupling system diagram. L: lens; M: mirror; PBS: polarization beam splitter; SMF: single mode fiber.

Table 4.2: Commercial part list of fiber coupling.

Name	Description	Company
M	New Focus NIR Mirror 5102	New Focus
$\lambda/2$	Half-wave plate, NH-100-0780	Meadowlark optics
PBS	Polarization Beam Splitter.	Thorlabs
Coupling package	<ul style="list-style-type: none"> <li>• Thorlabs SM1 Z translator (SM1Z)</li> <li>• Thorlabs SM1 FC fiber adaptor (SM1FC)</li> <li>• Thorlabs SM1 thread cage plate (CP02)</li> <li>• Thorlabs SM1 retaining ring (SM1RR)</li> <li>• Thorlabs lens <math>f=11.00\text{mm}</math> <math>0.25\text{NA}</math> Mounted</li> <li>• Geltech™ Aspheric Lens (C220TM-B)</li> <li>• Thorlabs SM1 Aspheric Lens Adapter (S1TM09)</li> </ul>	Thorlabs
SMF	Single Mode Fiber, OZ Optics PMJ-3838-850-5/125-3-2-1	OZ Optics
L	Lens, $f=35\text{mm}$ , Thorlabs achromatic doublet LAC628-B	Thorlabs

## 4.7 Atom-chip cell optical table

We use a  $61 \times 61 \times 1.9$  cm aluminum optical board to accept the atom-chip cell and polarization optical setup for laser cooling, trapping and imaging. A photo graph of the atom-chip cell table is shown in figure 4.18. The optical polarization configuration is shown in figure 4.2.



All laser inputs come from the fiber coupling described in section 4.7. The cooling laser splits into four beams for the mirror MOT configuration. The repumping and pumping laser beams, from the same fiber, are separated by a  $\lambda/2$  wave plate and the PBS. The circularly polarized imaging beam, along the y direction, reflects from the atom-chip mirror and goes to an Apogee CCD camera, which is not shown in figure 4.18.

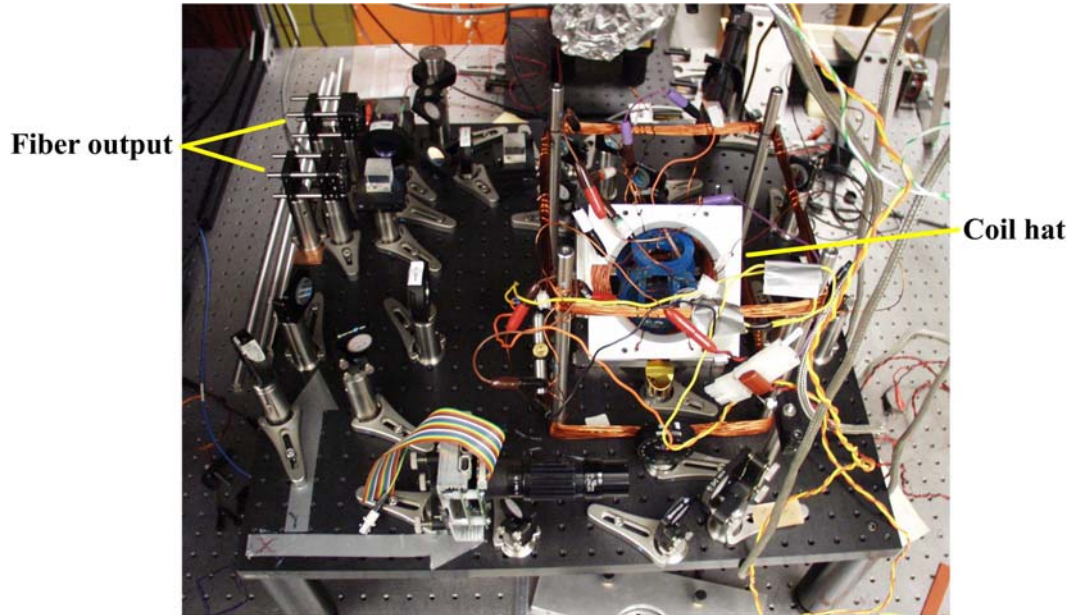


Figure 4.18: Atom-chip cell table ( $61 \times 61$  cm).

## 4.8 Imaging setup

### 4.8.1 Camera configuration

The camera system shown in figure 4.19 includes three video CCD cameras (WATEC censor WAT-902C), one PixelLink CMOS camera (PixelLINK PL-A633), and one Apogee CCD camera (APIE). In the MOT alignment, video cameras 1, 2 and 3 are involved. Video cameras 1 and 3 are used to adjust the coil hat (defined in section 5.3) to optimize the mirror MOT position. After the mirror MOT is located at the center of the chip, the coil hat is locked down. Then we adjust the laser beams to optimize the MOT atom number by looking at the images from video cameras 1 and 3. This is a coarse adjustment. Further optimization of the mirror MOT and chip

MOT require video camera 2, with a large zoom and an interference filter. The PixelLink camera, with a calibration of  $50\mu\text{m}/\text{pixel}$ , is used to take absorption images for the MOT, which is typically  $>0.8\text{ mm}$  away from the chip surface. The Apogee camera with a calibration of  $5\sim 6\mu\text{m}/\text{pixel}$  is used to take reflection images of the microchip traps very close to the chip surface ( $<0.5\text{ mm}$ ).

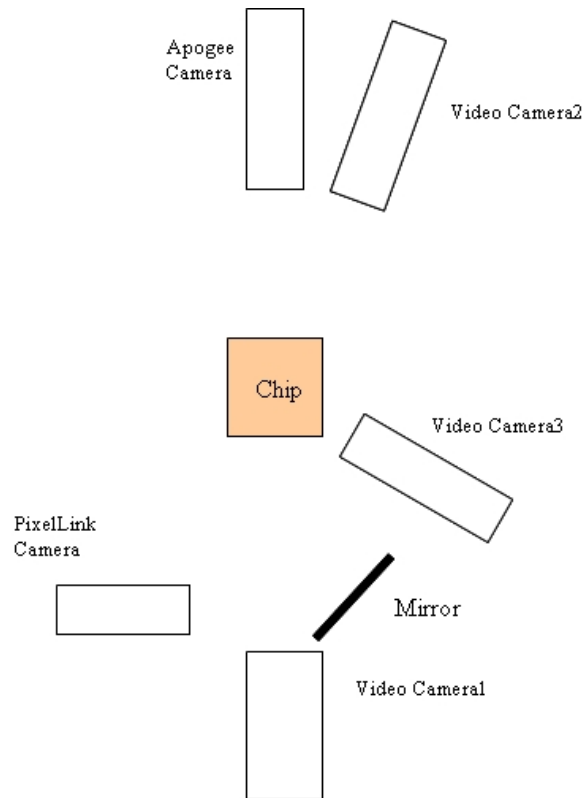


Figure 4.19: Camera setup for atom-chip experiments.

#### 4.8.2 Atom-chip surface reflection imaging

It is a challenge to image an atom cloud very close to a surface directly because of the diffraction pattern of the chip. A typical technical limit of the distance from the chip surface is about  $100\mu\text{m}$ . To image an atom cloud beyond this limit with a probe-beam passing through, the cloud must be moved farther away from the chip surface, e.g.,  $200\mu\text{m}$ . In our atom-chip cell, the limiting condition is even worse because the chip is used to seal the glass cell and there is roughness in the junction between the chip and the glass cell due to the use of epoxy. This

condition prevents us from imaging atoms directly less than  $500\ \mu\text{m}$  away from the surface.

Fortunately, we can use the sliver mirror integrated on top of the chip surface for the absorption reflection imaging as shown in figure 4.20(a). We get two atom clouds in images because of the reflection, as shown in figure 4.20(b). The distance from the surface can be determined precisely by measuring the separation of the two cloud images.

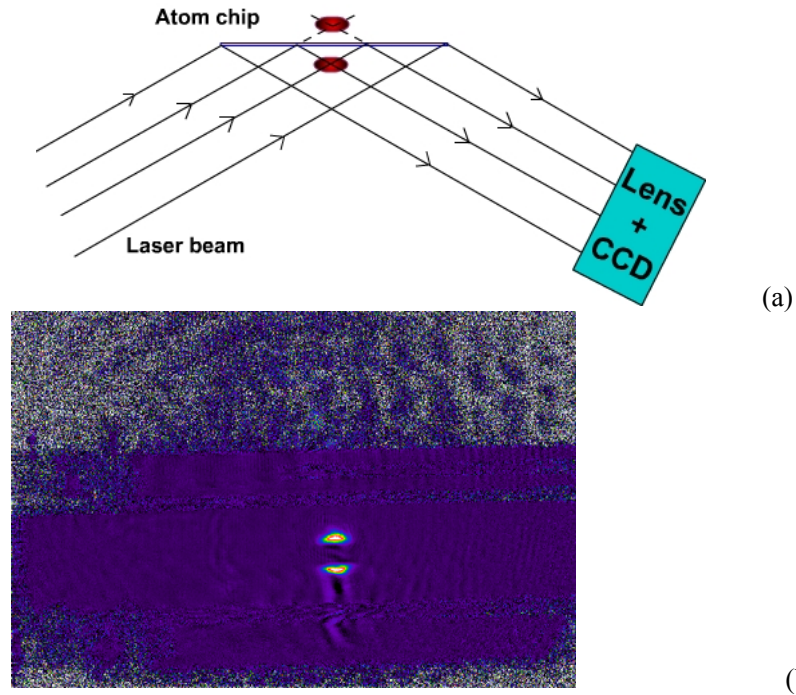


Figure 4.20: Atom-chip surface reflection imaging. (a) Absorption reflection imaging setup. (b) An atom-chip in-trap reflection image.

## Chapter 5. Electronic system

We take advantage of commercial electronic technologies such as high speed computers, multiple-channel analog output boards, imaging data acquisition (DAQ) systems, and ultrastable current power supplies. Without them, we would not be able to run our atom-chip experiments.

The schematic block diagram of our computer-based electronic system is shown in figure 5.1. We use two Gateway computers, a controller computer and a DAQ computer, to run our atom-chip experiments. By sending commands from the controller computer via the NI PXI-1002 chassis, we use a 32-channel analog output board, PDXI-AO-32/16, to control all terminal devices, including current power supplies, optical shutters, AOM drivers, and the camera trigger, etc.. The DAQ computer takes imaging data from the camera and does data processing. We developed LabView programs with user friendly interfaces for controlling the atom-chip experiment, DAQ, and file management.

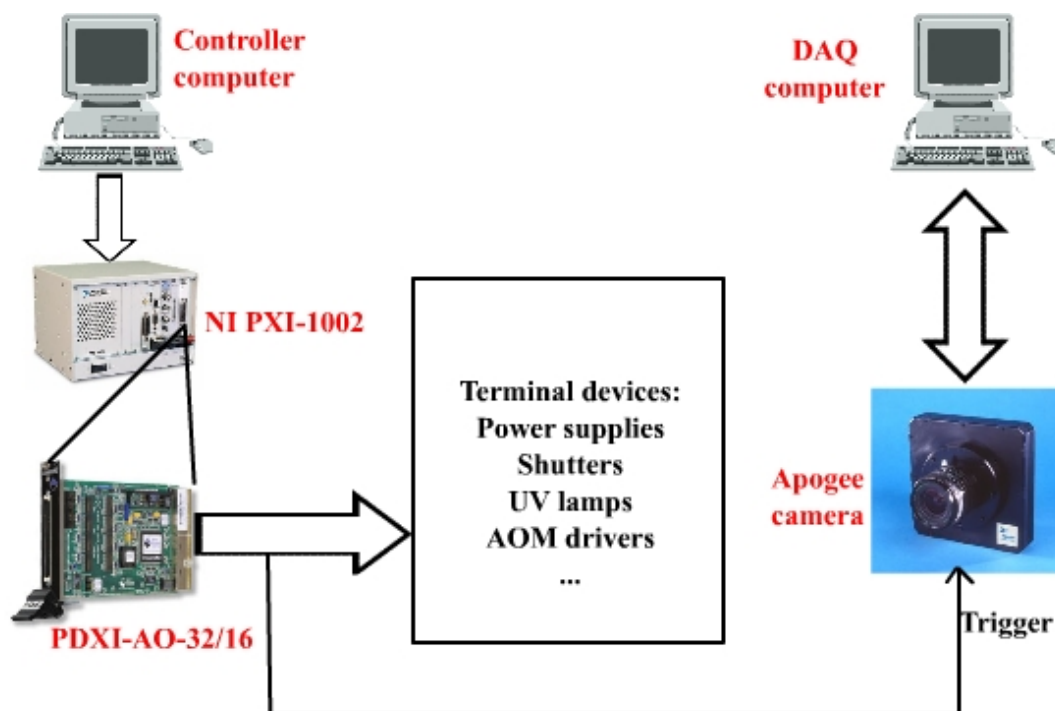


Figure 5.1: Schematic diagram of the atom-chip computer-based control and DAQ system. NI PXI-1002: National Instrument PXI Chassis; PDXI-AO-32/16: UEIDAQ 16-bit 32-channel PXI analog output board.

In the following sections, we describe in detail the most important parts of the electronic system for controlling and DAQ. Then we provide technical information about the magnetic coil hat, current power supplies, and RF drivers.

## 5.1 Computer-control system

The computer-control system includes the controller computer, the NI PXI-1002 chassis, the PDXI-AO-32/16 board (shown on the left side of figure 5.1), and the LabView control programs. The NI PXI-1002 is a 4-slot, 3U PXI chassis that forms the basis for low-cost PXI systems. The PDXI-AO-32/16 board, purchased from UEIDAQ, has 32-channel analog outputs ( $\pm 10\text{V}$ , 16 bit). The analog output can be operated at a very fast speed of  $<100 \mu\text{s}$  per channel even when all 32 channels are on simultaneously. We have demonstrated that such an analog output board can be used to control BEC experiments, replacing the many-channel DIO (digital input output) board used in most cold-atom systems. Using the PDXI-AO-32/16 analog output board dramatically reduces the work load and cost of developing user software.

The PDXI-AO-32/16 board can be configured to work in either single update mode or buffered output mode. When the board works at single update mode, the analog output channels change value only when they receive a command from the computer; thus the speed is limited by the software and the computer. In the buffered output mode, the computer fills the on-board buffers first, and then the board starts to output waveforms when it receives a software trigger signal. The output speed of the buffered mode, determined by the configuration of the on-board internal clock, is independent of the computers and their operating systems. Inside the analog board, there are a total of four buffers to allow cycling the buffers without interrupting the output with infinitely long wave forms. The single update mode has a typical response time of  $>1 \text{ ms}$ , and the buffered mode of  $<100 \mu\text{s}$ .

We use the single update mode to control the experiment continuously from the computer front panel, as shown in figure 5.2. This program is used to optimize the atom-chip mirror MOT.

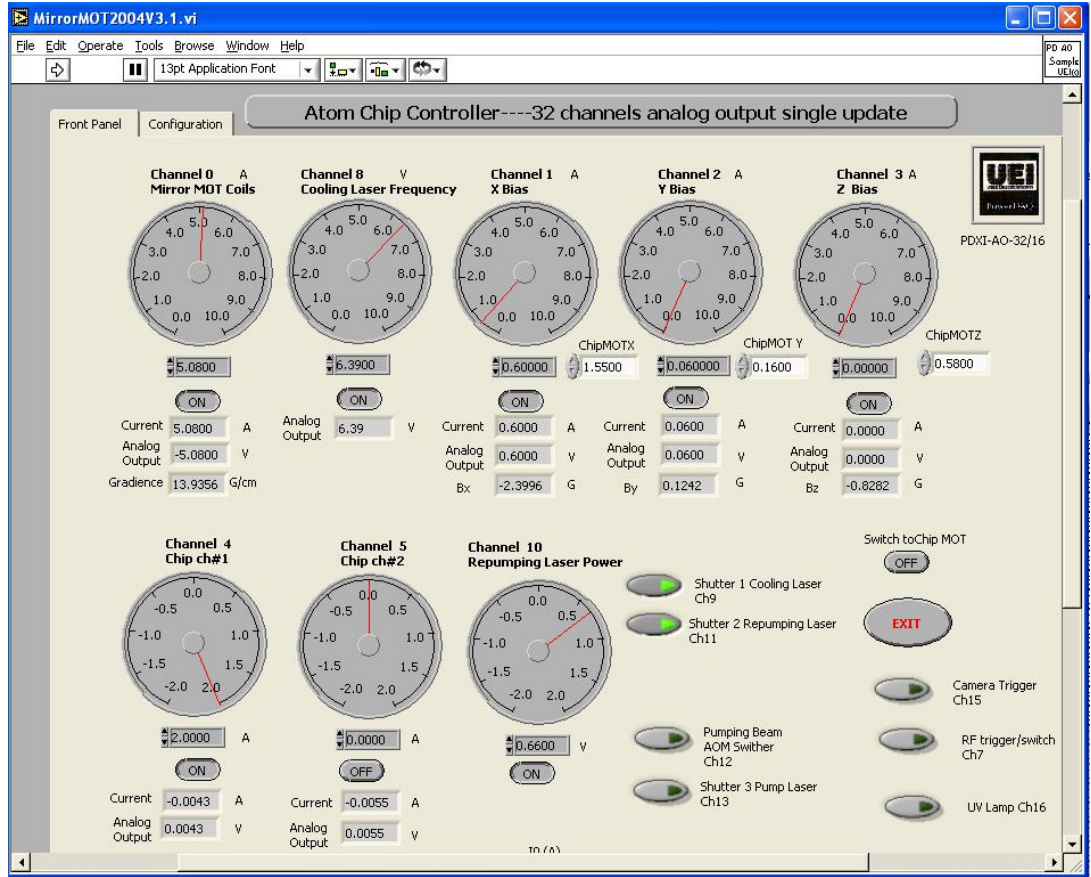


Figure 5.2: Front panel of MirrorMOT2004V3.1.VI with single update

We use the buffered output for running atom-chip BEC experiments, where it is critical to control different devices with precise relative timing. In this mode, the computer generates all the waveform data once before the output. For the buffered output mode, we have developed and demonstrated the concept of universal many-channel timing management, which is independent of hardware. The key feature of this management concept is how it represents and edits arbitrary wave forms. Here we consider only the wave forms with linear ramps such as the one shown in figure 5.3. We represent the single wave form as a 2D array vector, as shown in table 5.1.

For many channels, we use two methods to represent timing vector array information. The first method uses a 3D array to record all channel timing vectors, and the second extends the 2D array to a 2D table. Here we take a two-channel output, as shown in figure 5.4, as an example. The 3D array representation has two independent 2D arrays (see table 5.2), and the extended timing table has only one 2D array (see table 5.3).

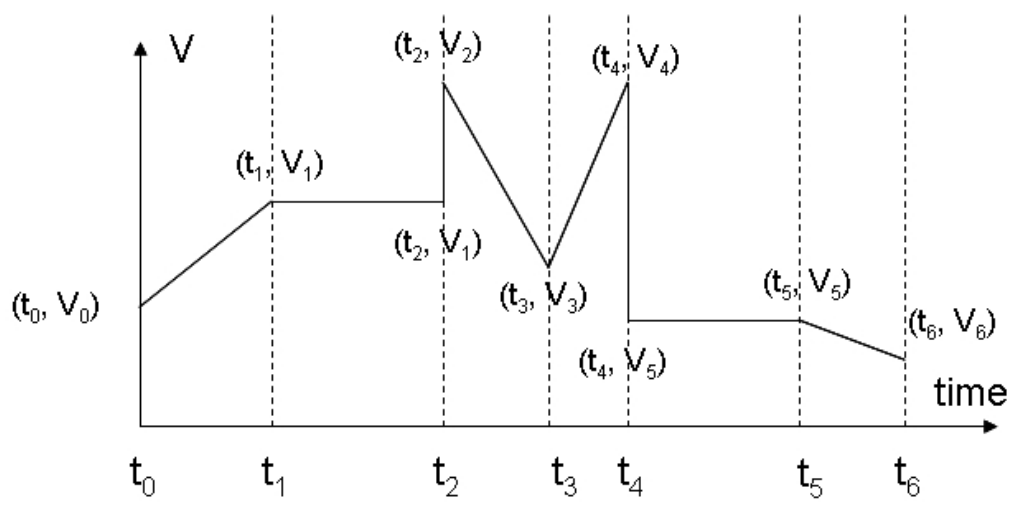


Figure 5.3: An example of a single channel wave form with only linear ramps.

Table 5.1: 2D array representation of the wave form shown in figure 5.1-2.

Time	Output
$t_0$	$V_0$
$t_1$	$V_1$
$t_2$	$V_1$
$t_2$	$V_2$
$t_3$	$V_3$
$t_4$	$V_4$
$t_4$	$V_5$
$t_5$	$V_5$
$t_6$	$V_6$

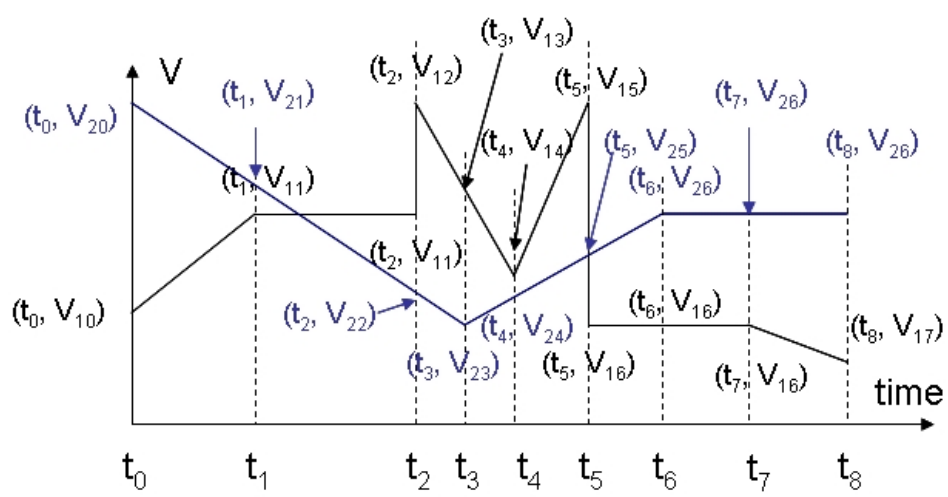


Figure 5.4: An example of a 2-channel wave forms with only linear ramps.

Table 5.2: 3D timing array for 2-channel waveforms shown in figure 5.4.

<b>Time</b>	<b>Output 1</b>		<b>Time</b>	<b>Output 2</b>
$t_0$	$V_{10}$		$t_0$	$V_{20}$
$t_1$	$V_{11}$		$t_3$	$V_{23}$
$t_2$	$V_{11}$		$t_6$	$V_{26}$
$t_2$	$V_{12}$		$t_8$	$V_{26}$
$t_4$	$V_{14}$			
$t_5$	$V_{15}$			
$t_5$	$V_{16}$			
$t_7$	$V_{16}$			
$t_8$	$V_{17}$			

Table 5.3: Timing table for 2-channel waveforms shown in figure 5.4.

<b>Time</b>	<b>Output1</b>	<b>Output2</b>
$t_0$	$V_{10}$	$V_{20}$
$t_1$	$V_{11}$	$V_{21}$
$t_2$	$V_{11}$	$V_{22}$
$t_2$	$V_{12}$	$V_{22}$
$t_3$	$V_{13}$	$V_{23}$
$t_4$	$V_{14}$	$V_{24}$
$t_5$	$V_{15}$	$V_{25}$
$t_5$	$V_{16}$	$V_{25}$
$t_6$	$V_{16}$	$V_{26}$
$t_7$	$V_{16}$	$V_{26}$
$t_8$	$V_{17}$	$V_{26}$

We use both timing representations in the user interface. The timing table is used to edit and monitor the global timing between different channels, and the timing channel arrays are used to edit and monitor individual channels without affecting others. After the timing vector array is created, it is converted into 2D 16 bit integrals, the format required by the analog output board, when we run atom-chip experiments.

Our single LabView program provides a user interface not only for timing management, but also for configuring all hardware in the experiment, as shown in figures 5.5–5.10. The timing vector array information and channel configuration can be saved to files both in the timing table format (\*.txt) and the channel timing array format (\*.tim).



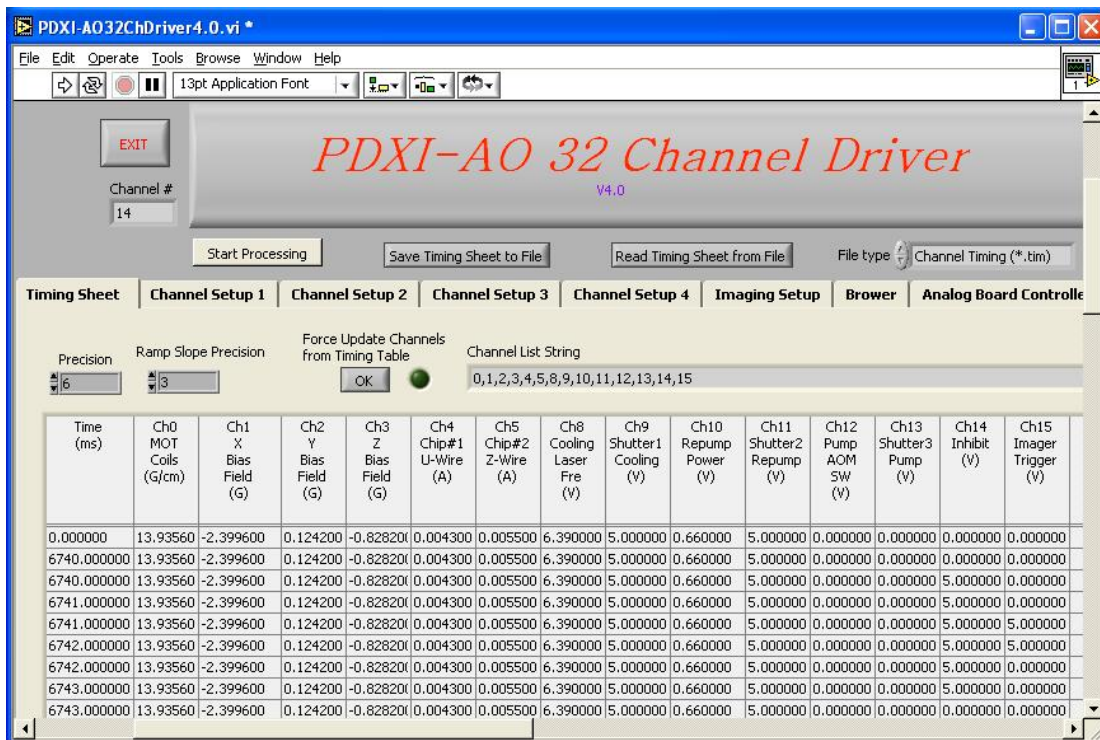


Figure 5.5: Timing table editor front panel sheet

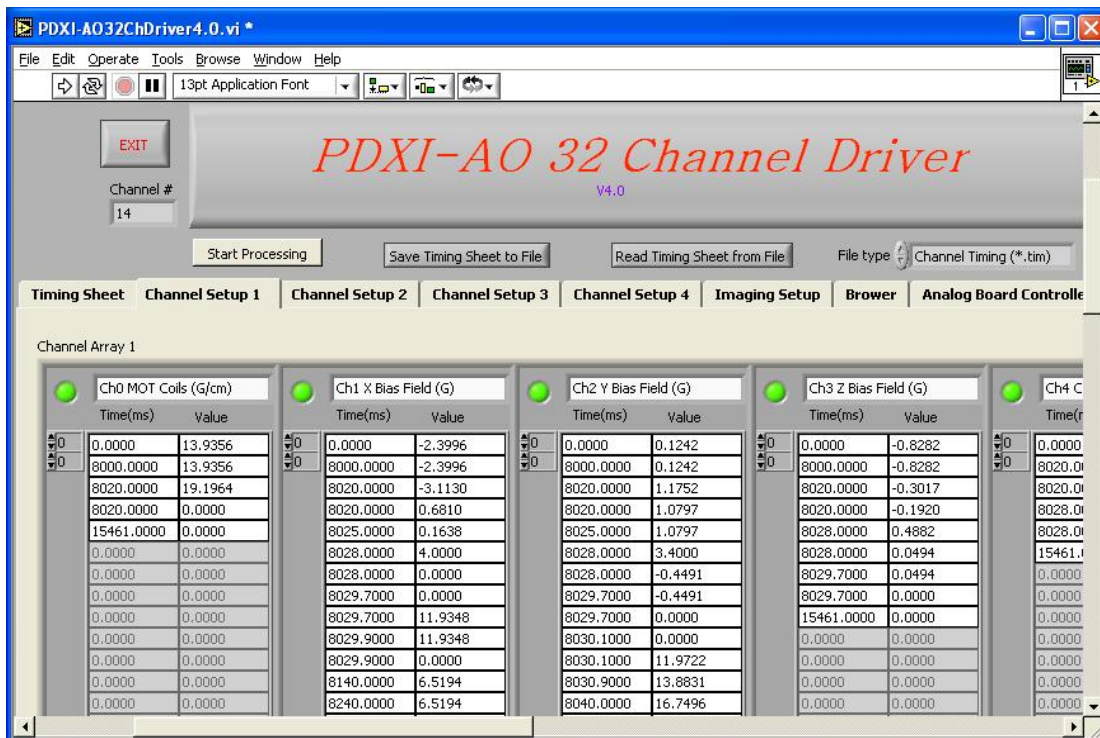


Figure 5.6: Channel timing array editor front panel.

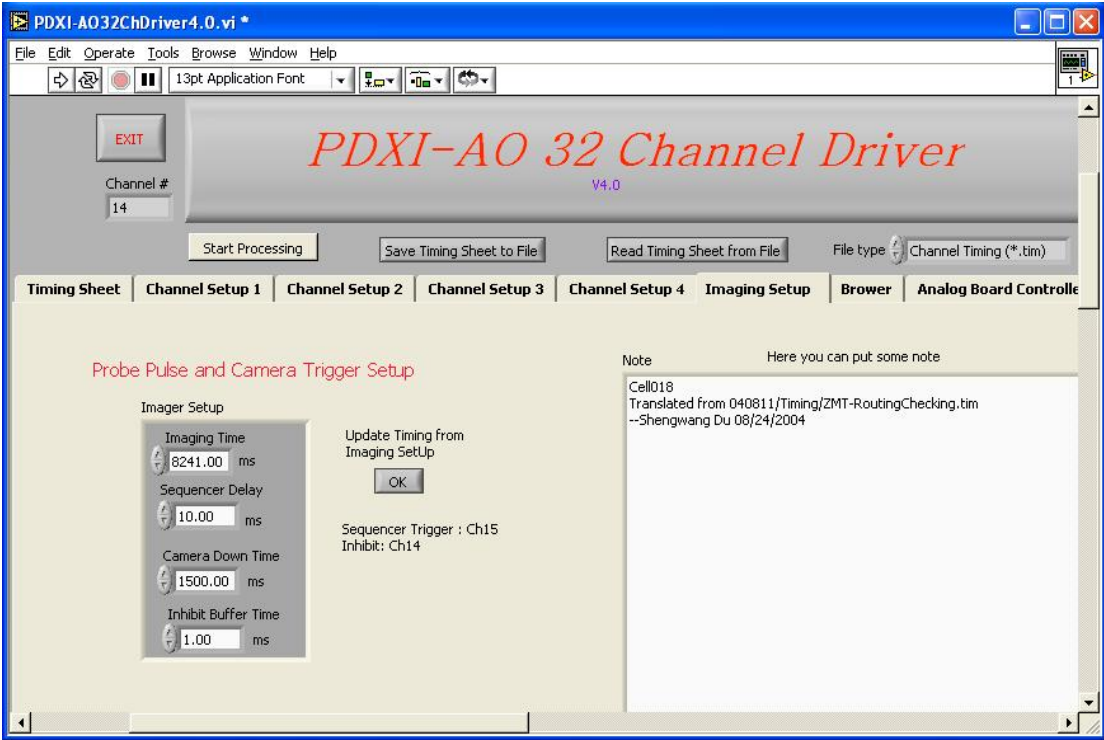


Figure 5.7: Imaging controller front panel.

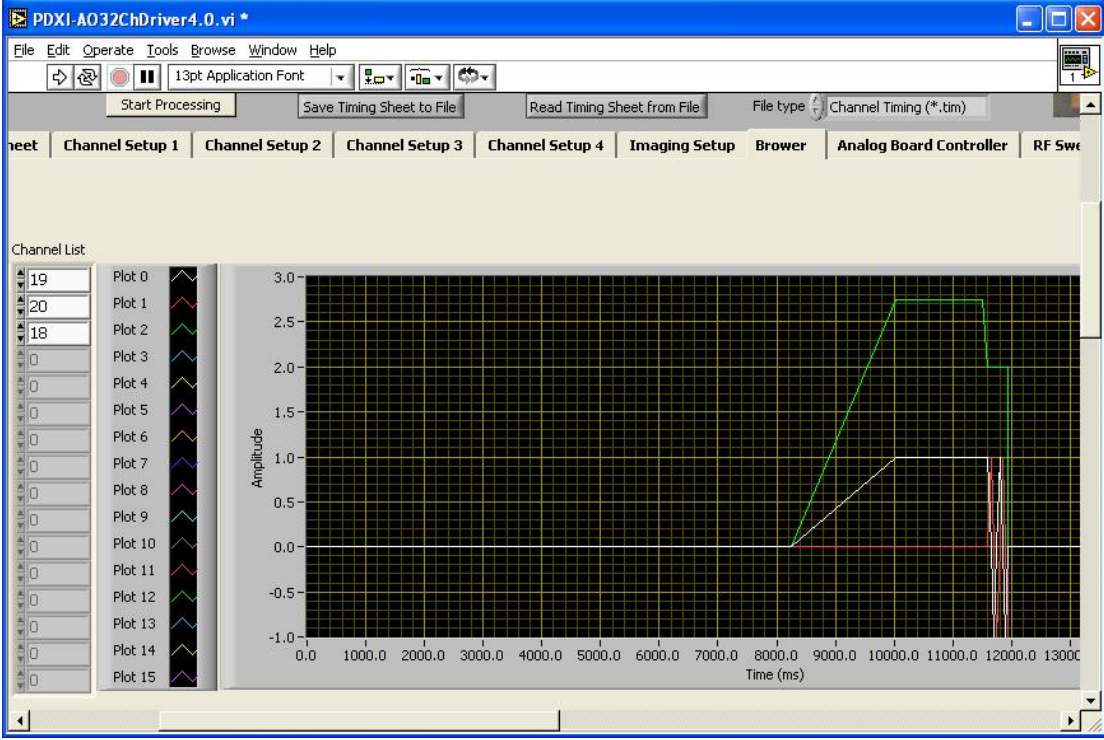


Figure 5.8: Wave form browser front panel.

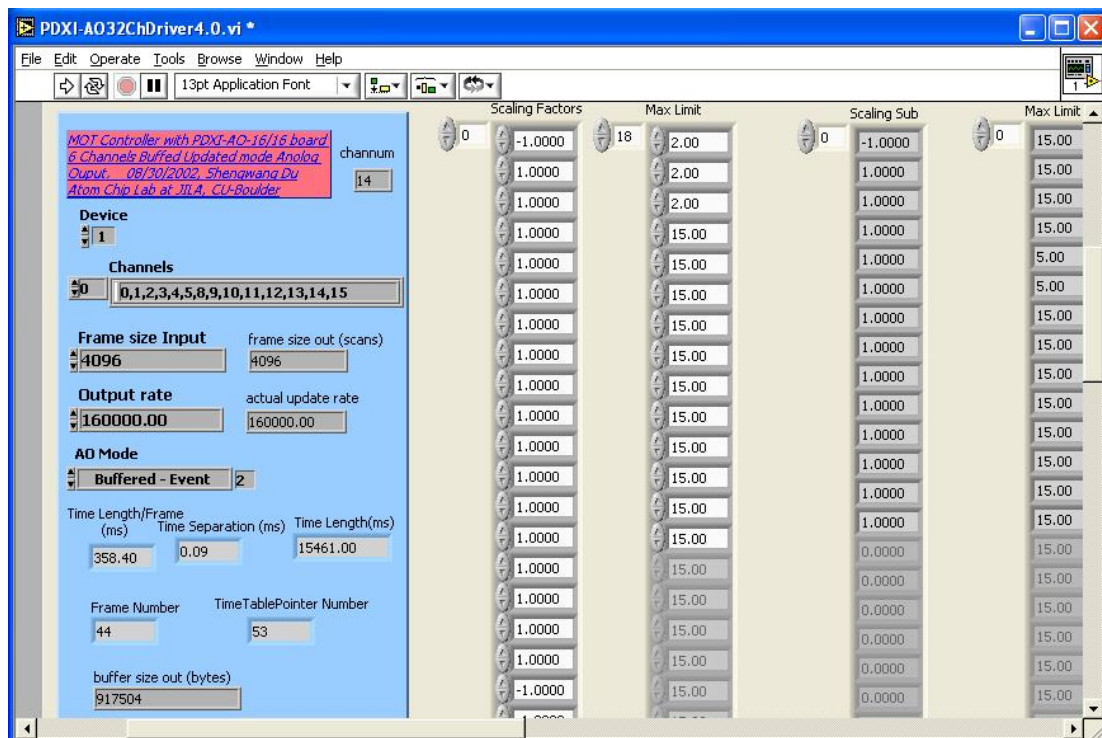


Figure 5.9: PDXI-AO-32/16 board configuration front panel sheet.

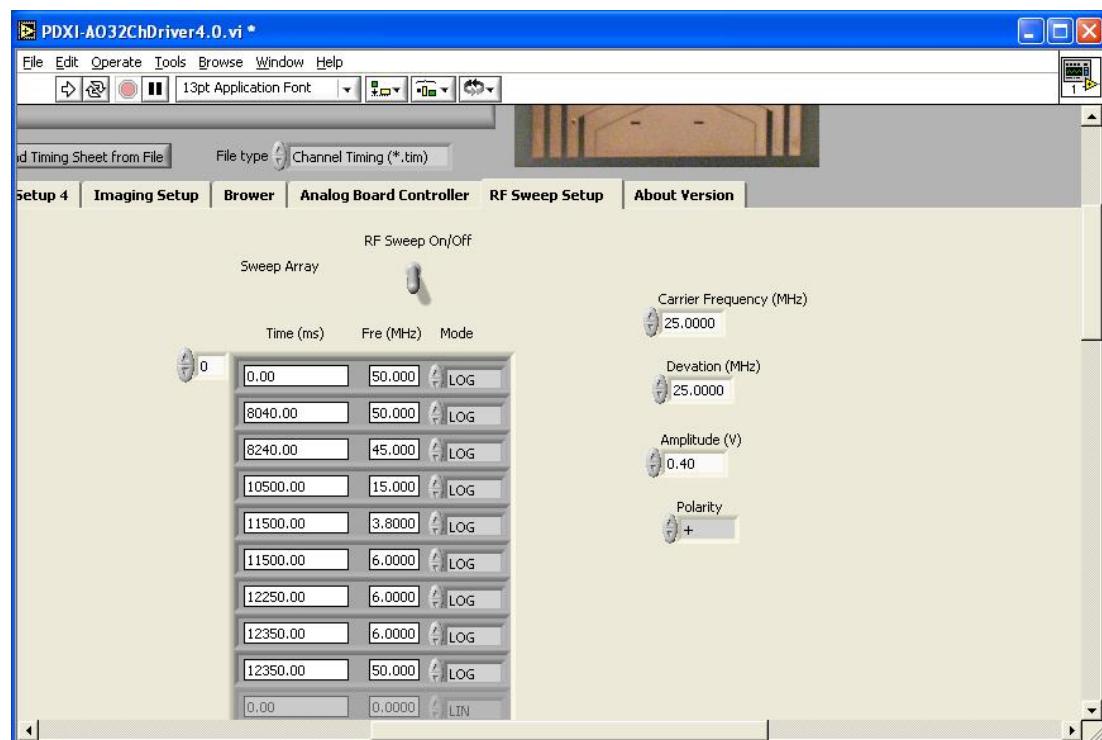


Figure 5.10: RF sweep controller front panel (for RF forced evaporative cooling).

## 5.2 Imaging control and DAQ

In our atom-chip experiments, we detect cold atom clouds using absorption imaging. The controller computer system, described in section 5.1, generates a 100  $\mu\text{s}$  probe laser pulse by controlling the AOM and mechanical shutters (described in chapter 4) to illuminate the atom cloud on the chip. When the Apogee camera receives the trigger signal associated with the probe pulse, it sends the imaging data to the DAQ computer for data processing.

For each measurement, we take three shots to determine atom cloud optical depth (OD). The first shot is an absorption frame with the atom cloud, described as  $I_{abs}(x, y)$ , where  $x$  and  $y$  are two-dimensional imaging plane coordinates. The second shot, called the background frame,  $I_{back}(x, y)$ , is taken in the same way as the first one but without atoms present. The third shot is the dark frame,  $I_{dark}(x, y)$ , made without flashing the probe pulse, that represents the bias reading from the CCD sensor. The OD can be calculated by

$$OD(x, y) = \ln \left( \frac{I_{back} - I_{dark}}{I_{abs} - I_{dark}} \right). \quad (5.1)$$

The three shots are taken within a very short time interval, 1.5 s in our experiment, to reduce the systematic noise between different shots. The control timings are shown in figures (5.11) and (5.12). The probe and repumping pulses are 100  $\mu\text{s}$  long. The camera shutter (25 mm aperture, Vincent Associates, Uniblitz VS35) is mounted in front of the camera lens without touching any part of the optical table. After an OD image is obtained from the three frames using equation (5.1), it is fitted to a 2D Gaussian profile. Combining the trap parameters, we get the atom number, atom density distribution, temperature, phase-space density, and other physics quantities from the OD absorption measurement (for details, see chapter 2). The Labview program front panel is shown in figures 5.13 and 5.14.

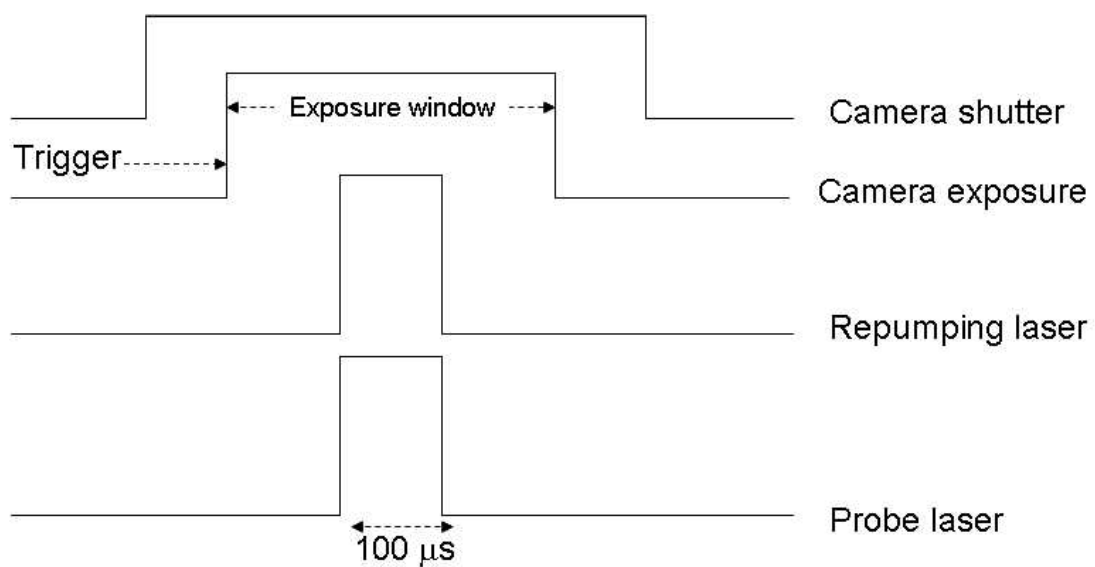


Figure 5.11: Absorption and background imaging timing with a probe pulse.

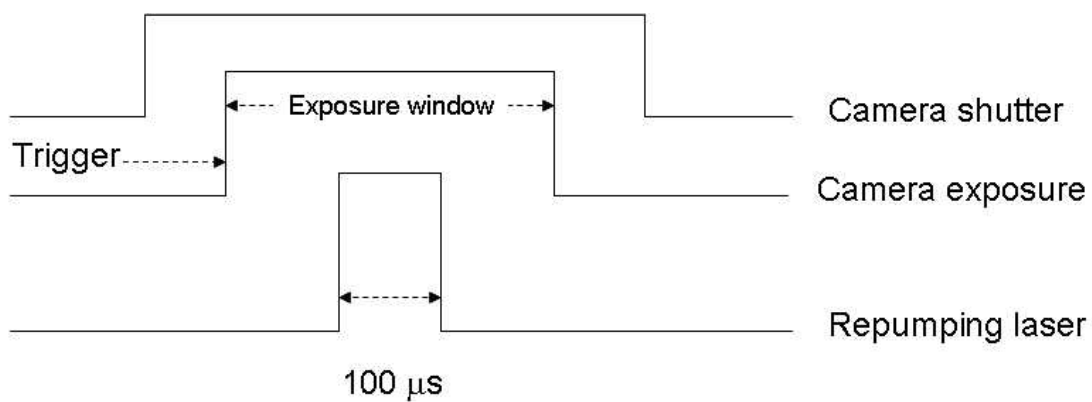


Figure 5.12: Imaging timing for the dark frame.



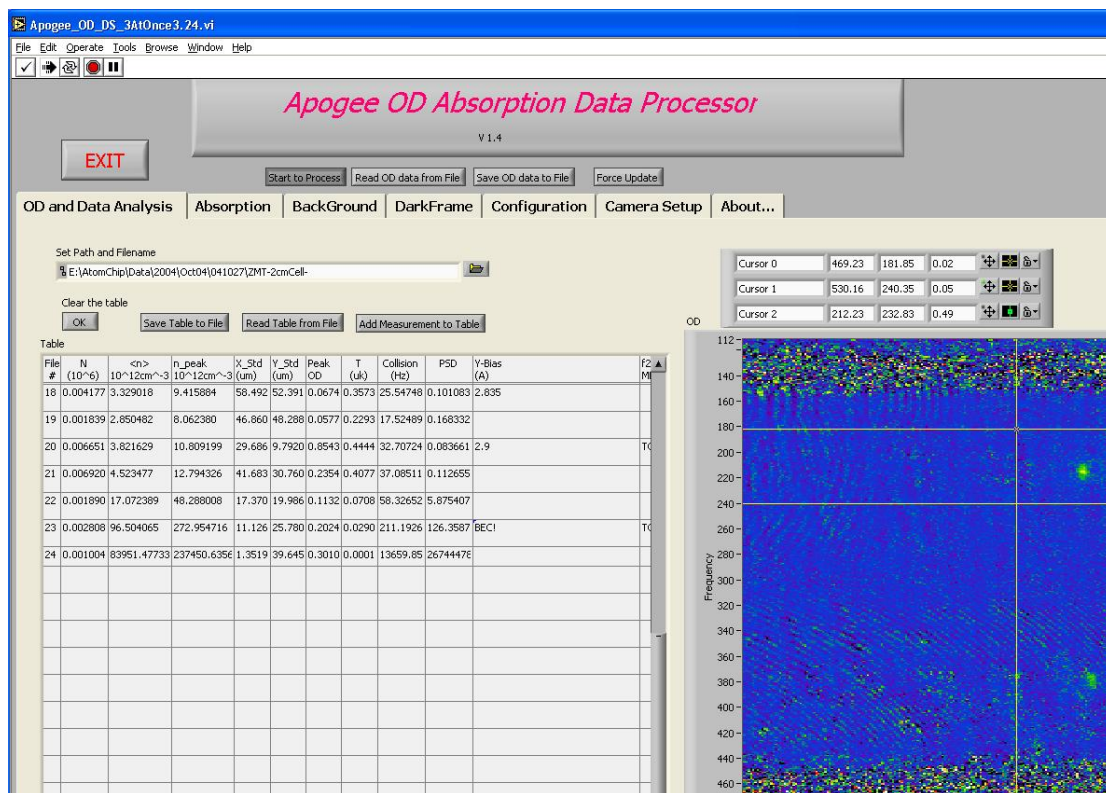


Figure 5.13: Part of the Labview front panel of the absorption imaging process

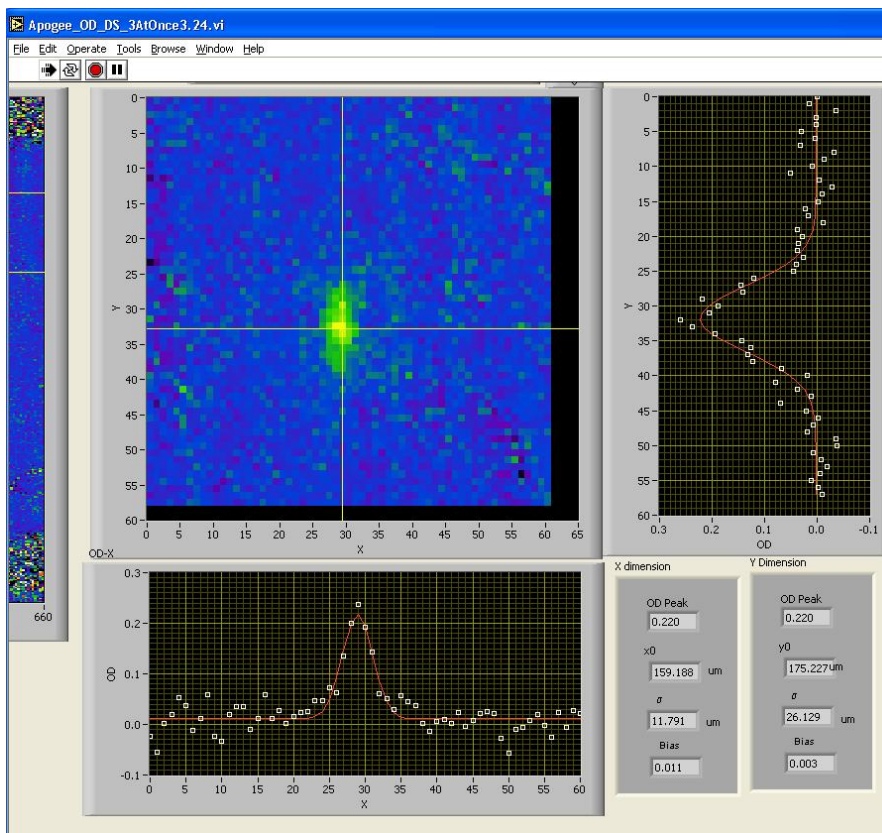


Figure 5.14: Part of the Labview front panel of the absorption imaging process program shows our first BEC on the atom chip with x and y cross-section plots and 2D fitting.

### 5.3 Magnetic coil hat

As discussed in chapter 2, we use the atom-chip mirror and external  $45^\circ$  anti-Helmholtz coil pair to load cold atoms into the mirror MOT. At the atom-chip U-wire surface MOT and the Z-wire microtrap, we apply external bias fields generated by the magnetic coils. The external magnetic bias fields are also used to manipulate the cold atoms. Therefore, the coils play one of the important roles in the entire atom-chip system.

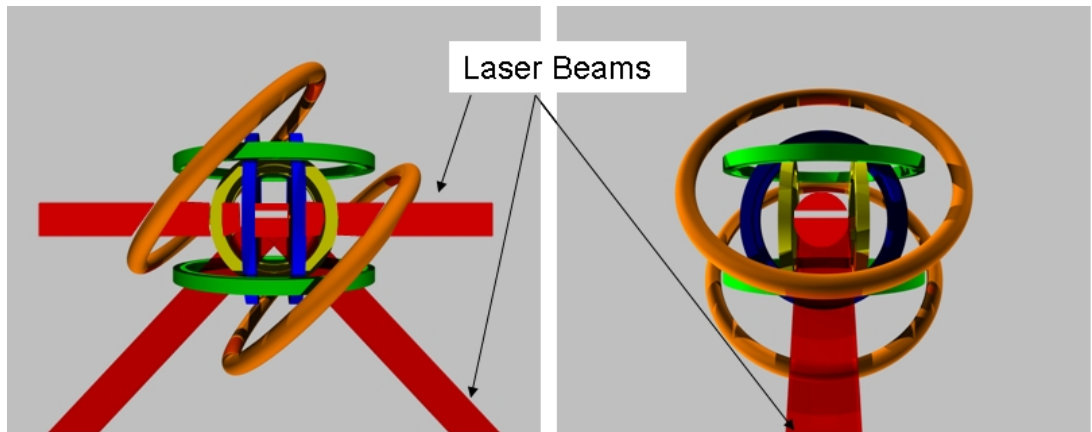


Figure 5.15: Atom-chip mirror MOT configuration with the coil hat.

The small size of the atom-chip cell ( $1 \times 1$  cm) allows us to easily assemble all the coils into a compact and rigid unit without using water cooling setup. Another advantage of small coils is that we can build them with very low inductances. Low coil inductances are important for switching the external magnetic fields on and off rapidly because the atom-chip experiments have much shorter time scales than traditional large BEC systems due to the shorter trap lifetime. Figure 5.15 shows the coils and laser beams configuration schematically. The assembly of all four pairs of coils, together with their mount structure, is called the atom-chip magnetic coil hat.

We have built two different versions of coil hats: one with circular coils and a second with rectangular coils. The circular coil hat was built in 2002 for  $1 \times 1$  cm atom-chip cells. After demonstrating atom-chip BEC in the  $1 \times 1$  cm cell, we built a second version, the rectangular coil hat, which is capable of accepting a larger cell with a size of  $2 \times 2$  cm. The following two subsections give detailed specifications for the two coil hats. However, all the experimental results

and measurements that do not specify the coils in this thesis are done with the circular coil hat.

### 5.3.1 Circular coil hat

The circular coil-pair dimensions are defined in figure 5.16. The coil hat specifications are shown in table 5.4. We use 18 AWG (American Wire Gauge, diameter 1 mm) magnetic wires and BIPAX Tra-bond epoxy (Tra-con, BA-2151, blue color) to make the coils. Then the MOT coils are mounted to an aluminum frame. The three pairs of bias coils are glued together by Devcon 5 minute epoxy. Finally, we assemble the bias coil set and MOT coils with the aluminum mount structure to form our coil hat, as shown in figure 5.17. The coil hat has a clear aperture size of  $25 \times 25$  mm for plugging an atom-chip cell vertically.

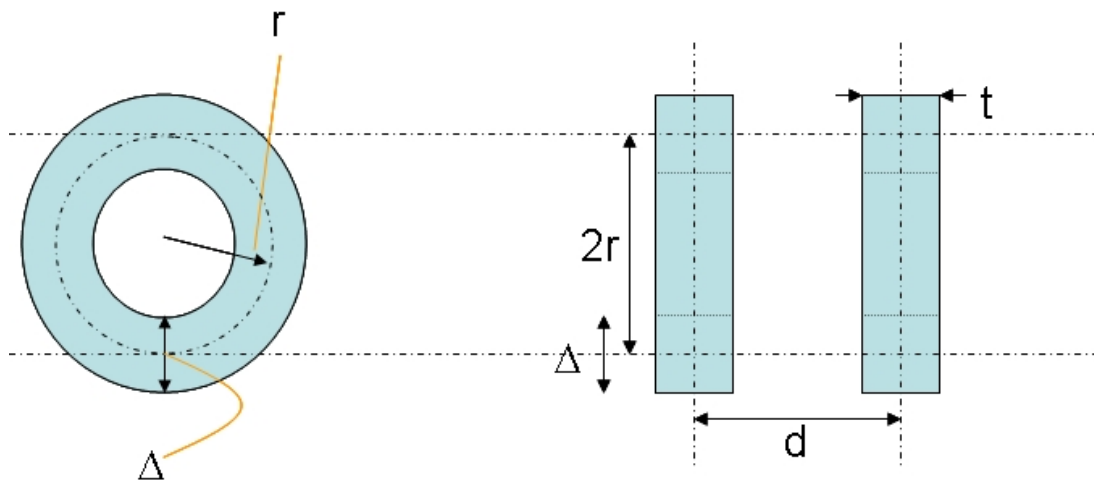


Figure 5.16: Dimensions of a circular coil pair.  $r$ : average radius;  $\Delta$ : difference of the radius;  $d$ : separation of the two coils;  $t$ : thickness of a single coil.

Table 5.4: Specifications of the circular coil hat

	X bias coil	Y bias coil	Z bias coil	MOT coil	
$r$ (mm)	23.5	33.5	23.5	56.72	
$\Delta$ (mm)	5	7	7	13	
$t$ (mm)	5	7	7	13	
$d$ (mm)	34	34	81	54	
$N$ (turns per coil)	16	36	36	100	
R, resistance ( $\Omega$ , per coil)	27 °C	0.045	0.14	0.1	0.68
	100 °C	0.062	0.2	0.14	0.94
L, inductance( $\mu$ H, per coil)	29	229	148	3377	
Field at the center	4.55 G/A	9.5 G/A	2.4 G/A	3.35 G/cm A	



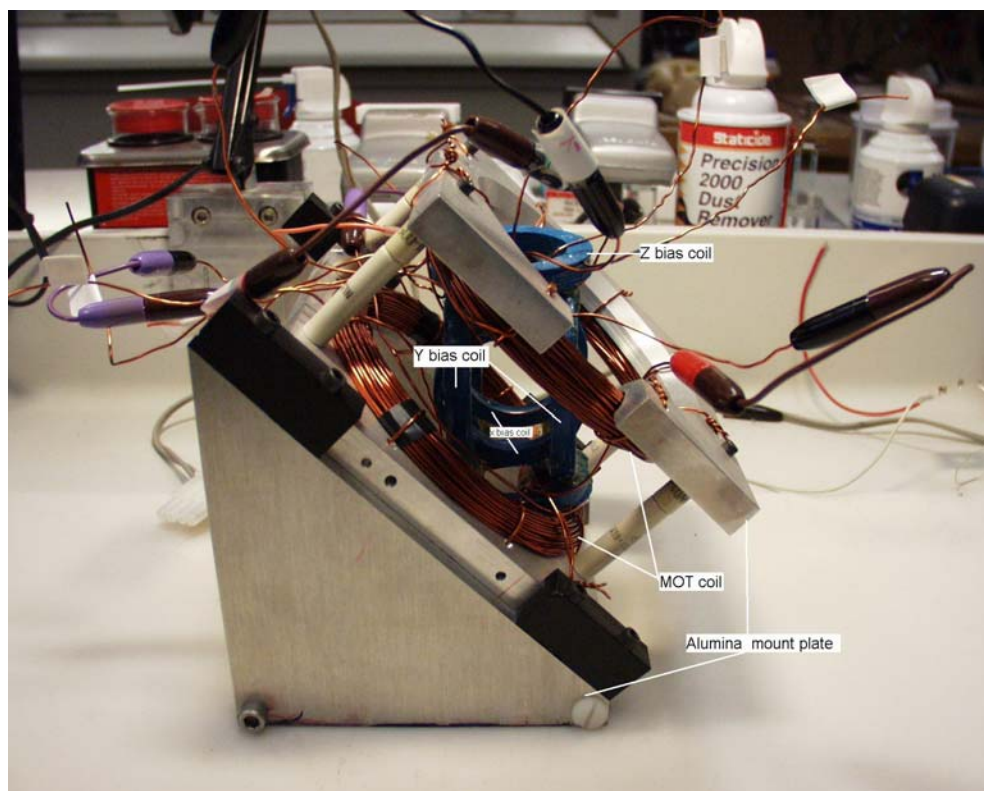
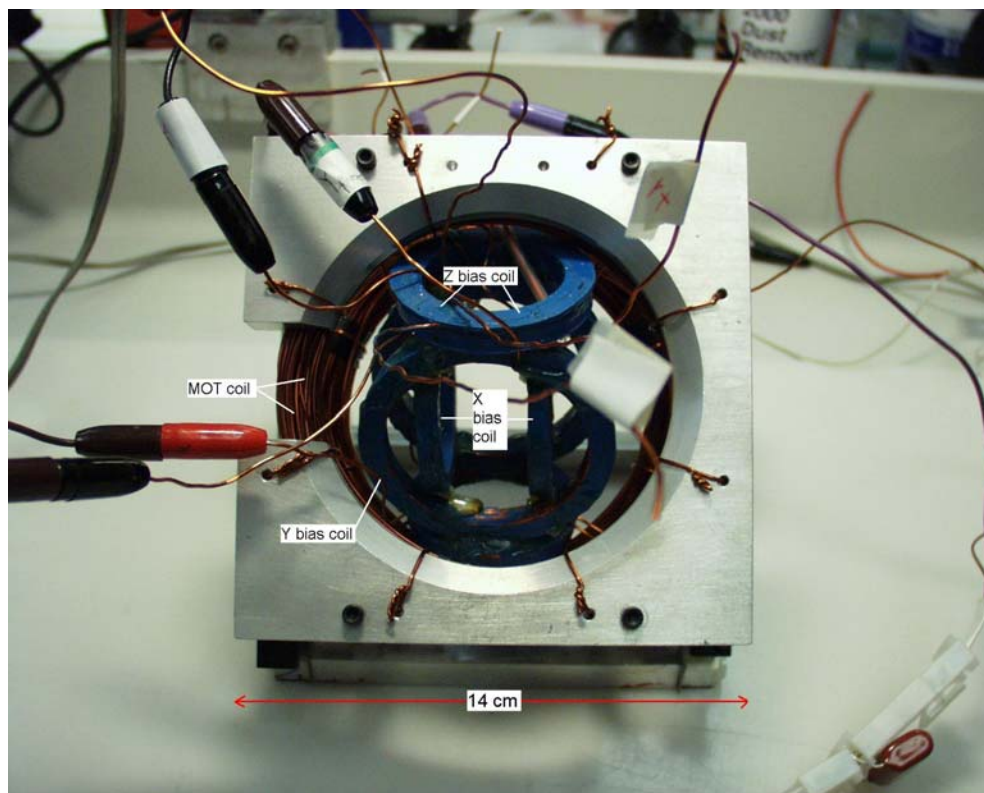


Figure 5.17: Pictures of the circular coil hat.

### 5.3.2 Rectangular coil hat

We built the second version of the coil hat with rectangular coils. The dimensions and specifications of the coils are given in figure 5.18 and table 5.5. There are two sets of x-bias coils which allow both high resolution and high field magnitude for many purposes. The rectangular coils are much easier to integrate into one hat unit because they have more contact area. Figure 5.19 shows two views of the entire coil hat with a size of  $12 \times 12 \times 16$  cm. The rectangular one is smaller than the circular coil hat ( $14 \times 14 \times 17$  cm, as shown in figure 5.17). However, it provides a larger aperture ( $35 \times 45$  mm) with more flexibility to accept different sizes of atom-chip cells.

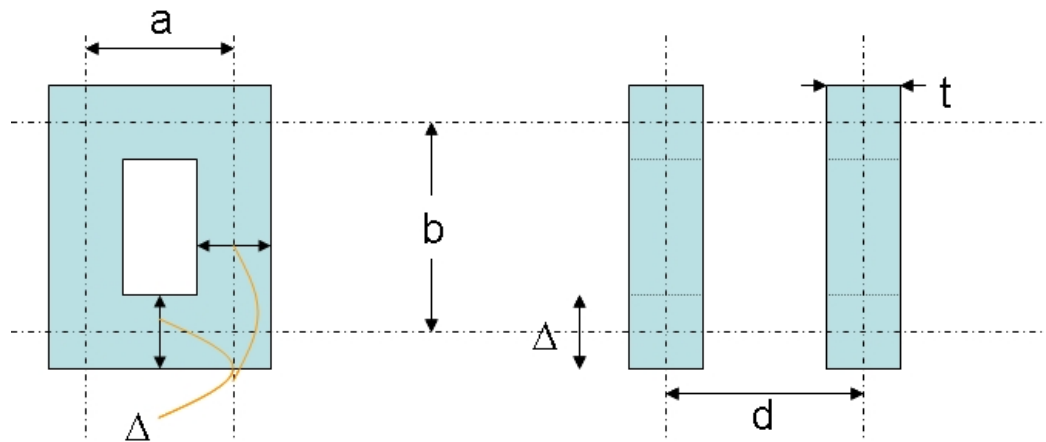


Figure 5.18: Dimensions of a rectangular coil pair. a: average width; b: average height;  $\Delta$ : wire coil thickness in the coil plane; d: separation of the two coils; t: thickness of a single coil.

Table 5.5: Specifications of the rectangular coil hat.

	Small X bias coil	Big X bias coil	Y bias coil	Z bias coil	MOT coil	
a×b (mm)	38×77	50×82	40×80	41×50	120×120	
$\Delta$ (mm)	5	10	8	5	10	
t (mm)	5	6.5	8	5	13	
d (mm)	40	56	51	94	48	
N (turns per coil)	15	35	50	20	120	
R, resistance ( $\Omega$ , per coil)	27 °C	0.07	0.18	0.23	0.07	1.1
	100 °C	0.09	0.24	0.32	0.1	1.52
L, inductance ( $\mu$ H, per coil)	39	257	460	53	6405	
Field at the center	3.33 G/A	5.66 G/A	8.58 G/A	1.06 G/A	2.74 G/cmA	

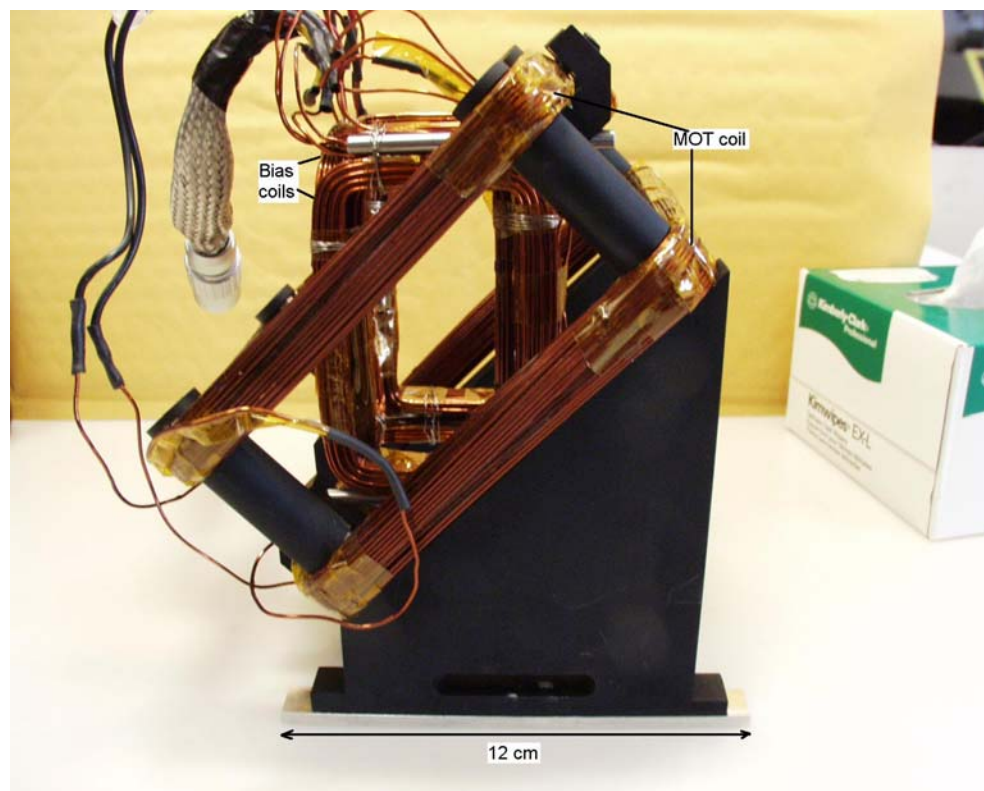
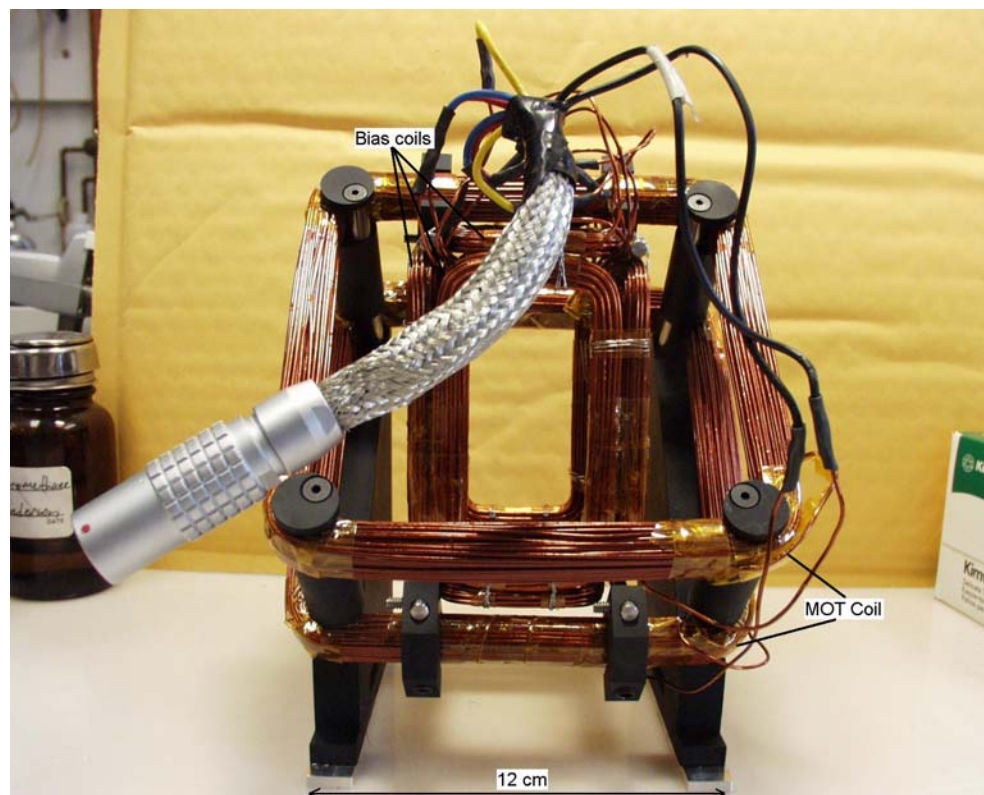


Figure 5.19: Pictures of the rectangular coil hat.

## 5.4 Current power supplies

Magnetic field fluctuations induced by current noise not only cause atom-trap loss due to spin flips, but also parametrically heats atoms in a magnetic trap [82]. Moreover, because the atoms in a chip trap are much closer to the wires, they are more sensitive to the current noise than those in a traditional large BEC system. Therefore, atom-chip experiments require ultrastable current sources to run the chip microwires and external bias-field coils. On the other hand, our x-direction optical-pumping time is only 100  $\mu\text{s}$ , which requires us to switch the x-bias field on and off fast enough that its rising and falling times are less than the pumping laser's pulse length. As we know, ultrastability often conflicts with high speed requirement. The faster the current can be switched off and on, the larger the bandwidth; the larger bandwidth a current source has, the more noise its controller cannot suppress. Fortunately, we find that KEPCO power supplies meet both requirements. We use unipolar KEPCO power supplies for the coil hat: one ATE 15-15M for the MOT coil and three ATE 6-10M for the bias coils. We use two bipolar KEPCO power supplies (BOP 20-10D) to run the U and Z wires on the atom chip.

We run the atom-chip wires with the full speed of the power supplies, i.e., 0.4 A/ $\mu\text{s}$ . The current modulation bandwidth of the bias coils is limited by their low inductance, i.e.,  $< 300 \mu\text{H}$  (Table 5.4), and their rising and falling time vs current is shown in figure 5.20. To the MOT coil, its large inductance (3.4 mH per coil) not only reduces the current modulation speed, but also induces a 4.0 kHz oscillation because of phase shift caused by the inductance. We connect a 1.9  $\mu\text{F}$  capacitor in parallel to the MOT coil to compensate for the phase shift. Figure 5.21 shows the difference between running the MOT coil without and with the capacitor.

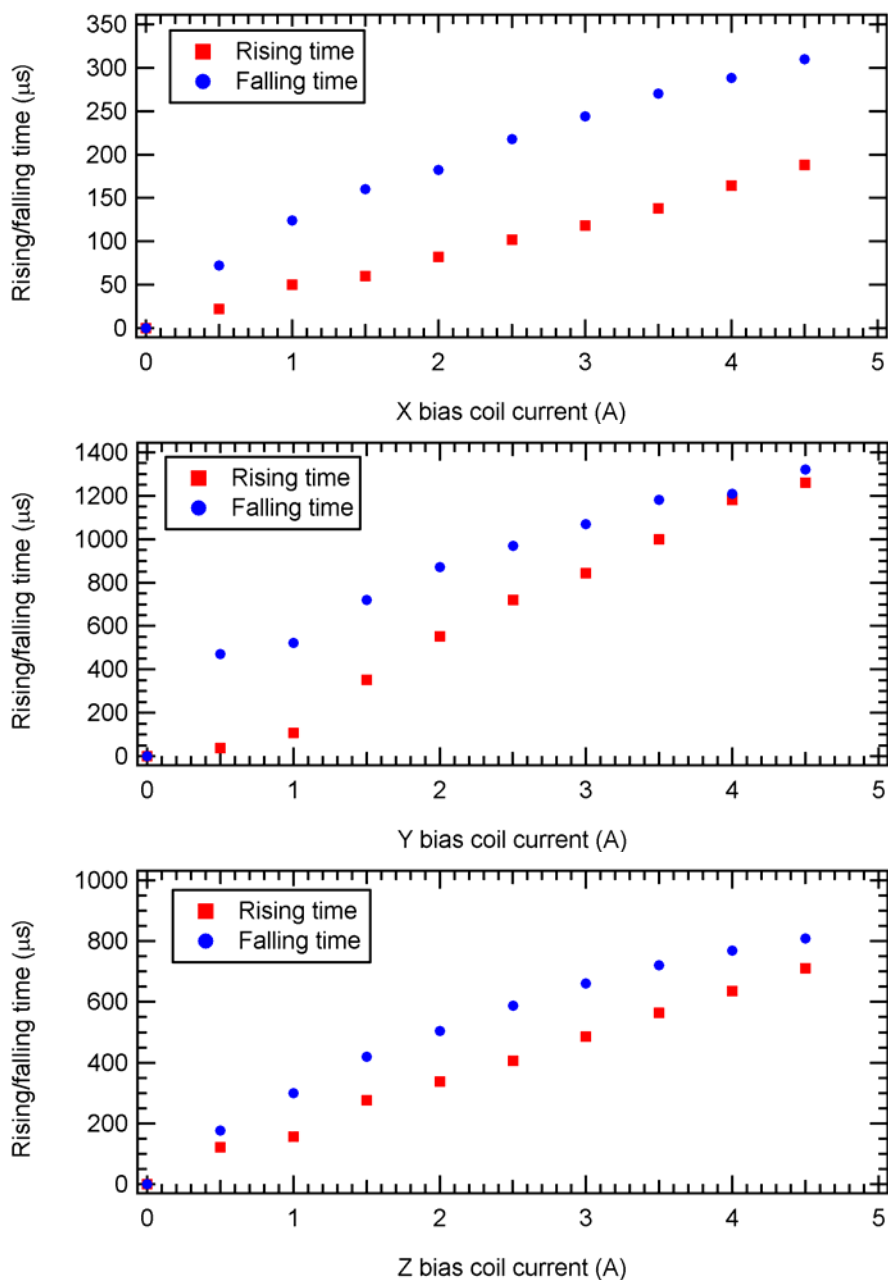


Figure 5.20: Switching on and off time of the x, y, and z-bias coils vs current.

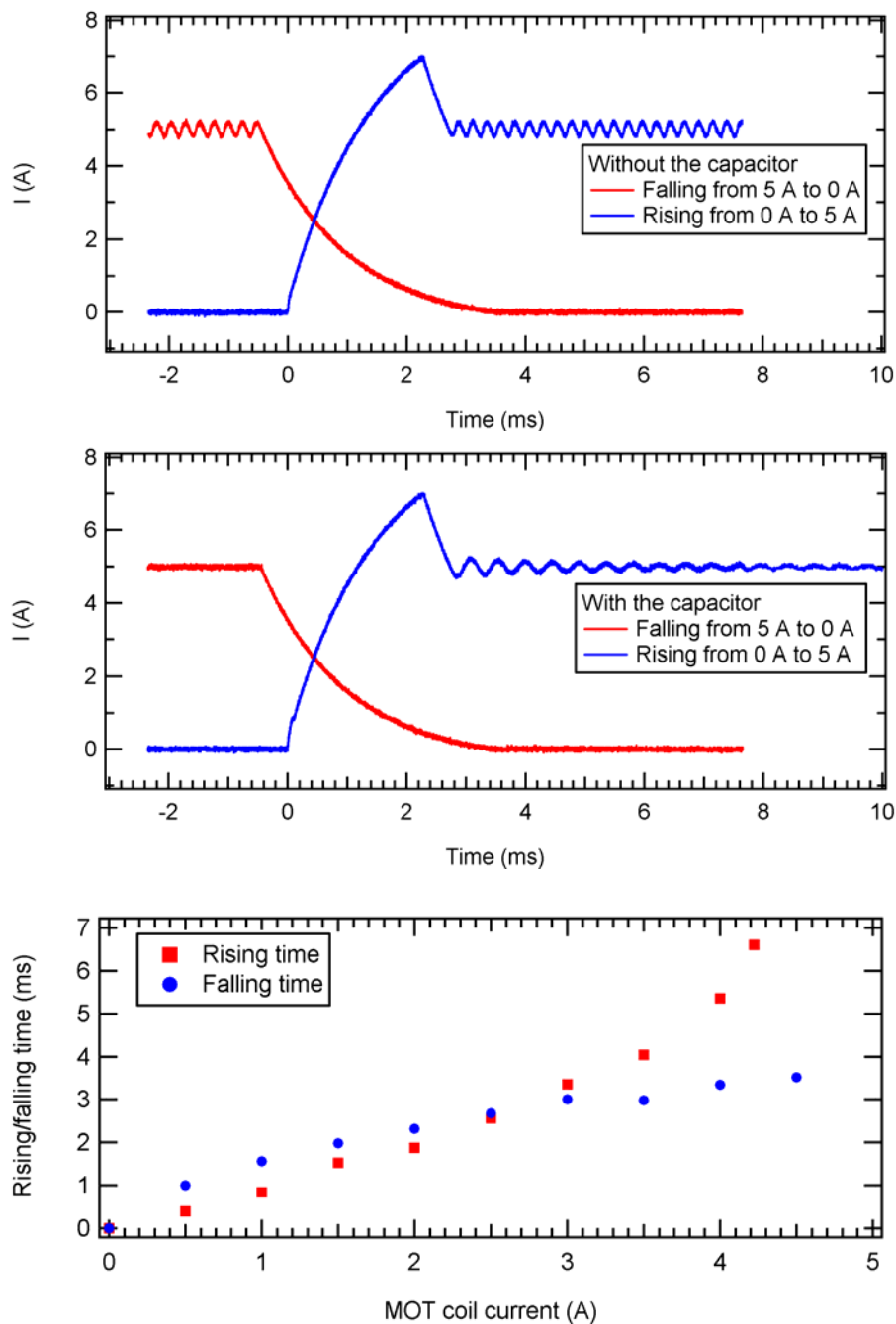


Figure 5.21: The effect of adding the  $1.9 \mu\text{F}$  capacitor to the MOT coil current stability and its switching time measurement.



## 5.5 RF drivers

We designed and built RF drivers for the AOMs and RF-forced evaporative cooling, using commercial RF components from Mini-Circuits.

### 5.5.1 AOM driver

We use four AOM drivers to control cooling laser injection locking, repumping laser power and frequency, pumping laser, and probe laser frequencies. The AOM RF driver block diagram is shown in figure 5.22, and its commercial components are listed in table 5.6. The voltage-controlled oscillator (VCO) generates a sine-wave RF signal in which the frequency is controlled by voltage at the control (CON) input port. The output of the VCO passes through, in order, a transistor-transistor logic (TTL) switch, an attenuator, and an amplifier. We use the TTL switch to turn the RF output on and off, and the attenuator to adjust the RF power level. The output power after the amplifier ranges from 1 to 2 W. The CON inputs are designed to be operated by either its front panel knobs or via remote voltage inputs.

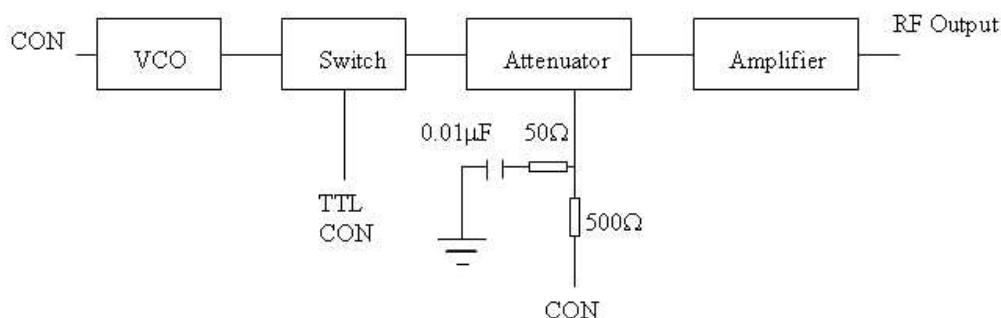


Figure 5.22: System diagram of the AOM RF driver.

Table 5.6: Commercial parts list of the AOM drivers purchased from Mini-Circuits.

Name	Model NO. (Mini-Circuits)	Description
VCO	ZOS-100	50-100 MHz, for repumping laser
	ZOS-150	75-150 MHz, for cooling laser double path AOM, pumping and probe lasers
Attenuator	ZMAS-3	Bandwidth 1-200 MHz
Switch	ZYSW-2-50DR	SPDT with TTL Driver, DC to 5 GHz
Amplifier	ZHL-1-2W	5-500 MHz, up to 2W output

## 5.5.2 RF coil driver

The difference between the RF coil driver (the dashed box part in figure 5.23) and the AOM driver, is that the RF source of the RF coil driver comes from an external function generator (Agilent 33250A, 80 MHz function/arbitrary wave form generator), instead of the VCO used in the AOM drivers. We use the external function generator because a single VCO does not cover the wide bandwidth from DC to 50 MHz, the operating range of RF-forced evaporative cooling. The function generator is remotely configured by the Labview program (section 5.1) via a GPIB card, and the frequency is controlled by one of the outputs from the PDXI-AO-32/16 analog board, as described in section 5.1. The RF coil is a single turn of a 18 AWG magnetic wire with a diameter of 13 mm, mounted at the top of the atom chip.

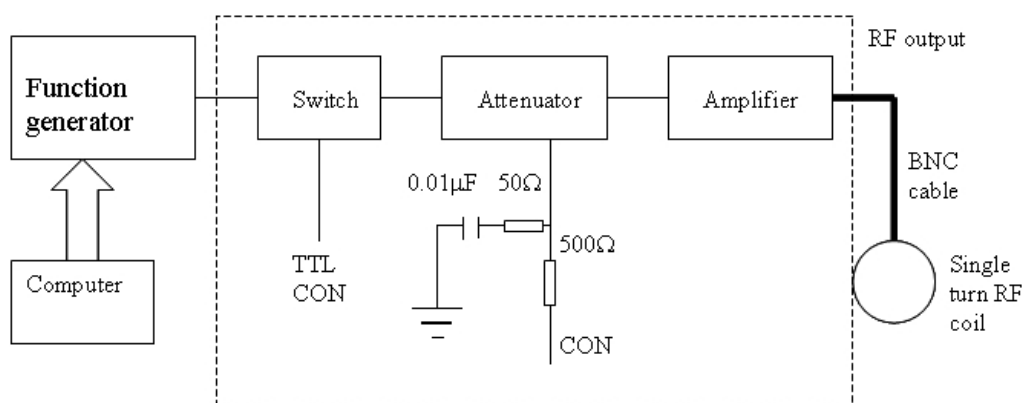


Figure 5.23: System diagram of the RF coil driver (the dashed box) and its input and output.

Table 5.7: Commercial parts list for the RF coil driver purchased from Mini-Circuits.

Name	Model NO.	Description
Function generator	Agilent 33250A	80 MHz function/arbitrary wave form generator
Attenuator	Mini-Circuits ZMAS-3	Bandwidth 1-200 MHz
Switch	Mini-Circuits ZYSW-2-50DR	SPDT with TTL driver, DC to 5 GHz
Amplifier	Mini-Circuits ZHL-1-2W	5-500 MHz, up to 2 W output



## Chapter 6. Preparation and optimization

This chapter describes in detail how to prepare and optimize the atom-chip system for Bose-Einstein condensation (BEC) experiments when a new chip cell is plugged in. It typically takes one week to optimize a new chip-cell system for making a successful BEC on the chip.

### 6.1 Atom-chip cell

After the portable atom-chip cell is pinched off from the pumping station, we plug it into the small atom-chip optical table (section 4.7) where the coil hat (section 5.3.1) has been removed. We carefully adjust the chip height to 101.6 mm above the table surface. Then we align all four magneto-optical trap (MOT) laser beams. The laser beams have a diameter of 8 mm. The two horizontal cooling beams are cutoff by the chip, leaving 2/3 of them inside the cell in the vertical direction. The central part of the atom-chip wire pattern is shown in figure 6.1.

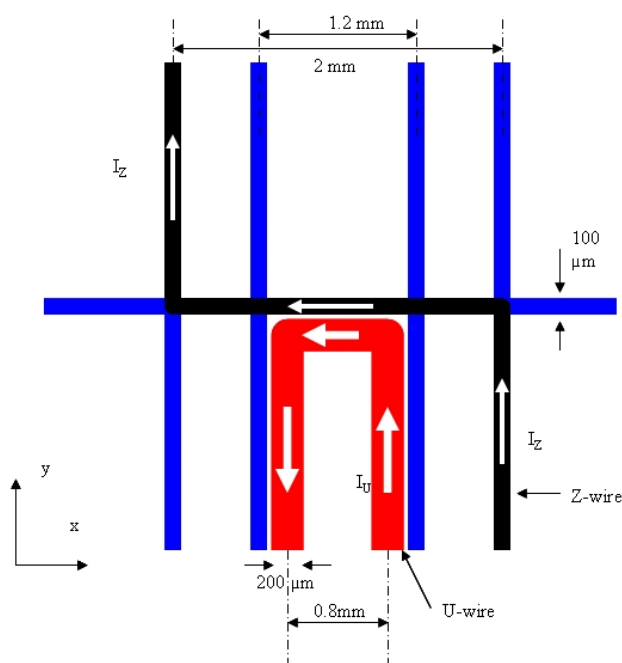


Figure 6.1: The atom-chip wire pattern. The U wire ( $I_U$ ,  $200\ \mu\text{m}$  wide) is used to create chip surface magneto-optical trap, and the Z wire ( $I_Z$ ,  $100\ \mu\text{m}$  wide) is used to create an IP type magnetic trap by applying a  $y$ -bias field. The wires have a height of about  $10\ \mu\text{m}$ .

## 6.2 Laser powers and frequencies

After the cell has been plugged into the system and the MOT laser beams aligned, we check the laser powers and frequencies before searching for the first mirror MOT.

The cooling laser, initially configured with 9 MHz red detuning from the  $^{87}\text{Rb}$  D2 transition  $F=2$  to  $F'=3$ , has 30 mW of power after the fiber output. The master laser is locked to the crossover of  $F=2$  to  $F'=3$  and  $F'=1$ . Because the different laser cooling stages, such as the MOT, compressed MOT (CMOT), and polarization gradient cooling (PGC), require different cooling-laser frequency detunings, the cooling laser injection locking must be able to freely jump from a red detuning of 9 MHz down to 70 MHz by changing the AOM frequency.

The repumping laser, fiber output has 6 mW of power at the on-resonance transition from  $F=1$  to  $F'=2$ . The pumping laser, blue detuned at 12.6 MHz from the transition  $F=2$  to  $F'=2$ , has 1 mW of power after its fiber output. The required probe laser power is less than 1 mW. To probe nonpolarized atoms in the MOT, CMOT and PGC, the probe laser is locked to the on-resonance transition from  $F=2$  to  $F'=3$ . To probe spin-polarized atoms in a magnetic trap, the circularly polarized probe laser is 10 MHz blue detuned from the transition  $F=2$  to  $F'=3$  and accompanied a bias magnetic field of 7.2 G along the beam direction, i.e., the y direction as shown in figure 4.2.

## 6.3 External coil mirror MOT

Now we are ready to search for the first mirror MOT using external coils after putting the coil hat on the atom-chip cell. The MOT coil center is prealigned to 99.6 mm above the table and 2 mm below the chip. Before starting to search for the mirror MOT, we turn on the dispenser to 3 A for more than 2 hours to charge the entire vacuum cell, especially the stainless steel part that acts like a rubidium pump before it is fully coated. After that, we see a very weak MOT from the video cameras if everything is all right. Because of our small chip size, the key point in making a mirror MOT is to locate the magnetic zero-field position precisely. The error between the geometric center of our MOT coil and the real magnetic zero-field position must be within 1 mm.

The real magnetic field position can be shifted if there is any stray field. We move the coil hat to make the MOT as big and bright as possible and then lock the hat on the table. After the dispenser has been turned on for more than 4–5 hours, the cell vacuum is fully coated and the MOT saturates. Such a long time for coating the cell wall is only required the first time we start a MOT experiment. From then on, we only need 15–30 minutes to load the cell with the rubidium dispenser.

After the cell rubidium vapor pressure reaches a steady state, we start to optimize the MOT fluorescence power by aligning the laser beams, adjusting the bias magnetic fields to move the MOT position, and changing the magnetic field gradient and the cooling laser frequency. The optimized MOT magnetic field gradient along its axis is 14 G/cm, and cooling laser red detuning is 9–10 MHz. Since the MOT fluorescence power is a function of both atom number and cooling laser frequency detuning, optimizing the cooling laser frequency to maximize the MOT fluorescence power does not necessarily mean maximizing the atom number. Further optimization of the cooling laser frequency detuning is done by measuring the atom number with absorption imaging, or optimizing the atom number in the chip Z-wire magnetic trap loading (see section 6.14). Fluorescence pictures of the mirror MOT are shown in figure 6.2.

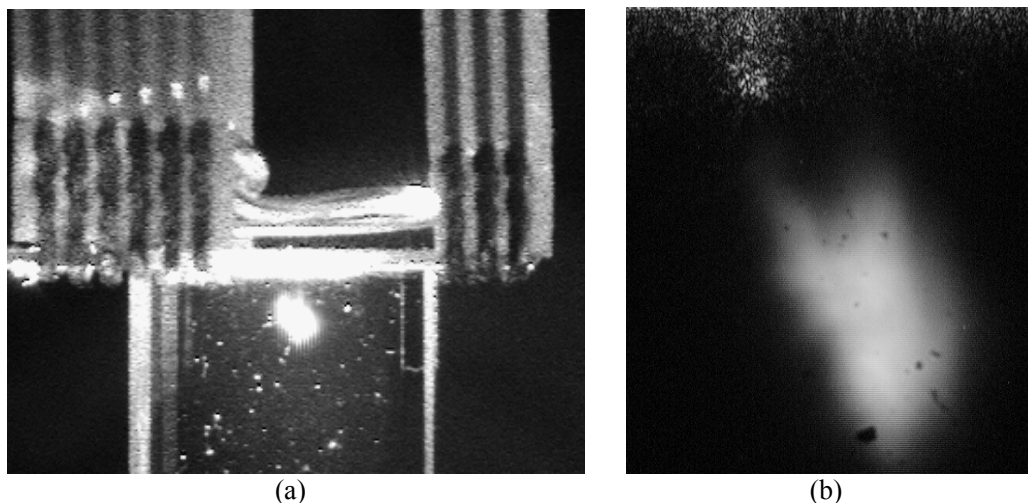


Figure 6.2: External coil mirror MOT fluorescence images. The video camera setup is shown in figure 4.19. (a) is taken by video camera 1 from the front side, and (b) is taken by video camera 2 from the back side. The dispenser is at 3.0 A.

We find that more than 30 mW of cooling laser power does not help much in loading more atoms, but rather makes the MOT unstable. With the total cooling laser power of 30 mW, the intensity is about  $60 \text{ mW/cm}^2$ , which is consistent with the theoretical saturation intensity value of  $35 \text{ mW/cm}^2$  with 9 MHz frequency detuning. The instability of the mirror MOT comes from the fact that we do not have any control over the two  $45^\circ$  reflection beams and cell wall reflection. As discussed later in section 6.7, this condition will be more serious for the chip U-wire surface MOT because of its much shallower trap depth.

## 6.4 Dispenser operating current

After optimizing the MOT, we determine the dispenser operating current for charging the cell for future experiments. If the dispenser is run at too high a current, the small ion pump will be saturated quickly and the dispenser lifetime will be shortened. On the other hand, a current that is too low cannot coat the cell wall efficiently for UV LIAD loading because of low rubidium partial pressure. To determine the optimal operating current, we measure the MOT loading vs dispenser current, as shown in figure 6.3. The operating current is defined as the value at which the loading time is about 2–4 s. The typical range of operating currents for different SAES Rb dispensers is 3.0–3.5 A. At the operating current, we load  $6\text{--}8 \times 10^6$  atoms in the external coil mirror MOT.

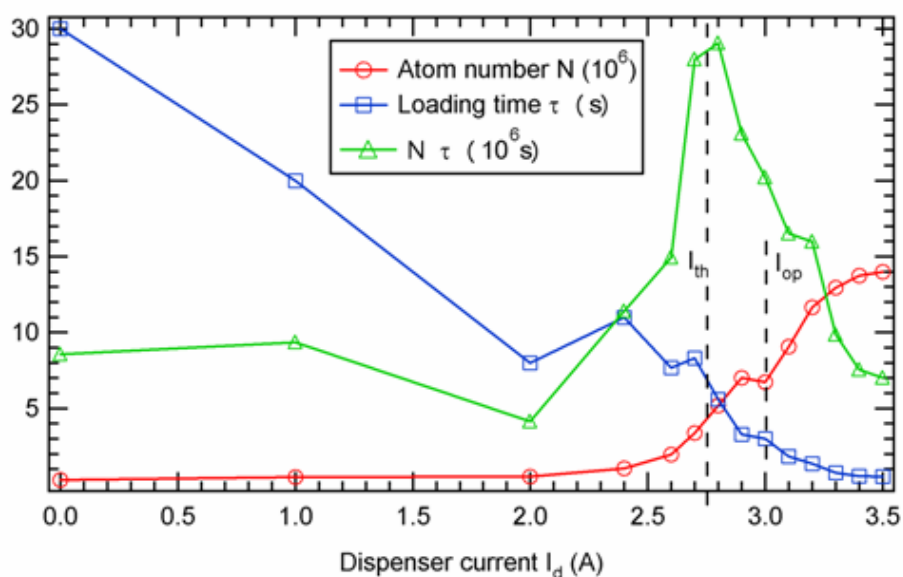


Figure 6.3: The external coil mirror MOT loading vs dispenser current. The threshold current  $I_{th}$  is about 2.75 A above which the Rb vapor pressure dominates the background. The operating current  $I_{op}$  is about 3.0 A.

## 6.5 UV mirror MOT

One of the questions frequently asked is how we know our atom-chip cell is good enough to achieve BEC on the chip. Answering this question is important because it saves time in evaluating the cell quality. In our atom-chip cell, the UV mirror MOT loading plays a key role in the final BEC on a chip production. Successful BEC production requires that the UV mirror MOT load at least  $6\text{--}8\times 10^6$  atoms and have a lifetime of more than 30 s. The atom number  $N$  and lifetime  $\tau$  are two parameters for judging how good the cell is and what the UV LIAD loading efficiency and the cell vacuum are.

The UV mirror MOT is loaded by a 3 s UV pulse that desorbs atoms from the cell wall to increase the rubidium vapor pressure by a factor of more than 30, followed with a 5 s holding time for recovering the cell pressure. The atom number  $N$  is defined as the atom number in the MOT at the end of the 8 s, and the UV MOT lifetime is the  $1/e$  decay time of the MOT atom number after the UV is switched off. The atom number  $N$  directly determines how many atoms can be loaded to the chip Z-wire magnetic trap and the initial collision rate for the evaporative cooling toward BEC. The UV MOT lifetime, determined by the base pressure and the vacuum recovery speed, indicates the vacuum pressure of the cell, which limits the final magnetic trap lifetime. On the other hand, a long UV MOT lifetime also leads to more atoms left at the end of the 8 s mirror MOT. Typical measured lifetimes are on the order of 30 s. We verify that the MOT lifetime is not determined by the Rb pressure decay after the LIAD loading. This is done by noting the number loaded into the MOT after introducing a delay between the UV lamp turn-off and MOT field turn-on. By this method, we observe that the Rb partial pressure in the cell decays very rapidly compared to the MOT lifetime, as shown in figure 6.5. Thus the MOT lifetime is determined by the background pressure in the cell. From the MOT lifetime, we infer the background pressure in the absence of the UV sources to be  $10^{-10}$  torr. From the MOT loading  $1/e$  time ( $\sim 1$  s), we estimate the UV light-induced pressure increase to be a factor of 30.

A typical UV mirror MOT loading and decay curve is shown in figure 6.4, where we also

measure the loading time from the background. The consistency between the UV MOT lifetime and background MOT loading time shows that the cell pressure recovers sufficiently rapidly that the UV MOT lifetime is determined only by the background pressure. Therefore, in our atom-chip cell, the UV MOT lifetime measurement is a reliable method for measuring the cell vacuum pressure.

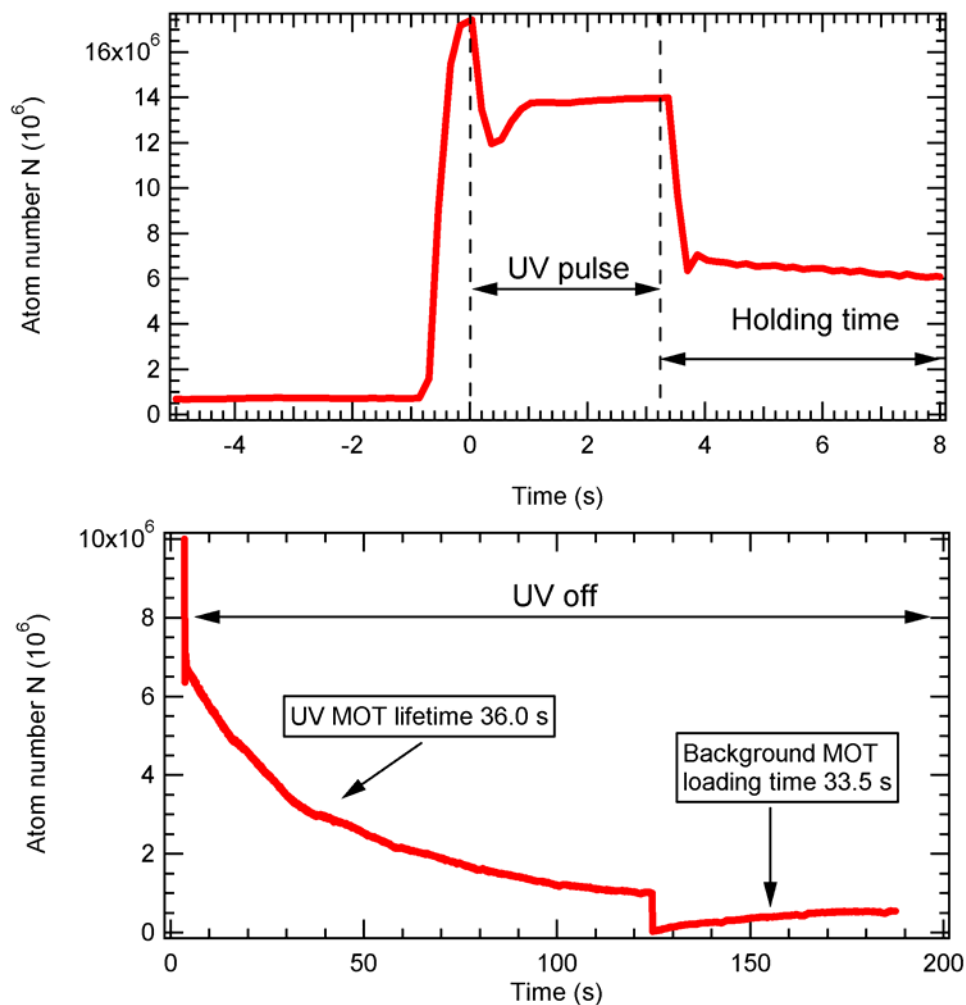


Figure 6.4: UV mirror MOT loading and lifetime measurement. The MOT atom number decay after the UV pulse is switched off is fitted to an exponential. The background MOT is loaded by turning the MOT magnetic field off and on again after several seconds.

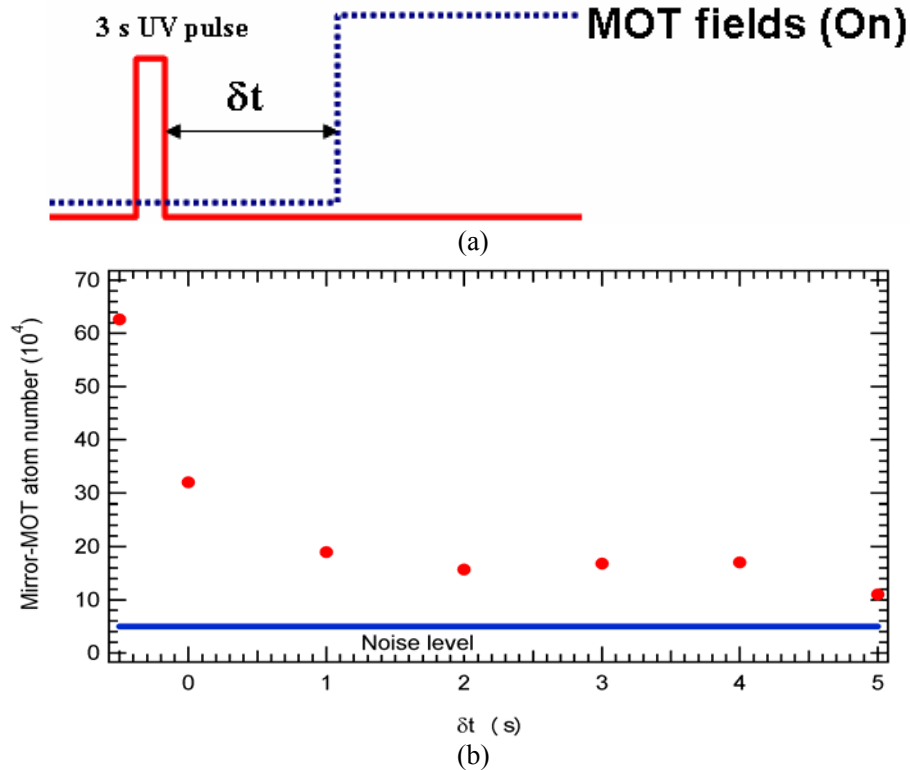


Figure 6.5: UV LIAD cell pressure recovery time measurement. (a) Experimental timing: the MOT fields switch on at  $\delta t$  after the UV pulse turns off. (b) MOT loading steady-state atom number vs  $\delta t$  shows a very short recovery time ( $<5$  s) after the UV light switches off.

## 6.6 Bias coils field calibration

After the external coil mirror MOT has been optimized and the coil hat is locked on the table, we calibrate the bias coils and background stray magnetic fields. The background stray magnetic field shifts the chip U-wire surface MOT position, reduces the cooling efficiency at PGC, and affects the absorption imaging. Calibrating the bias coils can balance the stray field completely if the stray field is uniform spatially. On the other hand, the calibration gives a much more precise relationship between the magnetic field and setting current because in the real system, the chip is not centered to the bias coils and the current power supplies have zero shifting.

The calibration is done by measuring the magnetic field vs current with a Gaussmeter (F.W. Bell 9500). However, there is some bias reading from the Gaussmeter even though it is zeroed carefully. To measure the absolute magnetic field, we take two measurements by flipping the

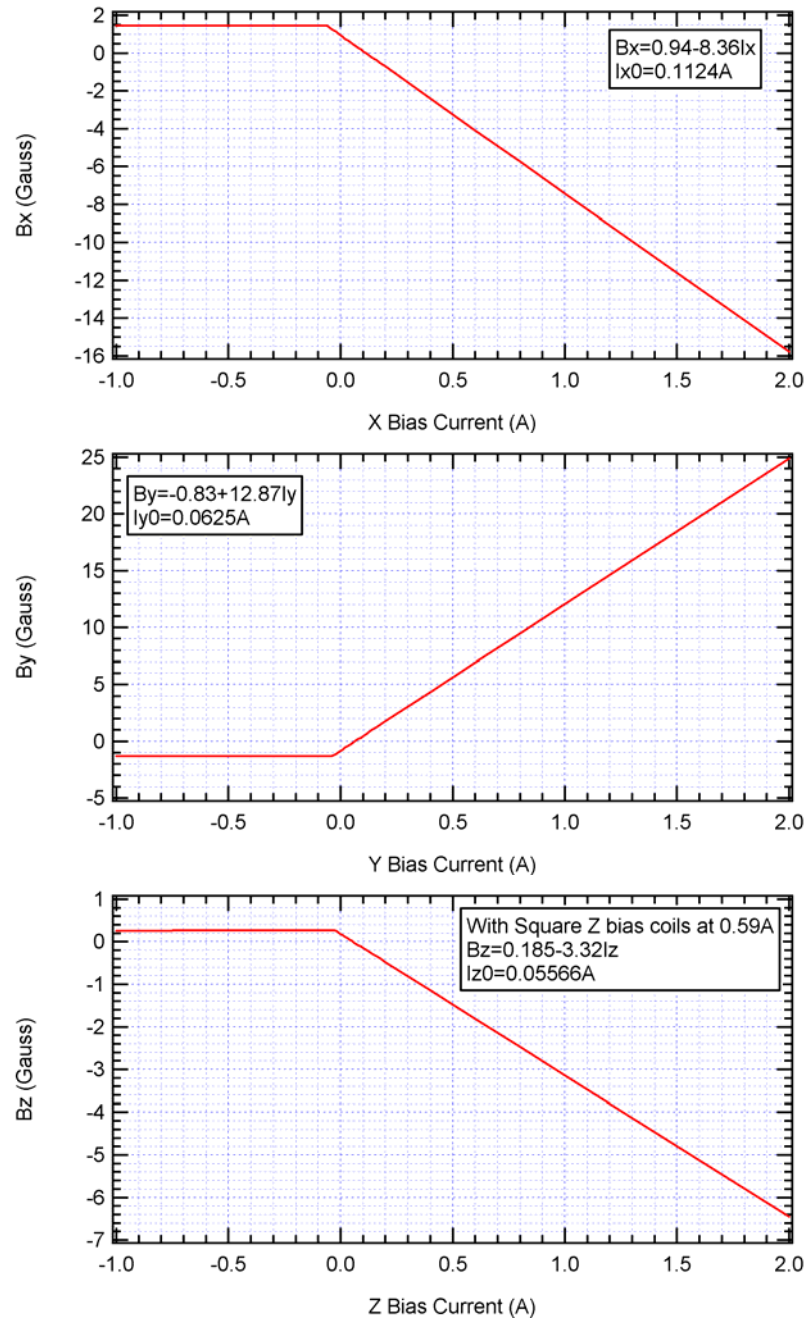


Figure 6.6: Bias coils calibration.

probe to cancel the bias reading. For example, the first measurement gives a reading

$$B_1 = B + B_0, \quad (6.1)$$

where  $B_1$  is the reading from the Gaussmeter,  $B$  is the unknown magnetic field, and  $B_0$  is the unknown bias reading. Then we flip the probe to take the second measurement that gives



$$B_2 = -B + B_0 \quad (6.2)$$

From equations (6.1) and (6.2), we get the magnetic field and bias reading

$$B = \frac{B_1 - B_2}{2} \quad \text{and} \quad (6.3)$$

$$B_0 = \frac{B_1 + B_2}{2}. \quad (6.4)$$

The x, y and z-bias coils calibration result is shown in figure 6.6.

## 6.7 Transferring to the chip U-wire MOT

After the atoms are loaded into the external coil mirror MOT, we transfer the atoms to the chip U-wire surface mirror MOT by replacing the external coil quadrupole magnetic field with the field generated by the U-wire on the chip (figure 6.1).

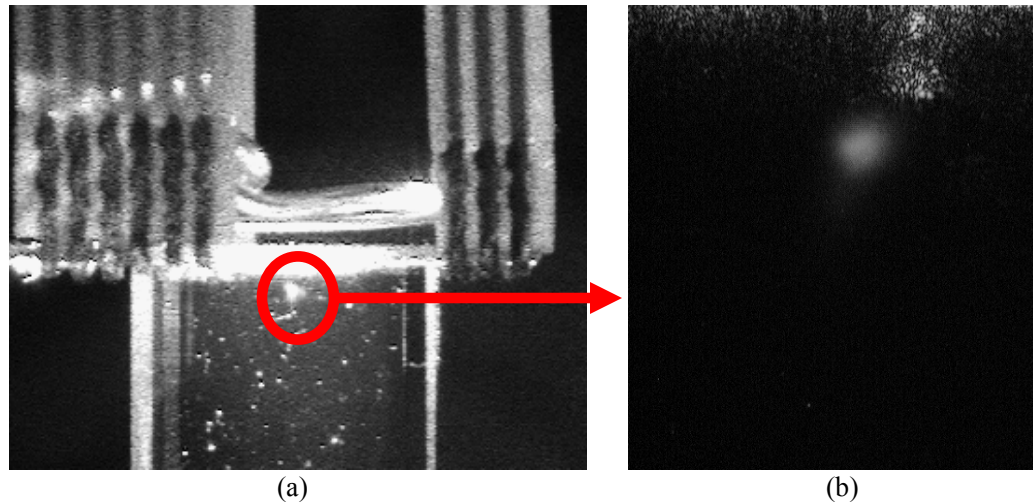


Figure 6.7: Chip U-wire surface mirror MOT fluorescence images. The video camera setup is shown in figure 4.19. (a) is taken by video camera 1 from the front side and (b) is taken by video camera 2 from the back side. The dispenser is at the operating current 3.0 A.

Often, because of the chip UMOT's small capture volume and light field defects, the chip UMOT does not show up visually. If this happens, transferring from the external mirror MOT to the chip UMOT helps us to locate the UMOT position. We have a Labview program that is able to switch between the external mirror MOT magnetic fields and the chip UMOT magnetic fields. By

observing where the atoms move when we switch the magnetic fields from the external mirror MOT to the chip UMOT, we can find where the UMOT zero potential is. Meanwhile, we adjust the bias fields until we get a visible chip UMOT. As soon as the chip UMOT is observed and its bias fields optimized, we optimize the cooling laser beams to make the UMOT as bright as possible. Remember, when we optimize the cooling laser beam alignments for the UMOT, we need to make sure that we do not reduce the atom number in the external coil mirror MOT. It takes some time to optimize the cooling laser beams to both the external coil mirror MOT and the chip UMOT. The power balancing plays a very important role in getting the chip UMOT because of its shallow trap depth.

A direct loading of the chip U-wire MOT (UMOT), with U-wire current  $I_U=2$  A, y bias field  $B_{y0}=1$  G, from the vacuum background is shown in figure 6.7. Although the direct chip MOT itself is tiny due to its small capture volume, it does not cause loss in transferring atoms from the external coil MOT onto the chip.

To load the atoms from the external coil mirror MOT to the chip U-wire CMOT, we first compress the external mirror MOT by increasing its axial magnetic field gradient from 14 G/cm to 21 G/cm. At the same time, we adjust the bias fields to overlap the compressed external mirror MOT with the chip U-wire MOT.

## 6.8 Imaging camera calibration

After the atoms are transferred from the external coil mirror MOT onto the atom chip, we use the absorption imaging method to probe and detect the cold atoms. We setup two cameras for absorption imaging, as shown in figure 4.19. The pixelLink CMOS camera is used to image the atoms before they are loaded into the chip Z-wire magnetic trap (ZMT), and the Apogee CCD camera is used to image the atoms at the ZMT, which is very close to the surface. The probe laser beam configuration is shown in figure 6.8. The probe beam to the PixelLink CMOS camera is passing directly through the chip, and the probe laser beam to the Apogee camera is reflected from the chip surface.

We calibrate the pixelLink CMOS camera image scale ( $50.42 \mu\text{m}/\text{pixel}$ ) by imaging the pin connectors that have  $1.27 \text{ mm}$  separation. The Apogee CCD camera ( $6 \mu\text{m}/\text{pixel}$ ) is calibrated to the atom-chip wire pattern dimensions measured by reflection imaging, as shown in figure 6.9.

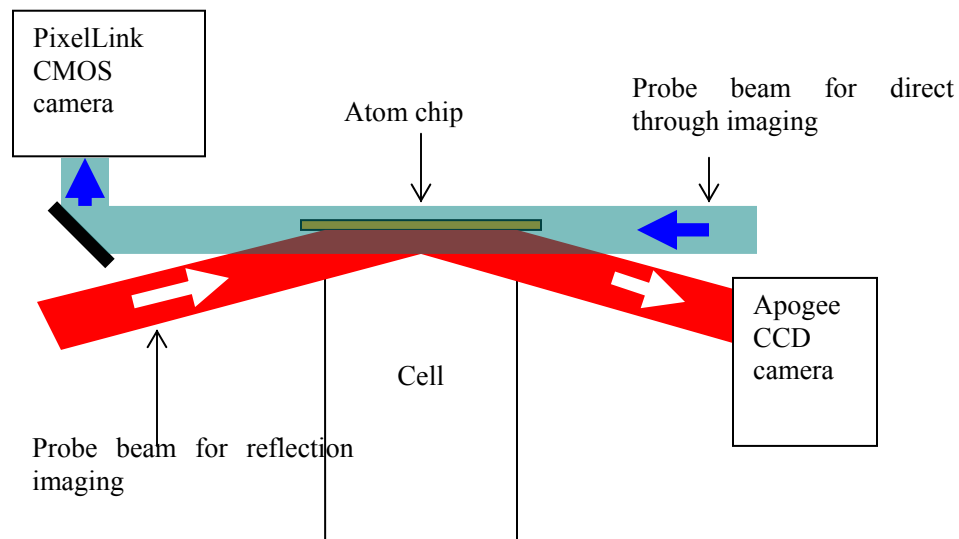


Figure 6.8: Imaging probe beam configuration for both direct-through and reflection imaging.

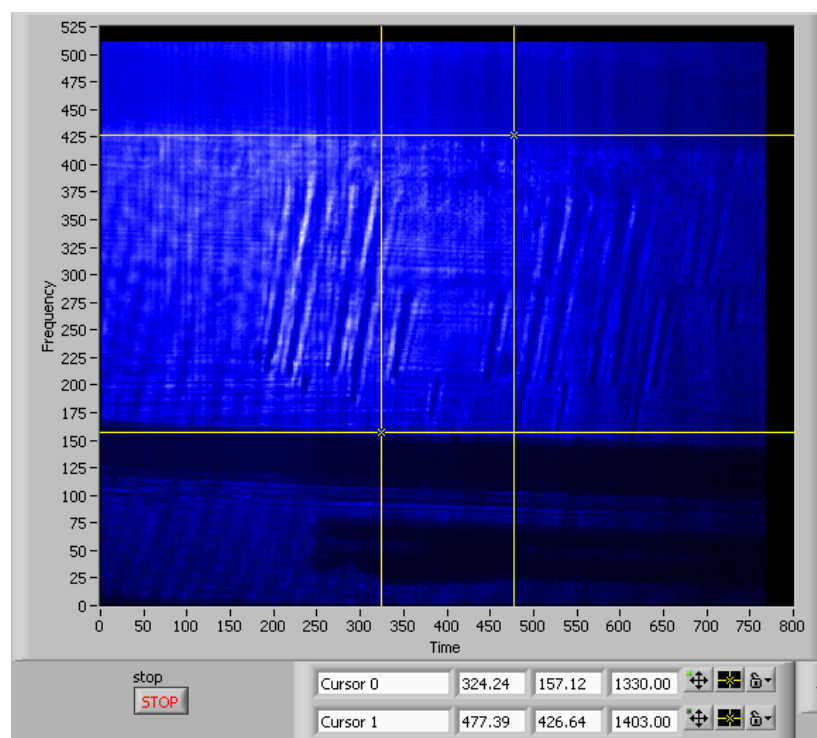


Figure 6.9: An Apogee CCD camera image of the atom-chip wire pattern.

## 6.9 Mirror CMOT

To transfer all the atoms from the external coil mirror MOT to the chip U-wire MOT, we must compress the atom cloud to fit the smaller chip MOT volume. We ramp the magnetic field gradient from 14 G/cm to 21 G/cm, which is determined by transferring from the Mirror MOT to the chip MOT in section 6.8. We optimize the ramp time, cooling laser frequency, and repumping power to achieve the maximum cooling efficiency. The optimized ramp time is 20 ms, and the cooling laser frequency is 23 MHz red detuned from the transition from  $F=2$  to  $F'=3$ , and the repumping power is 100  $\mu$ W. The mirror compressed MOT (CMOT) not only compresses the MOT into a smaller volume ready for loading to the atom chip, but also efficiently cools the atoms from 150–400  $\mu$ K down to 120  $\mu$ K by suppressing the light scattering with a further detuning of the cooling laser and a reduction of the repumping laser power.

## 6.10 Chip CMOT optimization

After the atoms are transferred from the external coil mirror CMOT to the chip U-wire CMOT ( $I_U=2$  A,  $B_y=1$  G), rethermalization takes 5 ms because of a slight mode mismatching. Then the atoms are further cooled and compressed by ramping the bias field from (0, 1, 0) G to (0, 2.6, -1.2) G and moved closer to the chip surface in 3 ms. The distance of the final chip CMOT from the chip surface is about 700  $\mu$ m. After a total of 8 ms in the U-wire chip CMOT, the atoms have a temperature of 100–110  $\mu$ K.

## 6.11 Polarization gradient cooling

After the chip U-wire CMOT, we use polarization gradient cooling (PGC) to cool the atoms below the Doppler limit. The CMOT cooling efficiency is very sensitive to any stray magnetic field and laser power balancing. The bias coil calibration described in section 6.6 helps us to set the magnetic field very close to zero. Further optimization of the magnetic field is done (as

described in section 6.14) by maximizing the loading efficiency of the atom-chip magnetic trap. The power unbalancing of the cooling laser beams adds additional heating to the atoms and pushes the cloud to one side. The fine balancing between the four cooling laser beams can be done by correcting the cloud position shift after a long time PGC, e.g., 20 ms. The PGC time is optimized to maximize the ZMT loading efficiency (as described in section 6.14) because both mode matching and temperature are important for ZMT loading. At the end of the PGC, the atoms are cooled down to 20–50  $\mu\text{K}$ .

## 6.12 Optical pumping

At this time, we simply add 100  $\mu\text{s}$  of an optical pumping pulse with a bias magnetic field of about 13 G after the PGC. The optimization can not be done until we have the chip magnetic trap. For more about optical pumping, please check section 4.5 in chapter 4.

## 6.13 ZMT loading optimization

Now we are ready to load the atoms into the chip Z-wire magnetic trap (ZMT). At first, we calculate the required Z-wire current and bias field to overlap the chip CMOT position by requiring the trap depth to be 10 times higher than the temperature after PGC. Then we take a reasonable amount of time to compress the atoms to some place where the trap has a high enough trap depth. After this initial configuration, we start to optimize the ZMT loading efficiency.

We first optimize the loading parameters when the atoms are transferred into the ZMT. Since the modes are completely mismatched from an isotropic cloud to the high nonisotropic ZMT, it takes a long time for rethermalization. First, we like to have a large trap volume initially, but a larger trap volume requires a larger Z-wire current and a smaller y bias field, which produces a shallower trap depth and lower trap frequencies. Thus, the atoms experience a trap loss and a low rethermalization rate. To increase the loading efficiency and reduce the rethermalization time, we ramp the Z-wire current from zero to some current within 1 ms. This Z-wire current

ramp scans the trap position from the chip surface to some distance away from the surface instead of just sitting at some fixed position, and effectively increases the trap volume. This ramp also forces a large volume of atoms into the trap center quickly and increases the rethermalization rate. After the fast Z-wire current ramp, we ramp the bias field to increase the trap depth. After this nonadiabatic loading, we adiabatically compress the ZMT with a long sweep by increasing y-bias field. The loading and compression are schematically shown in figure 6.10. The optimized values are  $t_1 = 0.3$  ms,  $t_2 = 10$  ms,  $t_3 = 110$  ms,  $I_{Z1} = 2\text{--}4$  A,  $I_{Z2} = 2.75$  A,  $B_{y0} = 10$  G,  $B_{y1} = 14$  G, and  $B_{y2} = 40\text{--}60$  G.

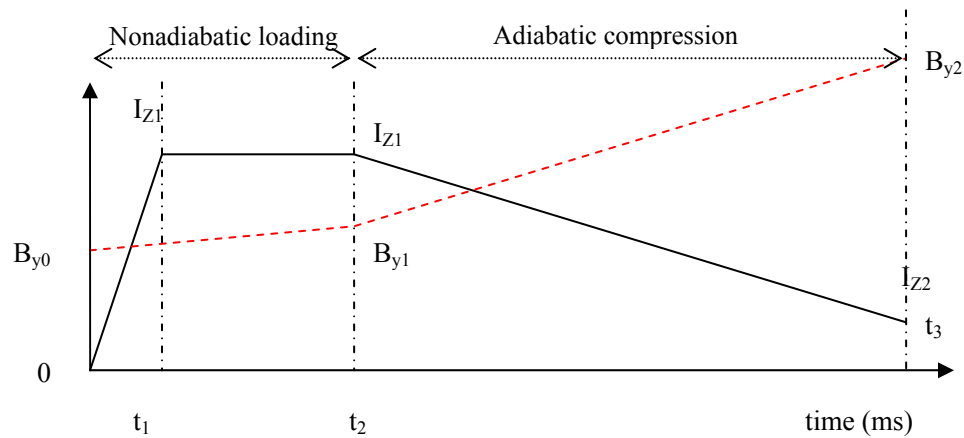


Figure 6.10: The Z-wire current and y bias field ramps during ZMT loading and compression.

## 6.14 Final loading optimization

As soon as we have a ZMT, we are able to perform a final optimization of the CMOT, PGC, and optical pumping to maximize the loading efficiency and mode matching.

We optimize the final ramp value of the chip CMOT y-bias field to maximize the ZMT loading efficiency.

We optimize the PGC cooling time and laser frequency to maximize the ZMT loading efficiency.

We optimize the optical pumping (pulse time length, power, frequency, and magnetic field strength) to maximize the ZMT loading efficiency.

Finally, we do the ZMT loading optimization described in section 6.13 again to optimize both loading efficiency and mode matching. The mode matching is critical to reduce the rethermalization time that will be discussed in section 8.2 of chapter 8. Experimentally, we simply maximize the aspect ratio of the atom cloud at the end of the compression. An optimized Z-trap reflection absorption image is shown in figure 6.11, where the Z-wire current is  $I_z=4\text{A}$  and y bias field is 40 G. The image is taken after a 1 ms time of flight (TOF).

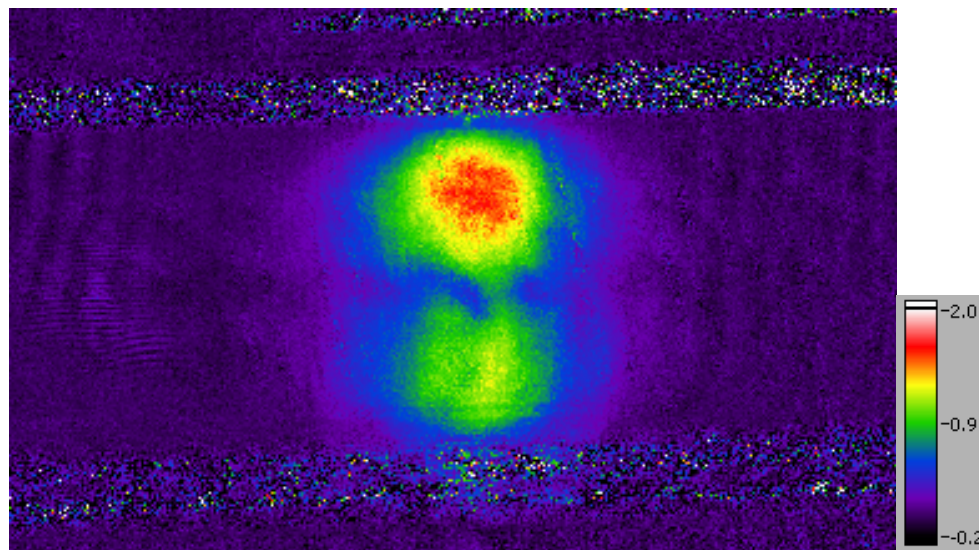


Figure 6.11: Reflection absorption image of atoms in a Z-wire trap initially loaded with UV mirror MOT. Atom number  $N = 2.55 \times 10^6$ . Peak optical depth (OD) is 1.55.

## 6.15 Summary and conclusion

The above optimization procedures are for beginners who are starting atom-chip experiments without any previous experience. As soon as the control timing has been determined, we do not need to repeat all the optimization procedures above for a new atom-chip cell. After a new cell is plugged into, we only need to redo the procedures from sections 6.3 to 6.7 to find the right operating parameters for the MOTs; then we can load the optimized timing file directly.

The optimized control timing recipe for atom-chip BEC production will be described in chapter 7. We find that this recipe works well for plugging in different cells. Only slight fine-tuning of the optimization is required.

## Chapter 7. Bose-Einstein condensation on the chip

As soon as the first Bose-Einstein condensate (BEC) in a neutral atom gas was demonstrated in 1995 [3, 4], J.D.Weinstein and K.G. Libbrecht proposed to use chip-patterned currents for microscopic magnetic traps and integrated atom optics [83]. Then the realization of cold-atom guiding [5, 7] and manipulation [6, 9, 10, 84] using lithographically patterned wires on substrates, or atom chips, attracted research interest in chip-scale cold-atom optics. However, because of the difficulty in loading large numbers of atoms to atom-chip traps, which have small volumes and shallow depths, the first BEC on a chip was not realized until 2001 [14, 15]. The realization of a chip-based BEC was a scientific and technical milestone towards chip-scale coherent atom-optics devices, opening the door for integrated matter-wave sensors and quantum computation. The number of BEC atom-chip systems developed around the world continues to grow[16, 61, 68, 85–87].

With the exception of our portable cell, all the chips in BEC atom-chip systems are embedded into large vacuum chambers, which enable them to load a large numbers of atoms into magneto-optical traps (MOT) [14, 15, 61, 68, 86], and transfer evaporative-precooled atoms or even BEC clouds from macroscopic traps into chip micropotentials [15, 85, 87]. Our portable  $1 \times 1$  cm atom-chip cell is the smallest BEC system in the world. We are pushing ultracold atom research and applications to an extreme limit and trying to answer the question how small of a vacuum cell can be used to achieve a suitable vacuum level and MOT capture volume for direct BEC production on an atom-chip. As in the rapid development of electronic and optical technologies in the past century (e.g., micro chip processors, semiconductor laser diodes, and optical fibers), portability and low cost will be the keys to real atom-chip applications in the future. Our work suggests that a chip-based BEC-compatible vacuum system can occupy a volume of less than 0.5 liter.

The vacuum cell has been described in detail in chapter 3. The atom-chip wire pattern has been shown in figure 6.1. This chapter presents how to create a BEC on the portable atom-chip



cell. It is organized by following the experimental procedures in order, from the magneto-optical trap (MOT), to the compressed MOT (CMOT), polarization gradient cooling (PGC), optical pumping (OP), chip Z-wire magnetic trap (ZMT), compression, RF-forced evaporation, and the final formation of a BEC.

## 7.1 Charging the cell

Before we start an atom-chip experiment, we turn on the dispenser at its operating current (see section 6.4) for 30 min to charge the cell by coating Rb on the cell wall and Pyrex helix spiral. This half hour is also a good time to check the system performance, e.g., the laser powers and ZMT loading efficiency. Then the dispenser is turned off, and we are ready to make a BEC on the atom chip.

## 7.2 UV mirror MOT

When the cell pressure has recovered after turning off the dispenser for 15–30 minutes, we start to load the external coil mirror MOT with UV light-induced atomic desorption (LIAD) [reference 6, 64–66, or see section 6.5 for details]. The mirror MOT is loaded by applying a 3 s UV pulse, which increases the cell rubidium vapor pressure by a factor of 30, followed by a 5 s holding time for recovering the pressure before going to the next cooling stage. The MOT magnetic field gradient along the external coil axis is 14 G/cm. The cooling laser is 30 mW and 9 MHz red detuned from the transition from  $F=2$  to  $F'=3$ . The repumping laser, locked to the on-resonance transition from  $F=1$  to  $F'=2$ , has a power of 6 mW. The UV mirror MOT traps about  $6\text{--}8 \times 10^6$   $^{87}\text{Rb}$  atoms, 2 mm away from the chip's sliver mirror surface. The MOT temperature, depending on the laser beam alignment, varies from 150 to 400  $\mu\text{K}$ , shown in figure 7.1. At the UV mirror MOT stage, the atom number is the most important parameter for optimization, not the temperature. The MOT temperature of 150–400  $\mu\text{K}$  is considered as “normal” and can be cooled down to below 50  $\mu\text{K}$  after the CMOT and PGC. The external coil mirror MOT is optimized to

obtain as large as possible number of atoms. A typical 330  $\mu\text{K}$  MOT absorption image, taken by the Pixelink CMOS camera, is shown in figure 7.2. The phase-space density (PSD) is about  $3.7 \times 10^{-9}$ .

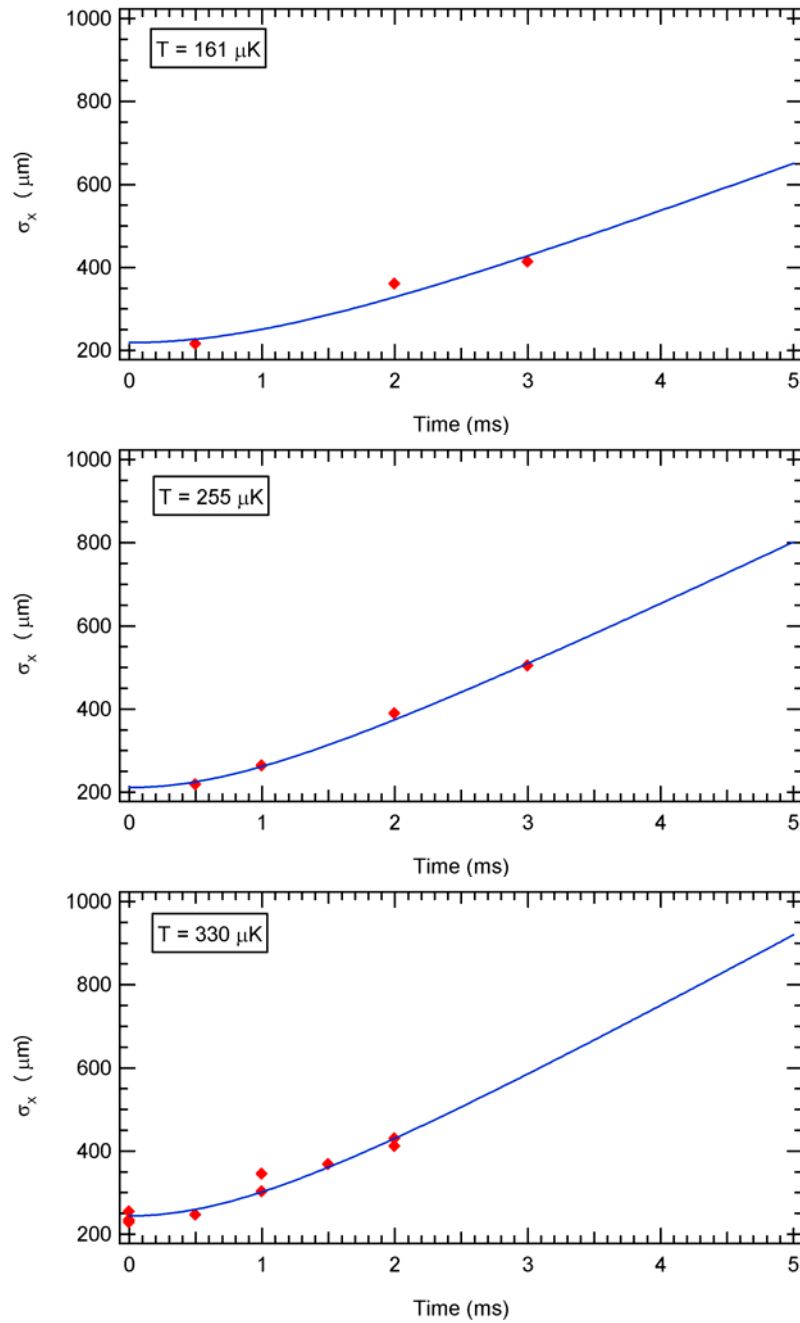


Figure 7.1: Time-of-flight (TOF) measurement of the external coil mirror MOT at  $T = 161 \mu\text{K}$ ,  $255 \mu\text{K}$ , and  $330 \mu\text{K}$ .

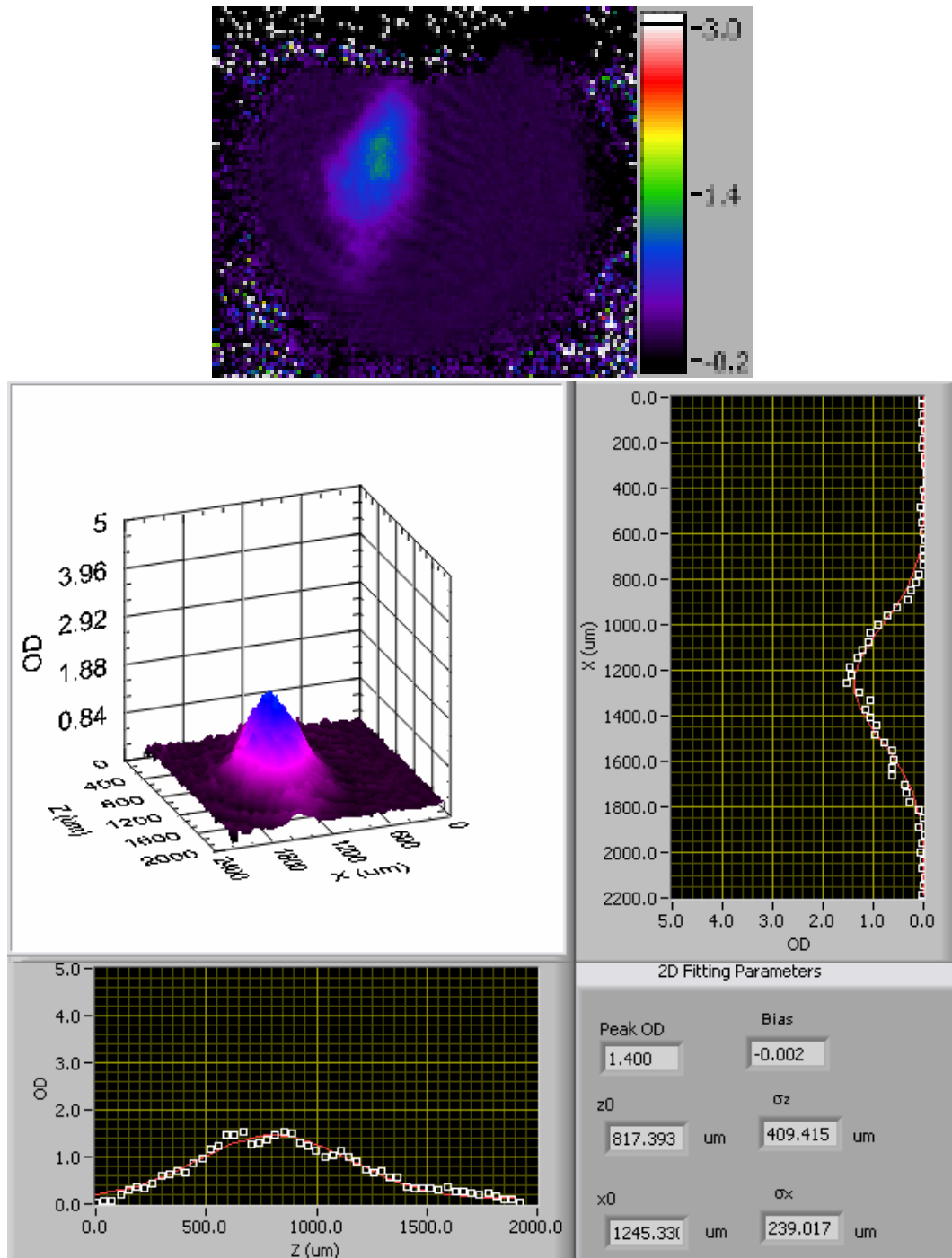


Figure 7.2: Absorption image of the external coil mirror MOT.  $N = 6.1 \times 10^6$ , Peak OD = 1.4,  $\sigma_x = 239 \mu\text{m}$ ,  $\sigma_z = 409 \mu\text{m}$ ,  $T = 330 \mu\text{K}$ , average PSD =  $3.7 \times 10^{-9}$ , and Collision rate = 0.8 Hz.

### 7.3 External coil Mirror CMOT

After the UV pulse is switched off and the external coil mirror MOT is held for 5 s, the cell ultrahigh-vacuum (UHV) pressure recovers and the atoms then undergo a compressed MOT (CMOT) stage. The cooling laser's red detuning jumps from 9 to 23 MHz. The repumping laser power is reduced from 6 mW to 100  $\mu$ W. Then we immediately ramp the external coil quadrupole magnetic field gradient from 14 to 21 G/cm in 20 ms. At the same time, by adjusting the bias fields, the atoms are moved toward the surface to overlap where the chip U-wire CMOT takes place at the next stage, about 1 mm away from the chip surface. The mirror CMOT not only compresses the MOT into a smaller volume ready for loading to the atom chip, but also efficiently cools the atoms from 150–400  $\mu$ K down to 120  $\mu$ K by suppressing the light scattering with an increase in the detuning of the cooling laser and a reduction of the repumping laser power. The time of flight (TOF) absorption measurement is shown in figure 7.3. It tells us the temperature at the end of the external coil mirror CMOT is about 123  $\mu$ K. The 3D surface and cross-section plots are shown in figure 7.4. The external coil mirror CMOT has a PSD of  $6.7 \times 10^{-8}$ , which is increased by one order of magnitude from the UV mirror MOT.

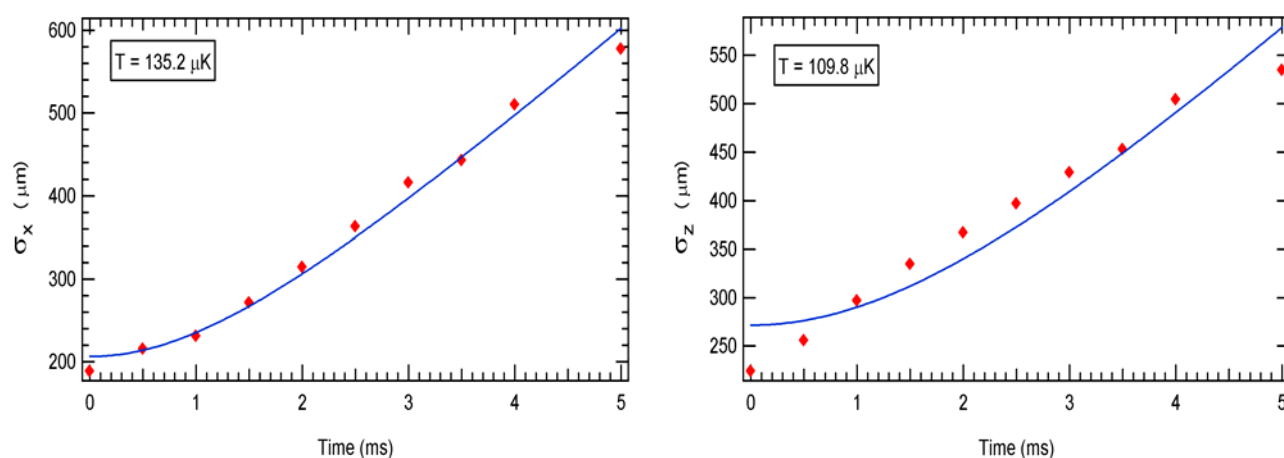


Figure 7.3: TOF measurement of the external coil mirror CMOT.

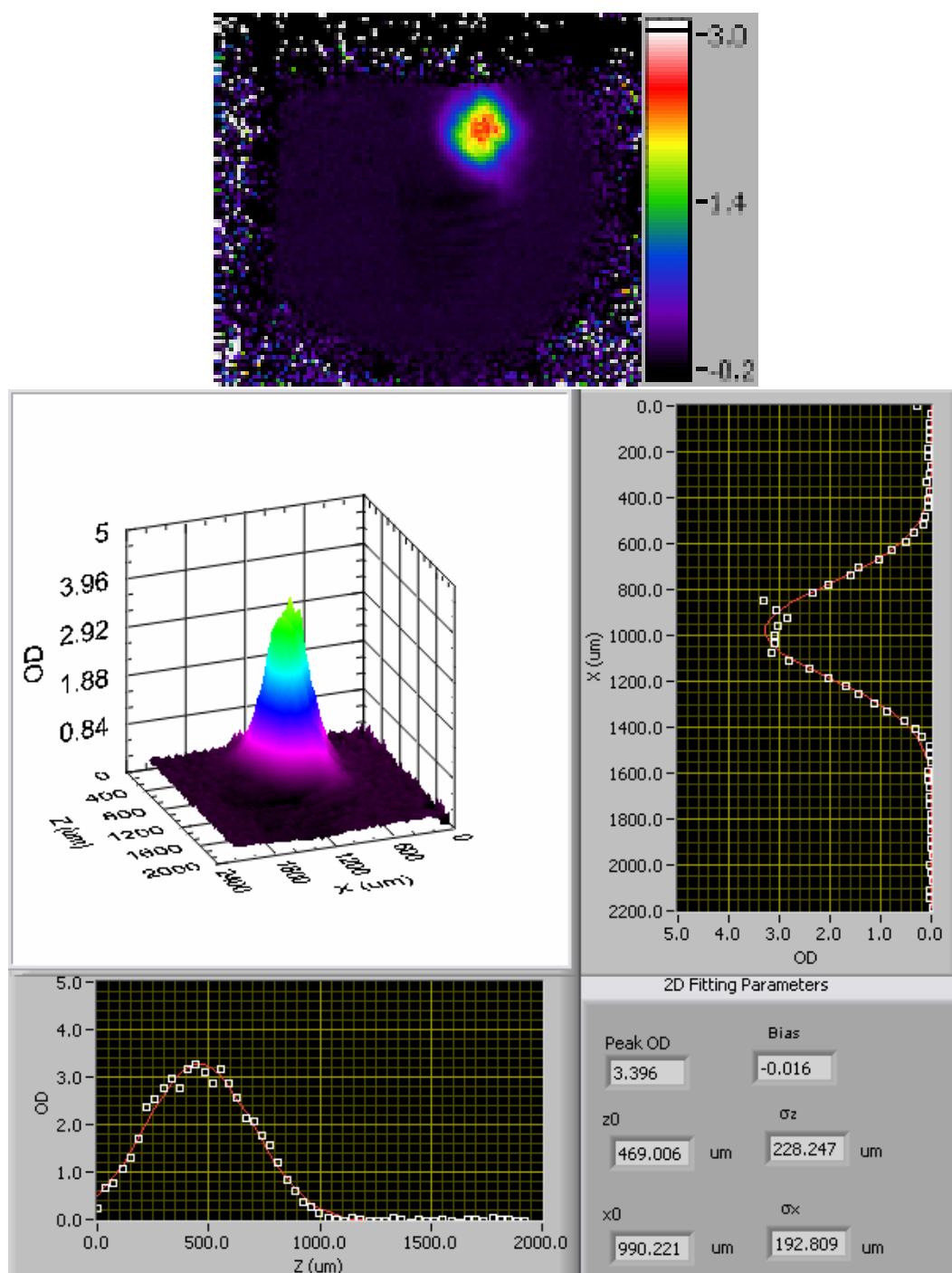


Figure 7.4: Absorption imaging of the external coil mirror CMOT.  $N = 6.3 \times 10^6$ , Peak OD = 3.4,  $\sigma_x = 193 \mu\text{m}$ ,  $\sigma_z = 228 \mu\text{m}$ ,  $T = 123 \mu\text{K}$ , average PSD =  $6.7 \times 10^{-8}$ , and Collision rate = 2 Hz.

## 7.4 Chip U-wire CMOT

At the end of the external mirror CMOT, the atoms are ready to be loaded into the chip U-wire CMOT. The external coil quadrupole magnetic field is switched off and replaced with the field generated by the U-wire ( $I_U = 2$  A) and the y bias field ( $B_y = 1$  G). The chip CMOT is about 1 mm below the chip surface. The atoms are held in this chip CMOT for 5 ms for rethermalization, and then are further cooled and compressed by ramping the bias field from (0, 1, 0) to (0, 2.6, -1.2) G and moved closer to the chip surface. The distance of the final chip CMOT from the chip surface is about 700  $\mu\text{m}$ . After the total 8 ms U-wire chip CMOT, the atoms have a temperature of 100–110  $\mu\text{K}$ . The TOF measurement result is shown in figure 7.5 and absorption images in figure 7.6. The PSD, increased by another order of magnitude, now is  $1.9 \times 10^{-7}$ .

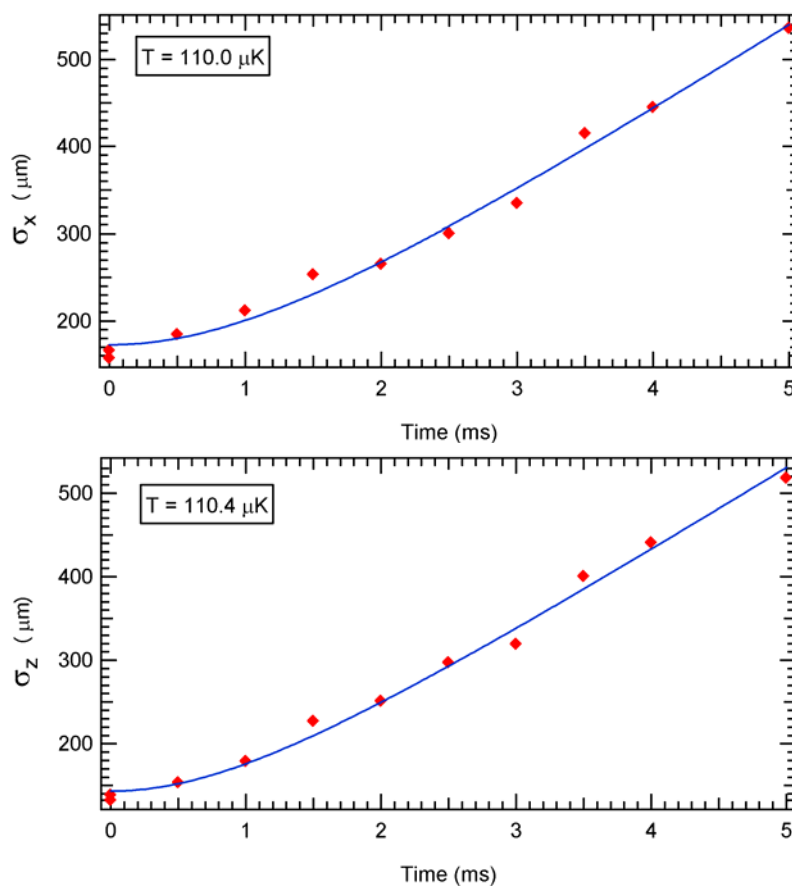


Figure 7.5: TOF measurement of the chip U-wire CMOT.

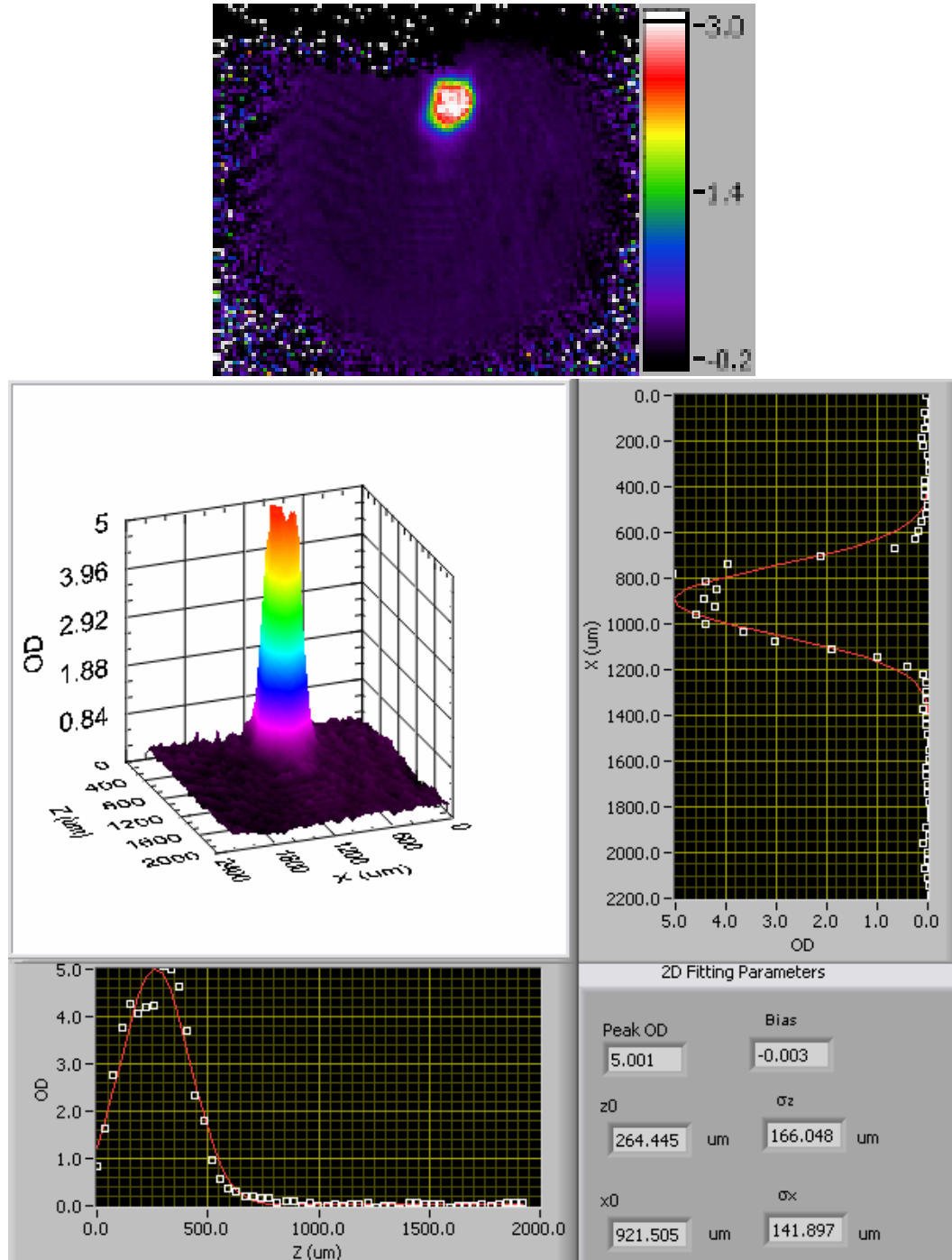


Figure 7.6: Absorption imaging of the Chip U-wire CMOT.  $N = 5.9 \times 10^6$ , Peak OD = 5.0,  $\sigma_x = 142 \mu\text{m}$ ,  $\sigma_z = 166 \mu\text{m}$ ,  $T = 110 \mu\text{K}$ , average PSD =  $1.9 \times 10^{-7}$ , and Collision rate = 4.5 Hz.

## 7.5 Polarization gradient cooling

After the chip U-wire CMOT, we apply a 1.7 ms polarization gradient cooling (PGC) by increasing the cooling laser red detuning to 70 MHz and switching off all magnetic fields. This further cools the atoms to 20–40  $\mu\text{K}$ , as shown in figure 7.7. The atom cloud's 3D surface and cross-section plots are shown in figure 7.8. As compared to the previous chip CMOT, the size of the cloud expands slightly because of the missing spatial magnetic field confinement, but the temperature drops significantly due to the sub-Doppler cooling. The PSD after the PGC is improved by another order of magnitude to  $6.2 \times 10^{-6}$ .

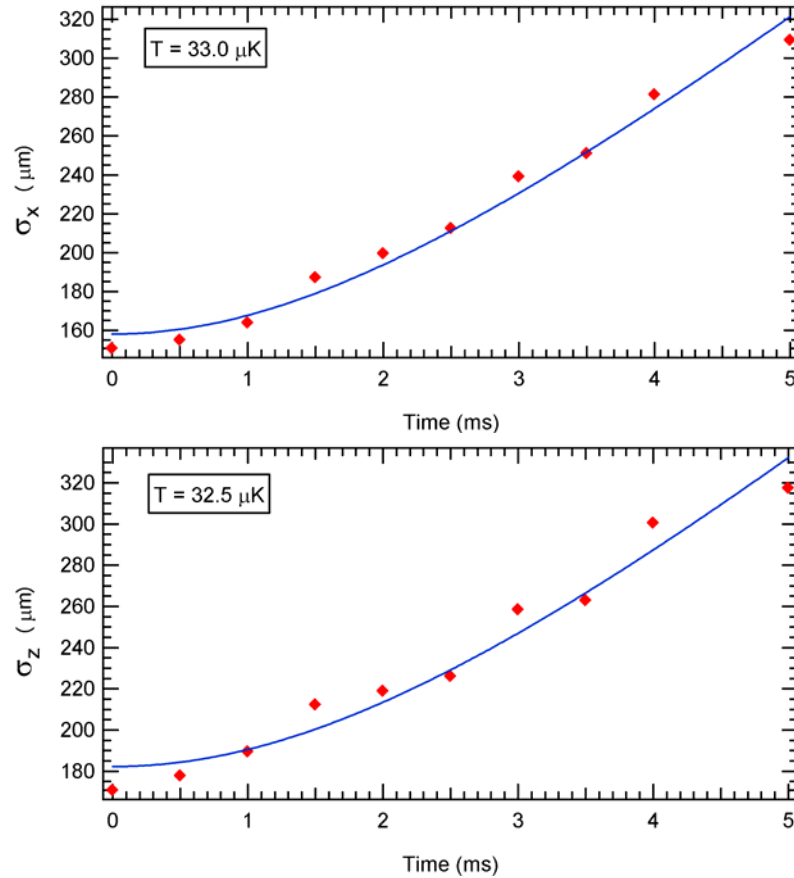


Figure 7.7: TOF measurement after PGC.



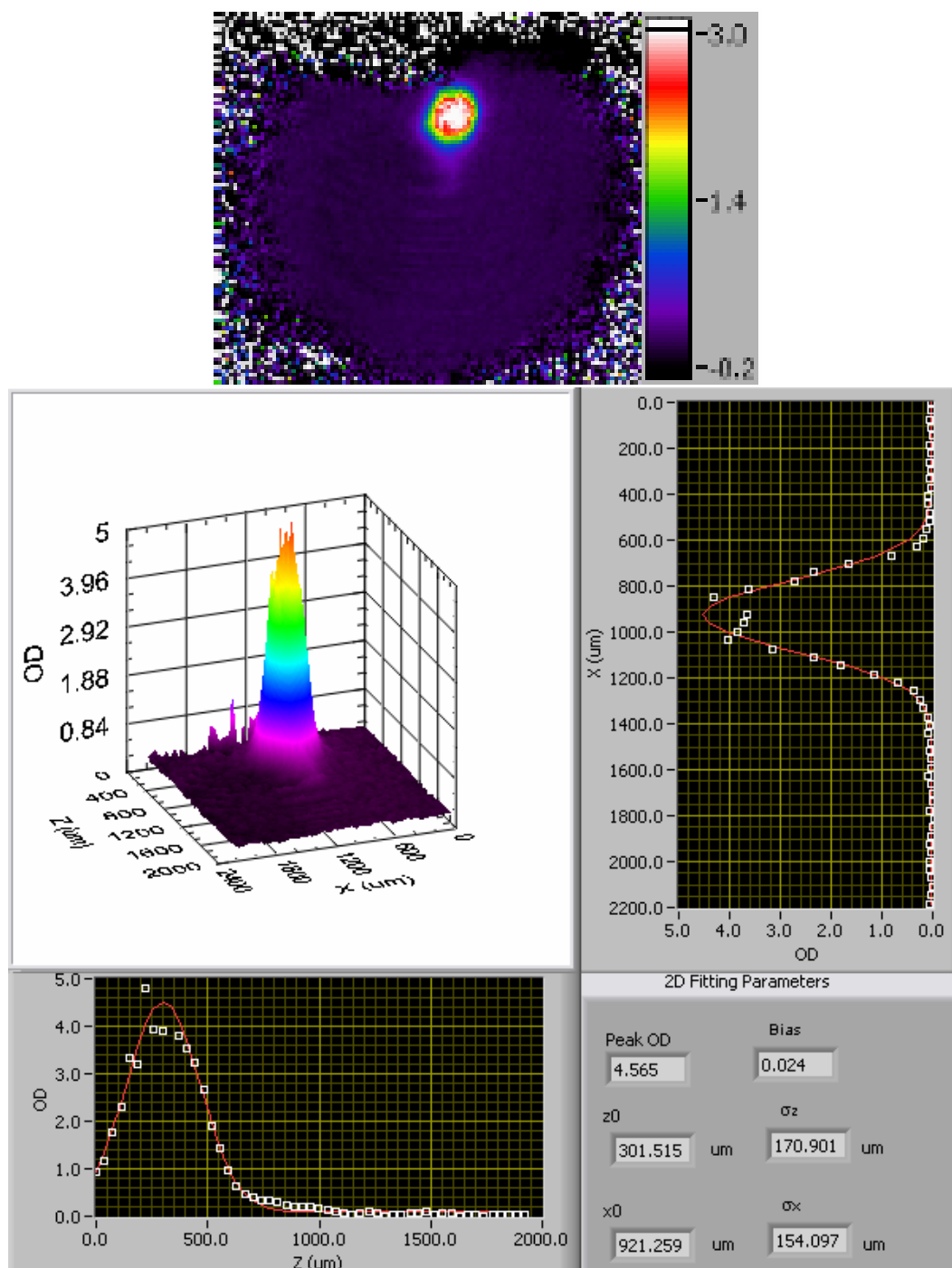


Figure 7.8: Absorption imaging after PGC.  $N = 6.2 \times 10^6$ , Peak OD = 4.6,  $\sigma_x = 154 \mu\text{m}$ ,  $\sigma_z = 171 \mu\text{m}$ ,  $T = 33 \mu\text{K}$ , average PSD =  $1.0 \times 10^{-6}$ , and Collision rate = 2.3 Hz.

## 7.6 Optical pumping

During the laser cooling stages from the mirror MOT to the chip surface PGC, no substantial atom loss is observed, the temperature drops from several hundred  $\mu\text{K}$  to  $30 \mu\text{K}$ , and the PSD increases by three orders of magnitude, from  $10^{-9}$  to  $10^{-6}$ . Before loading the atoms to the chip Z-wire magnetic trap (ZMT), we optically pump the atoms into the  $F=2$ ,  $M_F=2$  weak-field-seeking state to increase the loading efficiency. The  $100 \mu\text{s}$  pumping laser pulse, with a power of  $1 \text{ mW}$  and frequency of  $12.6 \text{ MHz}$  blue detuned from the transition  $F=2$  to  $F'=2$ , is accompanied by an x-bias field of  $-13 \text{ G}$ . During optical pumping, the repumping laser beam is on with its full power of  $6 \text{ mW}$ . As shown in figures 7.9 and 7.10, the optical pumping heats the atoms slightly. This heating is unavoidable in a real system where the laser circular polarization and magnetic field orientation are not ideal. The only goal of the optical pumping is to pump the atoms into the right single Zeeman state for the next atom-chip ZMT. With the help of optical pumping, the loading efficiency is improved by a factor of more than two, which is crucial to our portable system because we start with a minimal number of atoms from the mirror MOT.

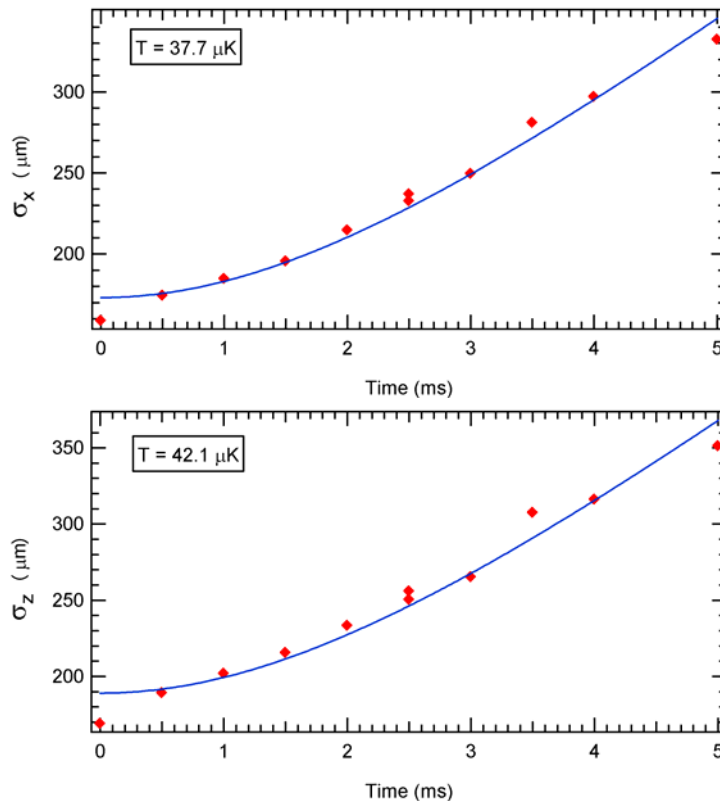


Figure 7.9: TOF measurement after optical pumping.

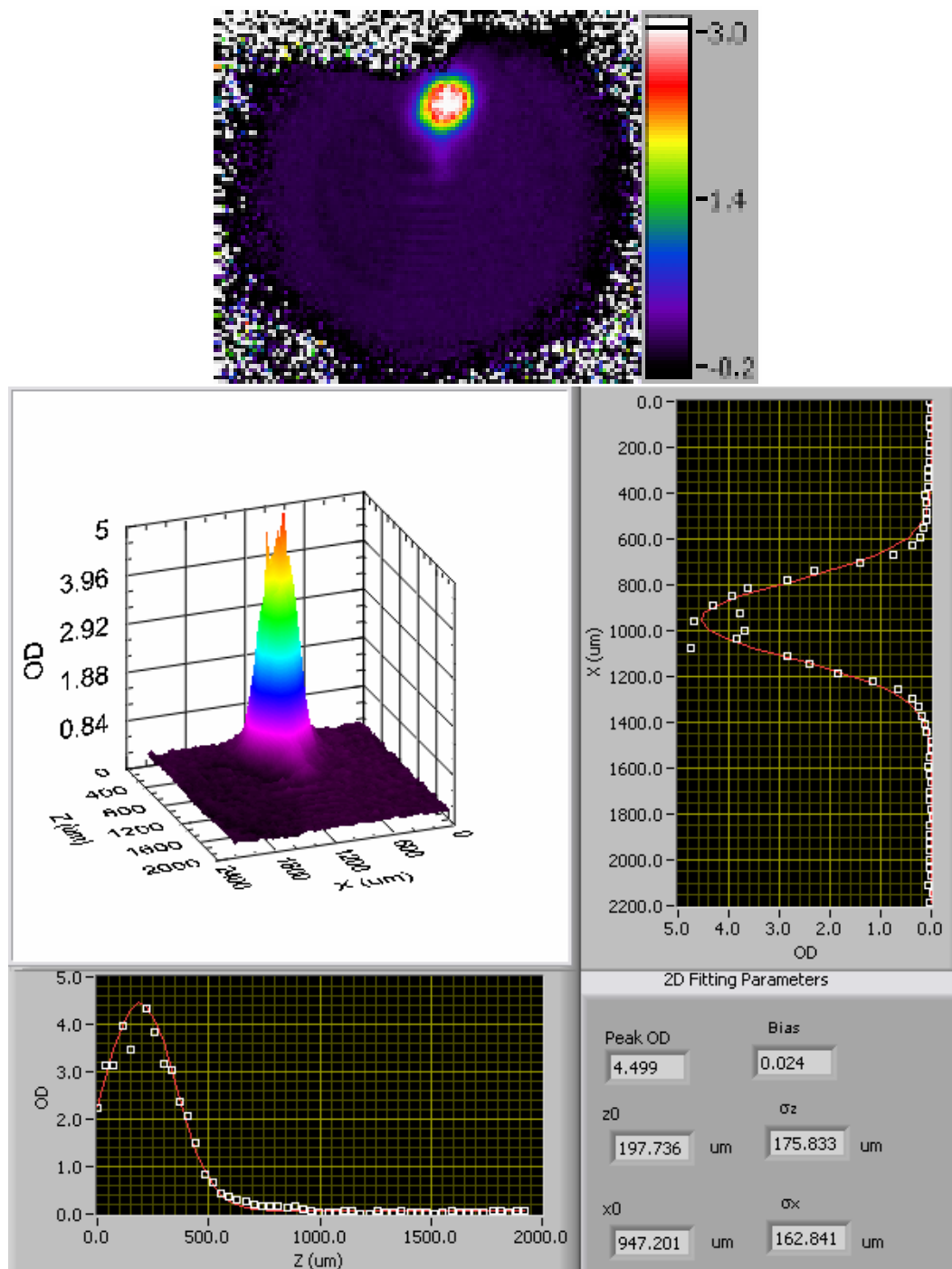


Figure 7.10: Absorption imaging after optical pumping.  $N = 6.1 \times 10^6$ , Peak OD = 4.5,  $\sigma_x = 163 \mu\text{m}$ ,  $\sigma_z = 176 \mu\text{m}$ ,  $T = 40 \mu\text{K}$ , average PSD =  $7.0 \times 10^{-7}$ , and Collision rate = 2.2 Hz.

## 7.7 Z-wire magnetic trap (ZMT)

After optical pumping, we turn on the chip Z-wire current and y-bias field to start transferring the atoms to an initial Z-wire magnetic trap (ZMT). The Z-wire current,  $I_z$ , ramps from 0 to 4 A within 0.3 ms. The y-bias field,  $B_y$ , ramps from 10 to 14 G within 10 ms. The 10 ms initial ZMT loading typically traps about  $2.5\text{--}3 \times 10^6$  atoms with a loading efficiency of more than 40%. At the end of 10 ms, we trap the atoms at a distance of 500  $\mu\text{m}$  below the chip surface, with trap frequencies of (36, 215, 215) Hz and a temperature of 100  $\mu\text{K}$ . Instead of turning on the ZMT immediately, our ramp loading schedule increases the effective trap loading volume by scanning the trap position back and forth to load as many atoms as possible. The PSD is about  $2 \times 10^{-7}$ , and the collision rate is about 5 Hz.

## 7.8 ZMT initial compression

Immediately after the ZMT initial loading, we start to compress the trap. At first, we keep the Z-wire current at 4 A and ramp the y-bias field from 14 to 60 G in 100 ms. At the same time, the x-bias field increases from 0 to -4 G to reduce the spin-flip loss at the trap bottom. At the end of this initial compression, the atoms are brought to 126  $\mu\text{m}$  below the chip surface, with trap frequencies of (30, 2500, 2500) Hz at the trap center. This initial 100 ms compression increases the trap depth and collision rate. The atoms, at this moment, mostly experience the linear trap slope rather than the harmonic trap bottom in the y-z plane. In the x axis, the second-order harmonic potential is not enough to describe the trap. The atom temperature in the compressed trap is about 400  $\mu\text{K}$ , measured by TOF images. The PSD is about  $2 \times 10^{-7}$ , and the collision rate is about 77 Hz.

## 7.9 ZMT compression and forced evaporative cooling

After the ZMT initial compression, we further compress the trap by reducing the Z-wire

current  $I_z$  from 4 to 2.75 A in 2 s and keeping the x, y-bias fields constant. The final trap position is 82  $\mu\text{m}$  away from the surface with trap frequencies of (23, 3600, 3600) Hz. The important goal of this compression is not only to increase the trap frequencies, but also reduce the Z-wire current to minimize heat dissipation. At the beginning of this compression, we also start the first RF sweep from 45 to 13 MHz for 2.46 s. It is then followed by a 1 s sweep from 13 to 5 MHz, a 500 ms sweep from 5 to 3.5 MHz, and a final 250 ms sweep from 3.5 to 2.85 MHz, as shown in figure 7.12. We must keep in mind that, during the compression and the first RF sweep, both surface-induced and RF-forced evaporation exist. The total RF evaporative cooling takes 4.21 s.

However, it is hard to observe evaporative cooling effect directly from the highly compressed ZMT. For example, after the first RF sweep, we have only  $0.5 \times 10^6$  atoms ( $T = 158 \mu\text{K}$ ) left and 1 ms TOF image has a peak OD of less than 0.1, which is below the background noise. To measure the cooling effect and the enhancement of PSD, we decompress the trap by ramping the y-bias field from 60 G to 36 G and the Z-wire current from 2.75 A to 4A in 100 ms before absorption imaging. The decompressed trap has frequencies of (35, 890, 890) Hz and a trap distance of 200  $\mu\text{m}$  from the chip surface. The adiabatic decompression improves the imaging quality dramatically by cooling the atoms to a lower temperature and moving the trap far away from the chip surface. On the other hand, the adiabatic decompression maintains the PSD. Therefore, all quantities reported in this thesis after the RF evaporation are measured after the decompression.

The four RF sweeps are optimized to maximize the peak OD at TOF imaging but not the PSD, because the OD is proportional to the collision rate [88]. The optimization of the RF sweeps is crucial to achieve run-away evaporation. If the collision rate drops all the way through the RF evaporation (i.e., there is no runaway evaporation), the PSD may not be able to reach the BEC transition before evaporating away all the atoms. In our atom-chip experiment, by carefully optimizing RF sweeps, we demonstrate that the runaway evaporation condition and BEC are reached with  $2.5\text{--}3.0 \times 10^6$  atoms at the initial ZMT. For the first logarithmic sweep, we fix the RF frequency from 45 MHz to  $\nu_1 = 13$  MHz and optimize the sweep time. During the

optimization of the first sweep, we measure the bottom RF frequency  $\nu_b$  to be about 2.9 MHz. After the first sweep of 2.46 s ( $t_1$ ), we extend the sweep with the same linear slope to the bottom frequency  $\nu_b$  to determine the next stop time  $t_2$ . Then we optimize the second logarithmic sweep from  $t_1$  to  $t_2$  with the stop RF frequency  $\nu_2$  where the peak OD at 5 ms TOF starts to drop. Then we fix the stop RF frequency  $\nu_2$  to optimize  $t_2$  for the final optimization of the second sweep. In a similar way, we optimize all RF sweeps until finally we observe a BEC phase transition at 2.85 MHz.

Figure 7.11 shows the peak OD and PSD as functions of the stop frequency  $\nu_3$  at the third RF sweep. The tuning point, 3.5 MHz, where the OD starts to drop, is the optimized stop frequency  $\nu_3$ . Table 7.1 gives the atom number  $N$ , temperature  $T$ , peak OD, collision rate  $\gamma$ , and PSD after each RF sweep and shows clearly the efficient cooling. The phase transition at the last RF sweep vs the final stop frequency is shown in figure 7.13(a).

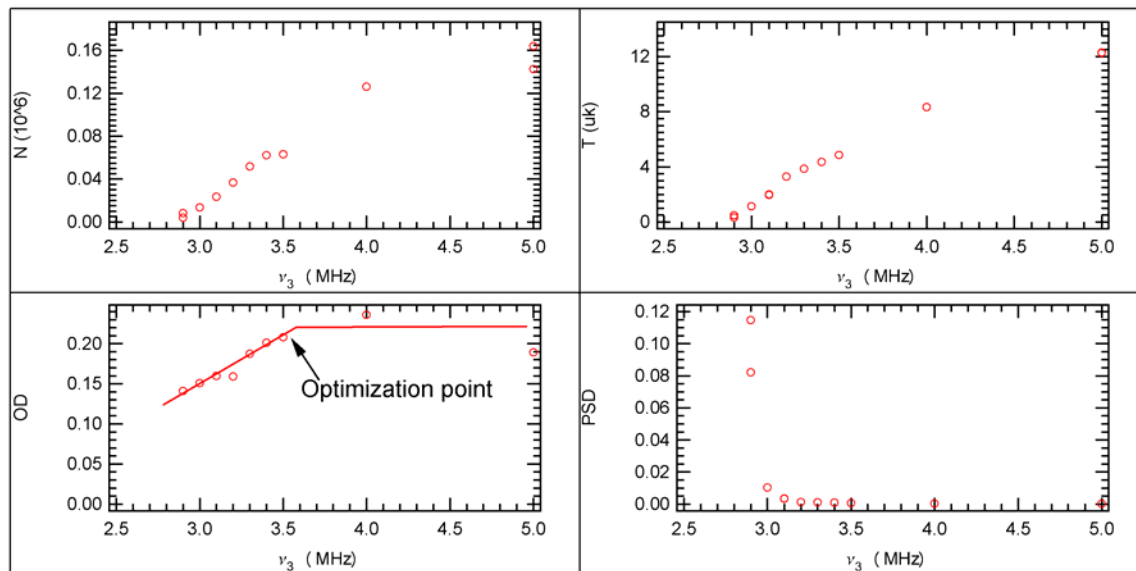


Figure 7.11: The atom number  $N$ , temperature  $T$ , peak OD, and average PSD as functions of the stop frequency  $\nu_3$  at the third RF sweep (TOF 5ms images).

Table 7.1: Atom number  $N$ , temperature  $T$ , peak OD, collision rate  $\gamma$ , and PSD after each RF sweep.  $T_1, \gamma_1$  are the temperature and collision rate before the imaging decompression; and  $T_2, \gamma_2$  measured after the decompression.

RF sweep (MHz)	Time (ms)	Atom number $N (10^3)$	Temperature $T_1 : T_2 (\mu\text{K})$	Collision rate $\gamma_1 : \gamma_2 (\text{Hz})$	PSD
45	2460	850	246 : 100	111 : 18	$1.0 \times 10^{-6}$
45→13	2460	500	158 : 64	102 : 17	$2.0 \times 10^{-6}$
13→5	1000	186	32 : 13	186 : 31	$9.0 \times 10^{-5}$
5→3.5	500	42	11 : 4.4	124 : 21	$5.3 \times 10^{-4}$
3.5→2.85	250	3	0.57 : 0.23	NA	>10

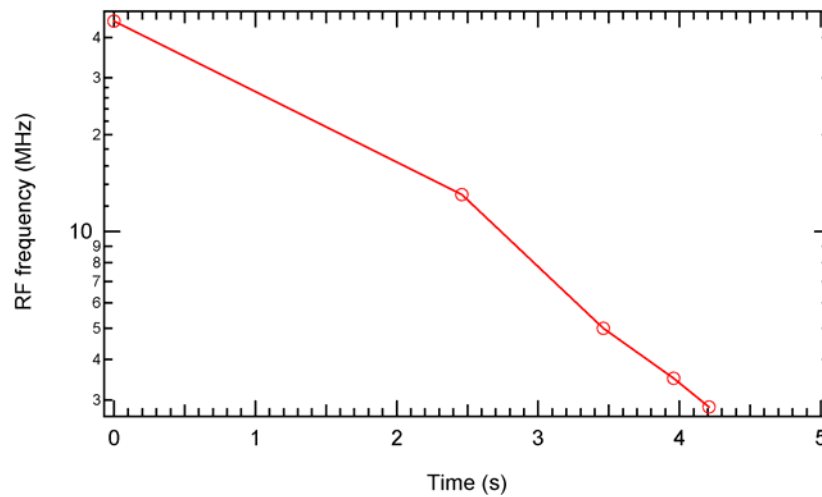


Figure 7.12: RF logarithmic sweeps for forced evaporative cooling.

## 7.10 BEC on the chip

At the end of the final sweep, we observe a Bose-Einstein condensate of  $2000 \text{ }^{87}\text{Rb}$  atoms at a transition temperature of about 300 nK [Figure 7.13(a)]. As shown in figure 7.13(b), the nonisotropic shape during a 9 ms TOF is a clear signature of a Bose-Einstein condensate. The BEC lifetime is about 300 ms, limited by the heating from technical noises and mechanical vibrations (will be discussed in section 8.6 of the next chapter).

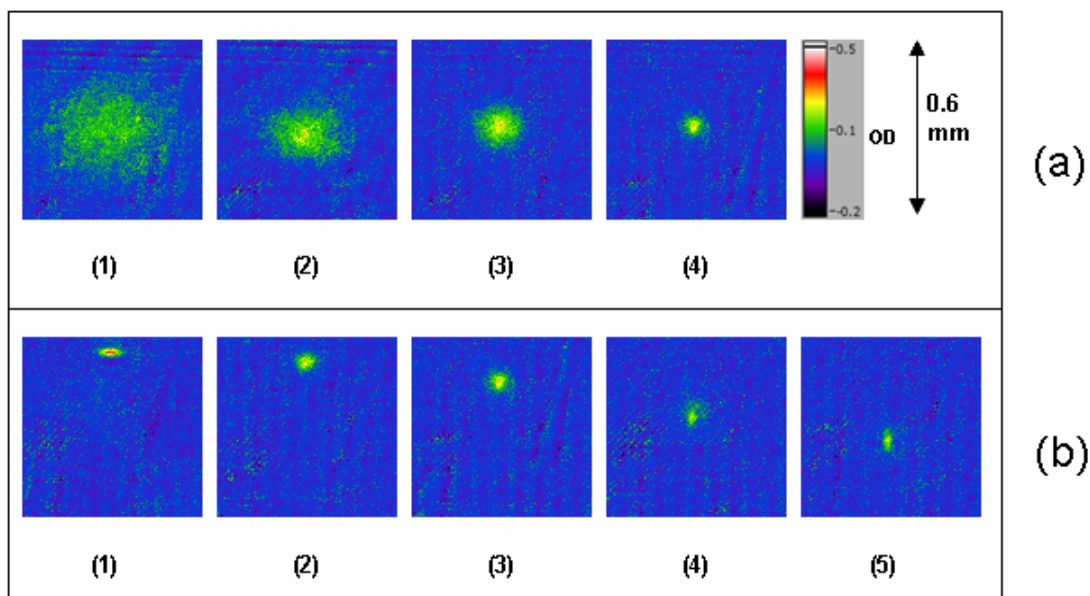


Figure 7.13: Images of a Bose-Einstein Condensation on the atom chip. (a) Absorption images are taken after a 5 ms TOF with different final RF frequencies. From left to right: (1)  $\nu = 3.5$  MHz,  $N = 42 \times 10^3$ ,  $T = 4.4 \mu\text{k}$ ,  $\langle\text{PSD}\rangle \approx 6 \times 10^{-4}$ ; (2)  $\nu = 3.0$  MHz,  $N = 20 \times 10^3$ ,  $T = 1.4 \mu\text{k}$ ,  $\langle\text{PSD}\rangle \approx 7 \times 10^{-3}$ ; (3)  $\nu = 2.9$  MHz,  $N = 10 \times 10^3$ ,  $T = 515$  nk,  $\langle\text{PSD}\rangle \approx 10^{-1}$ ; (4)  $\nu = 2.85$  MHz,  $N = 3 \times 10^3$ ,  $T = 230$  nk,  $\langle\text{PSD}\rangle \approx 10$ . (b) TOF images of BEC cloud after release with final RF frequency 2.85MHz. From left to right: TOF (1) 1 ms, (2) 3 ms, (3) 5 ms, (4) 7 ms, and (5) 9 ms. The nonisotropic shape during TOF is a key signature of BEC.

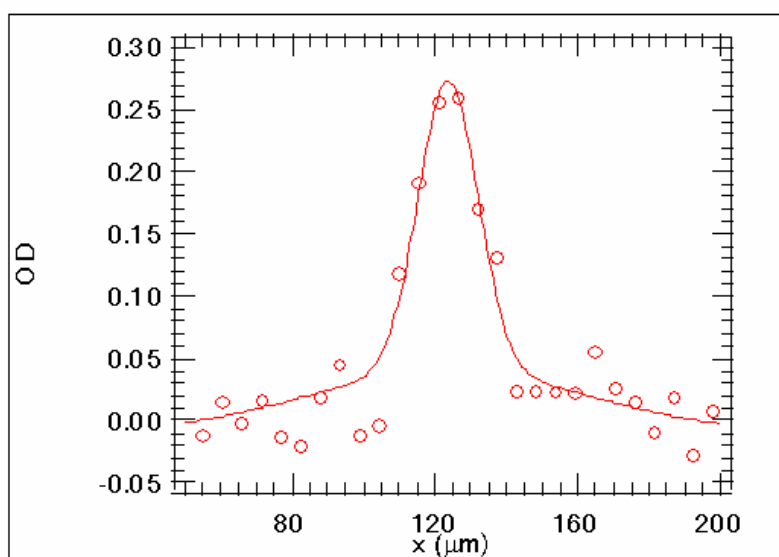


Figure 7.14: Longitudinal BEC atom cloud's optical depth profile, taken at TOF 9 ms, fitted to a double gaussian distribution.



## 7.11 Summary and conclusion

We have successfully demonstrated Bose-Einstein condensation in our compact and portable atom-chip vacuum cell. At the low-cost input side, we have a  $1 \times 1$  cm glass cell pumped by a small 8 L/s ion pump, total laser power of less than 40 mW, and low current power supplies ( $<7$  A). At the output side, we load  $6-8 \times 10^6$  atoms in the mirror MOT, transfer about 40 % of the atoms into the chip ZMT, and finally create  $2 \times 10^3$  atoms in a pure condensation. The total time of a cycle, including the 8 s UV mirror MOT loading and 4 s forced evaporative cooling, is only about 12 s.

## Chapter 8. Other atom-chip experiments

### 8.1 Atom splitting during polarization gradient cooling

Atom beam splitting is one of the important steps in realizing an atom interferometer. It plays a role much like that of optical beam splitting in photon-based interferometers. However, coherently splitting a Bose-Einstein condensate (BEC) or cold atom cloud is not as obvious as the optical beam splitting. So far, all coherent cold-atom splitting are only realized by optical methods, e.g., Raman transitions and Bragg diffractions [87, 89–91]. Here we report an observation of coherent atom splitting during polarization gradient cooling (PGC) below the atom-chip surface, induced by red-detuned optical standing waves.

As we described in section 7.5, the PGC time is optimized at 1.7 ms. Under the same cooling and repumping laser powers and frequencies, we observe that a cold atom cloud splits into three parts when we increase the PGC time up to 4 ms, as shown in figure 8.1. The different ratios, shown in figures 8.1(a), (b) and (c), are obtained by controlling the cooling laser power balancing in the horizontal direction. The result indicates that the splitting is induced by the Bragg diffraction effect of the optical standing wave.

The experiment also shows that it is possible to coherently split a cold atom cloud at a temperature higher than 20  $\mu\text{K}$  by using an optical standing wave. A BEC ultracold atom cloud is not a necessary condition for observing Bragg diffraction splitting. Our result also suggests that coherent atom-beam splitting can be achieved by a near-resonance ( $\Delta\nu = 50\text{--}70$  MHz) optical standing wave field.

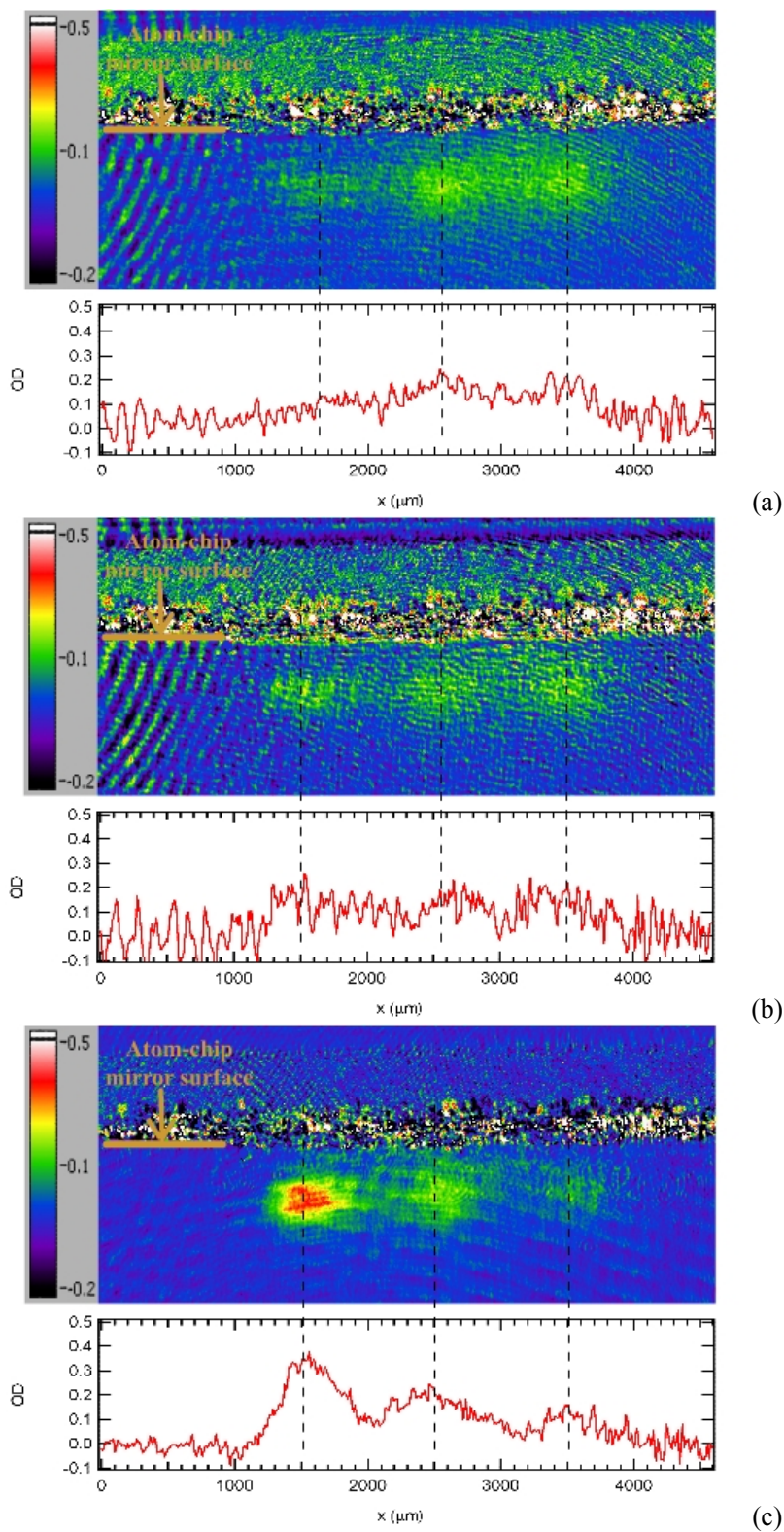


Figure 8.1: One atom cloud split into three after 4 ms polarization gradient cooling (PGC). Different ratios as shown in (a), (b), and (c) are obtained by adjusting the cooling laser power balancing in the horizontal direction.

## 8.2 Rethermalization in a Z-wire magnetic trap

In general, a Z-wire atom-chip micro magnetic trap is neither a three-dimensional (3D) harmonic trap nor a 3D linear trap because of its magnetic field pattern. The IP type trap approximation, i.e., 3D harmonic trap with axial rotation symmetry, is only valid for the atoms near the trap center, and thus only valid for very cold atoms. To the atoms far away from the trap center, they experience a linear trap slope on the transverse plane where the effective trap frequencies are position dependent. On the other hand, the atom number density varies a lot in such a trap. The difference of thermalization and collision rate, which are not uniform over the whole trap volume and may be up to several orders of magnitude. In this section, we report our observation of two different orders of rethermalization times in a single Z-wire trap.

In chapter 7, we described the compression procedure. In the experiment for measuring the rethermalization times, the final trap has a Z-wire current  $I_z = 4$  A, y-bias field  $B_{y0} = 50$  G, and compression time of 100 ms. The trap is  $150 \mu\text{m}$  away from the chip surface where the atoms are free from surface-induced evaporation (section 8.3). Because of the mode-mismatching and low trap frequencies at the initial loading, the atoms distribute over a large volume. Thus, during the 100 ms compression, atoms far away from the trap center experience a longer rethermalization time than the atoms at the trap center. The long rethermalization time is measured at more than 100 ms and depends on the loading procedure. The fast rethermalization time is about 12 ms and corresponds to most of the atoms being at the trap center.

As shown in figure 8.2(a), when the initial loading is not optimized, i.e., more atoms are initially far away from the trap center, it takes about 1 s ( $1/e$  time constant is 500 ms) to rethermalize the whole cloud after compression. Figure 8.2(b) shows the aspect ratio as a function of time for different loading procedures. The optimized loading, which is used to achieve BEC on the atom chip, has the fastest rethermalization (150 ms).

To measure the fast rethermalization near the trap center, we perturb the atom cloud along the transverse direction by ramping the  $I_z$  from 4 to 2A and back to 4 A quickly. Each ramp takes

10 ms. The axial size of a 1 ms TOF,  $\sigma_x$ , after the 20 ms perturbation is shown in figure 8.3. The rethermalization time constant is about 2–10 ms. We also observe a 70 Hz oscillation of  $\sigma_x$  excited by the perturbation. This oscillation frequency is consistent with the axial trap frequency of 35 Hz.

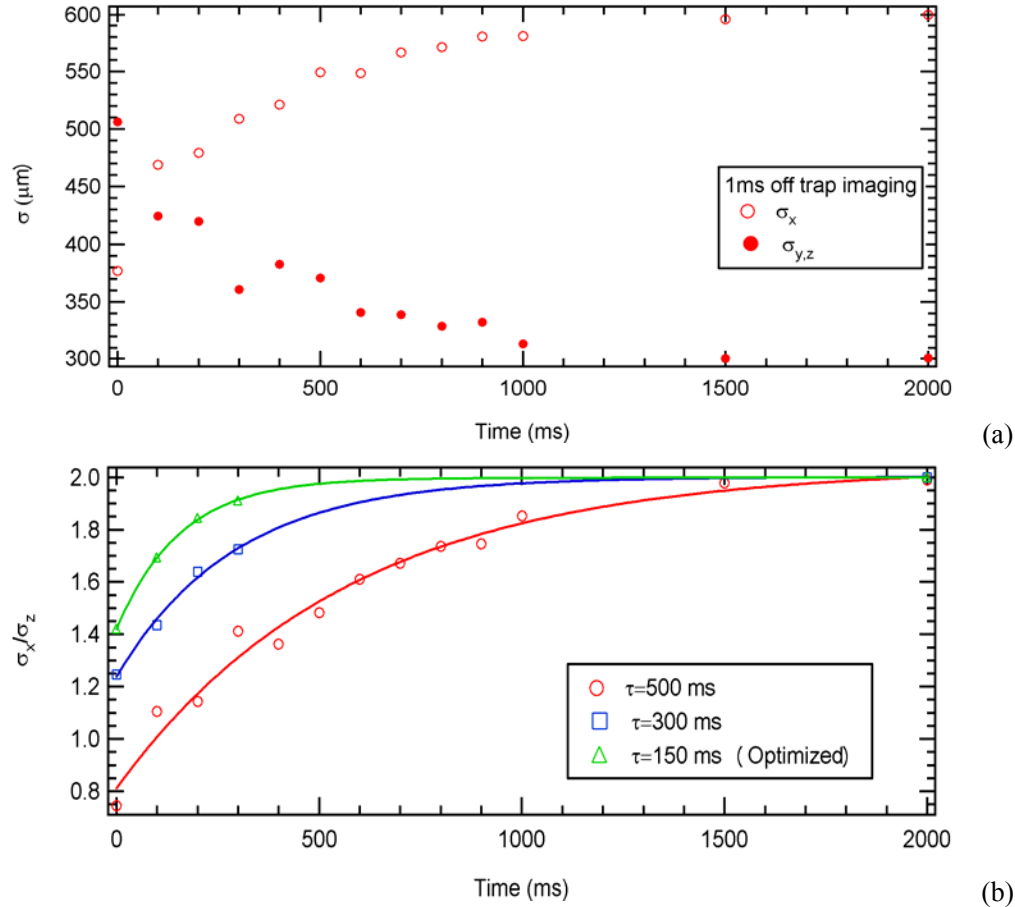


Figure 8.2: The long rethermalization of atoms in the Z-wire trap. (a) The atom cloud size vs time when the loading is not optimized. (b) the aspect ratio of atom cloud size vs time with different loading procedures. The size of cloud is measured after a 1 ms time of flight (TOF). The Z-wire current is 4 A, y bias field is 50 G, and the compression time is 100 ms.

In summary, we observe two different orders of rethermalization time in a compressed Z-wire micro magnetic trap. The longer thermalization time ( $>100$  ms) is contributed by atoms initially loaded off center of the trap. We optimize the initial loading and compression time to maximize the cloud aspect ratio and reduce this long rethermalization time. On the other hand, we use a transverse perturbation to detect the rethermalization time along the axial direction. The

atom cloud's axial size changes with time, giving not only the trap center rethermalization time of 2–10 ms, but also the axial trap frequency of 35 Hz.

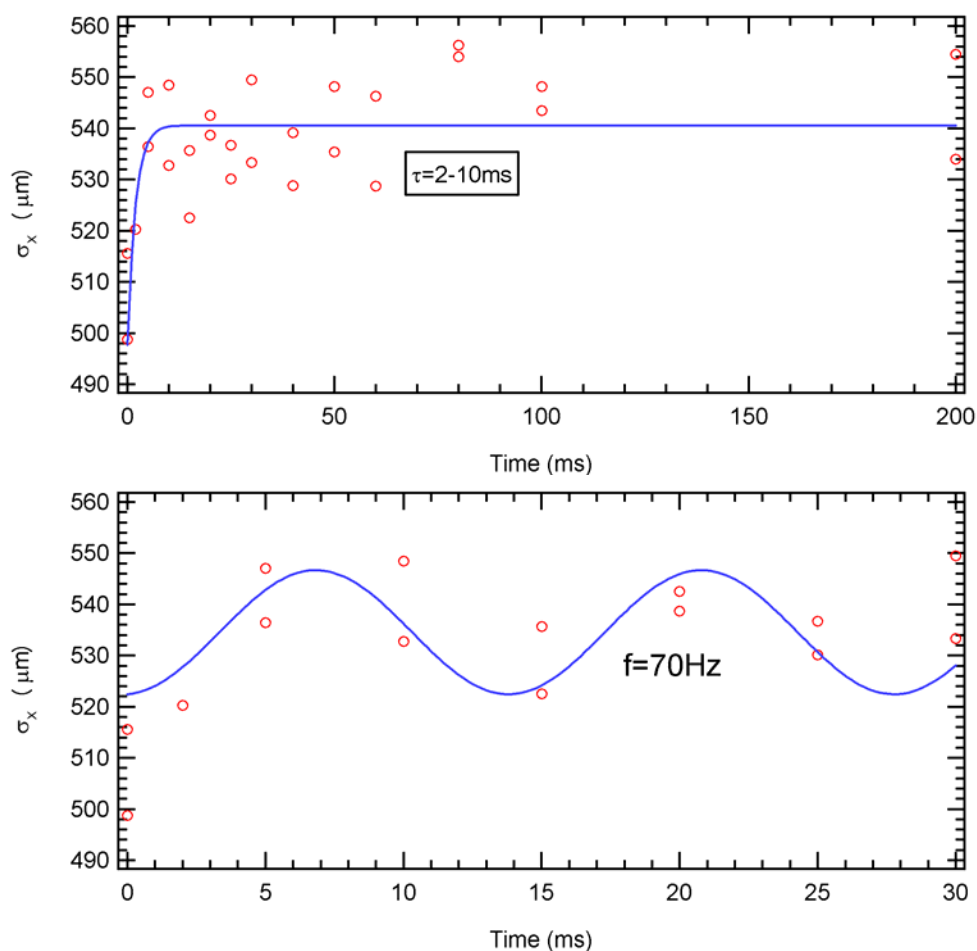


Figure 8.3: The fast rethermalization of atoms in the Z-wire trap. The size of the cloud is measured after 1 ms TOF. The Z-wire current is 4 A, y-bias field is 50 G, and the compression time is 100 ms.

### 8.3 Surface-induced evaporative cooling

In chapter 2 (section 2.6.2), we discussed theoretically the surface-induced evaporative-cooling mechanism. In this section, we report results from our one-step surface-induced evaporation, which provides some insight into the cooling efficiency of silver-mirror surface-induced evaporative cooling.

The Z-wire magnetic trap loading is the same as the procedure described in chapter 7. At the end of a 100 ms compression, the final Z-wire current is 2 A, and the bias field is (-4, 50, 0) G. The trap distance from the silver mirror surface is 70  $\mu\text{m}$ . After holding the atoms there for an amount of time, we ramp the Z-wire current from 2 A to 4 A in 100 ms for absorption imaging (1 ms TOF). The atom number and axial size after a 1 ms TOF expansion as functions of the holding time are shown in figure 8.4. Because the cloud size is proportional to its temperature, the decrease of the axial size with the holding time indicates a surface-induced cooling effect, as shown in figure 8.4(b).

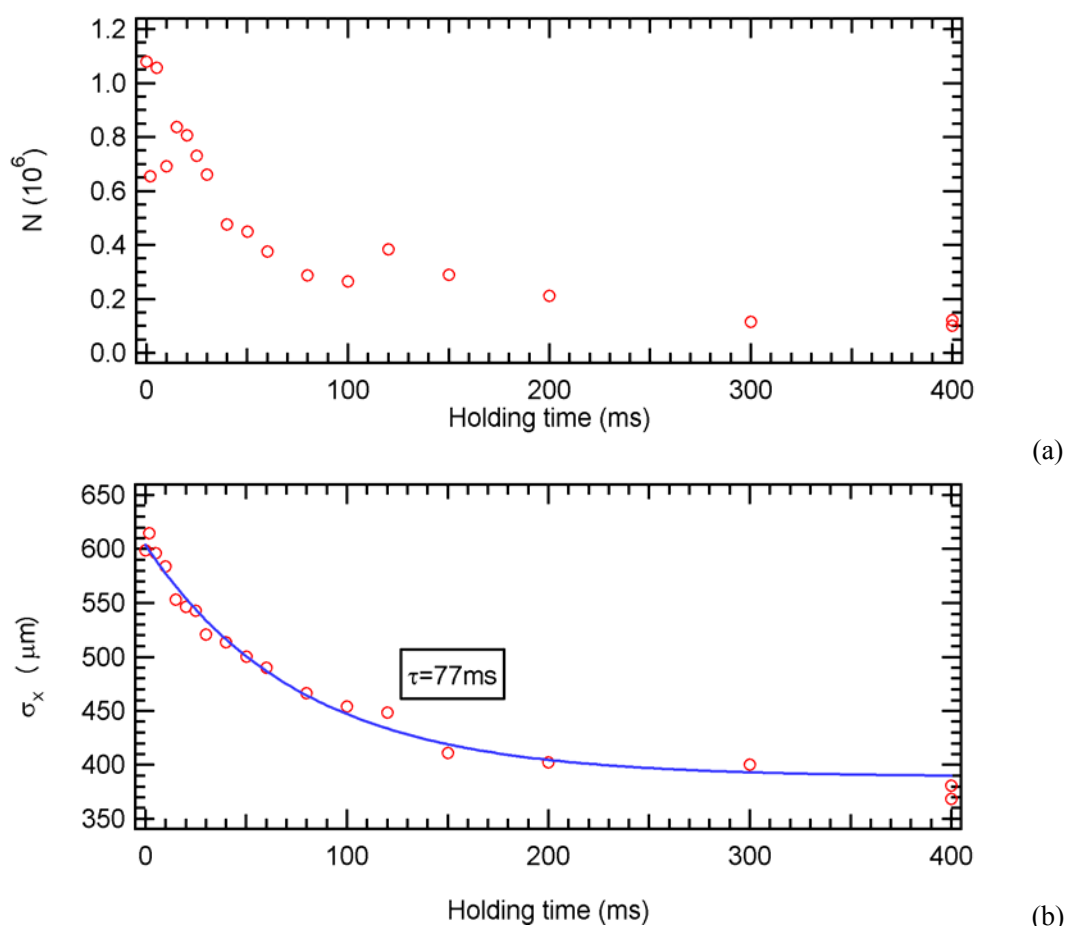


Figure 8.4: Surface-induced evaporative cooling. (a) Atom number  $N$  vs holding time on the chip mirror surface. (b) Atom cloud axial size after a 1 ms TOF,  $\sigma_x$ , vs holding time.

A further forced evaporative cooling can be achieved by moving the trap close to the surface continuously while keeping the trap frequencies constant, as described in section 2.6.2.

However, because of the limitation of the two-dimensional plane surface, the cooling efficiency of the surface-induced evaporation is much lower than the traditional RF evaporation that removes hot atoms from a curved surface. Therefore, a successful forced surface-induced evaporative cooling toward BEC production requires either a very long magnetic trap lifetime [92] or RF pre-evaporative cooling [55]. Instead of using only one forced-evaporative cooling method, we implement the surface-induced evaporative cooling into our RF-forced evaporation toward production of BEC on a chip. As described in section 7.9, during the first RF sweep, the atom cloud is compressed and brought closer and closer to the mirror surface such that both the RF- and surface-induced evaporative cooling are utilized simultaneously.

## 8.4 Sloshing in the Z-wire magnetic trap

It is important to detect the magnetic trap parameters experimentally. For example, we have calibrated the magnetic fields produced by the bias coils with a Gaussmeter probing outside of the cell. However, ascertaining the exact field inside the cell is still a challenge. Measuring the trap frequencies and other parameters can help to reveal errors in calibration. The experimental results can also help us to see if we are working in the right physics regime and to understand the atomic physics more deeply.

We use two different measurements to determine the Z-wire nonisotropic trap frequencies. The sloshing method described in this section is used to measure the x-direction axial slow frequency, which is typically below 100 Hz.

To introduce a sloshing mode to the Z-wire magnetic trap, we shift the chip U-wire CMOT along the x direction before loading the atoms to the Z-wire trap. The final Z-wire trap has trap frequencies of (37, 215, 215) Hz with a 4 A Z-wire current and (0, 14, 0) G bias field, located 500  $\mu\text{m}$  away from the chip surface. We observe a decay oscillation of the center of mass along the axial direction, as shown in figure 8.5. The experimental data is fitted to the following curve

$$x_{cm}(t) = a \sin(2\pi ft + \phi_0) \exp(-t/\tau) + b, \quad (8.1)$$



where the fitted parameters are  $a = 105 \mu\text{m}$ ,  $f = 40 \text{ Hz}$ ,  $\phi_0 = 0.1$ ,  $\tau = 47 \text{ ms}$ , and  $b = 0.05 \mu\text{m}$ . The 40 Hz sloshing frequency is consistent with the theoretically calculated 37 Hz axial trap frequency. The oscillation amplitude's exponential decay time constant of 47 ms is the same order of magnitude as the trap rethermalization time.

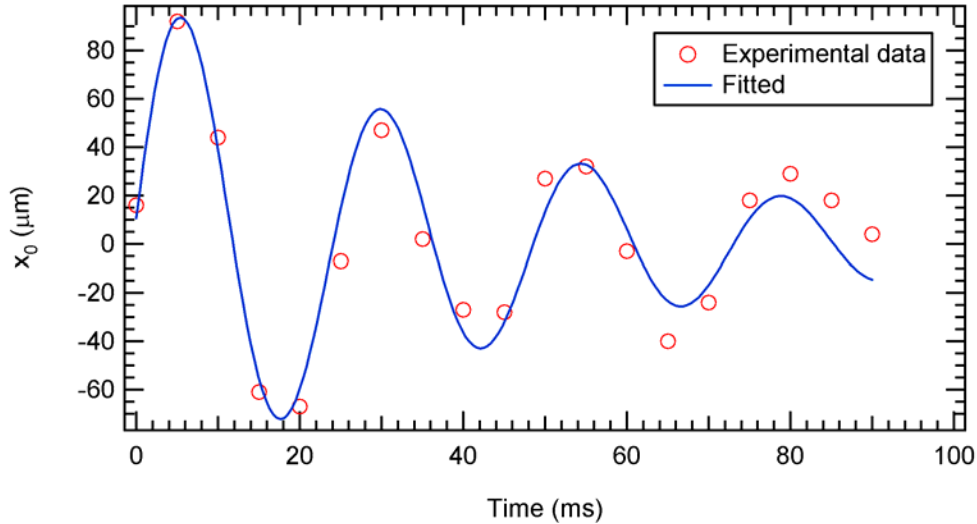


Figure 8.5: Axial sloshing fitted to an exponential decay oscillation. The oscillation frequency is 40 Hz, and the exponential decay time constant is 47 ms.

Thus, we can use the sloshing excitation along the trap's axial direction not only to obtain the axial slow trap frequency precisely, but also to get the trap rethermalization information. The rethermalization of the Z-wire trap, or the damping of the sloshing, provides an experimental way to study collision and scattering physics in a nonisotropic trap with a large aspect ratio. Meanwhile, we also take the sloshing measurement to optimize the trap loading procedure by minimizing the sloshing amplitude introduced by mode mismatching.

To detect the higher transverse trap frequency requires not only a second camera imaging system along the axial direction, but also a shorter imaging time resolution. Moreover, the complex magnetic field pattern in the transverse plane, mixing with the harmonic trap bottom and linear slope, makes it more difficult to observe a transverse sloshing mode. We use parametric heating, described in next section, to measure the transverse trap frequency of more than 100 Hz.

## 8.5 Parametric heating in a tightly confined magnetic trap

Parametric excitations have been widely used to study cold atoms in both optical and magnetic traps [93–96]. When harmonic trap parameters, such as trap frequencies, trap depth, or trap center position, are periodically modulated by external fields, the excitation spectrum shows narrow peaks at the modulation frequency  $f = f_0$  and  $2f_0$ , where  $f_0$  is the trap frequency [97]. In our atom-chip experiment, we measure the heating induced by parametric excitations to detect the Z-wire magnetic trap transverse frequency.

We study parametric heating with an ultracold atom cloud just above the BEC transition temperature in a Z-wire magnetic trap with trap frequencies of (10, 830, 830) Hz. The Z-wire trap, generated by a 0.68 A Z-wire current and a (-6.4, 15.74, 0) G bias field, locates at 76  $\mu\text{m}$  below the atom-chip surface. To modulate the trap parameters, we add a single frequency sine-wave modulation to the Z-wire current

$$I_z(t) = I_{z0} + \Delta I \sin(2\pi ft + \phi_0) , \quad (8.2)$$

where  $I_{z0}$  is the 0.68 A Z-wire trap current,  $\Delta I$  is the current modulation amplitude, and  $f$  is the modulation frequency. The hardware block diagram for controlling the modulation is shown in figure 8.6, where a transistor-transistor logical (TTL) switch is used to turn the modulation on and off.

Figure 8.7 shows the parametric heating results with  $\Delta I = 10$  mA and a total of 90 ms modulation time window. There are two narrow peaks at  $f = 0.85$  and 1.7 kHz in the parametric heating spectrum. Thus, the measured transverse frequency is  $f_{0\text{exp}} = 850$  Hz, which is consistent with the theoretically calculated value of  $f_{0\text{the}} = 830$  Hz. The heating rate of the two peaks is about 15  $\mu\text{K/s}$ , and no observable heating is detected among other frequencies.

In conclusion, we have measured the Z-wire trap transverse frequency using a parametric heating method and observed two narrow parametric heating peaks at  $f = f_0$  and  $2f_0$ . The parametric heating is also an experimental tool to study the heating from current noise and other technical noises. By changing the trap frequencies to reduce the parametric heating from noises

and mechanical vibrations, we increase our atom-chip BEC lifetime from 100 ms to 300 ms, as reported in detail in the next section.

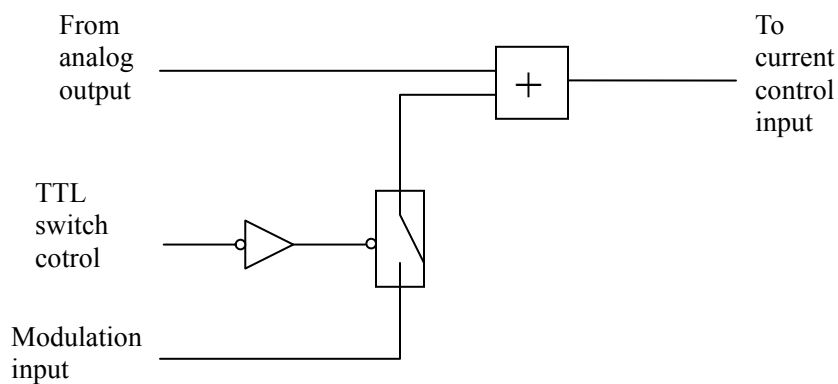


Figure 8.6: Z-wire current modulation block diagram for parametric heating experiment.

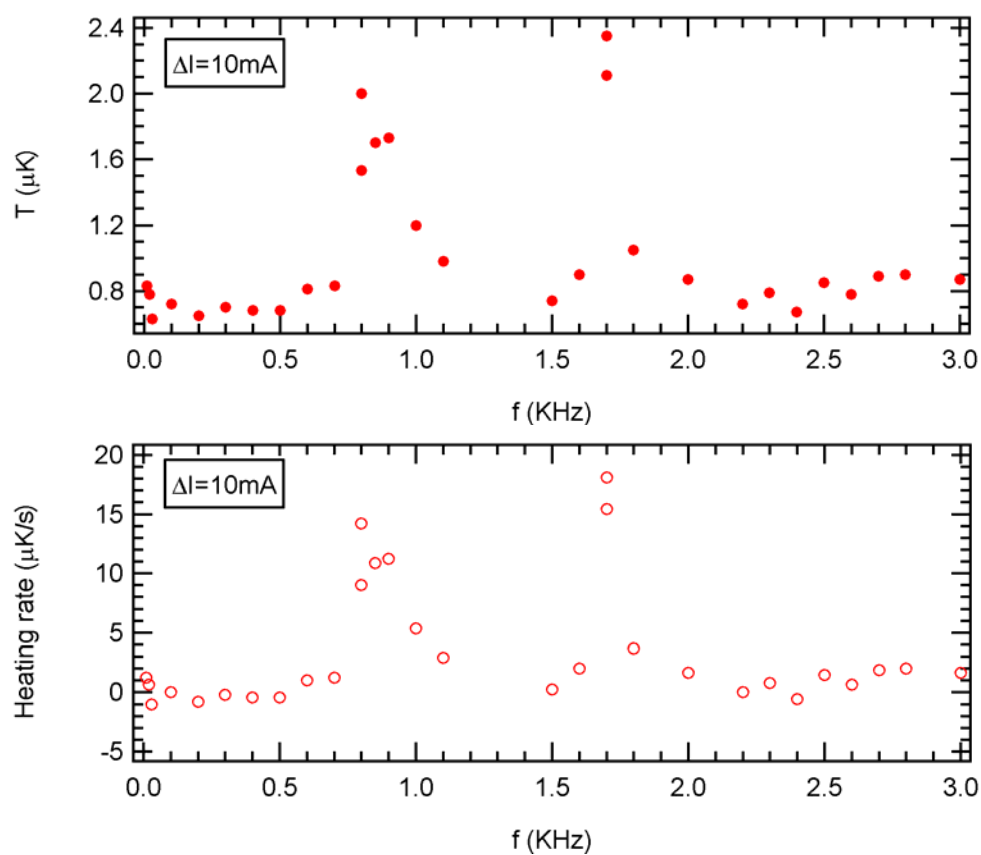


Figure 8.7: Parametric heating effect of the Z-wire magnetic trap with a 90 ms current modulation on the Z-wire. (a) Final temperature  $T$  and (b) heating rate vs modulation frequency  $f$ .

## 8.6 Atom-chip BEC lifetime

A BEC in a magnetic trap has a finite lifetime because of the loss of phase-space density (PSD) caused by the atom number loss and trap heating from background collisions, three-body recombination, atom-chip surface effects, and technical noises. Our atom-chip BEC has a lifetime of 100–300 ms, which is much shorter than the 3–5 s magnetic trap lifetime. Within the BEC lifetime, we observe no atom number loss; thus the loss of PSD is only caused by trap heating. This observation suggests that the atoms are far away from the three-body recombination region which induces both trap loss and heating [98]. On the other hand, our BEC trap distance from the chip surface ranges from 70 to 200  $\mu\text{m}$ , and is free from surface effects [54, 86]. Our measured trap frequency dependant heating rate indicates that the heating problem arise from some kind of technical noises.

We study the heating in both a tightly compressed trap and a decompressed trap after the RF evaporation. In the first experiment, we hold the BEC cloud in the compressed trap and measure the temperature as a function of the holding time. The compressed trap has trap frequencies of (23, 3600, 3600) Hz, and is 82  $\mu\text{m}$  away from the surface, generated by a Z-wire current of 2.75 A and a bias field of (-4, 60, 0) G, as described in detail in section 7.9. In the second experiment, we decompress the trap by ramping down the Z-wire current from 2.75 to 0.68 A and the bias field from (-4, 60, 0) to (-6.4, 15.7, 0) G rapidly after the RF evaporation. The decompressed trap has trap frequencies of (10, 830, 830) Hz and is 76  $\mu\text{m}$  away from the chip surface. To compare the heating effects, we adiabatically ramp the compressed trap to the decompressed trap for TOF absorption imaging and temperature measurement in the first experiment. The results are shown in figure 8.8, where we observe no atom number losses within 1 s in both traps, which exhibit different heating rates. The tightly compressed trap has a heating rate of more than 3  $\mu\text{K/s}$ , and the decompressed trap has a heating rate of 0.5  $\mu\text{K/s}$ .

The trap frequency-dependent heating rates lead to 100 and 300 ms BEC lifetimes, respectively. Figure 8.9 shows the PSD as a function of holding time in the decompressed trap.

After 300 ms, the PSD drops below 1 [figure 8.9(a)], and after a 9 ms TOF, the cloud becomes isotropic [figure 8.9(b)].

Considering this observation and the results from section 8.5, we suspect that the BEC lifetime is limited by parametric heating from magnetic field fluctuations and mechanical vibration. There are two types of sources of magnetic field noises: current noises of the bias coils and atom-chip wires and background RF radiation. Battery-powered current power supplies may provide a good solution to suppressing 60 Hz noise in the KEPCO AC-powered supplies. Meanwhile, inserting notch filters at the trap's single and double frequencies to the current output channels can effectively reduce the on-resonance and second-order parametric heating. It is most likely that the chip itself acts as an antenna in receiving RF noise from the background. This problem does not exist in a traditional atom-chip system where the chip is installed inside of a big stainless steel chamber that shields background RF radiation. We are not sure how seriously this RF pick-up affects the atom-chip experiments. The mechanical vibrations can be suppressed by carefully mounting and insulating the cell vacuum from the table.

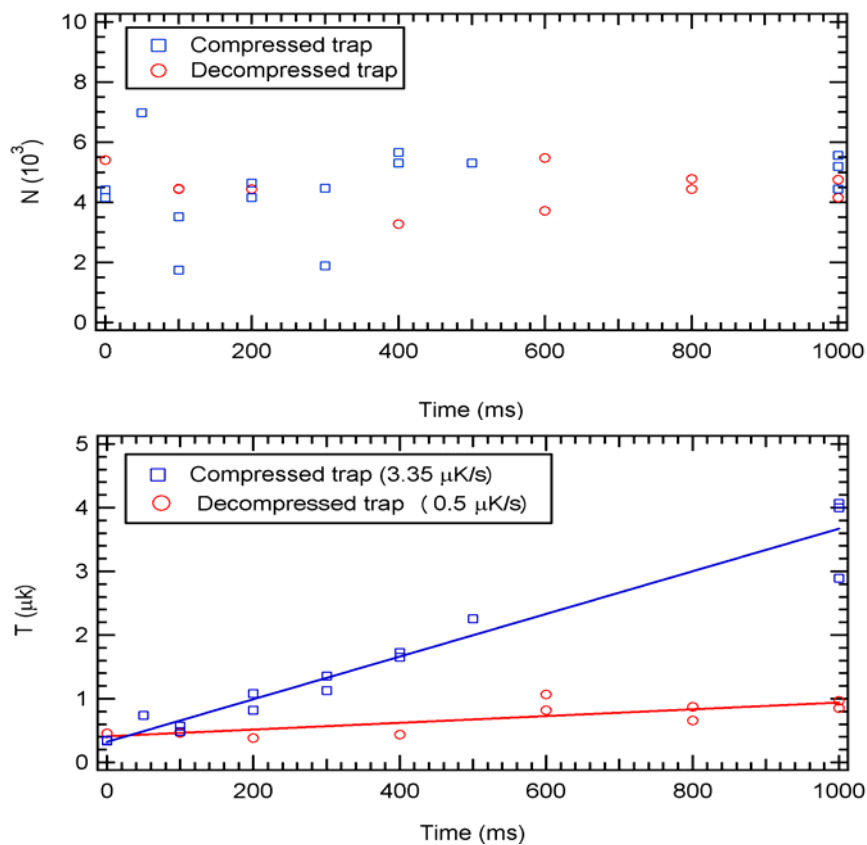


Figure 8.8: BEC heating measurement in the compressed and decompressed traps.

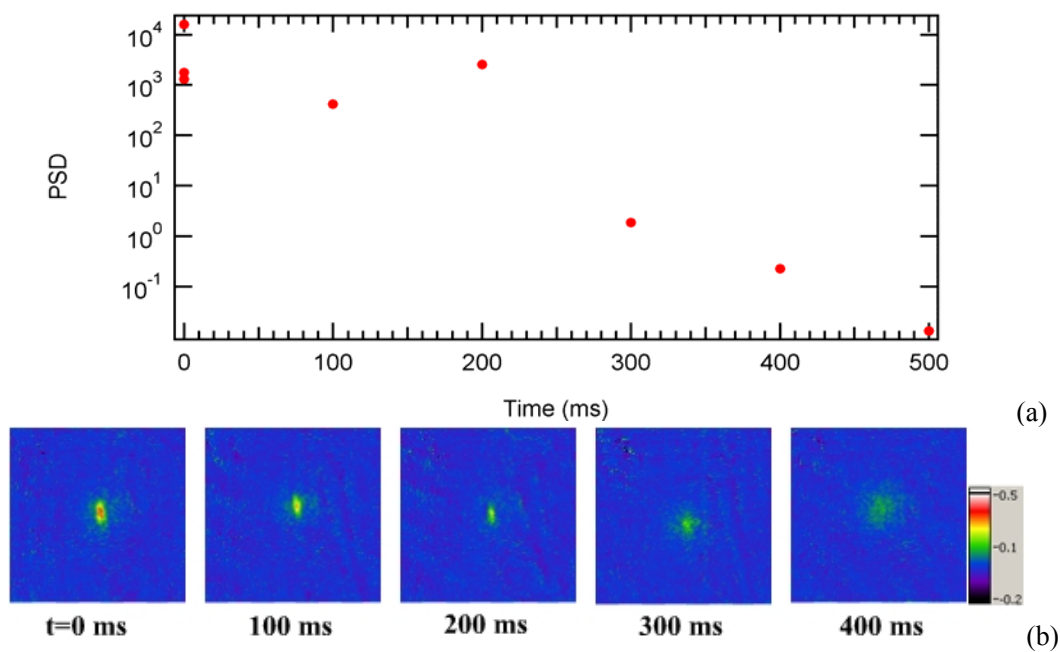


Figure 8.9: Atom-chip BEC lifetime. (a) Phase-space density PSD vs time. (b) 9 ms TOF absorption images with different holding times in the trap.

## Bibliography

- [1] A. Einstein, “Strahlungs-Emission und-Absorption nach der Quantentheorie,” *Deutsche Physikalische Gesellschaft*, **18**, 318 (1916).
- [2] A. Einstein, “Quantentheorie des einatomigen idealen Gases,” *Sitzungsber. Kgl. Preuss. Akad. Wiss.* 261 (1924).
- [3] M. H. Anderson, J. R. Ensher, M. R. Matthews, C. E. Wieman, and E. A. Cornell, “Bose-Einstein Condensation in a Dilute Atomic Vapor,” *Science* **269**, 198 (1995).
- [4] K. B. Davis, M.-O. Mewes, M. R. Andrews, N. J. van Druten, D. S. Durfee, D. M. Kurn, and W. Ketterle, “Bose-Einstein Condensation in a Gas of Sodium Atoms,” *Phys. Rev. Lett.* **75**, 3969 (1995).
- [5] D. Müller, D. Z. Anderson, R. J. Grow, P. D. D. Schwindt, and E. A. Cornell, “Guiding Neutral Atoms Around Curves with Lithographically Patterned Current-Carrying Wires,” *Phys. Rev. Lett.* **83**, 5194 (1999).
- [6] J. Reichel, W. Hänsel, and T. W. Hänsch, “Atomic Micromanipulation with Magnetic Surface Traps,” *Phys. Rev. Lett.* **83**, 3398 (1999).
- [7] N. H. Dekker, C. S. Lee, V. Lorent, J. H. Thywissen, S. P. Smith, M. Drndi, R. M. Westervelt, and M. Prentiss, “Guiding Neutral Atoms on a Chip,” *Phys. Rev. Lett.* **84**, 1124 (2000).
- [8] D. Mueller, E. A. Cornell, M. Prevedelli, P. D. D. Schwindt, A. Zozulya and D. Z. Anderson, “Waveguide Atom Beam Splitter for Laser-cooled Neutral Atoms,” *Opt. Lett.* **25**, 1382 (2000).
- [9] D. Cassettari, B. Hessmo, R. Folman, T. Maier, and J. Schmiedmayer, “Beam Splitter for Guided Atoms,” *Phys. Rev. Lett.* **85**, 5483 (2000).
- [10] R. Folman, P. Krüger, D. Cassettari, B. Hessmo, T. Maier, and J. Schmiedmayer, “Controlling Cold Atoms Using Nanofabricated Surfaces: Atom Chips,” *Phys. Rev. Lett.* **84**, 4749 (2000).
- [11] D. Mueller, E. A. Cornell, M. Prevedelli, P. D. D. Schwindt, Y.J. Wang and D. Z. Anderson, “Magnetic Switch for Integrated Atom Optics,” *Phys. Rev. A* **63**, 041602(R) (2001).
- [12] R. Folman, P. Kruger and J. Schmiedmayer, J. Denschlag, C. Henkel, “Microscopic Atom Optics: From Wires to an Atom chip,” *Advances in Atomic, Molecular, and Optical Physics*, **48**, 263 (2002).
- [13] J. Schmiedmayer, “Guided Matter Waves, an Atom and a Current,” *IQEC'92* (1992).
- [14] W. Hänsel, P. Hommelhoff, T. W. Hänsch, and J. Reichel, “Bose-Einstein Condensation on a Microelectronic Chip,” *Nature* **413**, 498 (2001).

- [15] H. Ott, J. Fortagh, G. Schlotterbeck, A. Grossmann, and C. Zimmermann, "Bose-Einstein Condensation in a Surface Microtrap," *Phys. Rev. Lett.* **87**, 230401 (2001).
- [16] S. Du, M. B. Squires, Y. Imai, L. Czaia, R. A. Saravanan, V. Bright, J. Reichel, T. W. Hänsch, and D. Z. Anderson, "Atom-chip Bose-Einstein Condensation in a Portable Vacuum Cell," *Phys. Rev. A* **70**, 053606 (2004).
- [17] W. D. Phillips, "Laser Cooling and Trapped Atoms," *Prog. Quant. Elect.* **8**, 115 (1984).
- [18] S. Chu and C. Wieman, "Laser Cooling and Trapping of Atoms," *J. Opt. Soc. Am. B* **2**, 1705 (1989).
- [19] H. J. Metcalf and P. van der Straten, "Laser Cooling and Trapping," Springer, New York (1999).
- [20] C. J. Pethick and H. Smith, "Bose-Einstein Condensation in Dilute Gases," Cambridge University Press (2002).
- [21] C. Cohen-Tannoudji, B. Diu, and F. Laloe, "Quantum Mechanics," Wiley. New York (1977).
- [22] J. T. Verdeyen, "Laser Electronics," Prentice Hall, New Jersey (1995).
- [23] M. O. Scully and M. S. Zubairy, "Quantum Optics," p207, Cambridge University Press, Cambridge (1997).
- [24] L. Allen and J. H. Eberly, "Optical Resonance and Two-Level Atoms," Wiley, New York (1975).
- [25] M. L. Citron, H. R. Gray, C. W. Gabel, and C. R. Stroud, Jr., "Experimental Study of Power Broadening in a Two-level Atom," *Phys. Rev. A* **16**, 1507 (1977).
- [26] S. Chu, J. E. Bjorkholm, A. Ashkin, and A. Cable, "Experimental Observation of Optically Trapped Atoms," *Phys. Rev. Lett.* **57**, 314 (1986).
- [27] C. S. Adams, H. J. Lee, N. Davidson, M. Kasevich, and S. Chu, "Evaporative Cooling in a Crossed Dipole Trap," *Phys. Rev. Lett.* **74**, 3577 (1995).
- [28] M. D. Barrett, J. A. Sauer, and M. S. Chapman, "All-Optical Formation of an Atomic Bose-Einstein Condensate," *Phys. Rev. Lett.* **87**, 010404 (2001).
- [29] E. Raab, M. Prentiss, A. Cable, S. Chu, and D. Pritchard, "Trapping of Neutral Sodium Atoms with Radiation Pressure," *Phys. Rev. Lett.*, **59**, 2631(1987).
- [30] S. Chu, L. Hollberg, J. Bjorkholm, A. Cable, and A. Ashkin, "Three-dimensional Viscous Confinement and Cooling of Atoms by Resonance Radiation Pressure," *Phys. Rev. Lett.* **55**, 48 (1985).
- [31] J. Dalibard and W. Phillips, "Stability and Damping Force of Radiation Pressure Traps," *Bull. Am. Phys. Soc.* **30**, 748 (1985).



- [32] J. Reichel, W. Hänsel, P. Hommelhoff and T. W. Hänsch, “Applications of Integrated Magnetic Microtraps,” *Appl. Phys. B* **72**, 81, (2000).
- [33] K. E. Gibble, S. Kasapi, and S. Chu, “Improved Magneto-optic Trapping in a Vapor Cell,” *Opt. Lett.* **17**, 526 (1992).
- [34] C. Monroe, W. Swann, H. Robinson, and C. Wieman, “Very cold trapped atoms in a vapor cell,” *Phys. Rev. Lett.* **65**, 1571 (1990).
- [35] J. R. Ensher, “The First Experiments with Bose-Einstein Condensation of  $^{87}\text{Rb}$ ,” PhD thesis, JILA (1998).
- [36] M. Stephens and C. Weiman, “High Collection Efficiency in a Laser Trap,” *Phys. Rev. Lett.* **72**, 3787 (1994).
- [37] J. Dalibard and C. Cohen-Tannoudji, “Laser Cooling below Doppler Limit by Polarization Gradients – Simple Theoretical Models,” *J. Opt. Soc. Am. B* **6**, 2023 (1989).
- [38] A. L. Migdall, J. V. Prodan, and W. D. Phillips, “First Observation of Magnetically Trapped Neutral Atoms,” *Phys. Rev. Lett.* **54**, 2596 (1985).
- [39] W.H. Wing, "On Neutral Particle Trapping in Quasistatic Electromagnetic Fields," *Prog. Quant. Electr.* **8**, 181 (1984).
- [40] D.E. Pritchard, “Cooling Neutral Atoms in a Magnetic Trap for Precision Spectroscopy,” *Phys. Rev. Lett.* **51**, 1336 (1983).
- [41] V. S. Bagnato, G. P. Lafyatis, A. G. Martin, E. L. Raab, R. N. Ahmad-Bitar, and D. E. Pritchard, “Continuous Stopping and Trapping of Neutral Atoms,” *Phys. Rev. Lett.* **58**, 2194 (1987).
- [42] T. Bergeman, G. Erez, and H. J. Metcalf, “Magnetostatic Trapping Fields for Neutral Atoms,” *Phys. Rev. A* **35**, 1535 (1987).
- [43] A.E. Leanhardt, Y. Shin, A.P. Chikkatur, D. Kielpinski, W. Ketterle, and D.E. Pritchard, “Bose-Einstein Condensates near a Microfabricated Surface,” *Phys. Rev. Lett.* **90**, 100404 (2003).
- [44] J. Fortágh, H. Ott, S. Kraft, A. Günther, and C. Zimmermann, “Surface Effects in Magnetic Microtraps,” *Phys. Rev. A* **66**, 041604(R) (2002).
- [45] W. Ketterle, D.D. Durfee, and D.M. Stamper-Kurn. “Making, Probing and Understanding Bose-Einstein Condensates,” Contribution to the proceedings of the 1998 Enrico Fermi summer school on Bose-Einstein condensation in Varenna, Italy (1999).
- [46] R. Newell, J. Sebby, and T. G. Walker, “Dense Atom Clouds in a Holographic Atom Trap,” *Opt. Lett.* **28**, 1266 (2003).
- [47] J.E. Bjorkholm, “Collision-limited Lifetimes of Atom Traps,” *Phys. Rev. A* **38**, 1599 (1988).

- [48] Z-Y. Ma, A. M Thomas, C.J. Foot and S.L. Cornish, "The Evaporative Cooling of a Gas of Caesium Atoms in the Hydrodynamic Regime", *J. Phys. B: At. Mol. Opt. Phys.* **36**, 3533 (2003).
- [49] H. J. Lewandowski, "Coherences and Correlations in an Ultracold Bose Gas," Ph.D. thesis, University of Colorado, 2002.
- [50] D.E. Pritchard, K. Helmerson, and A.G. Martin, in Atomic Physics 11, edited by S. Haroche, J.C.Gay, and G. Grynberg (World Scientific, Singapore) p179, (1989).
- [51] T.W. Hijmans, O.J. Luiten, I.D. Setija, and J.T.M. Walraven, "Optical Cooling of Atomic Hydrogen in a Magnetic Trap," *J. Opt. Soc. Am. B* **6**, 2235 (1989).
- [52] W. Ketterle, K.B. Davis, M.A. Joffe, A. Martin, and D.E. Pritchard, invited oral presentation at OSA Annual Meeting, Toronto, Canada, October 3-8 (1993).
- [53] J.J. Sakurai and S. F. Tuan, "Modern Quantum Mechanics," Addison-Wesley (1994).
- [54] D. M. Harber, J. M. McGuirk, J. M. Obrecht, E. A. Cornell, "Thermally Induced Losses in Ultra-Cold Atoms Magnetically Trapped Near Room-Temperature Surfaces," *J. Low Temp. Phys.* **133**, 229 (2003)
- [55] Y. J. Wang, "An On-Chip Atom Interferometer Using a Bose-Einstein Condensate," PhD thesis, JILA (2004).
- [56] L.P. Pitaevskii, "Vortex Lines in an Imperfect Bose Gas," *Zh. Eksp. Teor. Fiz.* **40**, 646 (1961).
- [57] E.P. Gross, "Structure of a Quantized Vortex in Boson Systems," *Nuovo Cimento* **20**, 454 (1961).
- [58] E. P. Gross, "Hydrodynamics of a Superfluid Condensate," *J. Math. Phys.* **4**, 195 (1963)
- [59] H. J. Lewandowski, D. M. Harber, D. L. Whitaker, and E. A. Cornell, "Simplified System for Creating a Bose-Einstein Condensate," *J. Low Temp. Phys.* **132**, 309 (2003).
- [60] C. J. Myatt, N. R. Newbury, R. W. Ghrist, S. Loutzenhiser, C. E. Wieman, "Multiply Loaded Magneto-optical Trap," *Opt. Lett.* **21**, 290 (1996).
- [61] S. Schneider, A. Kasper, Ch. vom Hagen, M. Bartenstein, B. Engeser, T. Schumm, I. Bar-Joseph, R. Folman, L. Feenstra, and J. Schmiedmayer, "Bose-Einstein Condensation in a Simple Microtrap," *Phys. Rev. A* **67**, 023612 (2003).
- [62] P. D. D Schwindt, "Magnetic Traps and Guides for Bose-Einstein Condensates on an Atom Chip: Progress toward a Coherent Atom Waveguide Beamsplitter", PhD thesis, JILA, (2003).
- [63] J. Fortagh, A. Grossmann, T.W. Hänsch, and C. Zimmermann, "Fast Loading of a Magneto Optical Trap from a Pulsed Thermal Source," *J. Appl. Phys.* **84**, 6499 (1998).
- [64] B. P. Anderson and M. A. Kasevich, "Loading a Vapor-cell Magneto-optic Trap Using Light-induced Atom Desorption," *Phys. Rev. A* **63**, 023404 (2001).

- [65] E. B. Alexandrov, M. V. Balabas, D. Budkler, D. English, D. F. Kimball, C.-H. Li, and V. V. Yashchuk, "Light-induced Desorption of Alkali-metal Atoms from Paraffin Coating," *Phys. Rev. A* **66**, 042903 (2002).
- [66] S. N. Autov, R. Calabrese, V. Guidi, B. Mai, A. G. Rudavets, E. Scansani, L. Tomassetti, V. Biancalana, A. Burchianti, C. Marinelli, E. Mariotti, L. Moi, and S. Veronesi, "Fast and Efficient Loading of a Rb Magneto-optical Trap using Light-induced Atomic Desorption" *Phys. Rev. A* **67**, 053401 (2003).
- [67] C. Zimmermann, J. Fortagh, H. Ott, S. Kraft, and A. Günther, "Bose-Einstein Condensates in Magnetic Micro Traps," Atomic Physics 18, Proceedings of ICAP 2002, Boston (2002).
- [68] C. J. Vale, B. Upcroft, M. J. Davis, N. R. Heckenberg and H. Rubinsztein-Dunlop, "Foil-based Atom Chip for Bose-Einstein Condensates," *J. Phys. B.* **37** 2959 (2004).
- [69] [http://cua.mit.edu/ketterle\\_group/research.htm](http://cua.mit.edu/ketterle_group/research.htm).
- [70] [http://jilawww.colorado.edu/bec/BEC\\_for\\_everyone/index.html](http://jilawww.colorado.edu/bec/BEC_for_everyone/index.html).
- [71] M. W. Flemming and A. Mooradian, "Spectral Characteristics of External-cavity Controlled Semiconductor Lasers," *IEEE J. Quantum Electron.* **QE-17**, 44 (1981).
- [72] R. Wyatt and W. J. Devlin, "10 kHz Linewidth 1.5 m InGaAsP External Cavity Laser with 55 nm Tuning Range," *Electron. Lett.* **19**, 110 (1983).
- [73] A. S. Arnold, J. S. Wilson,<sup>a</sup> and M. G. Boshier, "A Simple Extended-cavity Diode Laser," *Rev. Sci. Instrum.* **69**, 1236 (1998)
- [74] C. J. Hawthorn, K. P. Weber, and R. E. Scholtena, "Littrow Configuration Tunable External Cavity Diode Laser with Fixed Direction Output Beam," *Rev. Sci. Instrum.* **72**, 4477 (2001)
- [75] C. E. Wieman, L. Hollberg, "Using Diode Lasers for Atomic Physics," *Rev. Sci. Instrum.* **62**, 1 (1991)
- [76] K. Liu and M. G. Littman, "Novel Geometry for Single-mode Scanning of Tunable Lasers," *Opt. Lett.* **6**, 117, (1980)
- [77] L. Nilse, H. J. Davies, and C. S. Adams, "Synchronous Tuning of Extended Cavity Diode Lasers: the Case for an Optimum Pivot Point," *Applied Optics* **38**, 548 (1999).
- [78] W. R. Trutna, Jr., and L. F. Stokes, "Continuously Tuned External Cavity Semiconductor Laser," *J. Lightwave Technol.* **11**, 1279 (1993).
- [79] K. Nakagawa, M. Teshima\* and M. Ohtsu, "Injection Locking of a Highly Coherent and High-power Diode Laser at 1.5  $\mu\text{m}$ ," *Opt. Lett.* **16**, 1590 (1991)
- [80] K. Kurokawa, "Injection-locking of Solid-state Microwave Oscillators," *Proc. IEEE* **61**, 1386 (1973)
- [81] D. W. Preston, "Doppler-free Saturated Absorption: Laser Spectroscopy," *Am. J. Phys.* **64**, 1432 (1996)

- [82] M. E. Gehm, K. M. O'Hara, T. A. Savard, and J. E. Thomas, "Dynamics of Noise-induced Heating in Atom Traps," *Phys. Rev. A* **58**, 3914 (1998).
- [83] J.D. Weinstein, K.G. Libbrecht, "Microscopic Magnetic Traps for Neutral Atoms," *Phys. Rev. A* **52**, 4004 (1995)
- [84] J. Fortagh , H. Ott , A. Grossmann , C. Zimmermann, "Miniaturized Magnetic Guide for Neutral Atoms," *Appl. Phys. B* **70**, 701 (2000).
- [85] A.E. Leanhardt, A.P. Chikkatur, D. Kielpinski, Y. Shin, T.L. Gustavson, W. Ketterle, and D.E. Pritchard, "Propagation of Bose-Einstein Condensates in a Magnetic Waveguide," *Phys. Rev. Lett.* **89**, 040401 (2002).
- [86] Y. Lin, I. Teper, C. Chin, and V. Vuletic, "Impact of the Casimir-Polder Potential and Johnson Noise on Bose-Einstein Condensate Stability near Surfaces," *Phys. Rev. Lett.* **92**, 050404 (2004).
- [87] Y.J. Wang, D. Z. Anderson, V. M. Bright, E. A. Cornell, Q. Diot, T. Kishimoto, M. Prentiss, R. A. Saravanan, S. R. Segal, S. Wu, "An Atom Michelson Interferometer on a Chip Using a Bose-Einstein Condensate," submitted to *Phys. Rev. Lett.* (2004)
- [88] J. E. Lye, C. S. Fletcher, U. Kallmann, H-A Bachor and J. D. Close, "Images of evaporative cooling to Bose-Einstein condensation," *J. Opt. B* **4**, 57(2002).
- [89] M. Kasevich and S. Chu, "Atomic interferometry using stimulated Raman transitions," *Phys. Rev. Lett.* **67**, 181 (1991).
- [90] J. E. Simsarian, J. Denschlag, M. Edwards, C. W. Clark, L. Deng, E. W. Hagley, K. Helmerson, S. L. Rolston, and W. D. Phillips, "Imaging the Phase of an Evolving Bose-Einstein Condensate Wave Function," *Phys. Rev. Lett.* **85**, 2040 (2000).
- [91] Y. Torii, Y. Suzuki, M. Kozuma, T. Sugiura, T. Kuga, L. Deng, and E. W. Hagley, "Mach-Zehnder Bragg Interferometer for a Bose-Einstein Condensate," *Phys. Rev. A* **61**, 041602 (2000).
- [92] D. M. Harber, J. M. McGuirk, J. M. Obrecht, E. A. Cornell, "Thermally Induced Losses in Ultra-Cold Atoms Magnetically Trapped Near Room-Temperature Surfaces," *J. Low Temp. Phys.* **133**, 229 (2003)
- [93] S. Friebe, C. D'Andrea\*, J. Walz, M. Weitz, and T. W. Hänsch, "CO<sub>2</sub>-laser optical lattice with cold rubidium atoms," *Phys. Rev. A* **57**, R20 (1998).
- [94] Vladan Vuletic, Cheng Chin, Andrew J. Kerman, and Steven Chu, "Degenerate Raman Sideband Cooling of Trapped Cesium Atoms at Very High Atomic Densities," *Phys. Rev. Lett.* **81**, 5768 (1998).
- [95] M. Hammes, D. Rychtarik, B. Engeser, H.-C. Nägerl, and R. Grimm, "Evanescent-Wave Trapping and Evaporative Cooling of an Atomic Gas at the Crossover to Two Dimensions," *Phys. Rev. Lett.* **90**, 173001 (2003)

- [96] M. D. Barrett, J. A. Sauer, and M. S. Chapman, "All-Optical Formation of an Atomic Bose-Einstein Condensate," *Phys. Rev. Lett.* **87**, 010404 (2001)
- [97] E. I Butikov, "Parametric excitation of a linear oscillator," *Eur. J. Phys.* **25**, 535, (2004).
- [98] E. A. Burt, R. W. Ghrist, C. J. Myatt, M. J. Holland, E. A. Cornell, and C. E. Wieman, "Coherence, Correlations, and Collisions: What One Learns about Bose-Einstein Condensates from Their Decay," *Phys. Rev. Lett.* **79**, 337 (1997).
- [99] Ketterle and D.E. Pritchard, "Trapping and Focusing Ground State Atoms with Static Fields," *Appl. Phys. B* **54**, 403 (1992).
- [100] C. R. Monroe, E. A. Cornell, C. A. Sackett, C. J. Myatt, and C. E. Wieman, "Measurement of Cs-Cs Elastic Scattering at  $T=30 \mu\text{K}$ ," *Phys. Rev. Lett.* **70**, 414 (1993).
- [101] S. Inouye, "Manipulating Bose-Einstein Condensates with Laser Light," PhD thesis, MIT (2001).

## Appendix 1. Atom-chip cell vacuum lifetime

The vacuum of our first portable Bose-Einstein condensation (BEC) atom-chip cell was broken when we changed the wire connector by putting too much force incidentally on the side of the chip, two months after we pinched off the cell, and one month after we achieved BEC. After that, we have built and tested more than three cells. However, we consistently observe finite vacuum lifetimes for these cells. Right after baking out and pinching off, we are able to achieve a good enough vacuum level for BEC production with a UV magneto-optical trap (MOT) lifetime of about 30 s. However, after one month, the cell vacuum becomes worse and worse and the UV MOT lifetime drops below 15 s and no BEC is achievable at this level.

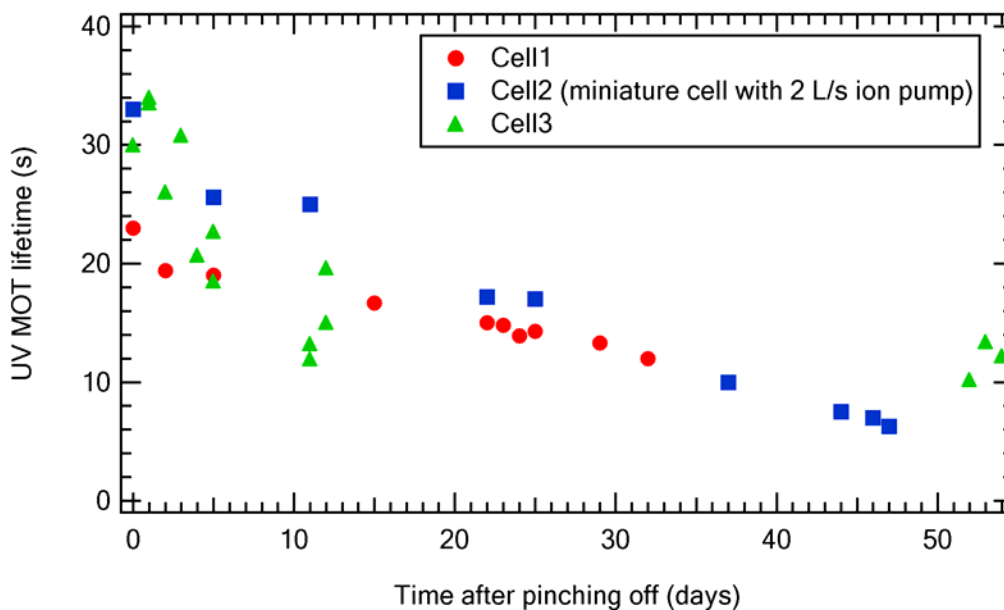


Figure A1.1: UV MOT lifetime history after pinching off.

Figure A1.1 shows the histories of UV MOT lifetime of three different cells. The UV MOT lifetime decay and finite vacuum lifetime reduce the possibility for further atom-chip BEC applications. My last year's research focuses on finding out what causes the problem. Here, I summarize what we have found out related to the cell vacuum lifetime:

1. The finite vacuum lifetime is consistent with cells prepared at different times, as shown in figure A1.1.
2. The finite vacuum lifetime is not caused by the negligible leak and diffusion of helium from air through the cell glass walls. At the experiment, we put helium gas around the quartz cell, and observe a rapid drop of the UV MOT lifetime. The helium leak and diffusion time constant is about 2–4 days, as shown in figure A1.2, much shorter than the UV MOT lifetime decay. After the helium source is turned off, the UV MOT lifetime recovers and follows its previous decay slope. This is a great way to measure the helium diffusion rate through the quartz cell if the helium pressure is well known. The difference between the vacuum lifetime (about 1 month) and the short helium diffusion/leak time constant (2–4 days) suggests that the finite vacuum lifetime is not caused by the negligible leaks and diffusion of helium in air through the cell glass walls.

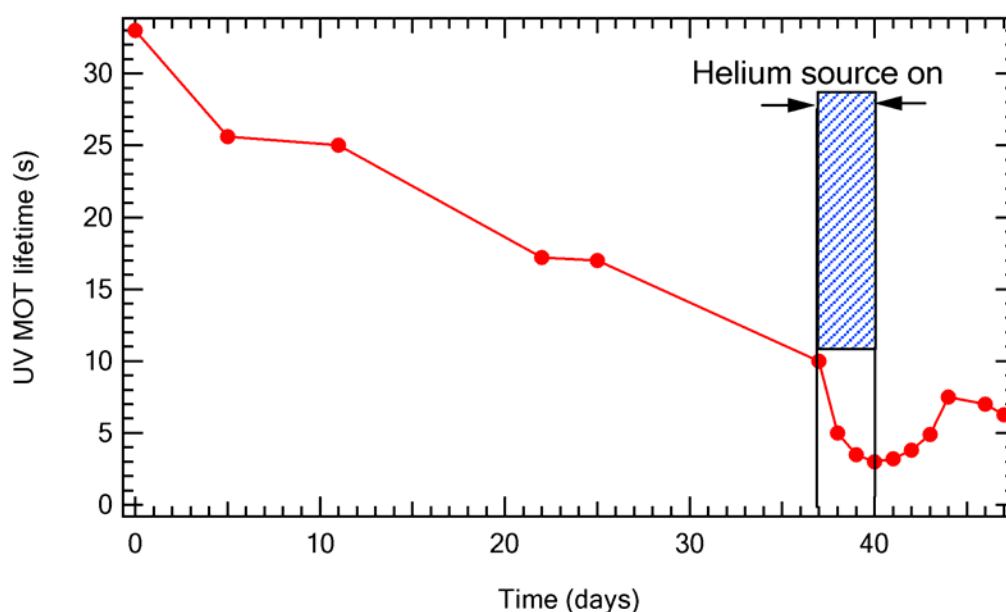


Figure A1.2: Helium leak and diffusion test. After we turn on the helium gas around the cell, the UV MOT lifetime reduces rapidly. After we turn off the helium source, the vacuum recovers and the UV MOT lifetime increases back in about 4 days.

3. The finite vacuum lifetime is not caused by the finite capacity of the small, 8 L/s, ion pump. From the manufacturer's specification, it is far from saturation under our

operating vacuum pressure level. We have built a miniature cell with a 2 L/s smaller ion pump, as described in appendix 2, and get the same long vacuum lifetime as 8 L/s ion pump, as shown in figure A1.1.

4. The finite vacuum lifetime is not caused by running the rubidium dispenser in daily routing for charging the cell (section 7.1) because the vacuum becomes worse even without running the dispenser.
5. The UV MOT lifetime goes back to 30 s after rebaking the cell at about 110 °C for 48 hours. However, it decays down again to the value before rebaking in about one week.
6. The procedure of cleaning the quartz cell inner walls with a flash lamp, as described in section 3.5, has influence on the vacuum lifetime. We have tested a cell without the flashing-cleaning procedure, and observe no decay of the UV MOT lifetime up to one month, as shown in figure A1.3. However, in such a cell without the flashing-cleaning procedure, we are not able to load enough atoms into the mirror MOT with UV light-induced atomic desorption (section 7.2).

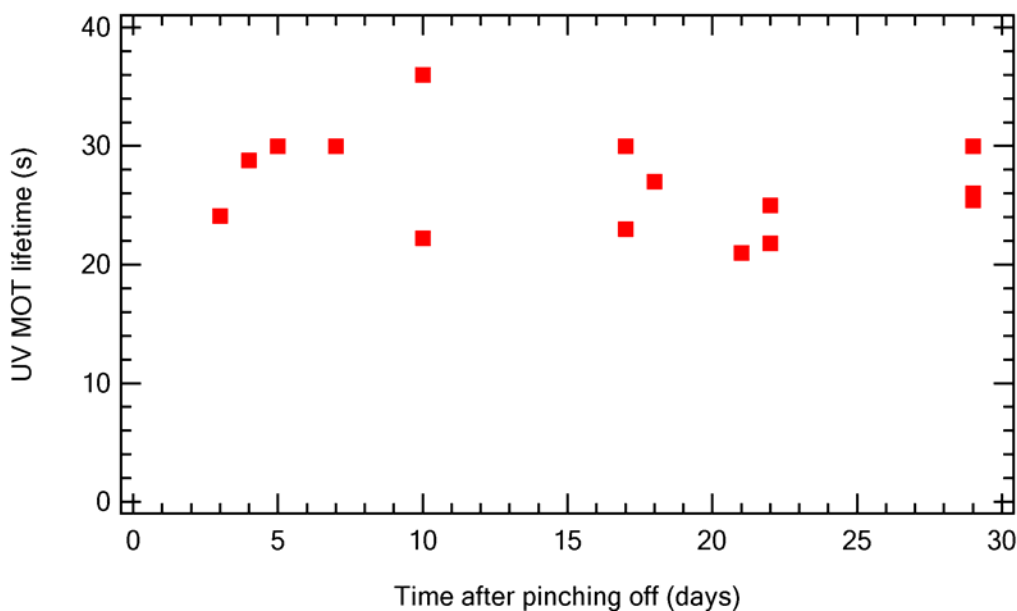


Figure A1.3: UV MOT lifetime of the cell without flashing.



Based on the above facts, we suspect that the “deterioration” of the cell vacuum, which reduces the UV MOT lifetime, results from the epoxy used to seal the vacuum with the atom chip. From the evidence shown in figure A1.3, we suspect that the high power flash light in the flashing-cleaning procedure may affect the properties of the epoxy such that the epoxy slowly releases something, which is difficult to be pumped away by the ion pump and nonevaporable getter, in the cell. Moreover, because of using epoxy, we are only able to bake the quartz cell part below 200 °C, which is not sufficient to remove all the water layers on the quartz walls and limits the vacuum pressure.

Our future improvement of the cell vacuum will rely on avoiding using the epoxy and baking the glass cell at a higher temperature. Cooperating with Rockwell Scientific Company and Sarnoff Corporation, we are developing atom via-chip and anodic bonding [A1-1–A1-6] technologies. The chip via avoids passing the wire pattern through the sealing junction and makes it possible to anodically bond the chip directly to a Pyrex cell without using any epoxy. The anodic bonding cell also allows for a high baking temperature of more than 450 °C.

---

[A1-1] T.R. Anthony, “Anodic Bonding of Imperfect Surfaces,” *J. Appl. Phys.* **54**, 2419 (1983).

[A1-2] A. Hanneborg, N. Nese, and P. Ohlckers, “Silicon-to-Silicon Anodic Bonding,” *Techn. Dig. Micromechanics Europe* (1990), *2nd Workshop on Micromechanics Berlin* (1990).

[A1-3] K.B. Albaugh, “Electrode Phenomena during Anodic Bonding of Silicon to Sodium Borosilicate Glass,” *J. Electrochem Soc.* **138**, 3089 (1991).

[A1-4] H.J. Quenzer, C. Dell, and B. Wagner, “Silicon-silicon Anodic Bonding with Intermediate Glass Layer Using Spin-on Glass,” *Proceedings IEEE, 9th Workshop on Micro Electro Mechanical Systems MEMS*, San Diego (1996).

[A1-5] A. Gerlach, D. Mass, D. Seidel, H. Bartuch, S. Schundau, K. Kaschilk, “Low-Temperature Anodic Bonding of Silicon to Silicon Wafers by Means of Intermediate Glass layers”, *Microsystem Technologies* **5**, 144 (1999).

[A1-6] H.J. Quenzer, A.V. Schulz, T. Kinkopf, and T. Helm, “Anodic Bonding on Glass Layers Prepared by a Spin-on Glass Process: Preparation Process and Experimental Results,” *The 11th International Conference on Solid-State Sensors and Actuators*, Munich, Germany, June 10-14 (2001).

## Appendix 2. A miniature atom-chip vacuum cell

As previously discussed in section 3.3.5, the conductance of the square quartz cell ( $1 \times 1 \times 4$  cm) for Rb atoms at room temperature is 2.2 L/s, and the conductance of the glass-to-metal transition tube (diameter 2.5 cm and length 9 cm) is 12.4 L/s. For air, they are 3.9 L/s and 21.2 L/s, respectively. Therefore, the small square quartz cell limits the overall system conductance and an ion pump with a pumping speed lower than 8 L/s is enough to maintain the UHV pressure of the cell after pinching off.



Figure A2.1: Miniature atom-chip vacuum cell with a 2 L/s ion pump.

We have designed, built, and tested a miniature version atom-chip vacuum cell with a 2 L/s mini ion pump, as shown in figure A2.1. The system size is much smaller than the portable atom-chip cell presented in chapter 3. After baking out and pinching off, the miniature cell has the same performance as the portable one with 8 L/s ion pump. Unfortunately, because of the finite vacuum lifetime issue (appendix 1), we have not been able to achieve Bose-Einstein condensation (BEC) in this miniature atom-chip cell. As discussed in appendix 1, the dimension of the vacuum system is not the cause of the finite vacuum lifetime. Therefore, in the future, after solving the vacuum deterioration problem possibly by via-chip and anodic bonding technologies, we expect to create BEC in the miniature cell.